SELECTED PRODUCTION MECHANISMS OF QUARKONIA WITH EVEN CHARGE PARITY

Izabela Magdalena Babiarz

Division of Nuclear Physics and Strong Interactions

The Henryk Niewodniczański
Institute of Nuclear Physics Polish Academy of Sciences

A thesis submitted for the degree of

Doctor of Philosophy

Prepared under supervision of
dr hab. Wolfgang Schäfer, prof. IFJ PAN

Thesis co-supervisor
dr hab. Marta Łuszczak, prof. UR

Kraków, 2021

I would like to dedicate this thesis to my loving family.

Acknowledgements

Abstract

The purpose of this dissertation is to analyze selected production mechanisms of quarkonia with positive charge parity. In particular, the quark-antiquark bound states such as $\eta_c(1S)$, $\eta_c(2S)$, $\chi_{c0}(1P)$ as well as a spinless bound state of the bottom quark and anti-bottom quark $\chi_{b0}(1P)$ were considered. The amplitude of the processes was formulated in the $k_\perp$-factorization approach using a newly developed model by means of the light cone wave functions of bound states. Namely, the wave functions on the light cone were used to construct the appropriate transition form factors $\gamma^*\gamma^* \to \eta_c$ and $\gamma^*\gamma^* \to \chi_Q$ and then adapted to the processes involving protons. In addition, the processes of producing a charmonium pairs $\chi_{c0}\chi_{c0}$, $\chi_{c1}\chi_{c1}$, $\chi_{c2}\chi_{c2}$ with additional gluon emission in three different configurations were discussed. Another mechanism taken under investigation in the thesis is the exclusive production of $\eta_c(1S)$ and $\chi_{c0}(1P)$ in proton-proton collisions using the model proposed by the Durham group with applied newly developed reaction vertex.

Streszczenie

Celem niniejszej rozprawy jest analiza wybranych mechanizmów produkcji kwarkonii o dodatniej parzystości ładunkowej. W szczególności rozważaniom zostały poddane bezspinowe stany związane kwarku powabnego i antykwarku antypowabnego takie jak $\eta_c(1S)$, $\eta_c(2S)$ $\chi_{c0}(1P)$, a także bezspinowy stan związany kwarku dolnego i antykwarku antydolnego χ_{b0}. Amplituda procesów została sformułowana w podejściu $k_\perp$-faktoryzacji z wykorzystaniem nowo opracowanego modelu za pomocą funkcji falowych stanów związanych na stożku świetlnym. Mianowicie, funkcje falowe na stożku świetlnym posłużyły do skonstruowania odpowiednich form faktorów przejścia $\gamma^*\gamma^* \to \eta_c$, $\gamma^*\gamma^* \to \chi_Q$, a następnie zaadoptowane do procesów z udziałem protonów. Ponadto dyskusji został poddany proces produkcji pary kwarkonii powabnych $\chi_{c0}\chi_{c0}$, $\chi_{c1}\chi_{c1}$, $\chi_{c2}\chi_{c2}$ z dodatkową emisją gluonu w trzech różnych konfiguracjach. Jednym z rozważanych aspektów jest również proces ekskluzywnej produkcji $\eta_c(1S)$ oraz $\chi_{c0}(1P)$ w zderzeniach proton-proton przy pomocy modelu zaproponowa-nego przez grupę z Durham z zastosowaniem nowo opracowanej amplitudy przejścia.

Contents

CONTENTS

List of Figures

List of Tables

Chapter 1

Introduction

The Standard Model (SM) of particle physics constitutes our best understanding of observed particles and their interactions in the framework of Quantum Field Theory. The SM involves the theory of electro-weak interactions and Quantum-Chromo-Dynamics (QCD), which is the quantum field theory of strong interaction. The unified electro-weak quantum field theory combines a description of phenomena induced by the photon and electrically charged fermions, Quantum-Electro-Dynamics (QED), and the weak interactions, which are mediated by the $W^{\pm}$ and Z bosons. The Standard Model is a gauge theory with the invariance under local transformations of the gauge group $SU(3)_c \times SU(2) \times U(1)$. A diagonal subgroup of the electro-weak gauge group $SU(2) \times U(1)$ is the $U(1)_{EM}$ group, which is associated with a massless spin-1 particle - the photon, which is exchanged in the electromagnetic processes.

Apart from flavor quantum numbers such as charm, strangeness, or isospin for light quarks, the fundamental spin-$\frac{1}{2}$ matter particles – the quarks – also carry color. The local gauge symmetry $SU(3)_c$ has a non-Abelian character, which besides requiring an exchange of a gauge particle with spin 1 (the gluon) also enforces the gluons to interact between themselves. The main property that arises directly from the self-interaction of gluons is asymptotic freedom. Historically, Quarkonia played a leading role in the confirmation of *asymptotic freedom* phenomenon. In the analogy to positronium, a heavy quark-antiquark bound state is named quarkonium, for instance, charmonium (charm-anticharm) or bottomonium (bottom-antibottom) states. In fact, at a short distance, the strong interaction force was observed to be weak [1, 2]. Today the effective color charge squared α_s is determined mainly from the description of hard processes involving the production of jets. The the

1. INTRODUCTION

smallness of the strong coupling constant at a short distance allows to present complicated QCD formulas in the form of perturbative series in $\alpha_s(\mu_R)$, where μ_R is a renormalization scale, which must be much larger than the intrinsic QCD scale $\Lambda_{QCD} \sim 250\,\text{MeV}$.

Physical states, including mesons and baryons, are experimentally observed to be colorless, which imposes that all hadrons have to be $SU(3)_c$ singlets. This phenomenon stands for the intricate dynamics of QCD at a large distance and is known as *color confinement*.

The quarkonium production processes are one of the main research tools for investigation Quantum Chromodynamic properties in high-energy particle collisions. They do offer an opportunity to describe both the production dynamics as well as their bound structure in terms of QCD degrees of freedom – quarks and gluons. Despite decades of studies on quarkonium physics there is still wide group of problems to concern oneself with. The strong interest in the subject at present is reflected in the fact that recently there appeared a new review of charmonium prospects at high luminosity project at CERN [3] as well as a review dedicated new theoretical developments of inclusive quarkonia production [4]. Still new approaches are under consideration including the light front formalism which we set out to further develop in our work or formalisms based on effective field theory methods, such as pNRQCD [5].

$$\star\,\star\,\star$$

Various analyses of quarkonia, excited states of quarkonia or associated production with another particle are some of the crucial points to understand the perturbative and non-perturbative nature of QCD. The main aim of the thesis was to study mechanisms of quarkonia production induced by gluons, but in the course of our studies we were also led to investigate the analogous virtual-photon induced processes.

One of the points was to develop a coherent approach starting from form factors using the smallest amount of arbitrary parameters to apply them into hadroduction in $k_\perp$-factorization approach. Furthermore, to find out if the structure of the $Q\bar{Q}$ system wave function has an impact on the transition form factors or differential distributions related to quarkonium production.

This thesis is organized in the following order. In subsequent sections, we will introduce essential properties of the discussed quarkonia and briefly comment on phenomenological concepts of calculating relevant cross-sections in a proton-proton collision.

In Chapter 2, we focus on $\chi_{cJ}\chi_{cJ}$ pairs production in collinear approach in high-energy proton-proton collision with real gluon *mini* jet production. We discuss emissions in the central rapidity region in between $\chi_{cJ}\chi_{cJ}$ pair as well external emissions.

In Chapter 3, we put under investigation space-like $\gamma^*\gamma^*$ transition form factors. We present the salient properties of the light-cone wave functions of $Q\bar{Q}$ bound states. We consider (in a spectroscopic notation explained below) the (1S), (2S), and (1P) states in the case of $c\bar{c}$ while in the case of $b\bar{b}$ system we restrict ourselves to the (1P) system. We introduce step by step the construction of the transition form factor $\gamma^*\gamma^* \to \mathcal{Q}$, where $\mathcal{Q}$ denotes a quarkonium state of even charge parity. We derive a master formula that expresses the relevant $\gamma^*\gamma^* \to \mathcal{Q}$ amplitudes in terms of the relevant "radial" light-cone wave functions. We analyze related observables such as the radiative decay rate or the so-called decay constant. Additionally, we investigate symmetry properties of those form factors and illustrate the behavior of normalized the symmetry quantities $|F_{TT}(Q^2, 0)/F_{TT}(0, 0)|$.

In Chapter 4, we consider prompt hadroproduction of $\eta_c(1S)$, $\eta_c(2S)$ and $\chi_{c0}(1P)$ $\chi_{b0}(1P)$ in $k_\perp$-factorization approach. We start with deriving the matrix element in the $k_\perp$-factorization approach and give some general comments on unintegrated gluon distributions function in a proton. In particular, we investigate the asymmetric kinematic region $2 < y < 4.5$ in the center of the mass system (c.m.s.), which corresponds to acceptance of the LHCb experiment. We then move on to applying form factors to the matrix element. Subsequently, we present predicted distributions in meson transverse momentum, rapidity, transverse momentum of the fusing gluons, as well as the fraction of the longitudinal momentum of the colliding protons carried by a parton.

In Chapter 5, we again take advantage of the prepared $g^*g^* \to \mathcal{Q}$ vertex within the adopted color singlet model, which we employ to central exclusive production (CEP) in a proton-proton collision. The central exclusive process provides a unique environment where we can test our vertex. We begin with an introduction to the process kinematics and amplitude formulation in the framework of the Durham model. Relevant pieces of this model are off-diagonal gluon densities which we

build with the help of various approaches. We analyze several differential cross-sections including transferred momentum squared, rapidity of $\eta_c(1S)$ and $\chi_{c0}(1P)$ with incorporated skewness correction, and the distribution in the relative azimuthal angle of outgoing protons. We illustrate the projection on transverse momentum of the produced meson. We estimate the absorptive correction to the Born level cross-section.

In Chapter 6, we summarize the performed analysis with essential conclusions and outlook.

$\star\,\star\,\star$

The presented thesis is based on the following original articles:

- I. Babiarz, W. Schäfer, A. Szczurek, *Associated production of χ_c pairs with a gluon in the collinear-factorization approach*,
  Phys. Rev. D99 (2019)7, 074014 [6]

- I. Babiarz, V.P. Goncalves, R. Pasechnik, W. Schäfer, A. Szczurek,
  $\gamma^*\gamma^* \to \eta_c(1S, 2S)$ transition form factors for spacelike photons,
  Phys. Rev. D100 (2019), 054018 [7]

- I. Babiarz, R. Pasechnik, W. Schäfer, A. Szczurek, *Prompt hadroproduction of $\eta_c(1S, 2S)$ in the k_T-factorization approach*,
  JHEP 02 (2020), 037 [8]

- I. Babiarz, R. Pasechnik, W. Schäfer, A. Szczurek, *Hadroproduction of scalar P-wave quarkonia in the light-front k_T-factorization approach*,
  JHEP 06 (2020), 101 [9]

- I. Babiarz, R. Pasechnik, W. Schäfer, A. Szczurek, *Central exclusive production of scalar and pseudoscalar charmonia in the light-front k_T-factorization approach*, Phys. Rev. D102 (2020), 114028 [10]

The research results were also presented at the following conferences:

- I. Babiarz, W. Schäfer, A. Szczurek, *Production of χ_c meson pairs with additional emission* 15th International Workshop on Meson Physics (MESON 2018), 7-12 June 2018. Kraków, Poland [11]

- <u>I. Babiarz</u>, V.P. Goncalves, R. Pasechnik, W. Schäfer, A. Szczurek, *The $\gamma^*\gamma^* \to \eta_c(1S, 2S)$ transition form factor from Quarkonium wave functions*, International Conference on the Structure and the Interactions of the Photon (Photon 2019), 3-7 June 2019. Frascati, Italy [12]

- <u>I. Babiarz</u>, V.P. Goncalves, R. Pasechnik, W. Schäfer, A. Szczurek, *The $\gamma^*\gamma^* \to \eta_c(1S, 2S)$ transition form factors for two spacelike photons* 2019 European Physical Society Conference on High Energy Physics (EPS-HEP2019), 10-17 July 2019. Ghent, Belgium [13]

- <u>I. Babiarz</u>, W. Schäfer, A. Szczurek, *Production of η_c(1S,2S) in e^+e^- and pp collisions*, 40th International Conference on High Energy Physics (ICHEP2020), 30 July-5 August 2020. Prague, Czechia [14]

- <u>I. Babiarz</u>, R. Pasechnik, W. Schäfer, A. Szczurek, *Central exclusive production of η_c and χ_{c0} in the light-front $k_\perp$-factorization approach*, 28th International Workshop on Deep Inelastic Scattering and Related Subjects (DIS2021), 12-16 April 2021. United States, Online conference [15]

$\star\,\star\,\star$

The articles beyond of the thesis scope

- I. Babiarz, R. Staszewski, A. Szczurek, *Multi-parton interactions and rapidity gap survival probability in jet–gap–jet processes* Phys. Lett. B 771 (2017), 532-538 [16]

- M. Łuszczak, R. Maciuła, A. Szczurek, I. Babiarz, *Single-diffractive production of dijets within the k_T-factorization approach*, Phys. Rev. D 96 (2017), 054018 [17]

- R. Maciuła, A. Szczurek, J. Zaremba, I. Babiarz, *Production asymmetry of ν_τ neutrinos and $\overline{\nu}_\tau$ antineutrinos from a fixed target experiment SHiP*, JHEP 01 (2020), 116 [18]

1.1   Charmonium and Bottomonium Spectra

Similarly to atoms, charmonia and bottomonia are observed also in excited states of higher energy. The interest of this work is mainly centered around the charmonium ground state $\eta_c(1S)$, the excited state $\eta_c(2S)$ and the family of $\chi_{cJ}(1P)$ with total angular momentum $J = 0, 1, 2$. We also paid attention to the spinless χ_{b0} meson.

In the nonrelativistic picture of quark-antiquark $c\bar{c}$ or $b\bar{b}$ pairs, the bound state is characterized by total angular momentum J composed of the relative orbital angular momentum L and the spin S of the pair [19]. It is convenient to introduce a scheme $(n_r + 1)^{(2S+1)}L_J$, which encodes characteristic quantum numbers of particles. Moreover, n_r number is recognized as *radial* excitation number, whereas $L = 0, 1, 2, \ldots$, as in atomic physics, are labeled by $L = S, P, D, \ldots$ and determine together with the intrinsic parity of quarks, parity of each state to be $P = (-1)^{L+1}$. Therefore, corresponding quarkonium states are commonly denoted as $S - waves$, $P - waves$ or $D - waves$.

The two body quark-antiquark $(s_c = \pm 1/2, s_{\bar{c}} = \pm 1/2)$ system could appear in the form of spin singlet $(2S + 1 = 1),^1S_0$ or spin triplet $(2S + 1 = 3)$, $^3S_1$ states.

Another convenient quantum number to label quarkonium states is by the eigenvalue of the charge conjugation operator. The charge conjugation is an exact symmetry of strong and electromagnetic interactions, but is violated in the weak interactions. For the spin-1/2 fermion-antifermion pair, $C = (-1)^{L+S}$, hence we can recognise the C-even or C-odd quarkonia states. Note that there are some constraints on the allowed values of J^{PC} for systems composed out of quark and antiquark. Several combinations such as 0^{--}, 0^{+-} or 1^{-+} apparently would not found in this scheme. In the case, when particle system has such a set of quantum numbers , we often call them an exotic state, as they cannot be quark-antiquark "quarkonia".

Especially in the main text, we will refer to pseudoscalar η_c (spin: 0 and P-parity: -1, C-parity: +1) and scalar χ_{c0} or χ_{b0} (spin: 0 and P-parity: +1, C-parity: +1) mesons.

In Tab. 1.1 we reveal characteristic properties of the quarkonium bound state, including mass, full decay width and fraction of a radiative decay rate to full width. In addition, we summarize quantum numbers and information about isospin I (all of the quarkonia are $I = 0$) and G-parity of multiplets, where eigenvalues of the G-parity operator are determined by $(-1)^{(L+S+I)}$.

Table 1.1: Properties and quantum numbers of considered quarkonia [20].

Meson name	$(n_r + 1)^{(2S+1)}L_J$	$J^{PC}(I^G)$	Mass (MeV)	Γ (MeV)	$\Gamma_{\gamma\gamma}/\Gamma \times 10^{-4}$
$\eta_c\,(1S)$	1^1S_0	$0^{-+}(0^+)$	2983.9 ± 0.4	32.0 ± 0.7	(1.61 ± 0.12)
$\eta_c\,(2S)$	2^1S_0	$0^{-+}(0^+)$	3637.5 ± 1.1	$11.3^{+3.2}_{-2.9}$	(1.9 ± 1.3)
$\chi_{c0}\,(1P)$	1^3P_0	$0^{++}(0^+)$	3414.71 ± 0.30	10.8 ± 0.6	(2.04 ± 0.09)
$\chi_{c1}\,(1P)$	1^3P_1	$1^{++}(0^+)$	3510.67 ± 0.05	0.84 ± 0.04	$< 6.3 \times 10^{-2}$
$\chi_{c2}\,(1P)$	1^3P_2	$2^{++}(0^+)$	3556.17 ± 0.07	1.97 ± 0.09	(2.85 ± 0.10)
$\chi_{b0}\,(1P)$	1^3P_0	$0^{++}(0^+)$	$9859.44^{\pm0.42}_{\pm0.31}$	undetermined	undetermined

Conventionally masses of the $D\bar{D}$ (for charmonia) and $B\bar{B}$ (for bottomonia) are refered to as an open flavour threshold. Heavy $Q\bar{Q}$ systems, which are placed below the threshold can decay to lighter $Q\bar{Q}$ states e.g. via radiative transitions, or as the lightest quarkonia decay via the annihilation of the quark-antiquark pair.

All of the analysed mesons in the thesis have masses below the open flavour thresholds, see Figs. 1.1, 1.2.

The overview of Quarkonium levels, their decay channels, and decay rates, together with a more detailed discussion, is included in Ref. [21] and references therein. For illustration, Fig. 1.1 depicts the currently observed and possible $c\bar{c}$ state in spectroscopic level scheme. The solid black lines correspond to the states confirmed experimentally, while $c\bar{c}$ bound systems indicated by the dashed lines need further verification. The dotted lines mark open charm thresholds. Fig. 1.2 reveals spectra of mesons contained $b\bar{b}$ quarks. The arrows indicate the most dominant hadronic transitions.

States above the open flavor thresholds are under much discussion recently and are expected to be understood as meson-meson molecules, multiquark systems (e.g. tetraquarks) or other exotic phenomena, see e.g. [22]. The potential model alone cannot work in this domain, as one has to take into account the coupling of $Q\bar{Q}$ states to the meson-meson continua.

A potential toponium state contributes less than one percent to $t\bar{t}$ pair production in a proton-proton collision at Large Hadron Collider (LHC) [23] and has a

substantial decay rate. It is often pointed out that the top quarks decay faster than the bound state is created. However, searching for top-meson via two gluon fusion near the open threshold is still an ongoing problem.

In this work, we will focus on charmonium systems, including η_c, η'_c, χ_{c0} and bottomonium system χ_{b0}. All mentioned mesons are spinless and characterized by an even value of charge parity.
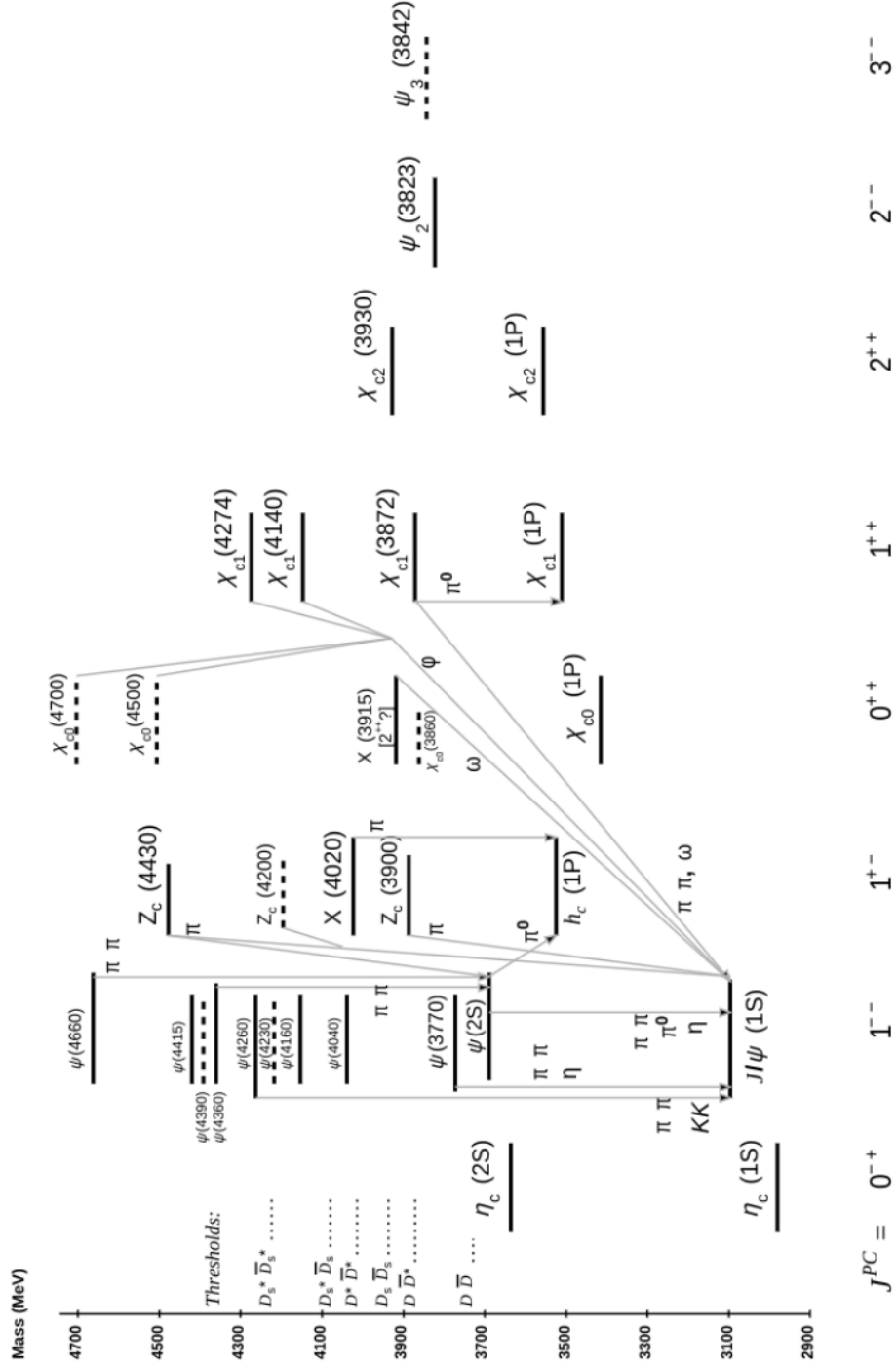
Figure 1.1: *The scheme of the spectra of mesons with a $c\bar{c}$ quark content, the plot originates from an updated review of Particle Data [20].*
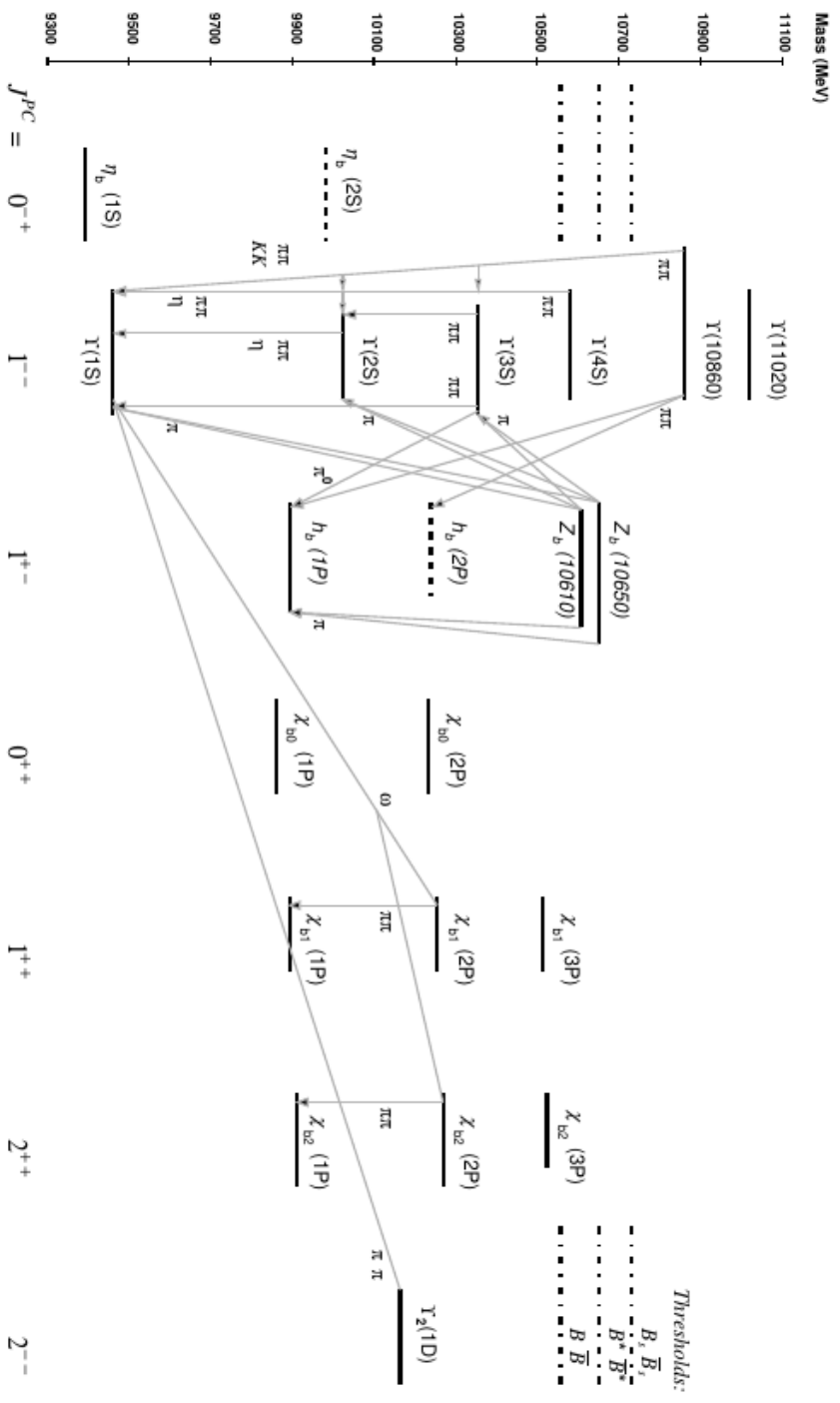
Figure 1.2: The scheme of the spectra of mesons with a $b\bar{b}$ quark content, the plot originates from an updated review of Particle Data [20].

1.2 Phenomenological models of heavy quarkonia production

Since the announcement of the first discovery of a charmonium state (the J/ψ) in 1974 [1, 24] physicists have put much effort to develop a theory, which describes the charmonium production in hadron collisions. In the beginning, two major approaches were proposed, the color-singlet model and the color evaporation model.

In the color evaporation model (CEM), it is assumed that invariant mass M of the $c\bar{c}$ or $b\bar{b}$ pair is produced between $D\bar{D}$ or $B\bar{B}$ threshold $2m_c < M < 2m_D$, $2m_b < M < 2m_B$ for charmonium and bottomonium states, respectively. Then the $Q\bar{Q}$ pair hadronizes [25, 26, 27] into $\mathcal{Q}$ meson accompanied by randomly emitted soft particles. The general expression for CEM production can be written as

$$\frac{d\sigma_{\mathcal{Q}}(P)}{d^3P} = F_{\mathcal{Q}} \int_{2m_c}^{2m_D} dM \frac{d\hat{\sigma}_{c\bar{c}}(M,P)}{dM d^3P}, \quad \text{or} \quad \frac{d\sigma_{\mathcal{Q}}(P)}{d^3P} = F_{\mathcal{Q}} \int_{2m_b}^{2m_B} dM \frac{d\hat{\sigma}_{b\bar{b}}(M,P)}{dM d^3P},$$

(1.1)

where $\hat{\sigma}_{Q\bar{Q}}$ can be calculated perturbatively as a function of m_Q, $m_{D,B}$ and $\alpha_s(m_Q)$, and $F_{\mathcal{Q}}$ is phenomenological parameter, which corresponds to $Q\bar{Q}$ fraction that results in $\mathcal{Q}$ meson production. It is assumed that the hadronization factor $F_{\mathcal{Q}}$ is independent on the kinematics of the process. The conclusion drawn from the CEM is that the hadronization factors for quarkonia fulfill relations for instance

$$F_{\mathcal{Q}} = F_{J/\psi} \frac{\sigma(\mathcal{Q})}{\sigma(J/\psi)}.$$

(1.2)

Besides the simple and intuitive picture of the CEM, this approach suffers from disagreement with experimental data for the ratio Ψ' to J/ψ, which depends on their transverse momenta [28, 29]. However, an intensively discussed approach is the so-called improved color evaporation model (ICEM) introduced in Ref. [27].

The color-singlet model (CSM) is based on the assumption that $Q\bar{Q}$ state is a nonrelativistic bound state interacting through confining potential. The relative momentum of the $Q\bar{Q}$ pair in the rest frame of the bound state then has to be small in comparison to the heavy quark mass m_Q. It is assumed that the short-distance part of the amplitude is not affected by changes in the small relative momentum of the $Q\bar{Q}$ pair. Therefore the amplitude is constructed under the assumption that the $Q\bar{Q}$ length scale in the production amplitude is point-like on the scale corresponding to the quarkonium wave function. Thus, the only occurring phenomenological

1. INTRODUCTION

parameters in this approach are radial wave function $R_{\eta_c}(0)$ at the origin or the first derivative $R'(0)_{\chi_c/\chi_b}$ for χ_c and χ_b multiplets. The radial part of the wave function at $r = 0$ can be found by solving Schrödinger equation with the particular potential model of $Q\bar{Q}$ interaction (see Appendix A) as well as from their relation to the radiative decay constant.

In the color-singlet model all non-perturbative effects are stored in the wave function factor $\Psi_{\mathcal{Q}}^{(k)}(0)$, while the second part of the amplitude $\hat{\sigma}_{Q\bar{Q}}$ is calculated with the help of perturbative Quantum Chromo-Dynamic in α_s expansion. The general scheme of the cross-section is the following

$$\sigma_{\mathcal{Q}} = \int d\hat{\sigma}_{Q\bar{Q}} \, |\Psi_{\mathcal{Q}}^{(k)}(0)|^2 \,, \tag{1.3}$$

where $\Psi_{\mathcal{Q}}^{(k)}(0)$ is connected to the first term of the amplitude, which does not vanish in Taylor expansion around relative momentum of the quarks in the meson (see App. A).

$$\Psi_{n0}(0) = \frac{1}{\sqrt{4\pi}} R_{n0}(0) \,, \quad \Psi'_{n1}(0) = \sqrt{\frac{3}{4\pi}} R'_{n1}(0) \,. \tag{1.4}$$

Therefore, CSM provides an intuitive illustration of the perturbative production of heavy quarkonium. The main objection regarding this approach is that in the collinear factorization does not describe experimental data collected by the CDF group at the Tevatron.

Quarkonium states consist not only of valence pure $Q\bar{Q}$ bound state. It could exist in states which sub-cluster of quarks in color-octet configuration. This idea can be depicted in the superposition of gluons and quarks Fock states of the meson $\mathcal{Q}$

$$|\mathcal{Q}\rangle = \psi_{Q\bar{Q}}|Q\bar{Q}\rangle + \psi_{Q\bar{Q}g}|Q\bar{Q}g\rangle + \psi_{Q\bar{Q}q\bar{q}}|Q\bar{Q}q\bar{q}\rangle + \cdots \,. \tag{1.5}$$

In CSM, only the first Fock state is taken into account to construct quarkonium with specific quantum numbers.

In the Color-Octet model (COM) also higher component of the Fock state expansion contribute. The COM is in a similar spirit as the color evaporation model, namely the heavy quark pair can be produced not only with exact quantum numbers as physically observed meson state, but different produced states can evolve into the observed quarkonium after emission of a soft gluon. The COM is based on an effective field theory with special *scaling rules* or so-called *power counting* in

which non-relativistic $Q\bar{Q}$ system is factorized. Three scales can be specified: mass scale (m_Q), momentum scale $(m_Q v)$ and energy scale $(m_Q v^2)$ with the preserved separation between them

$$(m_Q)^2 \gg (m_Q v)^2 \gg (m_Q v^2)^2 \,. \tag{1.6}$$

The quark mass defines a scale at which perturbative expansion in α_s is applicable, $\alpha_s \ll 1$. Because $m_Q \gg \Lambda_{QCD}$ processes occurring at the scale m_Q can be calculated perturbatively. The momentum scale corresponds to the size of the quarkonium state and allows to distinguish the long-distance evolution region into meson. Here, v stands for the bound state relative momentum, which typically for $c\bar{c}$ is $v^2 \sim 0.3$ and for $b\bar{b}$ is $v^2 \sim 0.1$.

The application of the NRQCD scheme to quarkonium production, for example for the case of $P - wave$ quarkonia, is formulated in the following way [30]:

$$\sigma_{\chi_{QJ}} = \int \Big(d\hat{\sigma}_{Q\bar{Q}(^3P_J^{[1]})}(2J+1)\langle \mathcal{O}^{\chi_{Q0}}(^3P_0^{[1]})\rangle$$
$$+ d\hat{\sigma}_{Q\bar{Q}(^3S_1^{[8]})}(2J+1)\langle \mathcal{O}^{\chi_{Q0}}(^3S_1^{[8]})\rangle \Big). \tag{1.7}$$

This factorization formula, which represents the leading order in the NRQCD power counting scheme, contains two terms. Firstly, we have the color singlet piece, where the $Q\bar{Q}$ system is produced with the physical quantum numbers of the relevant χ_{QJ} state. Here $\mathcal{O}^{\chi_{Q0}}(^3P_0^{[1]})$ stands for color singlet operator, which can be related to the the first derivative of the radial wave function at the origin

$$\langle \mathcal{O}^{\chi_{Q0}}(^3P_0^{[1]})\rangle = \frac{3N_c}{2\pi}|R'_{\chi_{Q0}}(0)|^2 \,. \tag{1.8}$$

If we took this term into account alone, we would reproduce the non-relativistic color-singlet model.

Besides the color singlet piece, there is a color octet term, where the leading order in NRQCD counting the $Q\bar{Q}$ pair is produced in the hard process with the $^3S_1^{[8]}$ quantum numbers. During the nonperturbative evolution of the $Q\bar{Q}$ system after its production, it transforms, say by emission of soft gluons, into the color-singlet ^3P_J state. The operator matrix element quantify the strength of this transition $\mathcal{O}^{\chi_{Q0}}(^3S_1^{[8]})$. The latter has a priori no simple relation to the wave function of the bound state, and practical phenomenology has to be fitted.

1. INTRODUCTION

The NRQCD approach is potentially very powerful in making order-by-order improvable predictions as an effective field theory. In fact, it has many successes in describing quarkonium transitions and decays. However, for quarkonium production, its weak point is the proliferation of fit parameters (the operator matrix elements) with increasing order of the NRQCD expansion.

This is the reason why we stick to a color singlet formulation. However, we do not stop at the nonrelativistic expressions used in the "classic" color singlet model. We also utilize the k_T factorization, which is known to at least partially cure many quantitative problems of the collinear approach.

Chapter 2

Charmonium Pair Production with Real Gluon Emission

2.1 Introduction

Much attention has been drawn to charmonium pair production, for a few years. So far, J/ψ pairs have become accessible experimentally at large rates, but the origin of the pair production process is still mysterious. Indeed, two J/ψ mesons can be produced in either in the SPS (single parton scattering) mode as well as in the DPS (double parton scattering) mode [31, 32]. The sketch of χ_{cJ} pair production at LHC energies is depicted in Fig. 2.1. In fact, many properties of DPS processes can be mimicked by single parton scattering with large rapidity separation.
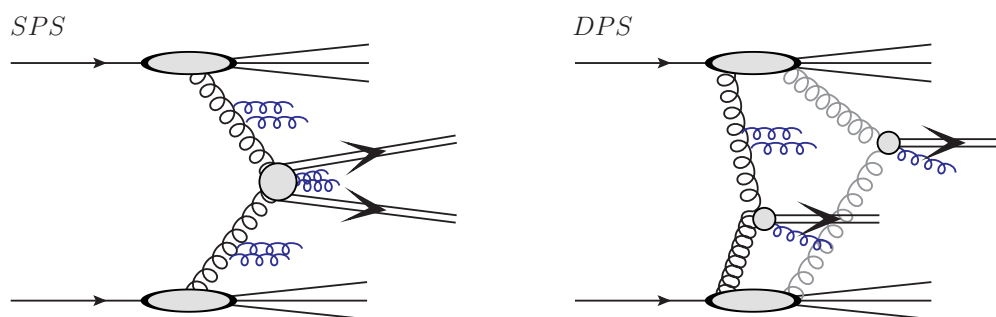
Figure 2.1: The sketch of single parton scattering (SPS) on l.h.s. and double parton scattering (DPS) r.h.s.

At energies accessible at the LHC, the preferred mechanisms are those where gluons carry small x. This feature implies a higher probability to observe more than

2. CHARMONIUM PAIR PRODUCTION WITH REAL GLUON EMISSION

one hard process in the same proton-proton collision. In Ref. [33] it was shown that SPS and DPS cross-sections are about the same order of magnitude. In the kinematic acceptance of the LHCb experiment [34, 35] the SPS mechanism of J/ψ's pair results in a good description of the collected data. However, if the rapidity distance between J/ψ's from the pair is large that is in practice $|\Delta y| > 2$, the single parton scattering model at leading order [36, 37] underestimates the experimental data collected by CMS [38] and ATLAS [39] at the Large Hadron Collider.

Another interesting mechanism in proton-proton collision, which may lead to $J/\psi J/\psi$ pair production is a tetraquark $T_{4c}(6900)$ decay [40]. The tetraquark is assumed to be composed of $cc\bar{c}\bar{c}$ and mainly produced via two gluon fusion in SPS ($gg \to T_{4c}$) as well as DPS ($gggg \to T_{4c}$, $ggq\bar{q} \to T_{4c}$) processes.

Moreover, one may expect a significant contribution from χ_{cJ} radiative decay to J/ψ mode. Previously in the literature J/ψ pair production was discussed in the k_T-factorization framework in pp and $PbPb$ collisions [36, 37, 41] within a perturbative nonrelativistic quantum chromodynamics (NRQCD) model. Relatively recent studies on quarkonium pair production in the color-evaporation model have been performed [42].

Relevant processes for the first-order correction to χ_{cJ}-pair production can be illustrated by the Feynman diagrams in Fig. 2.2. At high gluon-gluon c.m.-energies, the additional gluon jet may be emitted in three distinct, well-separated kinematical regions. Firstly it can be emitted in the central rapidity region between two χ_{cJ} (Fig. 2.2a), or as a "leading" jet carrying a large fraction of the energy/momentum of one of the incoming gluons, see diagram Fig. 2.2 b,c).

In this section we will discuss how to calculate the diagrams of Fig. 2.2 using the vertices of the Lipatov effective action [43, 44, 45] of high-energy QCD. In section 2.2 we will discuss parton level cross sections for the $2 \to 3$ process $gg \to g\chi_c\chi_c$, and in section 2.3 we calculate hadron-level cross sections using the collinear gluon distributions.

Let us discuss the kinematics of the processes of interest. At high c.m.-energies $\sqrt{s}$ we can neglect the masses of incoming protons so that their four-momenta in the pp-c.m. frame can be written as

$$P_{1,\mu} = \frac{\sqrt{s}}{2} n_\mu^+, \ P_{2,\mu} = \frac{\sqrt{s}}{2} n_\mu^-, \tag{2.1}$$
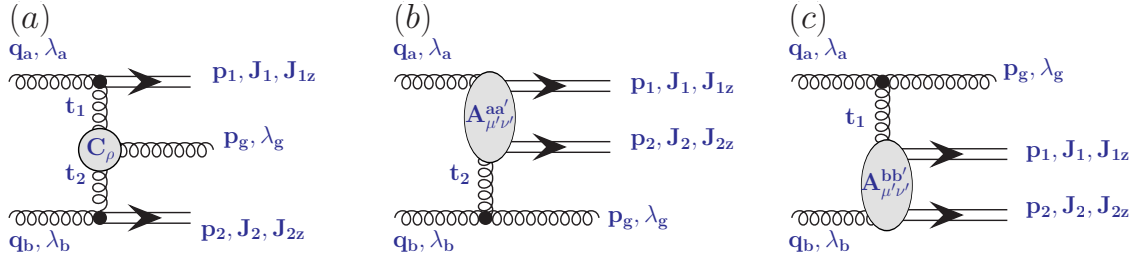
Figure 2.2: Real gluon emission in three particular processes $gg \to g\chi_{cJ_1}\chi_{cJ_2}$.
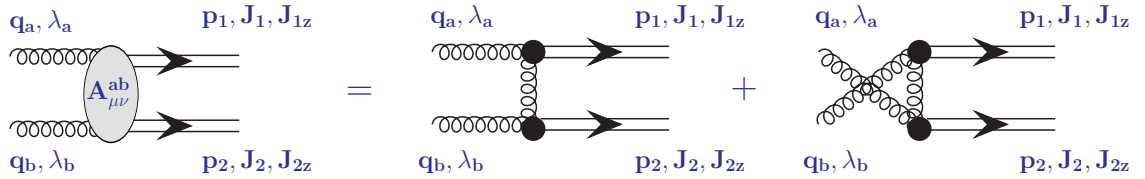
Figure 2.3: Exact form of the blob vertex from Fig. 2.2 (b),(c).

with the light-like basis vectors (see Appendix D for more details on the notation)

$$n^{\pm}_{\mu} = \frac{1}{\sqrt{2}}(1, 0, 0, \pm 1). \tag{2.2}$$

In our approximation, the incoming gluons are collinear to the protons, i.e.

$$q_{a\mu} = q^+_a n^+_{\mu} = x_1 P_{1\mu}, \quad q_{b\mu} = q^-_b n^-_{\mu} = x_2 P_{2\mu}, \tag{2.3}$$

The c.m.-energy squared of the gluon-gluon process is

$$(q_a + q_b)^2 = (x_1 P_1 + x_2 P_2)^2 = x_1 x_2 s. \tag{2.4}$$

We are interested in a situation in which the final state gluon is emitted at a large rapidity distance to the next (χ_c) final state particle. In this case, the vertical gluon lines in the diagrams of Fig. 2.2 have to bridge a large distance in rapidity. The exchange of so-called reggeized gluons describes these gluon exchanges within the Lipatov effective action approach. The vertices for the couplings of reggeized gluons to other fields can be found in a convenient form in Ref. [44]. We adapt them to the slightly different conventions regarding light-cone vectors $n^{\pm}_{\mu}$ used by us. Each propagator of a reggeized gluon with four-momentum q gets a factor

$$D_{\mu\nu}(q) = \frac{n^-_{\mu} n^+_{\nu}}{q^2}. \tag{2.5}$$

2. CHARMONIUM PAIR PRODUCTION WITH REAL GLUON EMISSION

Here the vector n_μ^+ multiplies the "upper" vertex, and n_ν^- the "lower" vertex connected by the propagator.

The central blob in diagram 2.2 a involves the *"Lipatov effective vertex"* [45], expressed by the equation

$$\Gamma_{\mu\rho\nu}(q_1, q_2) = n_\mu^- n_\nu^+ C_\rho(q_1, q_2),$$

$$C_\rho(q_1, q_2) = (q_1^+ + \frac{q_1^2}{q_2^-})n_\rho^+ - (q_2^- + \frac{q_2^2}{q_1^+})n_\rho^- + (q_2 - q_1)_\rho^\perp, \qquad (2.6)$$

in the BFKL (Balitsky-Fadin-Kuraev-Lipatov) approach, where q_1, q_2 are four momenta of gluons incoming into the vertex. In terms of light-cone components, the gluon momenta are parametrized as

$$q_{1\mu} = q_1^+ n_\mu^+ + q_{1\mu}^\perp, \ q_{2\mu} = q_2^- n_\mu^- + q_{2\mu}^\perp \text{ with } q_1^2 = -\vec{q}_{1\perp}^{\ 2}, q_2^2 = -\vec{q}_{2\perp}^{\ 2}, . \qquad (2.7)$$

It is important that within the range of validity of the Lipatov action approach, the momentum flow is such that there is always a dominant flow of $(+)$-momentum from "above" and $(-)$-momentum from "below" into a vertex.

In this way, the important conditions ("Ward identities")

$$q_1^\mu \Gamma_{\mu\rho\nu}(q_1, q_2) = 0, \ q_2^\nu \Gamma_{\mu\rho\nu}(q_1, q_2) = 0, \ (q_1 + q_2)^\rho \Gamma_{\mu\rho\nu} = 0, \qquad (2.8)$$

can be easily seen to be fulfilled. They are closely related to the gauge invariance of the approach.

In the two remaining diagrams 2.2 b,c, the blob vertex corresponds to amplitude comprised of t and u channels of $\chi_{cJ}\chi_{cJ}$ production (see Fig. 2.3). Notice that the gluon exchanged within in this blob (the vertical gluon lines in Fig. 2.3) are not assumed by us to be reggeized gluons. In our calculation, we use for them the covariant Feynman gauge, so that the corresponding amplitude can be written as:

$$A_{\mu\nu}^{ab}(q_a, q_b; p_1, p_2) = V_{\mu\mu'}^{aa'}(J_1, J_{z1}; q_a, p_1 - q_a)\frac{-g^{\mu'\nu'}\delta^{a'b'}}{\hat{t}}V_{\nu'\nu}^{bb'}(J_1, J_{z1}; p_2 - q_b, q_b)$$

$$+ V_{\nu\nu'}^{bb'}(J_1, J_{z1}; q_b, p_1 - q_b)\frac{-g^{\mu'\nu'}\delta^{a'b'}}{\hat{u}}V_{\mu'\mu}^{aa'}(J_1, J_{z1}; p_1 - q_a, q_a), \qquad (2.9)$$

where $V_{\mu\mu'}^{aa'}(J_1, J_{z1}; q_a, p_1 - q_a)$ is the $g^* g^* \to \chi_{cJ}$ vertex. These vertices were previously derived in the color singlet approximation of NRQCD in ref. [33], and can be written as

$$V_{\mu\nu}^{ab}(J, J_z; q_1, q_2) = -i4\pi\alpha_s \delta^{ab} \frac{2R'(0)}{\sqrt{\pi N_c M_{\chi_c}^3}}\sqrt{3}T_{\mu\nu}(J, J_z; q_1, q_2). \qquad (2.10)$$

where the first derivative of radial wave function at origin can be found by the relation (see e.g. [46])

$$\Gamma(\chi_{c0} \to \gamma\gamma) = \frac{27 e_c^4 \alpha_{em}^2}{m_c^4} |R'(0)|^2. \tag{2.11}$$

In our numerical calculations, the value $|R'(0)|^2 = 0.042\,\mathrm{GeV}^5$ is used.

For completeness, let us write down the explicit expressions from Ref. [33] for all possible spin states of the χ_{cJ} family:

1. scalar, $J = 0, J_z = 0$:

$$
\begin{aligned}
T_{\mu\nu}(0,0;q_1,q_2) &= \frac{1}{\sqrt{3}} \frac{M^2}{(2q_1 \cdot q_2)^2} \Big\{ g_{\mu\nu} \Big(6(q_1 \cdot q_2) - q_1^2 - q_2^2 + \frac{(q_2^2 - q_1^2)^2}{M^2} \Big) \\
&+ q_{1\mu} q_{2\nu}\, 2\Big(\frac{q_1^2 + q_2^2}{M^2} - 1\Big) + q_{2\mu} q_{1\nu}\, 2\Big(\frac{q_1^2 + q_2^2}{M^2} - 3\Big) \\
&+ q_{1\mu} q_{1\nu} \frac{4 q_2^2}{M^2} + q_{2\mu} q_{2\nu} \frac{4 q_1^2}{M^2} \Big\}
\end{aligned}
\tag{2.12}
$$

2. axial vector, $J = 1, J_z = \pm 1, 0$:

$$
\begin{aligned}
T_{\mu\nu}(1,J_z;q_1,q_2) &= \frac{i}{\sqrt{2}M} \frac{1}{(q_1 \cdot q_2)} \Big\{ (q_1^2 - q_2^2)\epsilon_{\mu\nu\alpha\beta}(q_1 + q_2)^\alpha \epsilon^\beta(P,J_z) \\
&+ \frac{q_1^2 + q_2^2}{(q_1 \cdot q_2)}(a_\mu q_{1\nu} - a_\nu q_{2\mu}) + 2(a_\nu q_{1\mu} - a_\mu q_{2\nu}) \Big\}
\end{aligned}
\tag{2.13}
$$

with

$$a_\mu = \epsilon_{\mu\rho\alpha\beta} q_1^\rho q_2^\alpha \epsilon^\beta(P,J_z). \tag{2.14}$$

3. tensor, $J = 2, J_z = \pm 2, \pm 1, 0$:

$$
\begin{aligned}
T_{\mu\nu}(2,J_z;q_1,q_2) &= \frac{-M^2}{(2q_1 \cdot q_2)^2} \Big\{ - g_{\mu\nu}(q_2 - q_1)^\alpha (q_2 - q_1)^\beta \epsilon_{\alpha\beta}(P,J_z) \\
&+ 4(q_1 \cdot q_2)\epsilon_{\mu\nu}(P,J_z) \\
&+ 2(q_2 - q_1)^\alpha \epsilon_{\alpha\nu}(P,J_z)q_{2\mu} - 2(q_2 - q_1)^\alpha \epsilon_{\alpha\mu}(P,J_z)q_{1\nu} \Big\},
\end{aligned}
\tag{2.15}
$$

Above $P = q_1 + q_2$ is the four-momentum of the bound state, and $\epsilon_\mu(P,J_z)$ is the polarization vector of the $J = 1$ state, while the $J = 2$ state has a polarization tensor

$$\epsilon_{\mu\nu}(P,J_z) = \sum_{m_1,m_2} \langle 2,J_z|1,m_1,1,m_2\rangle \epsilon_\mu(P,m_1)\epsilon_\nu(P,m_2). \tag{2.16}$$

2. CHARMONIUM PAIR PRODUCTION WITH REAL GLUON EMISSION

All the tensors $T_{\mu\nu}(J, J_z, q_1, q_2)$ fulfill the QED-like gauge invariance conditions

$$q_1^\mu T_{\mu\nu}(J, J_z, q_1, q_2) = 0, \; q_2^\nu T_{\mu\nu}(J, J_z, q_1, q_2) = 0. \tag{2.17}$$

In eq. 2.9 Mandelstam variables $\hat{t}$ and $\hat{u}$ are

$$\hat{t} = (q_a - p_1)^2, \quad \hat{u} = (q_a - p_2)^2. \tag{2.18}$$

To construct the full amplitude of Feynman diagrams 2.2a-c), we also need the couplings of the reggeized gluon to the leading *upper* and *lower* gluon jets. They are described as follows

$$n^{-\rho}\Gamma_{\mu\nu\rho}(q_a, p_1) = 2q_a^+ g_{\mu\nu} + n_\mu^-(p_1 - 2q_a)_\nu + (q_a - 2p_1)_\mu n_\nu^- - \frac{(p_1 - q_a)^2}{q_a^+} n_\mu^- n_\nu^-,$$

$$n^{+\rho}\Gamma_{\mu\nu\rho}(q_b, p_2) = 2q_b^- g_{\mu\nu} + n_\mu^+(p_2 - 2q_b)_\nu + (q_b - 2p_2)_\mu n_\nu^+ - \frac{(p_2 - q_b)^2}{q_b^-} n_\mu^+ n_\nu^+. \tag{2.19}$$

The last step is to construct proper scattering amplitude, thus the amplitude for the first diagram in Fig. 2.2 reads

$$\mathcal{A}(gg \to \chi_{cJ} g \chi_{cJ}) = ig_s f_{a'b'c'} \varepsilon^\mu(\lambda_a, q_a) V_{\mu\mu'}^{aa'}(J_1, J_{1z}; q_a, p_1 - q_a) n^{-\mu'}$$
$$\times \frac{1}{t_1} C^\rho(q_a - p_1, qb - p_2) \varepsilon_\rho^*(\lambda_g, p_g) \frac{1}{t_2} \varepsilon^\nu(\lambda_b, q_b) V_{\nu'\nu}^{bb'}(J, Jz; q_b, p_2 - q_b) n^{+\nu}. \tag{2.20}$$

For the next two processes with leading upper and leading lower gluon the amplitudes are as follow

$$\mathcal{A}(gg \to g\chi_{cJ}\chi_{cJ}) = ig_s f_{a'b'c'} \varepsilon^\mu(\lambda_a, q_a) \Gamma_{\mu\nu\rho}(q_a, p_g) n^{-\rho} \varepsilon^{\nu*}(\lambda_g, p_g)$$
$$\times \frac{1}{t_1} n^{+\mu'} A_{\mu'\nu'}^{b'b}(p_g - q_a, q_b; p_1, p_2)(gg \to \chi_c\chi_c) \varepsilon^{\nu'}(\lambda_b, q_b), \tag{2.21}$$

$$\mathcal{A}(gg \to \chi_c\chi_c g) = ig_s f_{a'b'c'} n^{-\nu'} \varepsilon^{\mu'}(\lambda_a, q_a) A_{\mu'\nu'}^{aa'}(q_a, p_g - q_a; p_1, p_2)(gg \to \chi_c\chi_c)$$
$$\times \frac{1}{t_2} \varepsilon^\mu(\lambda_b, q_b) \Gamma_{\mu\nu\rho}(q_b, p_g) n^{+\rho} \varepsilon^{\nu*}(\lambda_g, p_g), \tag{2.22}$$

where $\varepsilon^\mu(\lambda, q)$ is polarization vector of the gluon. Because of the gauge invariance of the approach, explicit expressions for gluon polarization vectors are not needed. When averaging/summing over gluon polarizations, we can use the relation:

$$\sum_\lambda \epsilon_\mu^*(\lambda, p)\epsilon_\nu(\lambda, p) = -g_{\mu\nu}. \tag{2.23}$$

2.2 Parton level observables

This section is devoted to the first order perturbative correction to the inclusive χ_{cJ}-pair production in gluon-gluon collisions [1] which contains real contribution $(d\sigma^{(1)}(gg \to \chi_{cJ}\chi_{cJ}gX))$ as well as virtual corrections $(d\sigma^{(1)}(gg \to \chi_{cJ}\chi_{cJ}X))$. In general, the inclusive cross section for these reactions can be written in the form

$$
d\sigma(gg \to \chi_{cJ}\chi_{cJ}X) = d\sigma^{(0)}(gg \to \chi_{cJ}\chi_{cJ}X)
$$
$$
+ d\sigma^{(1)}(gg \to \chi_{cJ}\chi_{cJ}X) + d\sigma^{(1)}(gg \to \chi_{cJ}\chi_{cJ}gX) , \quad (2.24)
$$

and 'X' indicates that in the final state, extra particles besides the $\chi_{cJ}\chi_{cJ}$-pair can be produced. In order to go deeper in our analysis, it is worth dividing the problem into different processes, firstly the one where gluon in the final state is produced in between two χ_c's, and secondly, the processes where the gluon is found to be beyond the χ_c's pair in rapidity.

We first want to focus on the most interesting reaction in this context, the central gluon production. The real gluon emission at large rapidity distance among χ_{cJ}'s is expected to enhance the cross-section, while the virtual correction decreases the result. The parton level cross-section in terms of transverse momentum of the χ_c's mesons $\vec{p}_{1(2)\perp}$ and gluon rapidity y_g can be written in the form

$$
d\sigma = \frac{1}{256\pi^5\hat{s}^2}\overline{|\mathcal{A}(gg \to \chi_{cJ}\, g\, \chi_{cJ})|^2}dy_g d^2\vec{p}_{1\perp}d^2\vec{p}_{2\perp} . \quad (2.25)
$$

Now, when squaring the amplitude, we will have to evaluate

$$
\sum_{\lambda=\pm 1} C_\rho(q_1, q_2)\epsilon^\rho(\lambda, p_g)\epsilon^\tau(\lambda, p_g)C_\tau(q_1, q_2) = -C_\rho(q_1, q_2)C^\rho(q_1, q_2) , \quad (2.26)
$$

where we used Eq.2.23. Using the fact that the final state gluon is on-shell, $p_g^2 = (q_1 + q_2)^2 = 0$, we can obtain $2q_{1+}q_{2-} = (\vec{q}_{1\perp} + \vec{q}_{2\perp})^2$. Then it is straightforward to show that the square of the Lipatov-vertex becomes

$$
-C_\rho(q_1, q_2)C^\rho(q_1, q_2) = 4\frac{\vec{q}_{1\perp}^{\,2}\vec{q}_{2\perp}^{\,2}}{(\vec{q}_{1\perp} + \vec{q}_{2\perp})^2} . \quad (2.27)
$$

---

[1]We refer to the process as "parton level", although there are mesons in the final state.

2. CHARMONIUM PAIR PRODUCTION WITH REAL GLUON EMISSION

Now, it is useful to write the squared amplitude $\mathcal{A}(gg \to \chi_{cJ}\, g\, \chi_{cJ})$ in an easier to handle impact factor representation.

$$
\begin{aligned}
\overline{|\mathcal{A}(gg \to \chi_{cJ}\, g\, \chi_{cJ})|^2} &= \frac{N_c}{N_c^2 - 1} 16\pi\alpha_s I_1(\vec{p}_{1\perp}) \frac{\hat{s}^2}{(\vec{p}_{1\perp} + \vec{p}_{1\perp})^2} I_2(\vec{p}_{2\perp}) \quad (2.28) \\
&= \frac{16\pi^3 \hat{s}^2}{N_c^2 - 1} I_1(\vec{p}_{1\perp}) \frac{C_A \alpha_s}{\pi^2 (\vec{p}_{1\perp} + \vec{p}_{1\perp})^2} I_2(\vec{p}_{2\perp}) , \quad (2.29)
\end{aligned}
$$

Here, we have expressed the result in terms of the transverse momenta of final state mesons, recall that $\vec{q}_{1\perp} = -\vec{p}_{1\perp}$, $\vec{q}_{2\perp} = -\vec{p}_{2\perp}$. We see that the real part of the BFKL kernel for the central gluon production [45] appears

$$
\mathcal{K}_r = \frac{C_A \alpha_s}{\pi^2 (\vec{p}_{1\perp} + \vec{p}_{1\perp})^2} . \quad (2.30)
$$

The impact factors are defined in terms of the $gg^* \to \chi_{cJ}$ vertices as

$$
\begin{aligned}
I_1(\vec{q}_{1\perp}) &= \frac{1}{\vec{q}_{1\perp}^{\,2}} \frac{1}{2q_{a+}} \frac{1}{2} \sum_{\lambda, J_z} |\varepsilon^\mu(\lambda_a, q_a) V_{\mu\mu'}^{aa'}(J_1, J_{1z}; q_a, p_1 - q_a) n^{-\mu'}|^2 , \\
I_2(\vec{q}_{2\perp}) &= \frac{1}{\vec{q}_{2\perp}^{\,2}} \frac{1}{2q_{b-}} \frac{1}{2} \sum_{\lambda, J_z} |\varepsilon^\mu(\lambda_a, q_b) V_{\mu'\mu}^{aa'}(J_1, J_{1z}; q_b, p_2 - q_b) n^{+\mu'}|^2 , \quad (2.31)
\end{aligned}
$$

Notice that an infrared singularity appears in the case of back-to-back situation, $\vec{p}_{g\perp} = -(\vec{p}_{1\perp} + \vec{p}_{2\perp}) \Longrightarrow 0$. Thereafter integration over gluon rapidity y_g in Eq. (2.25) leads to

$$
\begin{aligned}
d\sigma(gg \to \chi_{cJ}\, g\, \chi_{cJ}) = \frac{Y}{16\pi^2(N_c^2 - 1)} I_1(\vec{p}_{1\perp}) \\
\mathcal{K}_r(\vec{p}_{1\perp}, -\vec{p}_{2\perp}) I_2(\vec{p}_{2\perp}) d^2\vec{p}_{1\perp} d^2\vec{p}_{2\perp} , \quad (2.32)
\end{aligned}
$$

here note that Y is proportional to $\log(\hat{s}/M_{\chi_{cJ}}^2)$, the difference between the rapidities of outgoing mesons.[1] In fact it is needed to count all leading order contribution to the cross section. Hence, virtual correction to the Born-level $2 \to 2$ cross section in Balitsky-Fadin-Kuraev-Lipatov (BFKL) formalism is written with the help of a *reggeized gluon*, which effectively leads to the replacement of the gluon propagator

$$
\frac{1}{q^2} \to \frac{1}{q^2} \exp[\omega(\vec{q}_\perp)Y] , \quad (2.33)
$$

---

[1]One therefore also refers to this as a leading-log($\hat{s}$) approximation.

and the *gluon Regge trajectory* reads [47]

$$\omega(\vec{q}_\perp) = -\frac{\alpha_s N_c}{4\pi^2} \int d^2\vec{Q}_\perp \frac{\vec{q}_\perp^2}{\vec{Q}_\perp^2(\vec{Q}_\perp - \vec{q}_\perp)^2} \, . \tag{2.34}$$

This exchanged *quasi particle* can be interpreted as *reggeized gluon* with spin $j = 1 + \omega(\vec{q}_\perp)$. Then the cross section for $2 \to 2$ involving the virtual correction at first order in $\alpha_s Y$ is

$$d\sigma(gg \to \chi_{cJ}\chi_{cJ}) = d\sigma^{(0)}(gg \to \chi_{cJ}\chi_{cJ}) + \frac{Y}{16\pi^2(N_c^2 - 1)} I_1(\vec{p}_{1\perp})$$
$$\times \, \delta^{(2)}(\vec{p}_{1\perp} + \vec{p}_{2\perp}) 2\omega(\vec{p}_{1\perp}) I_2(\vec{p}_{2\perp}) d^2\vec{p}_{1\perp} d^2\vec{p}_{2\perp} \, . \tag{2.35}$$

To sum up all contribution to gluon-gluon scattering to two charmonia one can write BFKL kernel

$$\mathcal{K}_{BFKL}(\vec{p}_{1\perp}, -\vec{p}_{2\perp}) = \frac{\alpha_s N_c}{\pi^2}\bigg(\frac{1}{(\vec{q}_{1\perp} + \vec{q}_{2\perp})^2}$$
$$- \delta^{(2)}(\vec{q}_{1\perp} + \vec{q}_{2\perp})\frac{1}{2}\int d^2\vec{Q}_\perp \frac{\vec{q}_{1\perp}^2}{\vec{Q}_\perp^2(\vec{Q}_\perp - \vec{q}_{1\perp})^2}\bigg) \, , \tag{2.36}$$

hence

$$d\sigma(gg \to \chi_{cJ}\chi_{cJ}X) = d\sigma^{(0)}(gg \to \chi_{cJ}\chi_{cJ}X) + \frac{Y}{16\pi^2(N_c^2 - 1)}$$
$$\times \, I_1(\vec{p}_{1\perp})\mathcal{K}_{BFKL}(\vec{p}_{1\perp}, -\vec{p}_{2\perp})I_2(\vec{p}_{2\perp})d^2\vec{p}_{1\perp}d^2\vec{p}_{2\perp}. \tag{2.37}$$

We see that the inclusive cross section with to the leading-log$\hat{s}$ accuracy corresponds exactly to one iteration of the kernel of the BFKL equation. Note that BFKL kernel in Eq. (2.36) has infrared singularities. In this case in our numerical calculation at the parton level with initial state parton distributions, we cannot absorb IR divergences. Nevertheless, both singularities in virtual and real term in BFKL kernel will cancel out in inclusive cross section with soft gluon radiation. In our case, we will not perform a full NLO calculation, but rather estimate the contribution from the emission of a "minijet". It means that we put a lower cut-off on the transverse momentum of the gluon $p_{g\perp}^{cut} = 1$ GeV, thus $p_{g\perp} = |\vec{q}_{1\perp} + \vec{q}_{2\perp}| > 1$ GeV. This puts our calculation outside of the infrared singularity into a safe region. In addition, to provide applicability of the *effective Lipatov vertex*, we put a requirement on the central gluon in the final state is produced in a rapidity distance from meson at least

2. CHARMONIUM PAIR PRODUCTION WITH REAL GLUON EMISSION
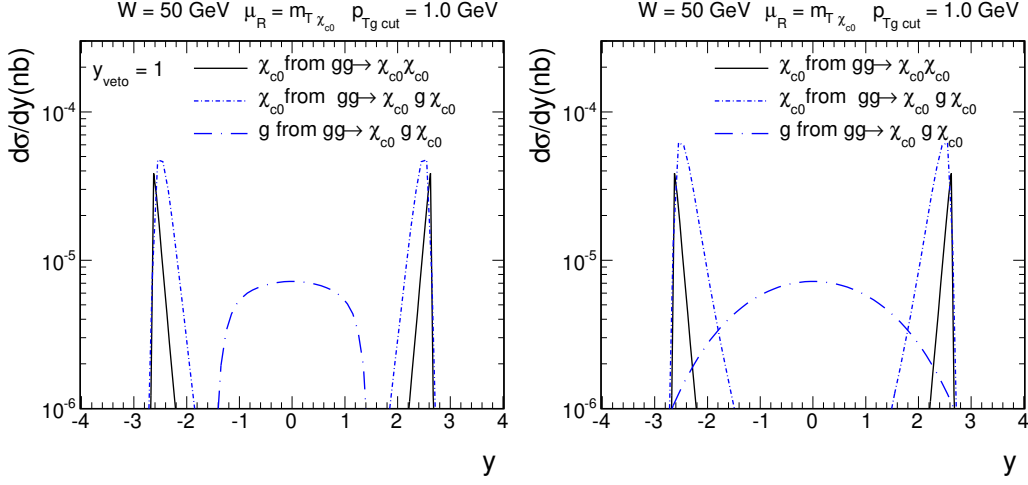
Figure 2.4: Differential cross section at the parton level for the reaction, where extra real gluon is produced in between two χ_{c0}'s.

$y_{veto} = 1$, thus $|y_{\chi_c} - y_g| > 1$. In the following we show observables of the parton-level process. Our numerical results were obtained at an energy $W = \sqrt{\hat{s}} = 50$ GeV in the c.m.-system of the two gluons.

Let us now turn to the processes shown by the second (b) and the third (c) diagram of the Fig. 2.2. Here, we are dealing with sub-processes where one of the fusing gluon is off-shell $g^*g \to \chi_{cJ}\chi_{cJ}$. In a complete NLO treatment, one would associate with the process a factorization scale μ_F, below which the off-shellness of incoming partons in the $g^*g \to \chi_{cJ}\chi_{cJ}$ sub-process can be neglected. As a result the cross-section at the parton level schematically is written as follows

$$d\sigma = \frac{2C_A\alpha_s}{\pi}\int^{\mu_F^2}\frac{dq_{1\perp}^2}{q_{1\perp}^2}\int_0^1\frac{dz_1}{z_1}d\sigma(2\to 2)$$
$$+ \frac{2C_A\alpha_s}{\pi}\int_{\mu_F^2}\frac{d^2\vec{q}_{1\perp}}{\pi q_{1\perp}^2}\int_0^1\frac{dz_1}{z_1}d\sigma(2\to 2; q_{1\perp}). \quad (2.38)$$

Here one can identify unintegrated gluon distribution factorised with incoming way

$$\frac{z\,dn(z,\vec{q_\perp})}{dz\,d\log q_\perp^2} = \frac{2C_A\alpha_s}{\pi}, \quad (2.39)$$

with strong coupling α_s, *Casimir* factor C_A and longitudinal fraction carried by gluon z. Then a genuine *Next-to-Leading-Order* contribution originates from the reaction with $q_\perp \gg \mu_F$. In the first term in Eq. (2.39), the virtuality of the gluon

in the pair production process can be neglected, and the $dq_{1\perp}^2/q_{1\perp}^2$ integration gives rise to the familiar collinear logarithm $\propto \log(\mu_F^2)$. A soft divergence will cancel after the full splitting function emerged by adding the relevant virtual correction. Here again, we avoid these subtleties, by just estimating the contribution to the cross section from the production of an additional mini-jet carrying transverse momentum $p_{g\perp} > 1$ GeV. For illustration in Fig. 2.4, we show differential distribution rapidity of χ_{c0}'s and gluon originating from $2 \to 3$ reaction as well as χ_{c0} pair from $2 \to 2$ process. In both processes χ_{c0}'s mesons are produced in the backward and forward direction, albeit the distribution from $gg \to \chi_{c0}g\chi_{c0}$ is a bit wider. In the left panel of Fig 2.4 one can notice that after application of *veto* to the rapidity of the centrally produced real gluon, the distribution becomes narrower in comparison to the right panel.

2.3 Observables in hadron collisions

The considered cases of χ_{cJ} pairs are restricted to be produced with identical spin configuration such as $\chi_{c0} + \chi_{c0} + g$, $\chi_{c1} + \chi_{c1} + g$, $\chi_{c2} + \chi_{c2} + g$. The inclusive cross section for the $2 \to 3$ processes is written in the form

$$d\sigma = x_1 g(x_1, \mu^2) x_2 g(x_2, \mu^2) \frac{1}{2!} \frac{1}{256\pi^5 \hat{s}^2} \overline{|\mathcal{A}(2 \to 3)|^2}$$
$$\times dy_1 dy_2 dy_g d^2\vec{p}_{1\perp} d^2\vec{p}_{2\perp} d^2\vec{p}_{g\perp} \delta^{(2)}(\vec{p}_{1\perp} + \vec{p}_{2\perp} + \vec{p}_{g\perp}), \quad (2.40)$$

where the statistical factor for identical particles $1/2!$ is included and the fraction of carried longitudinal momenta of the gluon are

$$x_1 = \frac{1}{\sqrt{s}}\left[m_{1\perp}e^{y_1} + m_{2\perp}e^{y_2} + p_{g\perp}e^{y_g}\right], \quad (2.41)$$

$$x_2 = \frac{1}{\sqrt{s}}\left[m_{1\perp}e^{-y_1} + m_{2\perp}e^{-y_2} + p_{g\perp}e^{-y_g}\right], \quad (2.42)$$

with transverse mass of the produced meson $m_{1(2)\perp} = \sqrt{M^2 + p_{1(2)\perp}^2}$ and $y_{1(2)}$ are rapidities of mesons.

Similarly to the Mueller-Navelet dijets production [48] with rapidity separation one would think of the cross section enhancement due to ressummation. However, it is worth to analyze each real gluon contribution separately.

2. CHARMONIUM PAIR PRODUCTION WITH REAL GLUON EMISSION
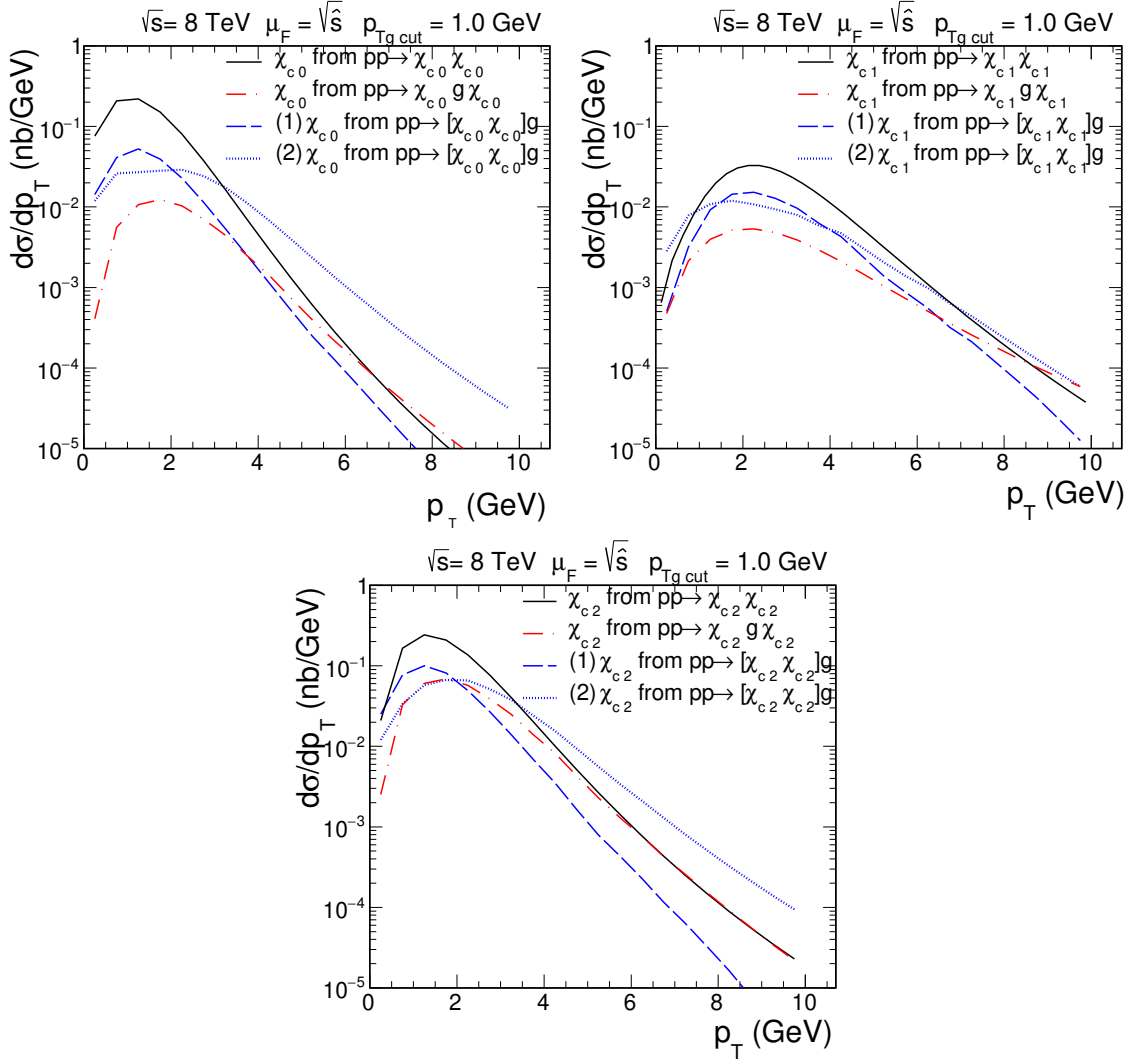
Figure 2.5: Differential distribution in transverse momentum of χ_{c0}(left panel), χ_{c1}(middle panel), χ_{c2} (right panel).

In Fig. 2.5, we compare the distribution in meson transverses momenta p_T for several processes from $pp \to \chi_{cJ}\chi_{cJ}$ with black solid line, which gives the largest cross-section for each χ_{cJ} production, from $pp \to \chi_{cJ}g\chi_{cJ}$ denoted by the dash-dotted red line. Blue curves are for external and internal meson in the final state of the process $pp \to \chi_{cJ}\chi_{cJ}g$. The slowly descending dotted curve represents centrally produced meson, this scheme is for χ_{c0} (left panel), χ_{c1} (middle panel) as well χ_{c2} (right panel). One can notice that results for inclusive χ_{c1} production are slightly

different from χ_{c0} and χ_{c2}, which might be caused by a strong dependence on fusion gluons transverse momenta[49].
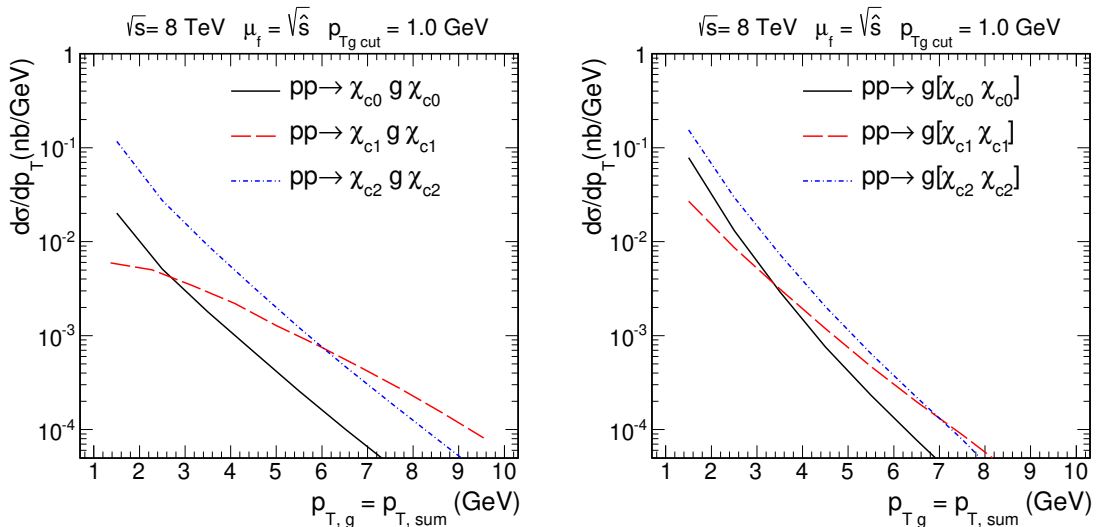
Figure 2.6: Differential distribution in transverse momenta of extra gluon, in the left panel for centrally produced gluon and in the right panel for externally produced gluon.

In Fig. 2.6, we present differential distribution for real gluon emission in two areas in the final state. As previously gluon(-mini jet) produced in between two mesons yields less steep plot (left panel) in contrast to external production (right panel).

Finally, in Fig. 2.7 differential distributions in rapidity are presented for $2 \rightarrow 3$ processes and compared to $2 \rightarrow 2$ inclusive process (black thick line). Considered $2 \rightarrow 2$ processes lead to χ_{cJ} productions in midrapidities region, while in $2 \rightarrow 3$ mechanisms one χ_{cJ} is emitted in forward or backward direction and the second χ_{cJ} is generated exactly on the opposite side or centrally. Note that in χ_{cJ} rapidity range $|y_{\chi_{cJ}}| > 3$ contributions from $2 \rightarrow 3$ mechanisms are not negligible. Gluon mini-jets in Fig. 2.7 are marked by the dotted curves for each $2 \rightarrow 3$ mechanism.

Another significant variable in the context of process with large rapidity separation is Δy defined as

$$\Delta y = y_{\chi_{cJ}} - y_g \,, \tag{2.43}$$

which informs about the distance in rapidity between gluon and one of the produced χ_{cJ}. In Fig. 2.8, one can observe that peaks arise at $|\Delta y| \sim 2$ for the case, where

2. CHARMONIUM PAIR PRODUCTION WITH REAL GLUON EMISSION
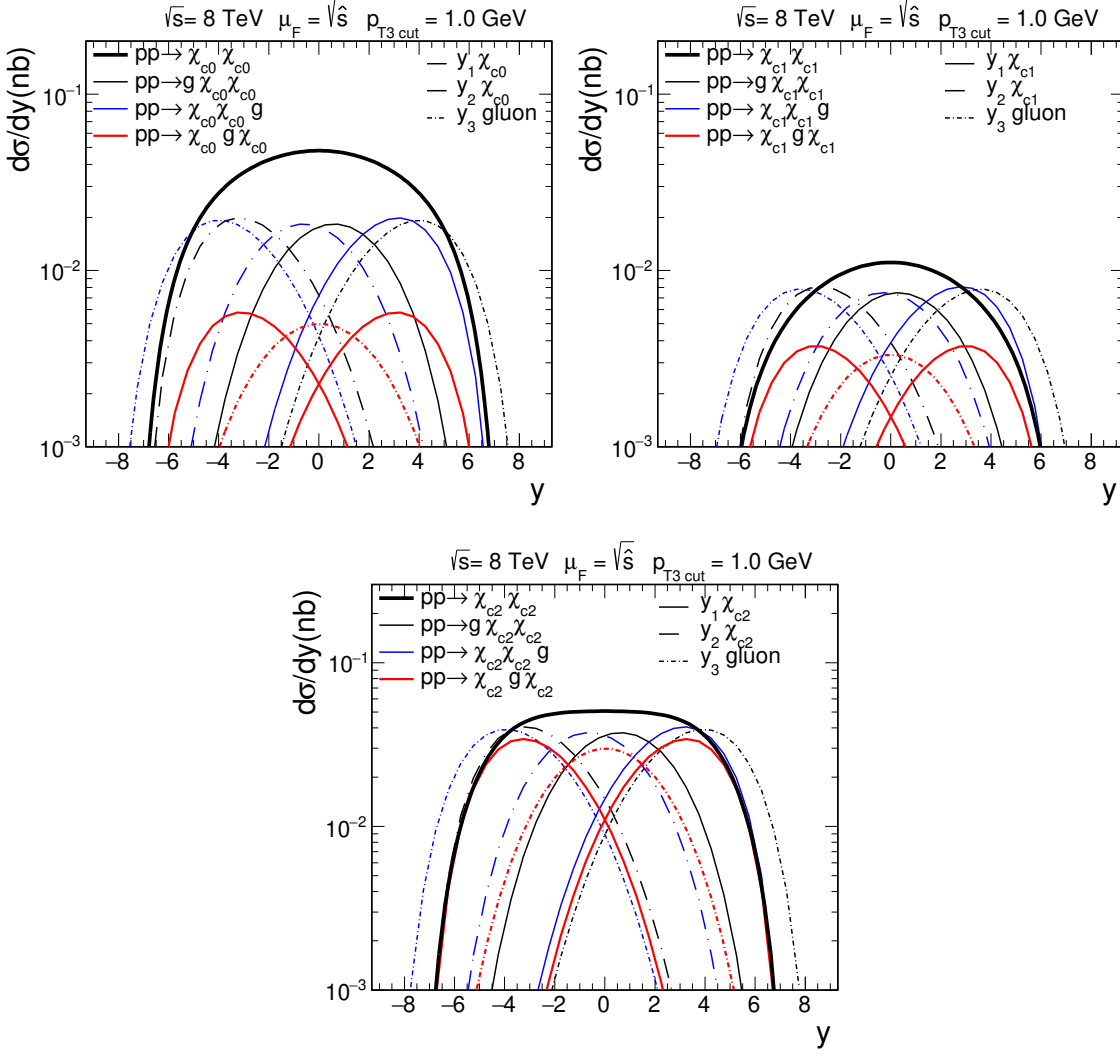
Figure 2.7: Differential distributions in rapidity of gluon and χ_{cJ}'s for $pp \to \chi_{cJ}\chi_{cJ}$, $pp \to g[\chi_{cJ}\chi_{cJ}]$, $pp \to [\chi_{cJ}\chi_{cJ}]g$ and $pp \to \chi_{cJ}\,g\,\chi_{cJ}$. In the upper-left panel plots for χ_{c0}, in the upper-right corner for χ_{c1} and the lower-central panel for χ_{c2}.

gluon is produced near the meson. The second group of peaks appears at the region $|\Delta y| \sim 6$, which corresponds to the distance between gluon and furthermost χ_{cJ}.

In the numerical results the Martin-Stirling-Thorne-Watt (MSTW) 2008 next-to-leading-order (NLO) parton distribution functions [50] is applied and the factorization scale is set equal to $\hat{s}$.

Figure 2.8: Distribution in the rapidity distance between gluon and one χ_{cJ} from the pair.

2.4 Remarks on results and perspectives

The main goal of this study was to estimate real gluon contribution associated with charmonium pair production in proton-proton collisions as well as at the level of parton-parton scattering. One of the most interesting results are distributions in the rapidity of the χ_{cJ} and the gluon in different configurations. In the rapidity range $|y| > 3$ processes with external gluon emission $pp \rightarrow g[\chi_{cJ}\chi_{cJ}]$ come into the picture. Nevertheless, leading-order sub-processes could suppress mesons originating

2. CHARMONIUM PAIR PRODUCTION WITH REAL GLUON EMISSION

from $2 \to 3$ processes at the mid-rapidity region.

Not all possible diagrams haven been taken into account, though. For example the "box"-type diagrams (as in [36]) of $\chi_{cJ}\chi_{cJ}$ production mechanism were not taken under consideration since, in the limit within increasing center-of-mass energy $\hat{s}$ of two scattered gluons, they quickly become negligible [33]. However, for more accurate predictions, "box" type contributions could emerge importantly. In the considered mechanisms (see Fig. 2.2, 2.3) due to gluon exchanges the Feynman amplitude is proportional to $\hat{s}$ as a result one can expect that $\chi_{cJ}\chi_{cJ}$ pair is produced with large rapidity separation. In this work, only χ_{cJ}'s pair with identical spin were analyzed. It is found that the leading order processes $(2 \to 2)$ in the collinear factorization approach give smaller distributions in rapidity and transverse momentum of the meson in contrast to results obtained from the k_T-factorization framework. The subsequently added real emission part of the next-to-leading order contribution leads to an enhancement of the cross-section, but it is still not entirely satisfactory. In general, we expect in the case of χ_{c1} pair production, next-to-next-to-leading order correction may play a significant role, but this issue will be studied elsewhere.

Note that the crucial ingredient of our approach is radial wave function at the origin for P-wave quarkonia $R'_{\chi_c}(0)$, which strongly depends on the model. Further discussion on this aspect will be found in the following sections.

Chapter 3

Transition Form Factors in the Light-Cone Wave Function Approach

Much progress has been made in our understanding of the partonic structure of hadrons during the last decades, thanks to data collected in ep and pp experiments [51]. A supplementary source of knowledge about meson internal structure can be found through meson - photon transition form factors as well as electromagnetic form factors. In general, meson production via photon fusion has been studied at e^+e^- colliders [52]. The main motivation for such studies is the expectation that the measurements of the cross-sections at large virtualities of the photon will imply constraints on the probability amplitudes for finding partons in the minimal Fock-state in the mesons [53, 54, 55, 56, 57]. Another interesting role of meson-photon transition form factors is their appearance in the context of light-by-light scattering in hadronic processes as a contribution to the muon anomalous magnetic moment (see Fig. 5.57a in Ref. [58]).

3.1 Light-cone wave functions of 1S and 2S $c\bar{c}$ bound states

The light-cone wave functions incorporate all essential information about the bound state of quark and antiquark. In the last few years, there has been increasing interest in calculating heavy quarkonia wave function in the light-cone regime, see for instance [59, 60, 61]. In our approach the charmonium meson is assumed to

3. TRANSITION FORM FACTORS IN THE LIGHT-CONE WAVE FUNCTION APPROACH

be constructed of a charm quark and antiquark, i.e. with the assumption that the dominant contribution comes from the $c\bar{c}$ term in the Fock-state expansion

$$|\eta_c; P_+, \vec{P}_\perp\rangle = \sum_{i,j,\lambda,\bar{\lambda}} \frac{\delta^i_j}{\sqrt{N_c}} \int \frac{dz d^2\vec{k}_\perp}{z(1-z)16\pi^3} \Psi_{\lambda,\bar{\lambda}}(z,\vec{k}_\perp)$$
$$\times |c_{i\lambda}(zP_+, \vec{k}_\perp + z\vec{P}_\perp)\, \bar{c}^j_{\bar{\lambda}}((1-z)P_+, -\vec{k}_\perp + (1-z)\vec{P}_\perp)\rangle + \dots \quad , \quad (3.1)$$

where the transverse momenta of c-quark and $\bar{c}$-antiquark are respectively $\vec{k}_\perp + z\vec{P}_\perp$ and $-\vec{k}_\perp + (1-z)\vec{P}_\perp$. Therefore the sum effectively gives the transverse momentum of the η_c meson. The fractions z and $(1-z)$ of the P_+ momentum of the considered meson are carried by c and $\bar{c}$ partons, while the light-cone helicities λ, $\bar{\lambda}$ take values ± 1. Including the fact that quarkonia properties are well described by nonrelativistic potential models, the pure $c\bar{c}$ Fock state probability of $\eta_c(1S, 2S)$ is close to one (see [62, 63]). More sophisticated studies have been performed within the assumption of the meson wave function, which composition encodes also the $u\bar{u}$, $d\bar{d}$, $s\bar{s}$ Fock states [64]. Those predictions are similar as for the pure $c\bar{c}$ state. Thus our approximation seems to be reasonable. The rest frame wave functions for the pseudoscalar meson can be introduce in the helpful notation

$$\Psi_{\tau\bar{\tau}}(\vec{k}) = \sum_{L_z,S_z} Y_{L,L_z}\left(\frac{\vec{k}}{k}\right)\left\langle \frac{1}{2}\frac{1}{2} \tau\bar{\tau} \middle| SS_z \right\rangle\left\langle LSL_zS_z \middle| JJ_z \right\rangle\frac{u_{nl}(k)}{k} , \quad (3.2)$$

where $u_{nl}(k)$ is the Fourier-Bessel transform of the radial wave function, and n is the radial quantum number, see Appendix A for more details. For $J = 0$ and the spin-singlet combination ($S = 0$, $L = 0$), we obtain

$$\Psi_{\tau\bar{\tau}}(\vec{k}) = \frac{1}{\sqrt{2}}\, \xi^{\tau\dagger}_Q\, \hat{\mathcal{O}}\, i\sigma_2\, \xi^{\bar{\tau}*}_{\bar{Q}}\, \frac{u_{n0}(k)}{k}\frac{1}{\sqrt{4\pi}} , \quad (3.3)$$

where the operator $\hat{\mathcal{O}}$ is equal to the 2×2 unit matrix, $\mathbb{1}$. The wave function can be easily divided into a spin-orbit term, which depends on helicities of quark/antiquark as well the radial part. The radial part is characterised by L and n quantum numbers, which for $\eta_c(1S)$ are $L = 0$, $n = 0$ and for $\eta_c(2S)$ are $L = 0$, $n = 1$. The canonical bispinors for c and $\bar{c}$ in Eq. (3.3) are represented by ξ^τ_Q, $\xi^{\bar{\tau}*}_{\bar{Q}}$ respectively. The rest frame wave function is normalized as follows:

$$\int d^3\vec{k} \sum_{\tau\bar{\tau}} |\Psi_{\tau\bar{\tau}}(\vec{k})|^2 = 1 , \quad (3.4)$$

so that the radial wave function u_{n0} fulfills:

$$\int_0^\infty dk\, u_{n0}^2(k) = 1\,.\tag{3.5}$$

The non-relativistic wave functions $u_{nl}(k)$ have been obtained by solving the Schrödinger equation in the rest frame of the quark-antiquark system and subsequently transformed from the r-dependent configuration space to the momentum space, see Appendix A. Different potential models from the literature have been applied and tested for $\eta_c(1S)$ and its radial excitation $\eta_c(2S)$, such as the Buchmüller-Tye, Cornell, logarithmic, oscillator and power-like potentials. The different choices of potential models give similar results, see Fig. 3.1. The wave functions differ somewhat in the peak position and more substantially in the large-momentum tail. The left panel of Fig. 3.1 represents results for $\eta_c(1S)$, while the right panel for $\eta_c(2S)$. The next
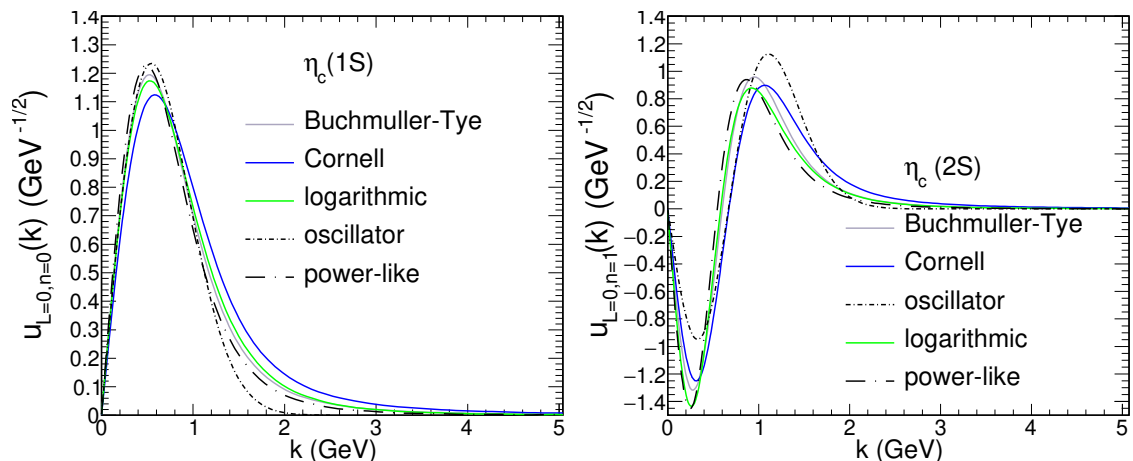
Figure 3.1: Radial momentum wave function in the rest frame of quark-antiquark for $\eta_c(1S)$ and $\eta_c(2S)$.

step towards to light-cone wave function (LCWF) is to transform components of Eq. (3.3) via the Melosh procedure [65, 66]. In general the LCWF can be written in terms of light-cone helicities $\lambda\bar{\lambda}$ for the $Q\bar{Q}$ system:

$$\Psi_{\lambda\bar{\lambda}}(z, \vec{k}_\perp) = \chi_Q^{\lambda\dagger}\, \mathcal{O}'\, i\sigma_2\, \chi_Q^{\bar{\lambda}*}\, \phi(z, \vec{k}_\perp)\,.\tag{3.6}$$

The relation between light-cone spinors and the canonical ones reads

$$\xi_Q = \hat{R}(z, \vec{k}_\perp)\, \chi_Q\,, \qquad \xi_{\bar{Q}}^* = \hat{R}^*(1-z, -\vec{k}_\perp)\, \chi_{\bar{Q}}^*\,,\tag{3.7}$$

3. TRANSITION FORM FACTORS IN THE LIGHT-CONE WAVE FUNCTION APPROACH

while $\hat{R}(z, \vec{k}_\perp)$ is the unitary matrix

$$\hat{R}(z, \vec{k}_\perp) = \frac{m_Q + zM - i\vec{\sigma} \cdot (\vec{n} \times \vec{k})}{\sqrt{(m_Q + zM)^2 + \vec{k}_\perp^2}} = \frac{m_Q + zM - i\vec{\sigma} \cdot (\vec{n} \times \vec{k})}{\sqrt{zM(M + 2m_Q)}}. \tag{3.8}$$

Here, it is convenient to introduce the vector $\vec{n} = (0, 0, 1)$, thus the vector product $\vec{n} \times \vec{k} = (-k_y, k_x, 0)$. The invariant mass of the $Q\bar{Q}$ system is denoted by M and expressed by the following equation:

$$M^2 = \frac{\vec{k}_\perp^2 + m_Q^2}{z(1 - z)}, \tag{3.9}$$

hence the second equality in Eq. (3.8). Notice also that the momentum $\vec{k}$ in the rest frame of quarkonium system is parameterized by the following prescription

$$\vec{k} = (\vec{k}_\perp, k_z) = \left(\vec{k}_\perp, \frac{1}{2}(2z - 1)M\right). \tag{3.10}$$

Moreover, there exists the relation

$$k = |\vec{k}| = \frac{1}{2}\sqrt{M^2 - 4m_Q^2}. \tag{3.11}$$

In the spin-orbit part of the WF given by Eq. (3.6) the operator $\hat{\mathcal{O}}$ is transformed through $\hat{R}$ and $\hat{R}^*$ matrices:

$$\hat{\mathcal{O}}' = \hat{R}^\dagger(z, \vec{k}_\perp) \, \hat{\mathcal{O}} \, i\sigma_2 \, \hat{R}^*(1 - z, -\vec{k}_\perp) \, (i\sigma_2)^{-1}, \tag{3.12}$$

using the property of Pauli-matrices: $i\sigma_2 \, \vec{\sigma}^* \, (i\sigma_2)^{-1} = -\vec{\sigma}$, the transformed operator $\hat{\mathcal{O}}'$ can be rewritten in the simple form:

$$\hat{\mathcal{O}}' = \hat{R}^\dagger(z, \vec{k}_\perp) \, \hat{\mathcal{O}} \, \hat{R}(1 - z, -\vec{k}_\perp). \tag{3.13}$$

Applying the exact form of $\hat{R}^\dagger$ and $\hat{R}$, one can obtain the general form of the transformed $\hat{O}'$ operator independent of the spin-orbit system is:

$$\begin{aligned}
\hat{\mathcal{O}}' = \frac{1}{\sqrt{z(1 - z)}} \frac{1}{M(M + 2m_Q)} &\left\{ (m_Q^2 + m_Q M + z(1 - z)M^2)\hat{\mathcal{O}} \right. \\
&- \vec{\sigma} \cdot (\vec{n} \times \vec{k}) \, \hat{\mathcal{O}} \, \vec{\sigma} \cdot (\vec{n} \times \vec{k}) \\
&+ (M + 2m_Q)\frac{i}{2}\left(\hat{\mathcal{O}}\vec{\sigma} \cdot (\vec{n} \times \vec{k}) + \vec{\sigma} \cdot (\vec{n} \times \vec{k})\hat{\mathcal{O}} \right) \\
&\left. + (2z - 1)M\frac{i}{2}\left(\hat{\mathcal{O}}\vec{\sigma} \cdot (\vec{n} \times \vec{k}) - \vec{\sigma} \cdot (\vec{n} \times \vec{k})\hat{\mathcal{O}} \right) \right\}. \tag{3.14}
\end{aligned}$$

In the case of $\eta_c\,(1S, 2S)$ meson, where the $\hat{\mathcal{O}} = \mathbb{1}$, Eq. (3.14) is reduced to

$$\hat{\mathcal{O}}' = \frac{1}{\sqrt{z(1-z)}} \frac{1}{M} \left(\mathbb{1}m_Q + i\vec{\sigma} \cdot (\vec{n} \times \vec{k}) \right),\qquad (3.15)$$

where z and $(1-z)$ are the meson's light-cone plus-momentum fractions carried by quark and antiquark. Furthermore, the radial part of the wave function needs to be translated to light-cone variables and it is indicated by

$$\phi(z, \vec{k}_\perp) = \frac{\sqrt{\mathcal{J}}}{\sqrt{4\pi}} \frac{u(k)}{k},\qquad (3.16)$$

with the transformation jacobian from $\vec{k}$-space to the LC integration measure of two-body phase space

$$d^3\vec{k} = \mathcal{J} \frac{dz\, d^2\vec{k}_\perp}{16\pi^3 z(1-z)}.\qquad (3.17)$$

Explicit calculation gives $\sqrt{\mathcal{J}} = 2\sqrt{M\pi^3}$, and thus

$$\phi(z, \vec{k}_\perp) = \pi\sqrt{M} \frac{u_{nl}(k)}{k}.\qquad (3.18)$$

Finally, one can insert Eqs. (3.7), (3.15),(3.18) to Eq. (3.6) and obtain

$$\begin{aligned}
\Psi_{\lambda\bar{\lambda}}(z, \vec{k}_\perp) &= \begin{pmatrix} \Psi_{++}(z, \vec{k}_\perp) & \Psi_{+-}(z, \vec{k}_\perp) \\ \Psi_{-+}(z, \vec{k}_\perp) & \Psi_{--}(z, \vec{k}_\perp) \end{pmatrix} \\
&= \frac{1}{\sqrt{z(1-z)}} \begin{pmatrix} -k_x + ik_y & m_Q \\ -m_Q & -k_x - ik_y \end{pmatrix} \psi(z, \vec{k}_\perp).
\end{aligned}\qquad (3.19)$$

Note that in Eq. (3.6) radial part is multiplied by Pauli matrix σ_2, which was crucial to obtain the matrix above. In order to present the result in readily usable form, in the referred below radial part of the LCWF are absorbed the jacobian terms as well as $(1/M)$ and $1/\sqrt{2}$ factors:

$$\psi(z, \vec{k}_\perp) = \frac{\phi(z, \vec{k}_\perp)}{\sqrt{2}M} = \frac{\pi}{\sqrt{2M}} \frac{u_{0n}(k)}{k}.\qquad (3.20)$$

Those $\psi(z, \vec{k}_\perp)$ functions are found in Fig. 3.2 for $\eta_c(1S)$ and $\eta_c(2S)$. For complete-
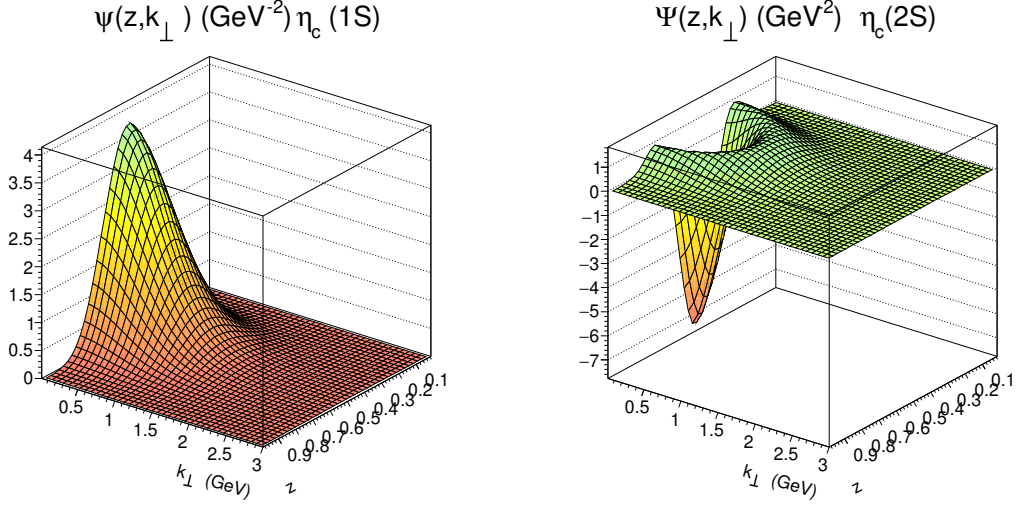
Figure 3.2: The helicity independent part of the light-cone wave function in $(z, \vec{k}_\perp)$ phase space (see Eq. (3.20)). For illustration there is shown result obtained for the Cornell potential model.

ness, let us take a look at normalization of all those functions:

$$
\begin{aligned}
1 &= \int_0^1 \frac{dz}{z(1-z)} \int \frac{d^2\vec{k}_\perp}{16\pi^3} \sum_{\lambda,\bar\lambda} |\Psi_{\lambda,\bar\lambda}(z,\vec{k}_\perp)|^2 \\
&= \int_0^1 \frac{dz}{z(1-z)} \int \frac{d^2\vec{k}_\perp}{16\pi^3} |\phi(z,\vec{k}_\perp)|^2 \\
&= \int_0^1 \frac{dz}{z(1-z)} \int \frac{d^2\vec{k}_\perp}{16\pi^3} 2M^2 |\psi(z,\vec{k}_\perp)|^2 . \quad (3.21)
\end{aligned}
$$

Note that the normalization condition for $\psi(z,\vec{k}_\perp)$ has a different form for P-wave charmonia system, due to the different spin-orbit operator.

3.2 1P light-cone wave functions for $c\bar{c}$ and $b\bar{b}$ bound states

In order to obtain the light-cone wave function for the 1P state it is convenient to recall the form of Eq. (3.3) with the specific set of quantum numbers, $n = 0, L = 1$, $(n_r + 1)^{2S+1}L_J$:

$$
\Psi_{\tau\bar\tau}(\vec{k}) = \frac{1}{\sqrt{2}} \xi_Q^{\tau\dagger} \hat{\mathcal{O}} \, i\sigma_2 \, \xi_{\bar{Q}}^{\bar\tau*} \frac{u_{01}(k)}{k} \frac{1}{\sqrt{4\pi}} , \quad (3.22)
$$

where the operator $\hat{\mathcal{O}}$ for P-wave states has the form:

$$\hat{\mathcal{O}} = \frac{\vec{\sigma} \cdot \vec{k}}{k}\,.\tag{3.23}$$

The spatial part of the wave function for spinless mesons χ_{c0} and χ_{b0} are again obtained for several potential models from Schrödinger equation (see Appendix A). The radial wave function u_{nl} in the momentum rest-frame k is presented in Fig. 3.3. For χ_{c0} as well as for χ_{b0}, the wave function has a negative sign. It is worth noticing that the mass of the b-quark in each presented potential model has a greater value than for c-quark, which implies the fact that the wave function u_{nl} for χ_{b0} has a longer tail in k. This feature has consequences in the transformation to the light-cone base.
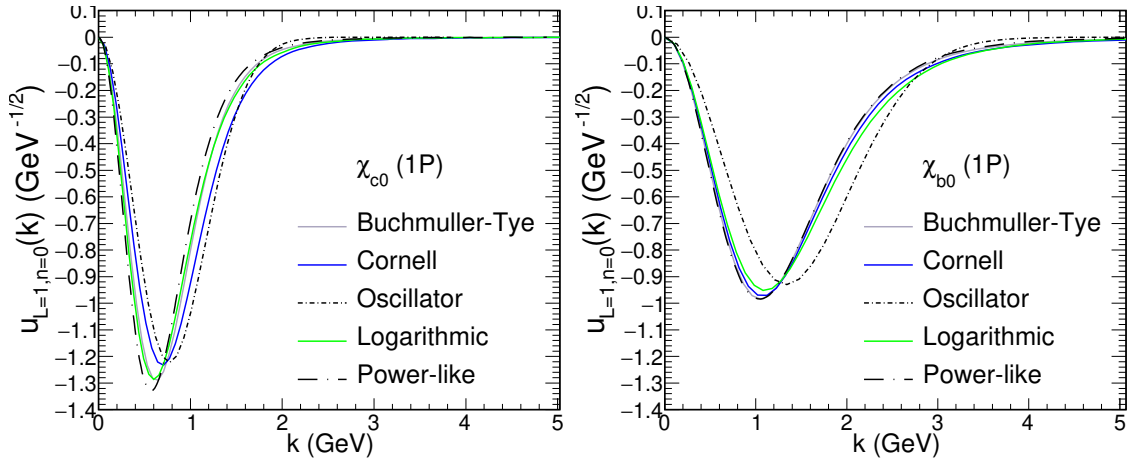
Figure 3.3: The relativistic wave functions $u_{nl}(k)$ obtained as a solution of the Schrödinger equation for several potential models for $c\bar{c}$ (left panel) and $b\bar{b}$ (right panel) bound states.

Although there is a dependency exact the same as Eq. (3.18) and normalization of $\Psi_{\tau\bar{\tau}}(\vec{k})$ is conserved, there is still needed $\psi(z, \vec{k}_\perp)$. The normalization of $\psi(z, \vec{k}_\perp)$ can be found after the transformation of the operator $\hat{\mathcal{O}}$ through the Melosh procedure using the general Eq. (3.14) and including Eq. (3.23). After simple but somewhat tedious manipulations one can get:

$$\hat{\mathcal{O}}' = \frac{1}{\sqrt{z(1-z)}}\frac{1}{2k}\{\vec{\sigma} \cdot \vec{k}_\perp + (2z-1)m_Q\vec{\sigma} \cdot \vec{n}\}\,,\tag{3.24}$$
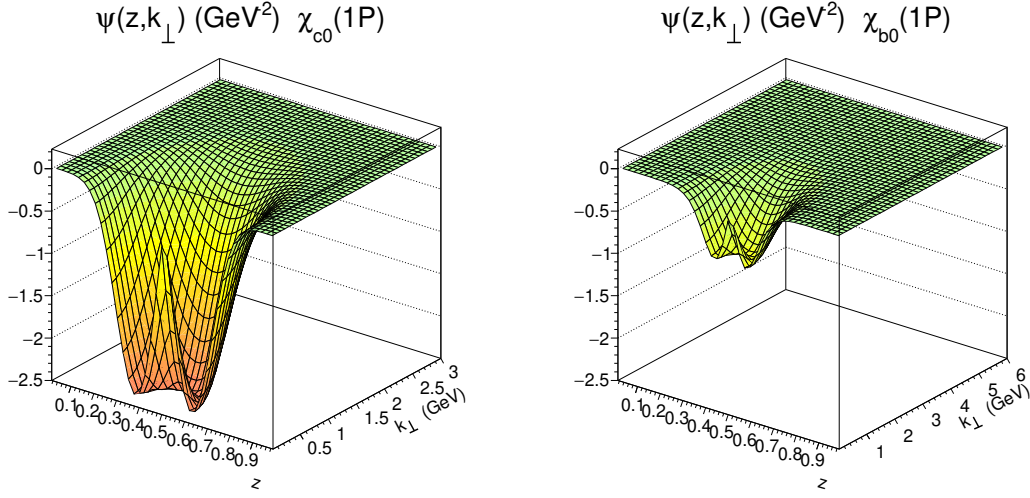
Figure 3.4: The example of the light-cone wave function founded for the Cornell potential model, χ_{c0}-left panel and χ_{b0}-right panel.

and as before $\vec{n} = (0, 0, 1)$, m_Q is referred to as the constituent quark mass and depends on the potential model.

Combining all transformations into the light-cone helicity dependent wave function of $Q\bar{Q}$ system, we obtain:

$$\Psi_{\lambda\bar{\lambda}}(z, \vec{k}_\perp) = \frac{-1}{\sqrt{z(1-z)}} \begin{pmatrix} k_x - ik_y & m_Q(1-2z) \\ m_Q(1-2z) & -k_x - ik_y \end{pmatrix} \psi(z, \vec{k}_\perp), \qquad (3.25)$$

and

$$\psi(z, \vec{k}_\perp) = \frac{\phi(z, \vec{k}_\perp)}{2\sqrt{2k}} = \frac{\phi(z, \vec{k}_\perp)}{\sqrt{2}\sqrt{M^2 - 4m_Q^2}}. \qquad (3.26)$$

In the last equality the relation from Eq. (3.11) is used.

3.3   Transition form factor and helicity amplitude

There are several methods to compute directly produced heavy quarkonia. In our approach it is required that $Q\bar{Q}$ pair is produced in the color singlet state. As a result only the $t - channel$ and $u - channel$ quark exchange diagrams shown in Fig.3.5 contribute to the scattering amplitude (diagrams A and B). Diagram C with an $s - channel$ gluon necessarily has a color octet $Q\bar{Q}$ system in the final state and thus will drop out of our calculation.

Figure 3.5: Feynman diagrams for the $g^*g^* \to Q\bar{Q}$ amplitude.

The general form of the gluon helicity amplitude[1] involving diagrams A and B from Fig. 3.5 (diagram C does not contribute in the color-singlet configuration) reads:

$$n_\mu^+ n_\nu^- \mathcal{A}_{\mu\nu}^{\lambda\bar{\lambda}} \Big(g^*(q_1)g^*(q_2) \to Q_\lambda(z, \vec{p}_{\perp Q}) \, \bar{Q}_{\bar{\lambda}}(1-z, \vec{p}_{\perp \bar{Q}}) \Big)$$

$$= \bar{u}_\lambda(p_Q)\, \hat{n}^+ \frac{\hat{p}_A + m_Q}{p_A^2 - m_Q^2}\, \hat{n}^-\, v_{\bar{\lambda}}(p_{\bar{Q}}) \; + \; \bar{u}_\lambda(p_Q)\hat{n}^- \frac{\hat{p}_B + m_Q}{p_B^2 - m_Q^2}\, \hat{n}^+\, v_{\bar{\lambda}}\,(p_{\bar{Q}}), \quad (3.27)$$

where $\hat{p} \equiv p^\mu \gamma_\mu$ is the standard Feynman contraction, while $\hat{n}_- = n_\mu^- \gamma^\mu \equiv \gamma_+$, $\hat{n}_+ = n_\mu^+ \gamma^\mu \equiv \gamma_-$. For further calculation the Dirac spinors $u(p)$ and $v(p)$ are taken in the form as in A3 in Ref. [67], see Appendix B. The momenta of outgoing quark and antiquark in the light-cone base reads:

$$p_Q \;=\; z q_1^+ n_\mu^+ + \frac{\vec{p}_Q^2 + m_Q^2}{2z q_1^+} n_\mu^- + p_{Q\perp\mu}\,, \quad (3.28)$$

$$p_{\bar{Q}} \;=\; (1-z)q_1^+ n_\mu^+ + \frac{p_{\bar{Q}}^2 + m_Q^2}{2(1-z)q_1^+} n_\mu^- + p_{\bar{Q}\perp\mu}\,, \quad (3.29)$$

---

[1]We omit coupling constant and color factors, see Eqs. **??**, 3.59.

3. TRANSITION FORM FACTORS IN THE LIGHT-CONE WAVE FUNCTION APPROACH

or with the help of the bound state momentum $\vec{P}_\perp = \vec{q}_{1\perp} + \vec{q}_{2\perp}$, the momentum of the internal motion $\vec{k}_\perp$ and the fraction of the longitudinal momentum z

$$\vec{p}_{Q\perp} = \vec{k}_\perp + z(\vec{q}_{1\perp} + \vec{q}_{2\perp}), \tag{3.30}$$

$$\vec{p}_{\bar{Q}\perp} = -\vec{k}_\perp + (1-z)(\vec{q}_{1\perp} + \vec{q}_{2\perp}). \tag{3.31}$$

From the kinematic situation presented in Fig. 3.5 one can reads

$$q_1 = q_1^+ n_\mu^+ + q_{1\perp\mu} \longrightarrow q_1^2 = -\vec{q}_{1\perp}^2, \tag{3.32}$$

$$q_2 = q_2^+ n_\mu^- + q_{2\perp\mu} \longrightarrow q_2^2 = -\vec{q}_{2\perp}^2, \tag{3.33}$$

and the momenta of the exchanged quark for diagram A and B

$$p_A = q_1 - p_{\bar{Q}} = zq_1^+ n_\mu^+ - \frac{p_{\bar{Q}}^2 + m_Q^2}{2(1-z)q_1^+} n_\mu^- + \vec{q}_{1\perp\mu} - \vec{p}_{\bar{Q}\perp\mu}, \tag{3.34}$$

$$p_B = p_Q - q_1 = -(1-z) q_1^+ n_\mu^+ + \frac{p_Q^2 + m_Q^2}{2zq_1^+} n_\mu^- + \vec{p}_{Q\perp\mu} - \vec{q}_{1\perp\mu}. \tag{3.35}$$

Therefore one can get the denominators of Eq. (3.27)

$$
\begin{aligned}
p_A^2 - m_Q^2 &= -\frac{2z}{2(1-z)}(p_{\bar{Q}\perp}^2 + m_Q^2) - (\vec{q}_{1\perp} - \vec{p}_{\bar{Q}\perp})^2 - m_Q^2 \\
&= \frac{-1}{(1-z)}\left((\vec{p}_{Q\perp} - (1-z)\vec{q}_{1\perp})^2 + (z(1-z)\vec{q}_{1\perp}^2 + m_Q^2)\right) \\
&= \frac{-1}{(1-z)}\left(\vec{l}_A^2 + \varepsilon^2\right), \tag{3.36}
\end{aligned}
$$

$$
\begin{aligned}
p_B^2 - m_Q^2 &= -2\frac{(1-z)(\vec{p}_{Q\perp}^2 + m_Q^2)}{2z} - (\vec{p}_{Q\perp} - \vec{q}_{1\perp})^2 - m_Q^2 \\
&= -\frac{1}{z}\left((\vec{p}_{Q\perp} - z\vec{q}_{1\perp})^2 + (z(1-z)\vec{q}_{1\perp}^2 + m_Q^2)\right) \\
&= -\frac{1}{z}(\vec{l}_B^2 + \varepsilon^2), \tag{3.37}
\end{aligned}
$$

$$\tag{3.38}$$

here $\vec{l}_A$, $\vec{l}_B$ and ε^2 are :

$$\vec{l}_A = \vec{p}_{\bar{Q}} - (1-z)\vec{q}_{1\perp} = -\vec{k} + (1-z)\vec{q}_{2\perp}, \tag{3.39}$$

$$\vec{l}_B = \vec{p}_{Q\perp} - z\vec{q}_{1\perp} = \vec{k}_\perp + z\vec{q}_{2\perp}, \tag{3.40}$$

$$\varepsilon^2 = z(1-z)\vec{q}_{1\perp}^2 + m_Q^2. \tag{3.41}$$

After having expressed the denominators of quark propagators in a concise form, let us turn to the numerators: the spinor and gamma-matrix algebra. Here we can use a convenient trick, which allows us to reduce our amplitude to some simple on–shell spinor bilinears. This trick is most easily demonstrated for diagram A. Here we have the virtual quark propagating with four-momentum p_A. Evidently it is off-shell, $p_A^2 \neq m_Q^2$, see Eq. (3.38). Let us have a look at its light-cone decomposition

$$p_{A\mu} = p_{A+}n_\mu^+ + p_{A-}n_\mu^- + p_{A\mu}^\perp = p_{A+}n_\mu^+ + \frac{p_A^2 + \vec{p}_{A\perp}^2}{2p_{A+}}n_\mu^- + p_{A\mu}^\perp . \tag{3.42}$$

We can add and subtract a piece $\propto m_Q^2/(2p_{A+})$ in the minus-component, so that

$$\begin{aligned} p_{A\mu} &= \underbrace{p_{A+}n_\mu^+ + \frac{m_Q^2 + \vec{p}_{A\perp}^2}{2p_{A+}}n_\mu^- + p_{A\mu}^\perp}_{\text{on-shell}} + \frac{p_A^2 - m_Q^2}{2p_{A+}}n_\mu^- \\ &= p_{A\mu}^{\text{os}} + \frac{p_A^2 - m_Q^2}{2p_{A+}}n_\mu^- , \end{aligned} \tag{3.43}$$

where $p_{A\mu}^{\text{os}}$ is an on-shell momentum, $(p_A^{\text{os}})^2 = m_Q^2$. Now, the crucial point is that for an on-shell momentum, we can write

$$\hat{p}_A^{\text{os}} + m_Q = \sum_\sigma u_\sigma(p_A^{\text{os}})\bar{u}_\sigma(p_A^{\text{os}}) , \tag{3.44}$$

so that the quark propagator becomes

$$\frac{\hat{p}_A + m_Q}{p_A^2 - m_Q^2} = \frac{\sum_\sigma u_\sigma(p_A^{\text{os}})\bar{u}_\sigma(p_A^{\text{os}})}{p_A^2 - m_Q^2} + \frac{1}{2p_{A+}}\hat{n}^- . \tag{3.45}$$

Now, in diagram A, the quark propagator is sandwiched between the matrices $\hat{n}^-$ and $\hat{n}^+$:

$$\hat{n}^-\frac{\hat{p}_A + m_Q}{p_A^2 - m_Q^2}\hat{n}^+ = \hat{n}^-\frac{\sum_\sigma u_\sigma(p_A^{\text{os}})\bar{u}_\sigma(p_A^{\text{os}})}{p_A^2 - m_Q^2}\hat{n}^+ + \frac{1}{2p_{A+}}\underbrace{\hat{n}^-\hat{n}^-\hat{n}^+}_{=0}, \tag{3.46}$$

where the second term vanishes because $\hat{n}^-\hat{n}^- = n^- \cdot n^- = 0$. It therefore turns out that in our diagrams, we can replace the quark/antiquark propagators by the spinor polarization sums. Subsequently in Eq. (3.27), there is made use of the polarization sum:

$$\hat{p}_A + m_Q \longrightarrow \sum_\sigma u_\sigma(p_A)\bar{u}_\sigma(p_A) , \tag{3.47}$$

$$\hat{p}_B + m_Q = -(-\hat{p}_B - m_Q) \longrightarrow -\sum_{\bar{\sigma}} v_{\bar{\sigma}}(-p_B)\bar{v}_{\bar{\sigma}}(-p_B) , \tag{3.48}$$

3. TRANSITION FORM FACTORS IN THE LIGHT-CONE WAVE FUNCTION APPROACH

where the summation is over the polarization $\bar{\sigma}$ and σ. Thus the spinor product in the form $\bar{u}\hat{n}^+v$, $\bar{u}\hat{n}^-u$, $\bar{v}\hat{n}^-v$ for diagram A is:

$$
\bar{u}_\lambda(p_Q)\hat{n}_-(\hat{p}_A + m_Q)\hat{n}_+ v_{\bar{\lambda}}(p_{\bar{Q}}) = \sum_\sigma [\bar{u}_\lambda(p_Q)\hat{n}^- u_\sigma(p_A)][\bar{u}_\sigma(p_A)\hat{n}^+ v_{\bar{\lambda}}(p_{\bar{Q}})]
$$

$$
= \sum_\sigma \left[2\delta_{\lambda\sigma}\sqrt{zq_1^+ zq_1^+}\right]
$$

$$
\cdot \left[\bar{u}_\sigma(z,\vec{k} - (1-z)\vec{q}_2 + z\vec{q}_1)\hat{n}^+ v_{\bar{\lambda}}(1-z, -\vec{k} + (1-z)(\vec{q}_1 + \vec{q}_2))\right], \quad (3.49)
$$

and for diagram B:

$$
\bar{u}_\lambda(p_Q)\hat{n}^+(\hat{p}_B + m_Q)\hat{n}^- v_{\bar{\lambda}}(p_{\bar{Q}}) = -\sum_{\bar{\sigma}} [\bar{u}_\lambda(p_Q)\hat{n}^+ v_{\bar{\sigma}}(-p_B)][\bar{v}_{\bar{\sigma}}(-p_B)\hat{n}^- v_{\bar{\lambda}}(p_{\bar{Q}})]
$$

$$
= -\sum_{\bar{\sigma}} \left[\bar{u}_\lambda(z,\vec{k} + z(\vec{q}_1 + \vec{q}_2))\hat{n}^+ v_{\bar{\lambda}}(1-z, -\vec{k} - z\vec{q}_2 + (1-z)\vec{q}_1)\right]
$$

$$
\cdot \left[2\delta_{\bar{\sigma}\bar{\lambda}}\sqrt{(1-z)q_1^+(1-z)q_1^+}\right]. \quad (3.50)
$$

Going further with spinor product $\bar{u}_\lambda \hat{n}^+ v_{\bar{\lambda}}$, it is convenient to express via auxiliary vectors $\vec{l}_A$ and $\vec{l}_B$: from Eq. (3.49)

$$
\bar{u}_\lambda(z, -\vec{l}_A + z\vec{q}_1)\,\hat{n}^+\, v_{\bar{\lambda}}(1-z, \vec{l}_A + (1-z)\vec{q}_1)\,, \quad (3.51)
$$

as well as from Eq. (3.50)

$$
\bar{u}_\lambda(z, \vec{l}_B + z\vec{q}_1)\,\hat{n}^+\, v_{\bar{\lambda}}(1-z, -\vec{l}_B + (1-z)\vec{q}_1)\,. \quad (3.52)
$$

In the case of the state, where the helicities satisfy $\lambda = \bar{\lambda}$

$$
n_\mu^+ n_\nu^- \mathcal{A}^{\lambda\bar{\lambda}}\big|_{\lambda=\bar{\lambda}} = \frac{m_Q\sqrt{2}(\vec{e}(-\lambda)\cdot\vec{q}_1)}{q_1^+\sqrt{z(1-z)}}\left\{-\frac{2z(1-z)q_1^+}{\vec{l}_A^{\,2} + \varepsilon^2} + \frac{2z(1-z)q_1^+}{\vec{l}_B^{\,2} + \varepsilon^2}\right\}, \quad (3.53)
$$

there is employed notation $a(-\lambda) = \sqrt{2}\,\vec{e}(-\lambda)\cdot\vec{a}$, the vector $\vec{e}(\lambda) = -1/\sqrt{2}(\lambda e_x + ie_y)$.

In order to consider the situation, where $\lambda = -\bar{\lambda}$ for diagram A one can obtain

$$
\bar{u}_\lambda(p_Q)\hat{n}^+\frac{\hat{p}_A + m_Q}{p_A^2 - m_Q^2}\,\hat{n}^-\, v_{\bar{\lambda}}(p_{\bar{Q}}) =
$$

$$
= 2\sqrt{z(1-z)}\Bigg(-m_Q^2 - \vec{l}_A^{\,2} + z(1-z)\vec{q}_1^{\,2} - (1-2z)\vec{l}_A\cdot\vec{q}_1
$$

$$
- i\lambda\left[\vec{l}_A, \vec{q}_1\right]\Bigg)\left\{\frac{1}{\vec{l}_A^{\,2} + \varepsilon^2}\right\}, \quad (3.54)
$$

42

or for diagram B

$$\bar{u}_\lambda(p_Q)\,\hat{n}^-\frac{\hat{p}_B+m_Q}{p_B^2-m_Q^2}\,\hat{n}^+\,v_{\bar\lambda}(p_{\bar{Q}}) =$$

$$= \frac{1}{q_1^+\,\sqrt{z(1-z)}}\Bigg(-m_Q^2+(\vec{l}_B+z\vec{q}_1)\cdot(-\vec{l}_B+(1-z)\vec{q}_1)$$

$$+ i\lambda\left[\vec{l}_B+z\vec{q}_1\,,\,-\vec{l}_B+(1-z)\vec{q}_1\right]\Bigg)\left\{-\frac{2z(1-z)q_1^+}{\vec{l}_B^{\,2}+\varepsilon^2}\right\}$$

$$= 2\sqrt{z(1-z)}\Bigg(-m_Q^2-\vec{l}_B^{\,2}+z(1-z)\vec{q}_1^{\,2}+(1-2z)\vec{l}_B\cdot\vec{q}_1$$

$$+ i\lambda\left[\vec{l}_B\,,\,\vec{q}_1\right]\Bigg)\left\{-\frac{1}{\vec{l}_B^{\,2}+\varepsilon^2}\right\}. \quad (3.55)$$

Notice that previously it was indicated $\varepsilon^2=z(1-z)q_1^2+m_Q^2$, thus the part of the amplitude, for $\lambda=-\bar\lambda$, takes the form:

$$n^{+\mu}n^{-\nu}\mathcal{A}_{\mu\nu}^{\lambda\bar\lambda}\big|_{\lambda=-\bar\lambda}=-2\sqrt{z(1-z)}\Bigg(2z(1-z)q_1^2\left(\frac{1}{\vec{l}_A^{\,2}+\varepsilon^2}-\frac{1}{\vec{l}_B^{\,2}+\varepsilon^2}\right)$$

$$+\frac{(1-2z)\vec{l}_A\cdot\vec{q}_1+i\lambda[\vec{l}_A,q_1]}{\vec{l}_A^{\,2}+\varepsilon^2}+\frac{(1-2z)\vec{l}_B\cdot\vec{q}_1+i\lambda[\vec{l}_B,q_1]}{\vec{l}_B^{\,2}+\varepsilon^2}\Bigg). \quad (3.56)$$

Finally, the full matrix element reads

$$n^{+\mu}n^{-\nu}\mathcal{M}_{\mu\nu}=\mathcal{N}\int\frac{dz\,d^2\vec{k}_\perp}{z(1-z)16\pi^3}\sum_{\lambda\bar\lambda}\Psi_{\lambda\bar\lambda}^*\,n^{+\mu}n^{-\nu}\mathcal{A}_{\mu\nu}^{\lambda\bar\lambda}. \quad (3.57)$$

Here $\mathcal{N}$ encodes information about color factors and coupling constant. For the two photons fusion

$$\mathcal{N}_{\gamma^*\gamma^*\to Q\bar{Q}}=\frac{4\pi\alpha_{em}e_Q^2\,\mathrm{Tr}\mathbb{1}_{\mathrm{color}}}{\sqrt{N_c}}, \quad (3.58)$$

where e_Q is the electric charge of the considered quark. For the two gluon fusion, one can apply

$$\mathcal{N}_{g^*g^*\to Q\bar{Q}}=\frac{4\pi\alpha_s\mathrm{Tr}[t^a t^b]}{\sqrt{N_c}}, \quad (3.59)$$

here N_c is the color factor. The convoluted amplitude with the bound state wave function can be presented in a universal form and used with the specific wave function $\Psi_{\lambda\bar\lambda}^*$ depending on the produced $Q\bar{Q}$ state. The subscripts $(\pm)$ below stand for

quark/antiquark helicities ($\pm 1/2$):

$$
\int \frac{dz\,d^2\vec{k}_\perp}{z(1-z)16\pi^3} \sum_{\lambda\bar{\lambda}} \Psi^*_{\lambda\bar{\lambda}} n^{+\mu} n^{-\nu} \mathcal{A}^{\lambda\bar{\lambda}}_{\mu\nu} = (-2) \int \frac{dz\,d^2\vec{k}_\perp}{\sqrt{z(1-z)}16\pi^3}
$$

$$
\times \Bigg\{ -m_Q \Big[\frac{1}{\vec{l_A}^2 + \varepsilon^2} - \frac{1}{\vec{l_B}^2 + \varepsilon^2} \Big]
$$

$$
\times \Big(\sqrt{2}(\vec{e}_\perp(-)\vec{q}_{1\perp})\Psi^*_{++}(z,\vec{k}_\perp) + \sqrt{2}(\vec{e}_\perp(+)\vec{q}_{1\perp})\Psi^*_{--}(z,\vec{k}_\perp) \Big)
$$

$$
+ \Big(2z(1-z)\vec{q}_{1\perp}^2 + (1-2z)(\vec{k}_\perp \cdot \vec{q}_{1\perp}) \Big) \Big[\frac{1}{\vec{l_A}^2 + \varepsilon^2} - \frac{1}{\vec{l_B}^2 + \varepsilon^2} \Big]
$$

$$
\times \Big(\Psi^*_{+-}(z,\vec{k}_\perp) + \Psi^*_{-+}(z,\vec{k}_\perp) \Big)
$$

$$
-(1-2z)(\vec{q}_{1\perp} \cdot \vec{q}_{2\perp}) \Big[\frac{1-z}{\vec{l_A}^2 + \varepsilon^2} + \frac{z}{\vec{l_B}^2 + \varepsilon^2} \Big] \Big(\Psi^*_{+-}(z,\vec{k}_\perp) + \Psi^*_{-+}(z,\vec{k}_\perp) \Big)
$$

$$
+ i[\vec{k}_\perp, \vec{q}_{1\perp}] \Big[\frac{1}{\vec{l_A}^2 + \varepsilon^2} - \frac{1}{\vec{l_B}^2 + \varepsilon^2} \Big] \Big(\Psi^*_{+-}(z,\vec{k}_\perp) - \Psi^*_{-+}(z,\vec{k}_\perp) \Big)
$$

$$
+ i[\vec{q}_{1\perp}, \vec{q}_{2\perp}] \Big[\frac{1-z}{\vec{l_A}^2 + \varepsilon^2} + \frac{z}{\vec{l_B}^2 + \varepsilon^2} \Big] \Big(\Psi^*_{+-}(z,\vec{k}_\perp) - \Psi^*_{-+}(z,\vec{k}_\perp) \Big) \Bigg\}. \tag{3.60}
$$

In our approach, it is assumed that the mass of the heavy quark, charm, or bottom, m_Q is large enough to satisfy perturbation theory and even in the limit of vanishing gluon/photon virtualities is applicable for our result.

3.4 Spacelike transition form factors for S-wave quarkonia

During the last years, the transition form factors have been extracted from e^+e^- collisions in the single-tag mode for π^0, η, and η' by CLEO, BaBar, Belle, and L3 Collaborations. Only one of the leptons in the final state of the single-tag event is measured, which imposes that one of the exchanged photons is almost real, while the other is off-shell. From the theoretical side, so far transition form factors have been studied within different approaches for instance lattice QCD [68, 69], perturbative QCD [70, 62], non-relativistic QCD[71, 72], QCD sum rules [73] and also from Bethe-Salpeter or Dyson-Schwinger equations[74]. Moreover, in the case of one real and one virtual photon, some studies in the light-cone quark model exist [64, 75].

The transition form factor $F(Q_1^2, Q_2^2)$ has a well known strict relation with the

two-photon helicity amplitude for spin-parity quantum numbers $J^{PC} = 0^{-+}$ [76]:

$$\mathcal{M}_{\mu\nu}(\gamma^*(q_1)\gamma^*(q_2) \to \eta_c) = 4\pi\alpha_{\rm em}\,(-i)\varepsilon_{\mu\nu\alpha\beta}q_1^\alpha q_2^\beta\, F(Q_1^2, Q_2^2)\,. \tag{3.61}$$

It can be also given by the projection on the photon polarization

$$n^{+\mu}n^{-\nu}\mathcal{M}_{\mu\nu}(\gamma^*(q_1)\gamma^*(q_2) \to \eta_c) = 4\pi\alpha_{\rm em}\,(-i)[\vec{q}_{1\perp}, \vec{q}_{2\perp}]\, F(Q_1^2, Q_2^2)\,, \tag{3.62}$$

and the vector product $[\vec{q}_{1\perp}, \vec{q}_{2\perp}] = q_{1x}q_{2y} - q_{1y}q_{2x}$. Here the spacelike photons have virtualities $Q_i^2 = -q_i^2 \ge 0, i = 1, 2$.

Our master formula - Eq. (3.60) - is presented in an easy to handle form, and one can notice that only a few combinations of the conjugated helicity wave functions $\Psi^*_{\lambda\bar\lambda}(z, \vec{k}_\perp)$ appear. Then it is a straightforward step to insert the results for the pseudoscalar meson (see Eq. (3.19)) and read off:

$$\sqrt{2}\Big((\vec{e}_\perp(-) \cdot \vec{q}_{1\perp})\Psi^*_{++}(z, \vec{k}_\perp) + (\vec{e}_\perp(+) \cdot \vec{q}_{1\perp})\Psi^*_{--}(z, \vec{k}_\perp)\Big) = \frac{i2[\vec{k}_\perp, \vec{q}_{1\perp}]}{\sqrt{z(1-z)}}\psi(z, \vec{k}_\perp) \quad,$$

$$\Big(\Psi^*_{+-}(z, \vec{k}_\perp) - \Psi^*_{-+}(z, \vec{k}_\perp)\Big) = \frac{2m_Q}{\sqrt{z(1-z)}}\psi(z, \vec{k}_\perp) \quad,$$

$$\Big(\Psi^*_{+-}(z, \vec{k}_\perp) + \Psi^*_{-+}(z, \vec{k}_\perp)\Big) = 0 \quad. \tag{3.63}$$

Hence the terms with $\Big(\Psi^*_{+-}(z, \vec{k}_\perp) + \Psi^*_{-+}(z, \vec{k}_\perp)\Big)$ are automatically canceled out, and we remain with

$$n^{+\mu}n^{-\nu}\mathcal{M}_{\mu\nu}(\gamma^*(q_1)\gamma^*(q_2) \to \eta_c) = 4\pi\alpha_{\rm em}e_c^2\frac{{\rm Tr}\,\mathbb{1}_{\rm color}}{\sqrt{N_c}}(-2)\int\frac{dz\,d^2\vec{k}_\perp}{\sqrt{z(1-z)}16\pi^3}$$

$$\left\{\left[\frac{1}{\vec{l}_A^{\,2} + \mu^2} - \frac{1}{\vec{l}_B^{\,2} + \mu^2}\right]\left[i[\vec{k}_\perp, \vec{q}_{1\perp}]\Big(\Psi^*_{+-}(z, \vec{k}_\perp) - \Psi^*_{-+}(z, \vec{k}_\perp)\Big)\right.\right.$$

$$\left. -\sqrt{2}m_Q\Big((\vec{e}_\perp(-)\vec{q}_{1\perp})\Psi^*_{++}(z, \vec{k}_\perp) + (\vec{e}_\perp(+)\vec{q}_{1\perp})\Psi^*_{--}(z, \vec{k}_\perp)\Big)\right]$$

$$\left. +\left[\frac{1-z}{\vec{l}_A^{\,2} + \mu^2} + \frac{z}{\vec{l}_B^{\,2} + \mu^2}\right]i[\vec{q}_{1\perp}, \vec{q}_{2\perp}]\Big(\Psi^*_{+-}(z, \vec{k}_\perp) - \Psi^*_{-+}(z, \vec{k}_\perp)\Big)\right\}\,. \tag{3.64}$$

After summation, the pieces proportional to $[\vec{k}_\perp, \vec{q}_{1\perp}]$ cancel, and only the term with

3. TRANSITION FORM FACTORS IN THE LIGHT-CONE WAVE FUNCTION APPROACH

cross product $i[\vec{q}_{1\perp}, \vec{q}_{2\perp}]$ is left

$$n^{+\mu}n^{-\nu}\mathcal{M}_{\mu\nu}(\gamma^*(q_1)\gamma^*(q_2) \to \eta_c) = 4\pi\alpha_{\text{em}}e_c^2 \frac{\text{Tr}\,\mathbb{1}_{\text{color}}}{\sqrt{N_c}}(-2)\int \frac{dz d^2\vec{k}_\perp}{\sqrt{z(1-z)}16\pi^3}\psi(z,\vec{k}_\perp)$$

$$\times \left\{ i2m_Q[\vec{q}_{1\perp},\vec{q}_{2\perp}]\left[\frac{1-z}{\vec{l}_A^{\,2}+\mu^2} + \frac{z}{\vec{l}_B^{\,2}+\mu^2}\right]\right\}. \quad (3.65)$$

By comparing Eq. (3.65) with Eq. (3.62) we find an expression of the form factor in terms of the light-cone wave function:

$$F(Q_1^2, Q_2^2) = e_c^2\sqrt{N_c}\,4m_Q \cdot \int \frac{dz d^2\vec{k}_\perp}{z(1-z)16\pi^3}\psi(z,\vec{k}_\perp)$$

$$\times \left\{ \frac{1-z}{(\vec{k}_\perp - (1-z)\vec{q}_{2\perp})^2 + z(1-z)\vec{q}_{1\perp}^{\,2} + m_Q^2} \right.$$

$$\left. + \frac{z}{(\vec{k}_\perp + z\vec{q}_{2\perp})^2 + z(1-z)\vec{q}_{1\perp}^{\,2} + m_Q^2} \right\}, \quad (3.66)$$

here e_c stands for is the electric charge of the c-quark/antiquark and it is taken as $e_c = 2/3$. Let us recall that the invariants Q_1^2 and Q_2^2 are expressed as

$$Q_1^2 = \vec{q}_{1\perp}^{\,2}, \quad Q_2^2 = \vec{q}_{2\perp}^{\,2}. \quad (3.67)$$

Notice that the integrand on the r.h.s. of Eq. (3.66) is not manifestly a function of $\vec{q}_{1\perp}^{\,2}$ and $\vec{q}_{2\perp}^{\,2}$ alone. However, after integrating over the azimuthal angle of $\vec{k}_\perp$ this will clearly be the case. We can put the dependence on $\vec{q}_{1\perp}^{\,2}, \vec{q}_{2\perp}^{\,2}$ in evidence by performing the azimuthal integration analytically, using

$$\int_0^{2\pi}\frac{d\phi}{2\pi}\frac{1}{A+B\cos\phi} = \frac{1}{\sqrt{A^2-B^2}}, \quad (3.68)$$

so that finally the $\gamma^*\gamma^* \to \eta_c$ transition form factor reads

$$F(Q_1^2, Q_2^2) = e_c^2\sqrt{N_c}\,4m_c \cdot \int \frac{dz k_\perp dk_\perp}{z(1-z)8\pi^2}\psi(z,\vec{k}_\perp)$$

$$\left\{ \frac{1-z}{\sqrt{(\vec{k}_\perp^2 - m_c^2 - z(1-z)\vec{q}_{1\perp}^{\,2} - (1-z)^2\vec{q}_{2\perp}^{\,2})^2 + 4\vec{k}_\perp^2(m_c^2 + z(1-z)\vec{q}_{1\perp}^{\,2})}} \right.$$

$$\left. + \frac{z}{\sqrt{(\vec{k}_\perp^2 - m_c^2 - z(1-z)\vec{q}_{1\perp}^{\,2} - z^2\vec{q}_{2\perp}^{\,2})^2 + 4\vec{k}_\perp^2(m_c^2 + z(1-z)\vec{q}_{1\perp}^{\,2})}} \right\}.$$

$$(3.69)$$
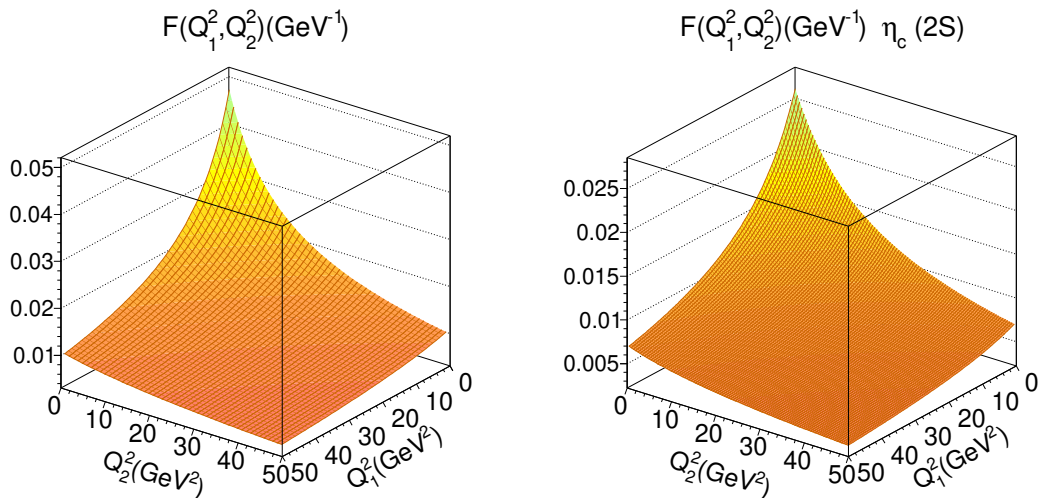
Figure 3.6: The transition form factor for η_c(1S)-left panel and η_c(2S)-right panel in terms of virtualities of the photons Q_1, Q_2. For illustration there is shown the result obtained from the Buchmüller-Tye potential model.

The formula we have just derived (Eq. (3.69)) can be employed for η_c(1S) as well as η_c(2S) with corresponding light-cone wave function $\psi(z, \vec{k}_\perp)$. If the proper corrections for flavor structure and quark masses/charges are made, it holds for any pseudoscalar quark-antiquark meson.

It is not easy to observe directly from Eq. (3.69) whether our form factor obeys Bose-symmetry under an exchange of the photon virtualities Q_1^2, Q_2^2. This feature is clearly seen in Fig. 3.6 for η_c(1S)-left panel and for η_c(2S)-right panel. The wave function obtained from the Buchmüller-Tye potential model with corresponding quark mass for the model was applied in the result presented in Fig. 3.6. However, the whole set of the wave functions, obtained as was discussed in the previous sections, have been tested. The form factors received with other wave functions from the set give similar shapes, but they differ in peak height, where $Q_1^2 = Q_2^2 = 0$. Therefore, a noteworthy feature of our form factor is its value at the so-called on-shell point (that means $Q_1 = Q_2 = 0$). This leads to reduced form of Eq. (3.69):

$$F(0,0) = e_c^2 \sqrt{N_c}\, 4m_c \cdot \int \frac{dz d^2\vec{k}_\perp}{z(1-z)16\pi^3} \frac{\psi(z, \vec{k}_\perp)}{\vec{k}_\perp^2 + m_c^2}\,. \tag{3.70}$$

Moreover, $F(0,0)$ is linked with $\gamma\gamma$ decay width as follows

$$\Gamma(\eta_c \to \gamma\gamma) = \frac{\pi}{4}\alpha_{\text{em}}^2 M_{\eta_c}^3\, |F(0,0)|^2\,, \tag{3.71}$$

47

3. TRANSITION FORM FACTORS IN THE LIGHT-CONE WAVE FUNCTION APPROACH

which can be treated as a check of our normalization condition. The value of the transition form factor at the on-shell point for each light-cone wave function obtained from a specific potential model as well as the mass quark used in the model, can be found in Tab. 3.1 for η_c (1S) and Tab. 3.2 (2S). Furthermore in *The Review of Particle Physics* [77] one can find $\eta_c \to \gamma\gamma$ decay width and using Eq. (3.71) extract $F(0,0)$, which in Tab. 3.1 for η_c (1S) and Tab. 3.2 for η_c (2S) is referred to as experimental value. Our results are listed in Tab. 3.1 for η_c(1S) are below the experimental values. We observe that the value of $F(0,0)$ from power-like potential model has the closest value to the experimental one. In the case of the η_c(2S), our results are in the range of experimental value, but at the same time, the experimental error bar is quite large.

Table 3.1: The transition form factor at the on-shell point $|F(0,0)|$ for $\eta_c(1S)$.

potential type	m_c [GeV]	$|F(0,0)|$ [GeV^{-1}]	$\Gamma_{\gamma\gamma}$ [keV]
harmonic oscillator	1.4	0.051	2.89
logarithmic	1.5	0.052	2.95
power-like	1.334	0.059	3.87
Cornell	1.84	0.039	1.69
Buchmüller-Tye	1.48	0.052	2.95
experiment	-	0.067 ± 0.003 [77]	5.1 ± 0.4 [77]

Table 3.2: The transition form factor at the on-shell point $|F(0,0)|$ for $\eta_c(2S)$.

potential type	m_c [GeV]	$|F(0,0)|$ [GeV^{-1}]	$\Gamma_{\gamma\gamma}$ [keV]
harmonic oscillator	1.4	0.03492	2.454
logarithmic	1.5	0.02403	1.162
power-like	1.334	0.02775	1.549
Cornell	1.84	0.02159	0.938
Buchmüller-Tye	1.48	0.02687	1.453
experiment [77]	-	0.03266 ± 0.01209	2.147 ± 1.589

The η_c transition form factor was first investigated by the L3 Collaboration at the Large Electron Positron Collider (LEP), however only with a poor statistics data sample [78]. More recently, in 2010 the BABAR Collaboration at the PEP-II asymmetric-energy storage rings at the Stanford Linear Accelerator Center (SLAC)

has published data for the normalized transition form factor $|F(Q_1^2, 0)/F(0,0)|$ in terms of photon virtuality Q_1^2. In the single tag mode, they considered η_c in the two-photon production reaction, $e^+e^- \to \eta_c$, where one of the outgoing electrons is measured, while the other electron is scattered at a small angle. The tagged electron emits a highly off-shell photon and the momentum transfer squared of the untagged electron is practically zero, $-q_2^2 \sim 0$ [79]. Moreover, they had measured no-tag mode to gain the normalization of the form factor. Therefore it was a great opportunity to compare our calculations with existing BABAR data, see left panel of Fig. 3.7.
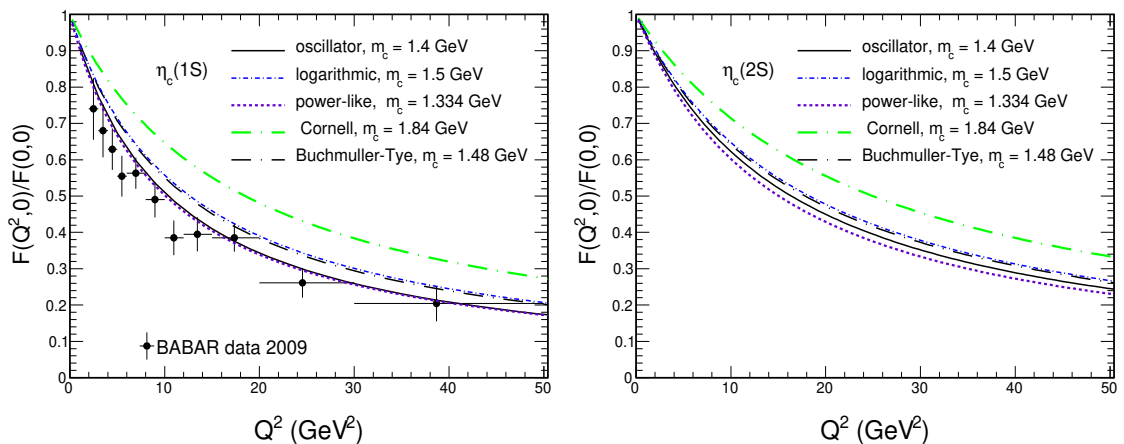
Figure 3.7: *The normalized transition form factor $F(Q^2, 0)/F(0,0)$ for one on-shell photon as a function of virtuality of the second photon. The normalization factors $F(0,0)$ can be found in Tab. 3.1 and Tab. 3.1, respectively for $\eta_c(1S)$ and $\eta_c(2S)$. The experimental data for η_c comes from the BABAR Collaboration [79].*

The findings of our study within the light-cone wave function approach for several potential models are rather promising. We emphasized here that the agreement with the data depends not only on the model of the light-cone wave function but, in particular, on the quark mass. The form factor for oscillator and power-like models seem to give the best description of the data, while the corresponding c-quark masses are $m_c = 1.4\,\mathrm{GeV}$ and $m_c = 1.334\,\mathrm{GeV}$. In the right panel of Fig. 3.7, we present predictions for $\eta_c(2S)$ normalized form factor.

In order to study a few more properties of our transition form factor, it is useful to introduce the asymmetry parameter ω and an average value of the photons virtualities $\bar{Q}^2$:

$$\omega = \frac{Q_1^2 - Q_2^2}{Q_1^2 + Q_2^2}, \quad \bar{Q}^2 = \frac{Q_1^2 + Q_2^2}{2}. \tag{3.72}$$

3. TRANSITION FORM FACTORS IN THE LIGHT-CONE WAVE FUNCTION APPROACH

From Fig. 3.8 one can clearly see that the $F(\omega, \bar{Q}^2)$ is practically independent of the parameter ω. For comparison, we mention that in the case of the transition form factor for the light meson, as $\gamma^*\gamma^* \to \pi^0$ a rather strong dependence on ω is observed [80, 81]. It could be an interesting research area for experiments such as Belle2 to study this subject.
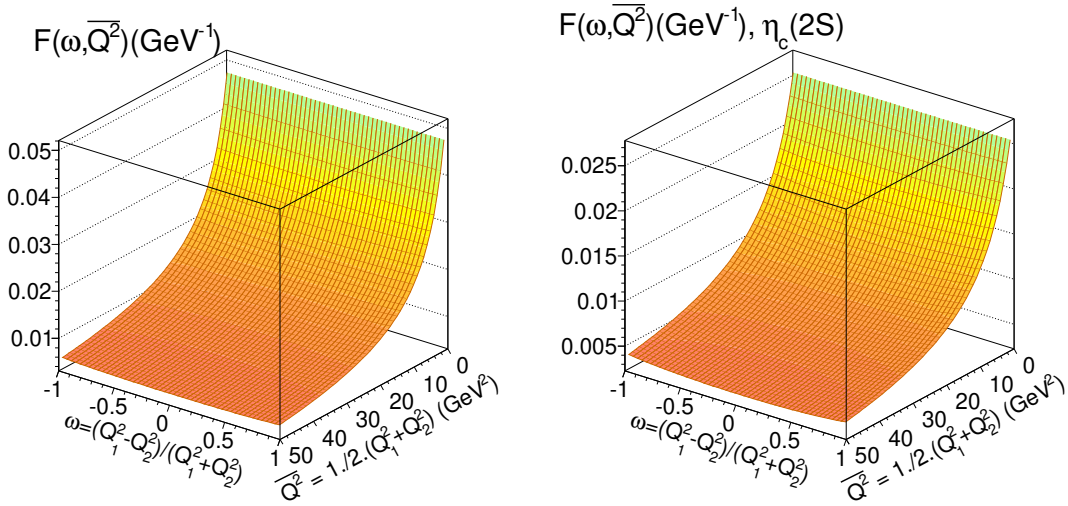
Figure 3.8: The transition form factor for $\eta_c(1S)$-left panel and $\eta_c(2S)$-right panel in terms of asymmetry parameter ω and average value of two virtualities of the photons $\bar{Q}^2$. As an example there is shown the result obtained from the Buchmüller-Tye potential model.

3.4.1 Transition form factor in the nonrelativistic limit

In the beginning, it is worthwhile to go back to the form factor at the on-shell point and rewrite this result as an integral over the three-momentum $\vec{k}$ introduced

in Eq. (3.10), involving the radial wave function $u_{n0}(k)$ for the S-wave

$$
\begin{aligned}
F(0,0) &= e_c^2 \sqrt{N_c}\, 4m_c \cdot \int \frac{dz\, d^2\vec{k}_\perp}{z(1-z)16\pi^3} \frac{\psi(z,\vec{k}_\perp)}{\vec{k}_\perp^2 + m_c^2} \\
&= e_c^2 \sqrt{N_c}\, 4m_c \int \frac{4d^3\vec{k}}{M_{c\bar{c}}16\pi^3} \frac{\psi(z,\vec{k}_\perp)}{\vec{k}_\perp^2 + m_c^2} \\
&= e_c^2 \sqrt{2N_c}\, \frac{m_c}{\pi} \int_0^\infty \frac{dk\, k\, u_{Ln}(k)}{\sqrt{M_{c\bar{c}}^3}(k^2+m_c^2)} \int_{-1}^1 \frac{d\cos\theta}{1-\beta^2\cos^2\theta} \\
&= e_c^2 \sqrt{2N_c}\, \frac{2m_c}{\pi} \int_0^\infty \frac{dk\, k\, u_{n0}(k)}{\sqrt{M_{c\bar{c}}^3}(k^2+m_c^2)} \frac{1}{2\beta}\log\left(\frac{1+\beta}{1-\beta}\right) .
\end{aligned}
\tag{3.73}
$$

Here in the polar coordinates $\vec{k}_\perp^2 = k^2\sin^2\theta$, thus $\vec{k}_\perp^2 + m_c^2 = (k^2+m_c^2)(1-\beta^2\cos^2\theta)$, while β is defined as

$$
\beta = \frac{k}{\sqrt{k^2+m_c^2}} \quad,
\tag{3.74}
$$

the velocity v/c of the quark in the $Q\bar{Q}$ c.m.s.-frame. A complementary analysis for the relativistic corrections to the radiative decay rates exist in the literature, see e.g., Ref. [82] and references therein. A difference of our results compared to the approach of Ebert et al. [82] lies in the fact that in our calculation, the invariant mass $M_{Q\bar{Q}}$ is running with k, while in [82] it is taken to be constant. In the non-relativistic limit, $k^2/m_c^2 \ll 1, \beta \ll 1$, the mass $M_{c\bar{c}}$ reaches $M_{c\bar{c}} = 2m_c$. If one suppresses the binding energy, one can further identify $2m_c = M_{\eta_c}$. We now use

$$
\lim_{\beta \to 0} \frac{1}{2\beta}\log\left(\frac{1+\beta}{1-\beta}\right) = 1 \,,
\tag{3.75}
$$

so that in the nonrelativistic limit, Eq. (3.73) reduces to

$$
\begin{aligned}
F(0,0) &= e_c^2 \sqrt{2N_c}\, \frac{2m_c}{\pi} \int_0^\infty \frac{dk\, k\, u_{n0}(k)}{\sqrt{M_{\eta_c}^3}\, m_c^2} \\
&= \frac{e_c^2 \sqrt{2N_c}}{\pi} \frac{4}{\sqrt{M_{\eta_c}^5}} \int_0^\infty dk\, k\, u_{n0}(k) \\
&= 4e_c^2 \sqrt{\frac{N_c}{\pi M_{\eta_c}^5}}\, R_{n0}(0) \,.
\end{aligned}
\tag{3.76}
$$

here $R_{n0}(0)$ is the value of the radial wave function $R_{n0}(r) = u_{n0}(r)/r$ at the origin $r = 0$ (for more details see Appendix A). In the above derivation we have used the

3. TRANSITION FORM FACTORS IN THE LIGHT-CONE WAVE FUNCTION APPROACH

relation

$$\int_0^\infty k \, dk \, u_{n0}(k) = \sqrt{\frac{\pi}{2}} R_{n0}(0) \,. \tag{3.77}$$

Inserting the result of Eq. (3.76) into Eq. (3.71), this finally leads to the well known expression for the $\gamma\gamma$-width (see e.g. Table 2.2 in Ref. [46])

$$\Gamma(\eta_c \to \gamma\gamma) = \frac{4\alpha_{\text{em}}^2 e_c^4 N_c}{M_{\eta_c}^2} |R_{n0}(0)|^2 \,. \tag{3.78}$$

In fact, there is an ambiguity in the way how to calculate the decay rate (Eq.3.78) which is related to the fact that in the NR limit $M_{\eta_c} = 2m_c$. This means that within the accuracy of the approximation one can either calculate the width using the physical meson mass M_{η_c} or with the help of the quark mass $M_{\eta_c} = 2m_c$. Therefore in Tabs. 3.3, 3.4 we have summarized our results of both methods, for $\eta_c(1S)$ and $\eta_c(2S)$, respectively. As one can observe for different potential models, the spread of the results is quite wide. In the case of $\eta_c(1S)$ only the value obtained for the harmonic-oscillator potential could be regarded as being in the range of the measured value $\Gamma(\eta_c(1S) \to \gamma\gamma) = 5.1 \pm 0.4 \, \text{keV}$. In the case of excited η_c all our findings in the NR limit are far way from the experimental value, $\Gamma(\eta_c(2S) \to \gamma\gamma) = 2.147 \pm 1.589 \, \text{keV}$ [77].

Table 3.3: *The radial wave function at the origin* $|R_{00}(0)|$ *and radiative decay width* $\Gamma(\eta_c(1S) \to \gamma\gamma)$ *for* $\eta_c(1S)$.

potential type	$|R_{00}(0)|[\text{GeV}^{3/2}]$	$\Gamma_{\eta_c(1S)\to\gamma\gamma}$ [keV] $M = M_{\eta_c(1S)}$	$\Gamma_{\eta_c(1S)\to\gamma\gamma}$ [keV] $M = 2m_c$
harmonic oscillator	0.6044	5.1848	5.8815
logarithmic	0.8919	11.290	11.157
power-like	0.7620	8.2412	10.297
Cornell	1.2065	20.660	13.568
Buchmüller-Tye	0.8899	11.240	11.409
experiment [77]		5.1 ± 0.4	5.1 ± 0.4

In the NR limit, which is obtained after expanding the amplitude in a Taylor series around $\vec{k}_\perp = 0$ and $z = 1/2$ in Eq. (3.69), the transition form factor emerges in the NRQCD-limit as,

$$F(Q_1^2, Q_2^2) = e_c^2 \sqrt{N_c} \frac{4}{\sqrt{\pi M_{\eta_c}}} \frac{1}{Q_1^2 + Q_2^2 + M_{\eta_c}^2} |R_{n0}(0)| \,. \tag{3.79}$$

Table 3.4: The radial wave function at the origin $|R_{10}(0)|$ and radiative decay width $\Gamma(\eta_c(2S) \to \gamma\gamma)$ for $\eta_c(2S)$.

potential type	$|R_{10}(0)|[\text{GeV}^{3/2}]$	$\Gamma_{\eta_c(2S)\to\gamma\gamma}$ [keV] $M = M_{\eta_c(2S)}$	$\Gamma_{\eta_c(2S)\to\gamma\gamma}$ [keV] $M = 2m_c$
harmonic oscillator	0.7402	5.2284	8.8214
logarithmic	0.6372	3.8745	5.6946
power-like	0.5699	3.0993	5.7594
Cornell	0.9633	8.8550	8.6493
Buchmüller-Tye	0.7185	4.9263	7.4374
experiment [77]		2.147 ± 1.589	2.147 ± 1.589

In Fig. 3.9 we present the ratio of two form factors, namely the form factor obtained through light-cone wave function for the Buchmüller-Tye (B-T) potential model and the form factor in the NRQCD-limit. In order to calculate the NRQCD form factor we have employed $|R_{00}(0)| = 0.8899 \, \text{GeV}^{3/2}$, $M_{\eta_c(1S)} = (2983.9 \pm 0.4) \, \text{MeV}$ for $\eta_c(1S)$ and $|R_{10}(0)| = 0.7185 \, \text{GeV}^{3/2}$, $M_{\eta_c(2S)} = (3637.5 \pm 1.1) \, \text{MeV}$ for $\eta_c(2S)$. The values of the radial wave function at the origin $|R_{n0}(0)|$ are taken from Tabs. 3.3, 3.2 for the Buchmüller-Tye potential model.
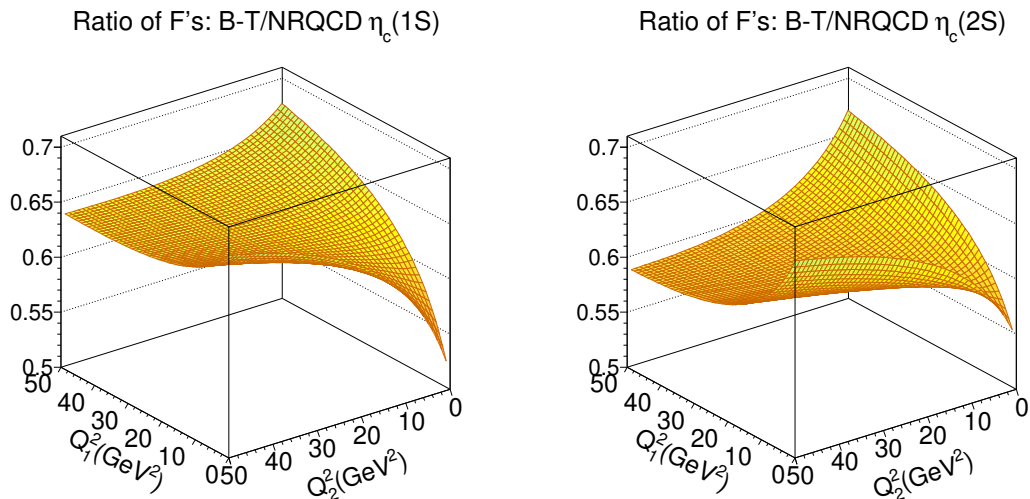
Figure 3.9: Ratio of the form factor constructed from light-cone wave function for the Buchmüller-Tye potential model and NRQCD form factor with $|R_{00}(0)| = 0.8899 \, \text{GeV}^{3/2}$ for $\eta_c(1S)$ and $|R_{10}(0)| = 0.7185 \, \text{GeV}^{3/2}$ for $\eta_c(2S)$, see Tabs. 3.3, 3.2.

3.4.2 Transition form factor and distribution amplitude

In the last two decades, physicists have investigated several properties of the η_c.
For instance in 2001 the CLEO Collaboration published results for two-body B
decays, $B \to \eta_c K$ in both neutral and charged modes [83]. By comparing the rates
of the decays η_c with J/Ψ, they extracted the η_c decay constant in the so-called
factorization approximation, $f_{\eta_c} = 335 \pm 75\,\text{MeV}$. So far the decay constant was
estimated within several methods including Light Front Quark Model (LFQM)[75,
64] as well as Lattice QCD [84].

Let us turn to the description in the light-cone wave function approach. The
relation between the distribution amplitude (DA) $\varphi(z, \mu)$ and the η_c light-cone wave
function $\psi(z, k_\perp)$ is

$$f_{\eta_c} \varphi(z, \mu^2) = \frac{1}{z(1-z)} \frac{\sqrt{N_c} m_c}{4\pi^2} \int^{\mu^2} dk_\perp^2 \psi(z, k_\perp) \,. \qquad (3.80)$$

Taking into account the normalization of the DA, $\int_0^1 dz \varphi(z, \mu_0^2) = 1$, and then
integrating over the momentum fraction z, the decay constant can be found as

$$f_{\eta_c} = \frac{\sqrt{N_c} m_c}{4\pi^2} \int_0^1 \frac{dz}{z(1-z)} \int^{\mu^2} dk_\perp^2 \psi(z, k_\perp) \,. \qquad (3.81)$$

Subsequently replacing f_{η_c} on the left hand side of Eq. (3.80) with Eq. (3.81) one
can obtain

$$\varphi(z, \mu^2) = \frac{\mathcal{N}}{z(1-z)} \int^{\mu^2} dk_\perp^2 \psi(z, k_\perp) \,, \qquad (3.82)$$

where the distribution amplitude is a function of momentum fraction z. The addi-
tional normalization constant is equal $\mathcal{N} = 1/\left(\int \frac{dz}{z(1-z)} \int dk_\perp^2 \psi(z, k_\perp) \right)$. In Fig. 3.10
we illustrate the distribution amplitudes at the hard scale $\mu_0 = 3\,\text{GeV}$ for our set
of the wave functions in the left panel for $\eta_c(1S)$ and in the right panel for $\eta_c(2S)$.
In the case of $\eta_c(2S)$ one can observe characteristic dip at the momentum fraction
$z = 1/2$, which is also observed in the light-cone wave function $\psi(z, \vec{k}_\perp)$ in Fig. 3.2.
The received values of the so-called decay constant f_{η_c} within light-cone approach
are listed in Tab. 3.5 for $\eta_c(1S)$ and in Tab. 3.6 $\eta_c(2S)$. For completeness, in Tab. 3.5,
there are cited results known from the literature. In the case of $\eta_c(1S)$, the difference
between the CLEO Collaboration result and our predictions is not significant. Nev-
ertheless, predictions from Lattice QCD [84] and light front quark model [75, 64],
where the $\Gamma_{\gamma\gamma}$ comes in as a parameter, differ from each other. The evolution with
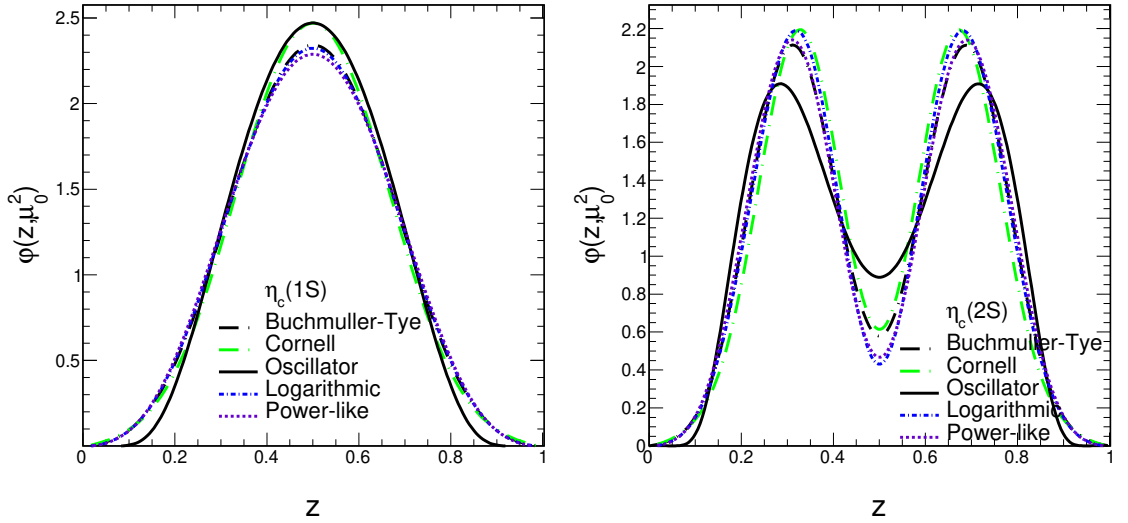
Figure 3.10: Distribution amplitudes at factorization scale $\mu_0 = 3\,\mathrm{GeV}$ for $\eta_c(1S)$-left panel and $\eta_c(2S)$-right panel.

Table 3.5: Decay width and decay constant f_{η_c} for $\eta_c(1S)$.

potential type	m_c [GeV]	$\Gamma_{\gamma\gamma}$ [keV]	f_{η_c} [GeV]
harmonic oscillator	1.4	2.89	0.2757
logarithmic	1.5	2.95	0.3373
power-like	1.334	3.87	0.3074
Cornell	1.84	1.69	0.3726
Buchmüller-Tye	1.48	2.95	0.3276
RYU, CHOI, and JI, set I [75]	1.80	1.55	0.326
RYU, CHOI, and JI, set II [75]	1.30	4.88	0.335
Geng, Lih, LFQM [64]	1.29	5.3±0.5	$0.2305^{+0.0522}_{-0.0610}$
Geng, Lih, LFQM [64]	1.29	7.2±2.1	$0.3036^{+0.1152}_{-0.1164}$
Davies et al., Lattice QCD [84]	-	7.2 ± 2.1	0.3947 ± 0.0024
experiment	-	5.1 ± 0.4 [77]	0.335 ± 0.075 [83]

the hard scale is included by the standard methods for light pseudoscalar mesons like π^0, η or η', see e.g. a recent NLO study [85]. The evolution of $\varphi(z, \mu^2)$ with the hard scale μ can be performed by making use of the Gegenbauer $C_n^{3/2}$ polynomials:

$$\varphi(z, \mu^2) = 6z(1-z)\left(1 + a_2(\mu^2)C_2^{3/2}(2z-1) + ...\right) . \tag{3.83}$$

3. TRANSITION FORM FACTORS IN THE LIGHT-CONE WAVE FUNCTION APPROACH

Table 3.6: Decay width and decay constant f_{η_c} for $\eta_c(2S)$.

potential type	m_c [GeV]	$\Gamma_{\gamma\gamma}$ [keV]	f_{η_c} [GeV]
harmonic oscillator	1.4	2.454	0.2530
logarithmic	1.5	1.162	0.1970
power-like	1.334	1.549	0.1851
Cornell	1.84	0.938	0.2490
Buchmüller-Tye	1.48	1.453	0.2149
experiment [77]	-	2.147 ± 1.589	-

Table 3.7: Extracted coefficients $a_n(\mu_0)$, for the Buchmüller-Tye potential.

n	$a_n(\mu_0)\ \eta_c(1S)$	$a_n(\mu_0)\ \eta_c(2S)$
2	-0.284	-0.0765
4	0.0635	-0.1627
6	-0.008157	0.128
8	-0.000619	-0.049
10	0.000216	0.0088

The Gegenbauer coefficients can be extracted by means of

$$a_n(\mu_0) = \frac{2(2n+3)}{3(n+1)(n+2)} \cdot \int_0^1 dz\, \varphi(z, \mu_0) C_n^{3/2}(2z-1) \,. \tag{3.84}$$

Their evolution with the hard scale is described as follows

$$a_n(\mu) = a_n(\mu_0) \cdot \left[\frac{\alpha_s(\mu)}{\alpha_s(\mu_0)} \right]^{\gamma_n/\beta_0} , \tag{3.85}$$

with the anomalous dimensions γ_n, which can be found for example in Ref. [67]

$$\gamma_n = C_F \left(1 - \frac{2}{(n+1)(2+n)} + 4 \sum_{m=2}^{n+1} \frac{1}{m} \right), \quad \beta_0 = \frac{11}{3} N_c - \frac{2}{3} N_f \,. \tag{3.86}$$

In the limit of large Q_i^2 in the hard matrix element Eq. (3.66), it is allowed to neglect the $\vec{k}_\perp$ dependence. Hence, only the light-cone wave function $\psi(z, \vec{k}_\perp)$ is left under the $\vec{k}_\perp$ integral. Subsequently, the transition form factor is written in terms of the distribution amplitude $\varphi(z, \mu_0^2)$ as follows

$$F(Q_1^2, Q_2^2) = e_c^2 f_{\eta_c} \cdot \int_0^1 dz \Big\{ \frac{(1-z)\,\varphi(z, \mu_0^2)}{(1-z)^2 Q_1^2 + z(1-z)Q_2^2 + m_c^2} $$
$$+ \frac{z\,\varphi(z, \mu_0^2)}{z^2 Q_1^2 + z(1-z)Q_2^2 + m_c^2} \Big\} \,. \tag{3.87}$$

In addition, from Ref. [67], one would learn about an asymptotic value, which $Q^2F(Q^2,0)$ is going to reach at large Q^2. In the case of the asymptotic distribution amplitude $\varphi(z,\mu_0^2) = 6z(1-z)$, one can show that $Q^2F(Q^2,0) \longrightarrow \frac{8}{3}f_{\eta_c}$. However, we do not observe our results approaching the limit determined by the value $\frac{8}{3}f_{\eta_c}$ neither for $\eta_c(1S)$-left panel nor $\eta_c(2S)$-right panel of Fig. 3.11. As an example, the Buchmüller-Tye potential model is taken under consideration. The horizontal line shown in Fig. 3.11 is the limit line obtained for this model, according to Tabs. 3.5, 3.6. For completeness, we compare three results, the first one directly from our full light-cone approach - red dashed curve, the second is obtained from the collinear form factor Eq. (3.87) - black dashed-dotted curve and the third one has incorporated the hard scale evolution with the scale $\mu_0 = 3\,\text{GeV}$ - blue solid line. The difference between these three results appears at low Q^2 and the effect of hard-scale evolution is rather negligible in the region of interest. Note that in Fig. 3.11 even for large Q^2, say in the left panel $Q^2 \to 400\,\text{GeV}$, and $Q^2 \to 1000\,\text{GeV}$ in the right panel the predicted asymptotic limit is not approached, even with inclusion of the evolution effects.
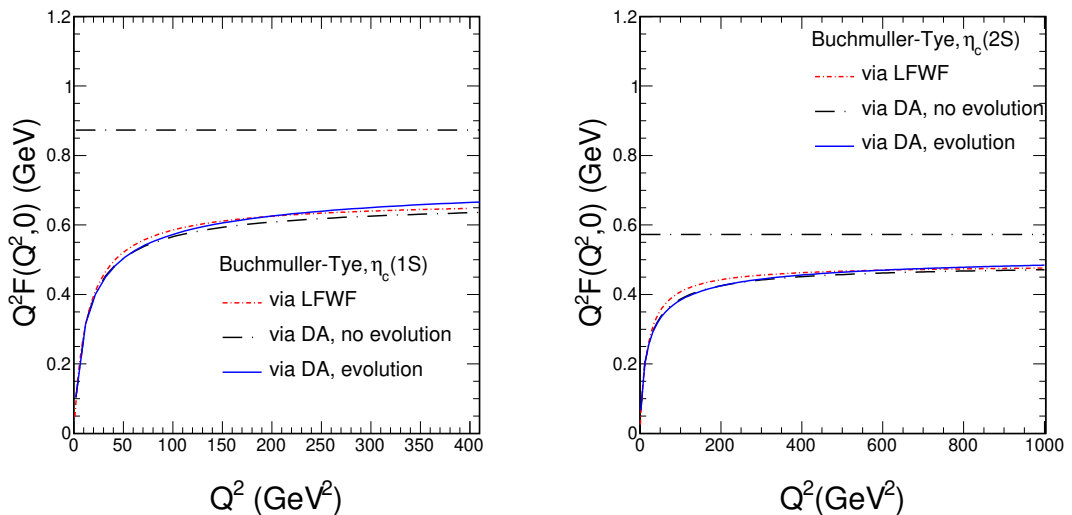
Figure 3.11: The plot of $Q^2F(Q^2,0)$ in terms of photon virtuality Q^2. The horizontal line is put as a reference for asymptotic value and it is calculated for the Buchmüller-Tye potential model.

3.5 Spacelike transition form factors for scalar P-wave quarkonia

The photon-photon fusion amplitude for the P-wave state can be considered in terms of two form factors - transverse F_{TT} and longitudinal F_{LL}. These form factors correspond to the polarizations of the fusing photons, where the quantization axis is taken along the $\gamma^*\gamma^*$ collision axis in the $\gamma^*\gamma^*$ c.m.s. frame. In covariant form, follwoing the standard procedure explained in [76], we can write

$$\mathcal{M}_{\mu\nu}(\gamma^*(q_1)\gamma^*(q_2) \to \chi_{Q0}(P)) =$$
$$4\pi\alpha_{\text{em}}\big(-\delta^\perp_{\mu\nu}(q_1, q_2)\, F_{TT}(q_1^2, q_2^2) + e^L_\mu(q_1)e^L_\nu(q_2)\, F_{LL}(q_1^2, q_2^2)\big)\,, \quad (3.88)$$

here the projector on transverse polarization states is:

$$-\delta^\perp_{\mu\nu}(q_1, q_2) = -g_{\mu\nu} + \frac{1}{X}\Big((q_1 \cdot q_2)(q_{1\mu}q_{2\nu} + q_{1\nu}q_{2\mu}) - q_1^2 q_{2\mu}q_{2\nu} - q_2^2 q_{1\mu}q_{1\nu}\Big), \quad (3.89)$$

and $X = (q_1 \cdot q_2)^2 - q_1^2 q_2^2$. The longitudinal polarization states of virtual photons read:

$$e^L_\mu(q_1) = \sqrt{\frac{-q_1^2}{X}}\Big(q_{2\mu} - \frac{q_1 \cdot q_2}{q_1^2}q_{1\mu}\Big)\,, \quad e^L_\nu(q_2) = \sqrt{\frac{-q_2^2}{X}}\Big(q_{1\nu} - \frac{q_1 \cdot q_2}{q_2^2}q_{2\nu}\Big)\,. \quad (3.90)$$

Now, we need to take into account also $n^{+/-}$ vector projections onto the amplitude, to this end we derive:

$$-n^{+\mu}n^{-\nu}\delta^\perp_{\mu\nu} = -1 + \frac{(q_1 \cdot q_2)}{X}q_1^+ q_2^- = \frac{1}{X}\Big(q_1^2 q_2^2 + (\vec{q}_{1\perp} \cdot \vec{q}_{2\perp})(q_1 \cdot q_2)\Big)\,, \quad (3.91)$$

and

$$e^L_\mu(q_1)e^L_\nu(q_2)n^{+\mu}n^{-\nu} = \frac{\sqrt{q_1^2 q_2^2}}{X}q_1^+ q_2^- = \frac{\sqrt{q_1^2 q_2^2}}{X}\Big((q_1 \cdot q_2) + (\vec{q}_{1\perp} \cdot \vec{q}_{2\perp})\Big)\,. \quad (3.92)$$

Hence the general form of the amplitude with the coefficients $(\vec{q}_{1\perp} \cdot \vec{q}_{2\perp})$ and $q_1^2 q_2^2$ put in evidence, reads:

$$n^{+\mu}n^{-\nu}\mathcal{M}_{\mu\nu} = 4\pi\alpha_{\text{em}}\Bigg[(\vec{q}_{1\perp} \cdot \vec{q}_{2\perp})\Big[\frac{(q_1 \cdot q_2)}{X}F_{TT}(q_1^2, q_2^2) + \frac{|\vec{q}_{1\perp}||\vec{q}_{2\perp}|}{X}F_{LL}(q_1^2, q_2^2)\Big]$$

$$+ |\vec{q}_{1\perp}||\vec{q}_{2\perp}|\Big[\frac{|\vec{q}_{1\perp}||\vec{q}_{2\perp}|}{X}F_{TT}(q_1^2, q_2^2) + \frac{(q_1 \cdot q_2)}{X}F_{LL}(q_1^2, q_2^2)\Big]\Bigg]\,. \quad (3.93)$$

Here we used $\sqrt{q_1^2 q_2^2} = |\vec{q}_{1\perp}||\vec{q}_{2\perp}|$. Note also

$$(q_1 \cdot q_2) = \frac{1}{2}\left(M_\chi^2 + \vec{q}_{1\perp}{}^2 + \vec{q}_{2\perp}{}^2\right)$$

$$\text{and} \quad X = \frac{M_\chi^4}{4}\left(1 + \frac{2(\vec{q}_{1\perp}{}^2 + \vec{q}_{2\perp}{}^2)}{M_\chi^2} + \frac{(\vec{q}_{1\perp}{}^2 - \vec{q}_{2\perp}{}^2)^2}{M_\chi^4}\right), \quad (3.94)$$

do not depend on the azimuthal angles of $\vec{q}_{1\perp}$ and $\vec{q}_{2\perp}$. Coming back to our master formula given by Eq. (3.60) and inserting result for P-wave helicity amplitude $\Psi^*_{\lambda\bar{\lambda}}(z, \vec{k}_\perp)$ Eq. (3.25), one can get

$$\sqrt{2}\left((\vec{e}_\perp(-) \cdot \vec{q}_{1\perp})\Psi^*_{++}(z, \vec{k}_\perp) + (\vec{e}_\perp(+) \cdot \vec{q}_{1\perp})\Psi^*_{--}(z, \vec{k}_\perp)\right) = \frac{2(\vec{q}_{1\perp}\vec{k}_\perp)}{\sqrt{z(1-z)}}\psi(z, \vec{k}_\perp) \quad ,$$

$$\Psi^*_{+-}(z, \vec{k}_\perp) + \Psi^*_{-+}(z, \vec{k}_\perp) = \frac{2m_Q(1-2z)}{\sqrt{z(1-z)}}\psi(z, \vec{k}_\perp) \quad ,$$

$$\Psi^*_{+-}(z, \vec{k}_\perp) - \Psi^*_{-+}(z, \vec{k}_\perp) = 0 \quad .$$

$$(3.95)$$

Hence, the master formula Eq. (3.60) is reduced to

$$\int \frac{dz\, d^2\vec{k}_\perp}{z(1-z)16\pi^3} \sum_{\lambda\bar{\lambda}} \Psi^*_{\lambda\bar{\lambda}} n^{+\mu} n^{-\nu} \mathcal{A}^{\lambda\bar{\lambda}}_{\mu\nu} = (-4m_Q)\int \frac{dz\, d^2\vec{k}_\perp}{z(1-z)16\pi^3}\psi(z, \vec{k}_\perp)$$

$$\times \left\{2z(1-z)(1-2z)\vec{q}_{1\perp}{}^2\left[\frac{1}{\vec{l}_A{}^2 + \varepsilon^2} - \frac{1}{\vec{l}_B{}^2 + \varepsilon^2}\right]\right.$$

$$- 4z(1-z)(\vec{k}_\perp\vec{q}_{1\perp})\left[\frac{1}{\vec{l}_A{}^2 + \varepsilon^2} - \frac{1}{\vec{l}_B{}^2 + \varepsilon^2}\right]$$

$$\left.- (1-2z)^2(\vec{q}_{1\perp}\vec{q}_{2\perp})\left[\frac{1-z}{\vec{l}_A{}^2 + \varepsilon^2} + \frac{z}{\vec{l}_B{}^2 + \varepsilon^2}\right]\right\} . \quad (3.96)$$

In order to extract the form factors F_{TT} and F_{LL} it is convenient to group them in a similar fashion as in Eq. (3.93):

$$\int \frac{dz\, d^2\vec{k}_\perp}{z(1-z)16\pi^3} \sum_{\lambda\bar{\lambda}} \Psi^*_{\lambda\bar{\lambda}} n^{+\mu} n^{-\nu} \mathcal{A}^{\lambda\bar{\lambda}}_{\mu\nu} = 4m_Q\int \frac{dz\, d^2\vec{k}_\perp}{z(1-z)16\pi^3}\psi(z, \vec{k}_\perp)$$

$$\times \left\{|\vec{q}_{1\perp}||\vec{q}_{2\perp}|\left[\frac{|\vec{q}_{1\perp}||\vec{q}_{2\perp}|}{\vec{q}_{2\perp}{}^2}2z(1-z)(2z-1)\left[\frac{1}{\vec{l}_A{}^2 + \varepsilon^2} - \frac{1}{\vec{l}_B{}^2 + \varepsilon^2}\right]\right]\right.$$

$$\left.+ (\vec{q}_{1\perp} \cdot \vec{q}_{2\perp})\left[\left[\frac{1-z}{\vec{l}_A{}^2 + \varepsilon^2} + \frac{z}{\vec{l}_B{}^2 + \varepsilon^2}\right] + 4z(1-z)\left[\frac{\vec{q}_{2\perp} \cdot \vec{l}_A}{\vec{l}_A{}^2 + \varepsilon^2} - \frac{\vec{q}_{2\perp} \cdot \vec{l}_B}{\vec{l}_B{}^2 + \varepsilon^2}\right]\right]\right\} . \quad (3.97)$$

3. TRANSITION FORM FACTORS IN THE LIGHT-CONE WAVE FUNCTION APPROACH

Now we introduce a convenient notation

$$\int \frac{dz d^2 \vec{k}_\perp}{z(1-z)16\pi^3} \sum_{\lambda\bar{\lambda}} \Psi^*_{\lambda\bar{\lambda}} n^{+\mu} n^{-\nu} \mathcal{A}^{\lambda\bar{\lambda}}_{\mu\nu} = |\vec{q}_{1\perp}||\vec{q}_{2\perp}|F_1 + (\vec{q}_{1\perp} \cdot \vec{q}_{2\perp})F_2 \,. \tag{3.98}$$

These form factors F_1 and F_2 have the integral form written as

$$
\begin{aligned}
F_1(\vec{q}_{1\perp}{}^2, \vec{q}_{2\perp}{}^2) &= |\vec{q}_{1\perp}||\vec{q}_{2\perp}| \frac{4m_Q}{\vec{q}_{2\perp}{}^2} \int \frac{dz d^2\vec{k}_\perp}{z(1-z)16\pi^3} \psi(z,\vec{k}_\perp) \\
&\times 2z(1-z)(2z-1)\Big[\frac{1}{\vec{l}_A{}^2 + \varepsilon^2} - \frac{1}{\vec{l}_B{}^2 + \varepsilon^2}\Big], \\
F_2(\vec{q}_{1\perp}{}^2, \vec{q}_{2\perp}{}^2) &= 4m_Q \int \frac{dz d^2\vec{k}_\perp}{z(1-z)16\pi^3} \psi(z,\vec{k}_\perp)\Big[\frac{1-z}{\vec{l}_A{}^2 + \varepsilon^2} + \frac{z}{\vec{l}_B{}^2 + \varepsilon^2}\Big] \\
&+ \frac{4m_Q}{\vec{q}_{2\perp}{}^2} \int \frac{dz d^2\vec{k}_\perp}{z(1-z)16\pi^3} \psi(z,\vec{k}_\perp) 4z(1-z)\Big[\frac{\vec{q}_{2\perp} \cdot \vec{l}_A}{\vec{l}_A{}^2 + \varepsilon^2} - \frac{\vec{q}_{2\perp} \cdot \vec{l}_B}{\vec{l}_B{}^2 + \varepsilon^2}\Big].
\end{aligned}
\tag{3.99}
$$

Let us now relate form factors F_1, F_2 to the ones for definite photon polarizations. To this end, comparing Eq. (3.98) with Eq. (3.93) we find the relation

$$\begin{pmatrix} F_1 \\ F_2 \end{pmatrix} = \frac{1}{e_Q^2 \sqrt{N_c} X} \begin{pmatrix} |\vec{q}_{1\perp}||\vec{q}_{2\perp}| & (q_1 \cdot q_2) \\ (q_1 \cdot q_2) & |\vec{q}_{1\perp}||\vec{q}_{2\perp}| \end{pmatrix} \begin{pmatrix} F_{TT} \\ F_{LL} \end{pmatrix}, \tag{3.100}$$

or, in its inverse form

$$\begin{pmatrix} F_{TT} \\ F_{LL} \end{pmatrix} = e_Q^2 \sqrt{N_c} \begin{pmatrix} -|\vec{q}_{1\perp}||\vec{q}_{2\perp}| & (q_1 \cdot q_2) \\ (q_1 \cdot q_2) & -|\vec{q}_{1\perp}||\vec{q}_{2\perp}| \end{pmatrix} \begin{pmatrix} F_1 \\ F_2 \end{pmatrix}. \tag{3.101}$$

These equations are applicable for P-wave spinless $Q\bar{Q}$ systems such as χ_{c0} or χ_{b0}.

Our findings for these form factors are illustrated in Figs. 3.12 and 3.13 for χ_{c0} and χ_{b0}, respectively. In the case of χ_{c0} as well as χ_{b0} the transverse part of the transition form factor is numerically larger. However, as we will see in the next chapter also the longitudinal part plays a significant role. The relative sign between F_{TT} and F_{LL} is negative, therefore in Figs. 3.12, 3.13 we are present the absolute values of these contributions. Although the two-dimensional plots we show are only for the Buchmüller-Tye potential model, the remaining models give rise to similar shapes. The main difference is in the position of the maximum, which for $F_{TT}(Q_1^2, Q_2^2)$ is at the on-shell point.
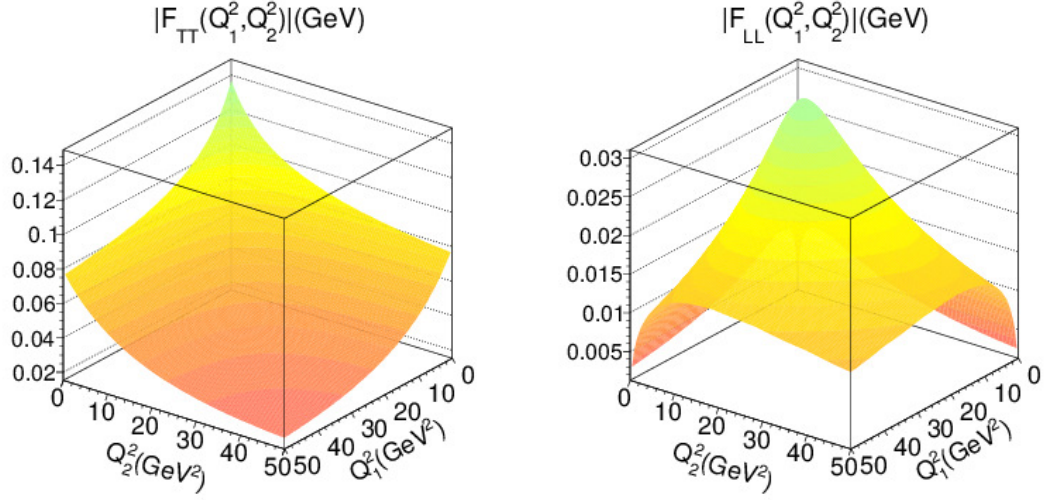
Figure 3.12: *Transverse part of the transition form factor $|F_{TT}(Q_1^2, Q_2^2)|$ (left panel) and longitudinal part of the transition form factor $|F_{LL}(Q_1^2, Q_1^2)|$ (right panel) as a function of the photons virtualities Q_1^2, Q_2^2 from χ_{c0} light-cone wave function obtained through the Buchmüller-Tye potential model.*
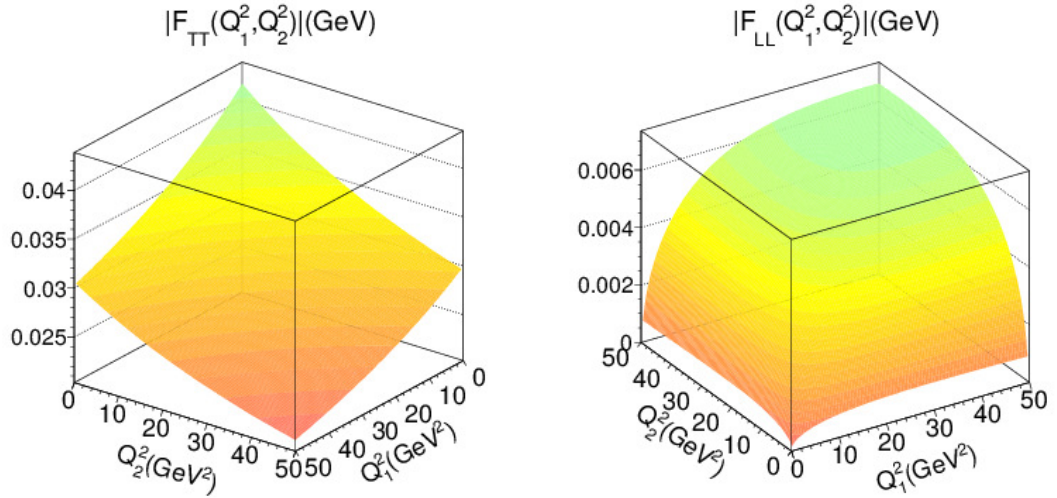
Figure 3.13: *Transverse part of the transition form factor $|F_{TT}(Q_1^2, Q_2^2)|$ (left panel) and longitudinal part of the transition form factor $|F_{LL}(Q_1^2, Q_1^2)|$ (right panel) as a function of the photons virtualities Q_1^2, Q_2^2 from χ_{b0} light-cone wave function obtained through the Buchmüller-Tye potential model.*

3. TRANSITION FORM FACTORS IN THE LIGHT-CONE WAVE FUNCTION APPROACH

At the on-shell point, where $Q_1^2 = Q_2^2 = 0$, the auxiliary form factor $F_1(0,0)$ as well as the longitudinal form factor $|F_{LL}(0,0)|$ are vanishing, thus the transverse form factor reads

$$F_{TT}(0,0) = \frac{M_\chi^2}{2} F_2(0,0),\qquad(3.102)$$

here M_χ is a mass of the scalar meson. The radiative decay width for χ_Q state is linked with transverse form factor according to

$$\Gamma(\chi_{Q0} \to \gamma\gamma)_{LO} = \frac{\pi\alpha_{\rm em}^2}{M_\chi}|F_{TT}(0,0)|^2,\qquad(3.103)$$

$\Gamma(\chi_{Q0} \to \gamma\gamma)_{LO}$ in the remaining part of this section is called Leading Order (LO) formula. Also the first QCD radiative correction is known [82], and can be accounted for by multiplying the radiative decay width by the expression shown below in the bracket:

$$\Gamma(\chi_{Q0} \to \gamma\gamma)_{NLO} = \Gamma(\chi_{Q0} \to \gamma\gamma)_{LO}\left[1 + \frac{\alpha_s}{\pi}\left(\frac{\pi^2}{3} - \frac{28}{9}\right)\right],\qquad(3.104)$$

here we have used $\alpha_s = 0.26$ for χ_{c0} and $\alpha_s = 0.18$ for χ_{b0} (see Ref. [82]). $\Gamma(\chi_{Q0} \to \gamma\gamma)_{NLO}$ is labeled as the Next-to-Leading Order expression in the following part of this section. In order to extract the "experimental" value of $|F_{TT}(0,0)|$ for χ_{c0}, one can take the experimentally measured value of the decay rate $\Gamma(\chi_{c0} \to \gamma\gamma)$ from Ref. [77] and put it into the left side of Eq. (3.104) and then combine it with Eq. (3.103). This value in Tab. 3.8 and Tab. 3.9 is indicated by "$\star$". In the practical calculation we have taken $M_{\chi_{Q0}} = 2m_Q$ and the decay rate in Tabs. 3.8, 3.10 for each potential model is obtained with the corresponding c-quark/b-quark mass. For comparison, in Tabs. 3.9, 3.11 the dependence of the quark mass on the model is abandoned, and the value according to the Particle Data Group review [77], $m_c = 1.27\,\mathrm{GeV}$ and $m_b = 4.18\,\mathrm{GeV}$ respectively for c-quark and b-quark has been used.

The normalized form factor $F_{TT}(Q^2,0)/F_{TT}(0,0)$ in the left panel of Fig. 3.14 is obtained in terms of the wave function for five specific potential models with their corresponding quark mass, whereas in the right panel with $m_c = 1.27\,\mathrm{GeV}$ and $m_b = 4.18\,\mathrm{GeV}$ for χ_{c0} and χ_{b0}, respectively [77]. The normalization factors $F_{TT}(0,0)$ can be found in Tabs. 3.8, 3.10 for the left panel and in Tabs. 3.9, 3.11 for the right panel. The spread of results obtained with specific quark mass for each potential

Table 3.8: *The transition form factor at the on-shell point $|F_{TT}(0,0)|$ and the decay rate $\Gamma(\chi_{c0} \to \gamma\gamma)$ at Leading Order and Next-to-Leading Order for five distinguished potentials models. "*" is explained in the text.*

potential type	m_c [GeV]	$|F(0,0)|$ [GeV]	$\Gamma(\chi_{c0} \to \gamma\gamma)_{LO}$ [keV]	$\Gamma(\chi_{c0} \to \gamma\gamma)_{NLO}$ [keV]
harmonic oscillator	1.4	0.18	1.56	1.58
logarithmic	1.5	0.14	0.91	0.93
powerlike	1.334	0.16	1.32	1.34
Cornell	1.84	0.10	0.44	0.46
Buchmülller-Tye	1.48	0.14	0.96	0.98
experiment [77]	1.27	0.21*		2.20 ± 0.16

Table 3.9: *The transition form factor at the on-shell point $|F_{TT}(0,0)|$ and the decay rate $\Gamma(\chi_{c0} \to \gamma\gamma)$ at Leading Order and Next-to-Leading Order for five distinguished potentials models. Here, the dependence quark mass on the model is neglected. The calculation is performed with $m_c = 1.27\,\text{GeV}$ for each potential model.*

potential type	$|F_{TT}(0,0)|$ [GeV]	$\Gamma(\chi_{c0} \to \gamma\gamma)_{LO}$ [keV]	$\Gamma(\chi_{c0} \to \gamma\gamma)_{NLO}$ [keV]
harmonic oscillator	0.21	2.06	2.09
logarithmic	0.18	1.54	1.56
power-law	0.18	1.54	1.56
Cornell	0.17	1.41	1.43
Buchmülller-Tye	0.18	1.54	1.56
experiment [77]	0.21*		2.20 ± 0.16

model (see the left panel of Fig. 3.14) is broader, while this effect almost disappears when quark mass is determined to the value given by the Particle Data Group [77].

Now, it is possible to compare our results derived for η_c with those obtained for χ_{c0}. We wish to present the results in terms of the previously introduced asymmetry parameter ω and the average value of photons virtuality $\bar{Q}^2$, see Eq. (3.72). For illustration, in Fig. 3.15 we show the form factors F_{TT} and F_{LL} for the Buchmüller-Tye potential model. In the case of χ_{c0} meson, we do not observe a scaling effect in ω as it is the case for η_c.

Table 3.10: *The transition form factor at the on-shell point $|F_{TT}(0,0)|$ and the decay rate $\Gamma(\chi_{b0} \to \gamma\gamma)$ at Leading Order and Next-to-Leading Order for five distinguished potentials models.*

potential type	m_b [GeV]	$|F_{TT}(0,0)|$ [GeV]	$\Gamma(\chi_{b0} \to \gamma\gamma)_{LO}$ [keV]	$\Gamma(\chi_{b0} \to \gamma\gamma)_{NLO}$ [keV]
harmonic oscillator	4.2	0.053	0.047	0.048
logarithmic	5.0	0.032	0.017	0.017
power-law	4.721	0.033	0.018	0.019
Cornell	5.17	0.028	0.014	0.014
Buchmülller-Tye	4.87	0.031	0.017	0.017

Table 3.11: *The transition form factor at the on-shell point $|F_{TT}(0,0)|$ and the decay rate $\Gamma(\chi_{c0} \to \gamma\gamma)$ at Leading Order and Next-to-Leading Order for five distinguished potentials models. Here, the dependence quark mass on the model is neglected. The calculation is performed with $m_b = 4.18$ GeV for each potential model.*

potential type	$|F_{TT}(0,0)|$ [GeV]	$\Gamma(\chi_{b0} \to \gamma\gamma)_{LO}$ [keV]	$\Gamma(\chi_{b0} \to \gamma\gamma)_{NLO}$ [keV]
harmonic oscillator	0.053	0.048	0.049
logarithmic	0.045	0.034	0.035
power-law	0.042	0.030	0.030
Cornell	0.043	0.031	0.031
Buchmülller-Tye	0.042	0.030	0.030
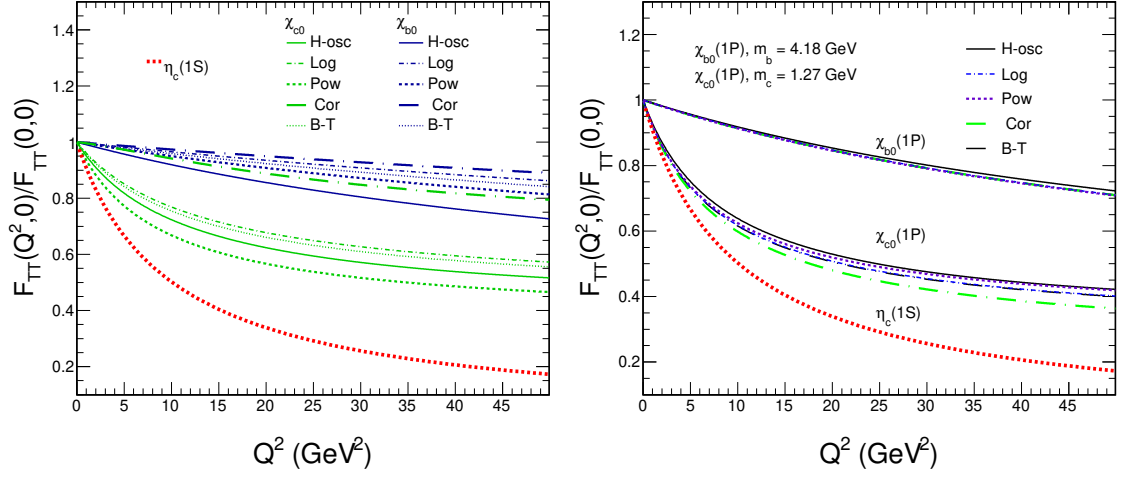
Figure 3.14: *The normalized form factor $F_{TT}(Q^2, 0)/F_{TT}(0, 0)$ as a function of the photon virtuality Q^2. In the left panel starting from the blue top set of lines for χ_{b0}, then below green set of lines for χ_{c0} and marked by red line $\eta_c(1S)$ is shown for comparison.*
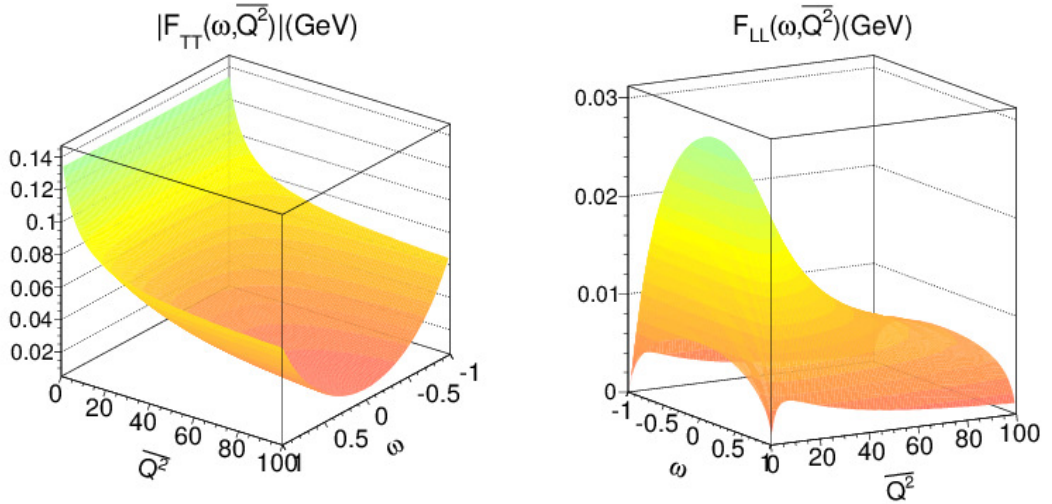
Figure 3.15: *Transverse form factor F_{TT} (left panel) and longitudinal F_{LL} (right panel) as a function of asymmetry parameter ω and $\bar{Q}^2$ average of the photons virtualities for the Buchmüller-Tye potential model.*

3. TRANSITION FORM FACTORS IN THE LIGHT-CONE WAVE FUNCTION APPROACH

3.5.1 Form factor in the nonrelativistic limit

Now let us consider the transition form factor $\gamma^* \gamma^* \to \chi_{Q0}$ in the nonrelativistic (NR) limit, where $k/m_Q \ll 1$ and $k/\sqrt{k^2 + m_Q^2} \ll 1$. Here, k is the momentum related to the internal motion of the quark in the $Q\bar{Q}$ system. For the purpose of the NR limit, one should make a Taylor expansion around $z = 1/2$ and $\vec{k}_\perp = 0$, thus

$$z = \frac{1}{2} + \zeta, \qquad 1 - z = \frac{1}{2} - \zeta. \tag{3.105}$$

Then, in zeroth order the form factors F_1, F_2 disappear. It is easy to show that to the first order in ζ and $\vec{k}_\perp$

$$\frac{1}{\vec{l}_A^2 + \varepsilon^2} - \frac{1}{\vec{l}_B^2 + \varepsilon^2} = \frac{2}{\mu^4} \left(\zeta \vec{q}_{2\perp}^2 + (\vec{k}_\perp \cdot \vec{q}_{2\perp}) \right), \tag{3.106}$$

with

$$\mu^2 = \frac{1}{4} \left(\vec{q}_{1\perp}^2 + \vec{q}_{2\perp}^2 + 4m_c^2 \right). \tag{3.107}$$

In the NR limit, we are allowed to substitute $2m_Q \to M_\chi$, and the two form factors take the following form

$$
\begin{aligned}
F_1(\vec{q}_{1\perp}^2, \vec{q}_{2\perp}^2) &= \frac{|\vec{q}_{1\perp}||\vec{q}_{2\perp}|}{\mu^4} \frac{4}{M_\chi} \int \frac{dz \, d^2\vec{k}_\perp}{z(1-z)16\pi^3} \psi(z, \vec{k}_\perp) \, \zeta^2 M_\chi^2, \\
F_2(\vec{q}_{1\perp}^2, \vec{q}_{2\perp}^2) &= \frac{2}{\mu^4} \frac{1}{M_\chi} \int \frac{dz \, d^2\vec{k}_\perp}{z(1-z)16\pi^3} \psi(z, \vec{k}_\perp) \left(\vec{k}_\perp^2 M_\chi^2 + 4\zeta^2 M_\chi^2 \mu^2 \right).
\end{aligned}
\tag{3.108}
$$

Consequently, replacing $\zeta M_\chi = k_z$, we obtain

$$\frac{dz \, d^2\vec{k}_\perp}{z(1-z)16\pi^3} \psi(z, \vec{k}_\perp) \to \frac{1}{4\pi^2 \sqrt{M_\chi}} \frac{1}{2\sqrt{2}} d^3k \frac{u_{nl}(k)}{k^2}. \tag{3.109}$$

Making use of the relation (an exact derivation is provided in Appendix A, we also omit an irrelevant global phase factor i.).

$$\int_0^\infty dk \, k^2 u_{nl}(k) = 3\sqrt{\frac{\pi}{2}} R'_{nl}(0), \tag{3.110}$$

one can notice that both F_1 and F_2 form factors are proportional to the first derivative of the radial wave function at the origin $R'_{nl}(0)$:

$$F_1(\vec{q}_{1\perp}^{\,2}, \vec{q}_{2\perp}^{\,2}) = \frac{8}{\sqrt{\pi}} \frac{R'_{nl}(0)}{M^{3/2}} \frac{2|\vec{q}_{1\perp}||\vec{q}_{2\perp}|}{[M_\chi^2 + \vec{q}_{1\perp}^{\,2} + \vec{q}_{2\perp}^{\,2}]^2}, \tag{3.111}$$

$$F_2(\vec{q}_{1\perp}^{\,2}, \vec{q}_{2\perp}^{\,2}) = \frac{8}{\sqrt{\pi}} \frac{R'_{nl}(0)}{M^{3/2}} \frac{3M_\chi^2 + \vec{q}_{1\perp}^{\,2} + \vec{q}_{2\perp}^{\,2}}{[M_\chi^2 + \vec{q}_{1\perp}^{\,2} + \vec{q}_{2\perp}^{\,2}]^2}. \tag{3.112}$$

Therefore combining with the proper prefactors as in Eq. (3.100), our amplitude is given by:

$$n^{+\mu}n^{-\nu}\mathcal{M}_{\mu\nu} = 4\pi\alpha_{\text{em}} \frac{8}{\sqrt{\pi}} \frac{R'_{01}(0)}{M^{3/2}} \frac{1}{[M_\chi^2 + \vec{q}_{1\perp}^{\,2} + \vec{q}_{2\perp}^{\,2}]^2}$$
$$\times \left(2\vec{q}_{1\perp}^{\,2}\vec{q}_{2\perp}^{\,2} + (\vec{q}_{1\perp}\vec{q}_{2\perp})(3M_\chi^2 + \vec{q}_{1\perp}^{\,2} + \vec{q}_{2\perp}^{\,2}) \right). \tag{3.113}$$

The same structure of the amplitude can be recognized in the results of Refs. [86, 87]. Notice that in Ref.[86] only the square of the matrix element is given. After accounting for different notation, our result for the squared amplitude completely agrees with [86]. In order to explore a relativistic correction inscribed in our light-cone form factor in Fig. 3.16 and Fig. 3.17 are presented ratios of our form factors and those obtained in non-relativistic limit. Although at small Q_i^2 the difference is only about a few percent, with increasing virtuality the difference is growing up to 20%.

In the nonrelativistic limit, there is a known relation of the radiative decay width and the first derivative of the radial wave function $R'_{01}(0)$ for the P-wave scalar meson [82], as written in Eq. (3.114a). In particular in this limit $M \to 2m_Q$, thus one can get Eq. (3.114b)

$$\Gamma(\chi_{Q0} \to \gamma\gamma) = \frac{9 \cdot 2^4 \alpha_{\text{em}}^2 e_Q^4 N_c}{M^4} |R'_{01}(0)|^2, \tag{3.114a}$$

$$\Gamma(\chi_{Q0} \to \gamma\gamma) = \frac{9\alpha_{\text{em}}^2 e_Q^4 N_c}{m_Q^4} |R'_{01}(0)|^2. \tag{3.114b}$$

Here M is the invariant mass of the $Q\bar{Q}$ system. Below in Tab. 3.12 as well as in Tab. 3.13 we have summarized the values of the first derivative of the radial wave function $R'_{01}(0)$ obtained from the expression in Eq. (3.110). Then in the two last columns in Tabs. 3.12, 3.13 we have adopted Eqs. (3.114) and also the Next-to-Leading correction Eq. (3.104). We have used two ways to choose the value of
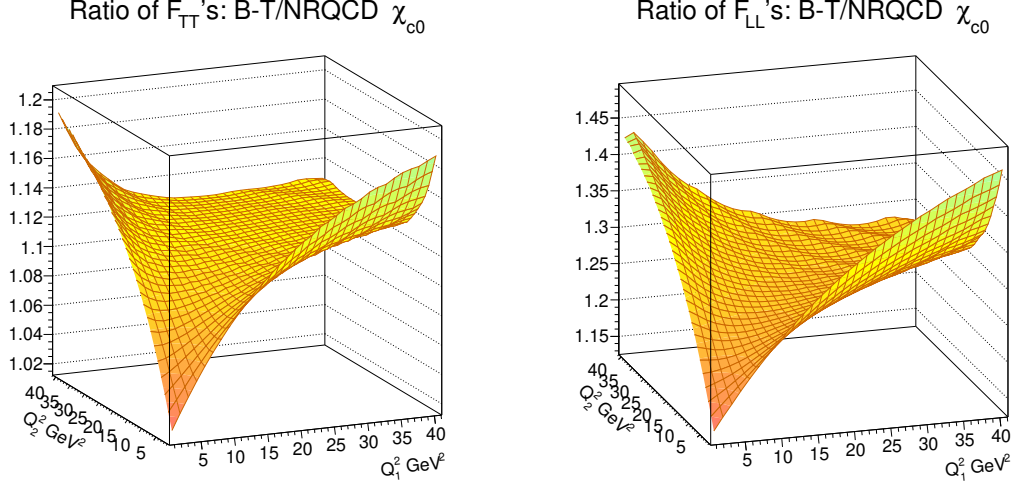
Figure 3.16: Ratio of the transversal form factor $F_{TT}(Q_1^2, Q_2^2)$ (left panel) and longitudinal form factor $F_{LL}(Q_1^2, Q_2^2)$ (right panel) obtained through light-cone procedure to the form factor obtained in the nonrelativistic limit for χ_{c0}.
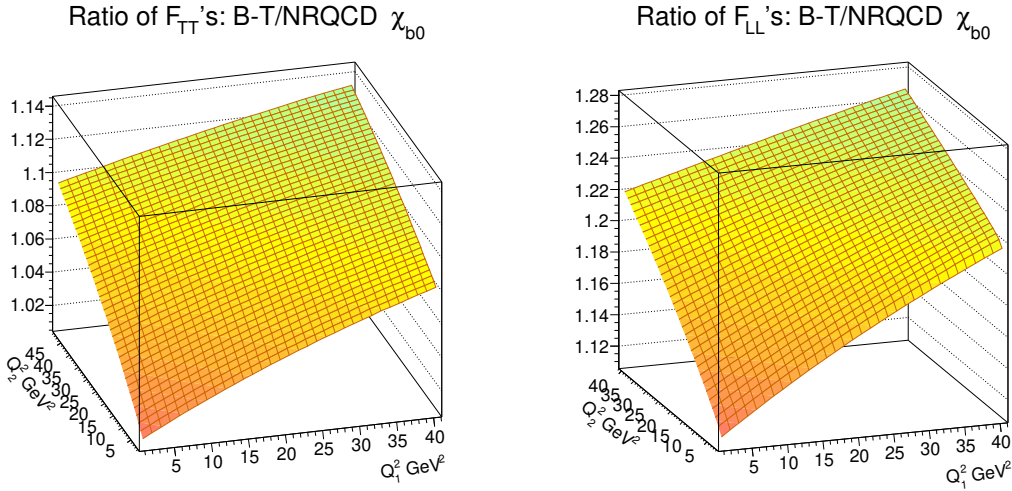
Figure 3.17: Ratio of the transversal form factor $F_{TT}(Q_1^2, Q_2^2)$ (left panel) and longitudinal form factor $F_{LL}(Q_1^2, Q_2^2)$ (right panel) obtained through light-cone procedure to the form factor obtained in the nonrelativistic limit for χ_{b0}.

the mass of the meson, firstly $M_{\chi_{c0}} = (3414.71 \pm 0.30)\,\text{MeV}$ or $M_{\chi_{b0}} = (9859 \pm 0.42 \pm 0.31)\,\text{MeV}$ - Eq. (3.114a) and secondly calculated from the c-quark/b-quark mass corresponding to the potential models Eq. (3.114b). Note that our results for the radiative decay width in Tab. 3.12 for $M = M_{\chi_{c0}}$ are around the value received by Particle Data Group [77]. Moreover, the extracted $R'_{01}(0)$ $(\star)$ from the experimental value of the $\Gamma(\chi_{c0} \to \gamma\gamma)_{NLO}$ by making use of Eqs. (3.114a), (3.104), is in agreement with two of our results (harmonic oscillator and the Buchmüller-Tye) and in the neighborhood of the rest of the potential models results.

Table 3.12: *The radiative decay width at Next-to-Leading Order $\Gamma(\chi_{b0} \to \gamma\gamma)_{NLO}$ and the first derivative of the radial wave function $|R'_{01}(0)|$, which is obtained with the help of the nonrelativistic wave function $u_{L=1,n=0}(k)$. "$\star$" is explained in the text.*

potential type	m_c [GeV]	$|R'_{01}(0)|$ [GeV$^{5/2}$]	$\Gamma(\chi_{c0} \to \gamma\gamma)_{NLO}$ [keV] $M = M_{\chi_{c0}}$	$\Gamma(\chi_{c0} \to \gamma\gamma)_{NLO}$ [keV] $M = 2m_c$
harmonic oscillator	1.4	0.27	2.42	5.54
logarithmic	1.5	0.24	1.85	3.11
powerlike	1.334	0.22	1.62	4.34
Cornell	1.84	0.32	2.51	3.38
Buchmüller-Tye	1.48	0.25	2.15	3.81
experiment [77]	-	$0.25 \pm 0.01^\star$	2.20 ± 0.16	-

Table 3.13: *The radiative decay width at Next-to-Leading Order $\Gamma(\chi_{b0} \to \gamma\gamma)_{NLO}$ and the first derivative of the radial wave function $R'_{01}(0)$, which is obtained with the help of the nonrelativistic wave function $u_{n=0,L=1}(k)$.*

potential type	m_b [GeV]	$R'_{01}(0)$ [GeV$^{5/2}$]	$\Gamma(\chi_{b0} \to \gamma\gamma)_{NLO}$ [keV] $M = M_{\chi_{b0}}$	$\Gamma(\chi_{b0} \to \gamma\gamma)_{NLO}$ [keV] $M = 2m_b$
Harmonic oscillator	4.2	1.07	0.035	0.066
Logarithmic	5.0	1.22	0.045	0.043
Powerlike	4.721	0.98	0.029	0.035
Cornell	5.17	1.37	0.057	0.047
Buchmüller-Tye	4.87	1.13	0.038	0.041

Chapter 4

Prompt Quarkonium Production in hadron collisions

The quarkonium production reactions in hadronic collisions at the Large Hadron Collider (LHC) continue to attract a lot of interest [4, 3]. In general, one distinguishes several classes of production mechanisms. The final state charmonia could appear as decay products of the hadron with bottom quarks content. This contribution is called *non-prompt* production. At the high energies of the LHC, the non-prompt production is a substantial contribution. However, it is experimentally distinguishable from the so-called *prompt* production, where the charm quarks were produced in a hard process. These are the processes of primary interest to us in this thesis. Within the subset of prompt production processes, one further distinguishes between *direct* production and *feed-down* from higher charmonium resonances. It would be a daunting task to do justice to review all theoretical works on quarkonium production in hadronic collisions.

We recall that one of the experiments discovering the J/ψ was a hadronic one, studying proton-Beryllium collisions at the Brookhaven Alternating-Gradient Synchrotron (AGS) [61]. There has thus been a focus on charmonium production mechanisms early on. The role of η_c production as a type of Drell-Yan process for gluons that can serve as a probe to measure the gluon distribution, has been stressed already in the early papers [88, 89]. Indeed, the dominant production mechanism for C-even quarkonia is through the $gg \to M$ gluon fusion $2 \to 1$ process. In the standard collinear-factorization approach, one must go to next-to-leading order (NLO) in α_s approximation to calculate the transverse momentum distribution of a given

quarkonium state and include $2 \to 2$ processes like $gg \to Mg$ [90]. Recent theoretical studies of prompt quarkonium production in collinear factorization are found in [91, 92].

4.1 Matrix elements in k_T-factorization approach

We now turn to the description of the gluon-fusion production mechanism within the k_T-factorization approach. Here the off-shell fusing gluons carry nonzero transverse momenta, which allows us to calculate the transverse momentum distribution of mesons already in the lowest order of perturbation theory. The inclusive cross-section for the $2 \to 1$ gluon-gluon fusion mode is obtained from

$$
d\sigma = \int \frac{dx_1}{x_1} \int \frac{d^2\vec{q}_{1\perp}}{\pi \vec{q}_{1\perp}^{\,2}} \mathcal{F}(x_1, \vec{q}_{1\perp}^{\,2}, \mu_F^2)
$$
$$
\times \int \frac{dx_2}{x_2} \int \frac{d^2\vec{q}_{2\perp}}{\pi \vec{q}_{2\perp}^{\,2}} \mathcal{F}(x_2, \vec{q}_{2\perp}^{\,2}, \mu_F^2) \frac{1}{2x_1 x_2 s} \overline{|\mathcal{M}|^2} \, d\Phi(2 \to 1). \quad (4.1)
$$

The unintegrated gluon distributions in the k_T-factorization approach $\mathcal{F}(x, \vec{k}_\perp^2, \mu_F^2)$ are normalized such that the collinear glue is calculated from

$$
xg(x, \mu_F^2) = \int^{\mu_F^2} \frac{d\vec{k}_\perp^2}{\vec{k}_\perp^2} \mathcal{F}(x, \vec{k}_\perp^2, \mu_F^2) \,. \quad (4.2)
$$

For brevity, from now on, we no longer show the dependence on the factorization scale μ_F^2 explicitly. We denote the four-momentum of the considered final state meson by p and parametrize it on a light-cone basis as

$$
p = [p_+, p_-, \vec{p}_\perp] = \left[\frac{m_T}{\sqrt{2}} e^y, \frac{m_T}{\sqrt{2}} e^{-y}, \vec{p}_\perp \right]. \quad (4.3)
$$

Here we have introduced the transverse mass

$$
m_T = \sqrt{\vec{p}_\perp^{\,2} + M^2}, \quad (4.4)
$$

where M is the mass of the considered meson, and y is its rapidity in the pp center-of-mass-frame (c.m.-frame). The $g^* g^* \to M$ element of the phase-space is

$$
d\Phi(2 \to 1) = (2\pi)^4 \delta^{(4)}(q_1 + q_2 - p) \frac{d^4 p}{(2\pi)^3} \delta(p^2 - M^2) \,. \quad (4.5)
$$

The k_T-factorization framework requires off-shell initial-state gluons, $q_i^2 = -\vec{q}_\perp i^2$, and their four momenta are written as:

$$q_1 = [q_{1+}, 0, \vec{q}_{1\perp}], \; q_2 = [0, q_{2-}, \vec{q}_{2\perp}], \quad (4.6)$$

$\sqrt{s}$ is the pp c.m.s.-energy, thus

$$q_{1+} = x_1\sqrt{\frac{s}{2}}, \; q_{2-} = x_2\sqrt{\frac{s}{2}}. \quad (4.7)$$

As a result the phase-space element is

$$d\Phi(2 \to 1) = \frac{2\pi}{s}\delta(x_1 - \frac{m_T}{\sqrt{s}}e^y)\delta(x_2 - \frac{m_T}{\sqrt{s}}e^{-y})$$
$$\times \, \delta^{(2)}(\vec{q}_{1\perp} + \vec{q}_{2\perp} - \vec{p}_\perp)\, dy\, d^2\vec{p}_\perp. \quad (4.8)$$

Therefore the formula for the inclusive cross section reads

$$\frac{d\sigma}{dyd^2\vec{p}_\perp} = \int \frac{d^2\vec{q}_{1\perp}}{\pi\vec{q}_{1\perp}{}^2}\mathcal{F}(x_1, \vec{q}_{1\perp}{}^2)$$
$$\times \int \frac{d^2\vec{q}_{2\perp}}{\pi\vec{q}_{2\perp}{}^2}\mathcal{F}(x_2, \vec{q}_{2\perp}{}^2)\, \delta^{(2)}(\vec{q}_{1\perp} + \vec{q}_{2\perp} - \vec{p}_\perp)\, \frac{\pi}{(x_1 x_2 s)^2}\overline{|\mathcal{M}|^2}, \quad (4.9)$$

where the momentum fractions of gluons are fixed as $x_{1,2} = m_T \exp(\pm y)/\sqrt{s}$. The off-shell matrix element is written in terms of the Feynman amplitude as:

$$\mathcal{M}^{ab} = \frac{q_{1\perp}^\mu q_{2\perp}^\nu}{|\vec{q}_{1\perp}||\vec{q}_{2\perp}|}\mathcal{M}_{\mu\nu}^{ab} = \frac{q_{1+}q_{2-}}{|\vec{q}_{1\perp}||\vec{q}_{2\perp}|}n^{+\mu}n^{-\nu}\mathcal{M}_{\mu\nu}^{ab} = \frac{x_1 x_2 s}{2|\vec{q}_{1\perp}||\vec{q}_{2\perp}|}n^{+\mu}n^{-\nu}\mathcal{M}_{\mu\nu}^{ab}, \quad (4.10)$$

here the color-indices ab are restored. In the BFKL formalism involving the reggeized gluons [43] one could derive the Feynman rules for off-shell gluons with effective polarization vectors $n_\mu^+ n_\nu^-$. The translation to $q_{1\perp}^\mu, q_{2\perp}^\nu$ is more convenient in comparison to on-shell or collinear approaches. Note that the covariant matrix element satisfies the gauge-invariance restriction, $q_1^\mu \mathcal{M}_{\mu\nu}^{ab} = q_2^\nu \mathcal{M}_{\mu\nu}^{ab} = 0$.

4.2 Unintegrated gluon distributions

In the context of the k_T-factorization approach a major role belongs to the unintegrated gluon distributions (UGDs) $\mathcal{F}(x, \vec{k}_\perp^2, \mu_F^2)$. Their important property is that

integrating over $\vec{k}_\perp$ reproduces the collinear parton distribution functions (PDFs) for gluons

$$xg(x, \mu_F^2) = \int^{\mu_F^2} \frac{d\vec{k}_\perp^2}{\vec{k}_\perp^2} \mathcal{F}(x, \vec{k}_\perp^2, \mu_F^2) \,, \tag{4.11}$$

where μ_F^2 is the factorization scale of the hard process, $\vec{k}_\perp$ is the transverse momentum of the incoming gluon and x is the momentum fraction carried by the gluon. In particular some effects of the gluons' virtualities or transverse momenta may occur in the cross section. As mentioned above, the clue of the $k_\perp$-factorization approach is that the phase space of the produced system is fully general. For example, in the $\gamma^* g^* \to Q\bar{Q}$ process, the final state quarks are not required to be in the back-to-back kinematics, but are aaimuthally decorrelated [93, 94]. In contrast, in the collinear approach one has to include $\gamma^* g \to Q\bar{Q}g$ processes in order to achieve an azimuthal decorrelation. One can thus say that in the $k_\perp$-factorization framework at the respective Leading Order (LO), higher order contributions of the collinear approach are effectively encoded in the unintegrated gluon distribution, see Fig. 4.1. This feature has been further investigated in the litaerature in processes at small x, where it is most important [95, 96]. In the literature there are available several numerical packages devoted to UGDs such as the CASCADE Monte Carlo [97] or packages from the library TMDLib [98] which supply unintegrated gluon distributions that have been fitted to various hard processes. The study of evolution equations is not the matter of the current thesis, we are rather interested in their implications on numerical results. Nevertheless, the brief overview of different concepts of the gluon distribution construction is worth mentioning.

4.2.1 Kimber-Martin-Ryskin, Martin-Ryskin-Watt

The unintegrated parton distributions developed by Kimber-Martin-Ryskin (KMR) were introduced to calculate hard sub-processes such as $Q_1\bar{Q}_2 \to M_V$ where $M_V = \gamma^*, W, Z$ or $g_1 g_2 \to H$ [99, 100, 101]. Further development of the KMR procedure was its application also in inclusive jet production [102]. As mentioned above, the collinear approach assumes that the transverse momenta of the incoming gluons/quarks are negligible. As a result, the transverse momentum of the on-shell produced system (meson) is zero at the Born level. Therefore to generate $p_\perp$ distributions in the collinear factorization, it is necessary to consider additional gluon

radiation. The KMR approach starts with the premise that the transverse momentum of the involved off-shell parton is entirely created in the last step of the evolution ladder. The KMR group takes into account both the leading logarithms from Dokshitzer-Gribov-Lipatov-Altarelli- Parisi (DGLAP) $\ln(Q^2)$ and Balitsky-Fadin-Kuraev-Lipatov (BFKL) $\ln(1/x)$ resummations, which effectively contains a part of the next-to-leading $\ln(1/x)$. The definition of unintegrated gluon densities makes use of the conventional collinear gluon densities $xg(x, k_\perp^2)$ [102]

$$
\begin{aligned}
f_g(x, k_\perp^2, \mu_F^2) &= \frac{\partial}{\partial \log(\mathrm{k}_\perp^2)} \left[xg(x, k_\perp^2) \, T_g(k_\perp^2, \mu_F^2) \right] \\
&= T_g(k_\perp^2, \mu^2) \frac{\alpha_s(k_\perp^2)}{2\pi} \sum_a \int_x^1 \mathrm{d}z \, P_{ga}(z) \, xa(x/z, k_\perp^2), \quad (4.12)
\end{aligned}
$$

where $a = q$ or $a = g$. The minimum scale μ_0, for which DGLAP evolution of the collinear parton distribution is valid, can be placed around 1 GeV. Thus, the conventional applicability range of the above definition is $k_\perp > \mu_0$. Additionally, for the case where $k_\perp < \mu_0$ the gluon density is defined to be constant at a fixed μ scale

$$
\frac{1}{k_\perp^2} f_g(x, k_\perp^2, \mu^2) \Big|_{k_\perp < \mu_0} = \frac{1}{\mu_0^2} \, xg(x, \mu_0^2) \, T_g(\mu_0^2, \mu^2). \quad (4.13)
$$

The Sudakov form factor $T_g(k_\perp^2, \mu_F^2)$ can be interpreted as an evolution probability without gluon/quark emission. In fact, the Sudakov form factor is simply resummation to all orders of virtual contributions to the DGLAP evolution equation

$$
T_g(k_\perp^2, \mu_F^2) = \exp\left[- \int_{k_\perp^2}^{\mu^2} \frac{d\kappa_\perp^2}{\kappa_\perp^2} \frac{\alpha_s(\kappa_\perp^2)}{2\pi} \right.
$$
$$
\left. \times \left[N_F \int_0^1 P_{qg}(z) dz + \int_0^{1-\Delta} z P_{gg}(z) dz \right] \right]. \quad (4.14)
$$

Here the infrared cutoff is defined as $\Delta \equiv k_\perp/(\mu_F + k_\perp)$. An active number of quark/antiquark flavors is donated by N_F. The factorization scale μ_F is specified by the kinematics at the top part of the evolution chain [102]. The splitting kernels $P_{qg}(z)$, $P_{gg}(z)$ with splitting fraction z are regulated through the angular ordering constraints to the last step of evolution. The explicit formula for unintegrated gluon
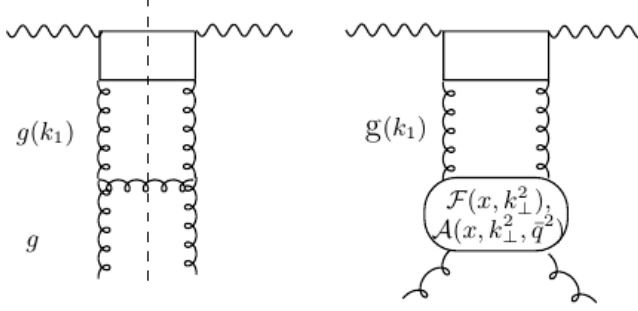
Figure 4.1: The first order correction to the Born level amplitude - left panel. The $k_\perp$ improvement with factorized structure function $\mathcal{F}(x, \vec{k}_\perp^2)$ / $\mathcal{A}(x, \vec{k}_\perp^2, \bar{q}^2)$ - right panel. The plot originates from [95].

distribution reads

$$f_g(x, k_\perp^2, \mu_F^2) = T_g(k_\perp^2, \mu_F^2) \frac{\alpha_s(k_\perp^2)}{2\pi} \int_x^1 \mathrm{d}z \left[\sum_q P_{gq}(z) \frac{x}{z} q\left(\frac{x}{z}, k_\perp^2\right) \right.$$
$$\left. + P_{gg}(z) \frac{x}{z} g\left(\frac{x}{z}, k_\perp^2\right) \Theta\left(\frac{\mu_F}{\mu_F + k_\perp} - z\right) \right], \quad (4.15)$$

with the gluon's Sudakov form factor and corresponding splitting functions. At the Next-to-Leading Order (NLO) accuracy, mentioned splitting kernels are supplied with 'LO+NLO' equations as well as involved PDFs have to be at NLO.

4.2.2 The CCFM unintegrated gluon density

The Ciafaloni-Catani-Fiorani-Marchesini (CCFM) evolution equation is regarded as a unified evolution method due to the resummation of logarithms type $\log(1/z)$ as well as $\log(1/(1-z))$. The emission angle determines the ordering in the gluonic chain at the initial state $\vartheta_n \gg \vartheta_{n-1} \gg \cdots$. The rapidities of gluons in the center of mass frame can be found by $y_i = -1/2 \ln(\vartheta_n)$. A different applications of CCFM evolution can be found in the literature [103, 104]. In our numerical results we have used the unintegrated gluon distribution implemented in the Monte Carlo generator CASCADE [98, 97], see Tab. 4.1. A concise form of the CCFM evolution equation is

$$\bar{q}^2 \frac{\mathrm{d}}{\mathrm{d}\bar{q}^2} \frac{x \mathcal{A}(x, k_\perp, \bar{q})}{\Delta_S(\bar{q}, Q_0)} = \int \mathrm{d}z \int \frac{\mathrm{d}\phi}{2\pi} \frac{\tilde{P}(z, \bar{q}/z, k_\perp)}{\Delta_S(\bar{q}, Q_0)} x' \mathcal{A}(x', k_\perp', \bar{q}/z). \quad (4.16)$$

Here the function $x\,\mathcal{A}(x, k_\perp, \bar{q})$ is related to the unintegrated glue in our convention by

$$x\,\mathcal{A}(x, k_\perp, \bar{q}) = \frac{\mathcal{F}(x, k_\perp^2, \mu^2)}{k_\perp^2} \,. \tag{4.17}$$

The Sudakov form factor is represented by

$$\Delta_S(\bar{q}, Q_0) = \exp\left[-\int_{Q_0^2}^{\bar{q}^2} \frac{\mathrm{d}q^2}{q^2} \int_0^{1-Q_0/q} \mathrm{d}z \frac{C_A \alpha_s(q^2(1-z)^2)}{\pi(1-z)} \right]. \tag{4.18}$$

The UGDs $x\mathcal{A}(x, k_\perp, \bar{q})$ are given as functions of the momentum fraction x, the transverse momentum of the exchanged gluon $k_\perp$ and the scale $\bar{q}$, which corresponds to maximum angle ϑ_n allowed for the emission. The collinear cut-off $k_\perp^{cut} = Q_0$ regulates the region, where $z \sim 1$. Finally, we have the color factor $C_A = 3$. The splitting functions are given by

$$\tilde{P}(z, \bar{q}/z, k_\perp) = \frac{C_A \alpha_s(q_i^2(1-z_i)^2)}{\pi} \left(\frac{1}{1-z_i} - 1 + \frac{z_i(1-z_i)}{2} \right)$$
$$+ \frac{C_A \alpha_s(k_{\perp i}^2)}{\pi} \left(\frac{1}{z_i} - 1 + \frac{z_i(1-z_i)}{2} \right) \Delta_{NS}(z_i, q_i^2, k_{\perp i}^2), \quad (4.19)$$

with the splitting variable $z = x/x'$ and $k_\perp'$, the so-called Non-Sudakov form factor is written in the form

$$\Delta_{NS} = \exp\left[-\frac{C_A \alpha_s(k_{\perp i}^2)}{\pi} \int \frac{\mathrm{d}q^2}{q^2} \Theta(k_{\perp i} - q) \int_0^1 \frac{\mathrm{d}z'}{z'} \Theta(q - z' q_{\perp i}) \right]. \tag{4.20}$$

The UGD sets JH 2013 set1/set2 [98] were determined from the combined HERA

Table 4.1: Distinguished Jung-Hautman CFFM unintegrated gluon distribution in Monte Carlo generator CASCADE.

UGD set	Λ_{QCD}	$k_\perp^{cut}$	Q_0
set A	0.25	1.3	1.3
JH 2013 set1	0.2	2.2	2.2
JH 2013 set2	0.2	2.2	2.2

$F_2(x, Q^2)$ data and using the full splitting function as well 2-loop α_s.

4.2.3 Kutak's small-x model

The unintegrated gluon distributions developed by Kutak [105] are based on the Balitsky-Kovchegov (BK) equation with linear and non-linear terms [106]. The linear approximation is a unified BFKL and Dokshitzer–Gribov–Lipatov–Altarelli–Parisi (DGLAP) evolution equation and includes a term, which allows a contribution of gluons radiated by quarks and antiquarks. The first line with α_s in Eq. (4.21) originates from the BFKL evolution equation. The crucial term in the BFKL kernel responsible for the sub-leading BFKL effects is the so-called consistency constraint $\Theta(k^2/z - l^2)$. The second contribution corresponds to DGLAP effects containing splitting functions $P_{gg}(z)$. The $\Sigma(x, k^2)$ indicates the singlet quark momentum distribution. Finally, the last term reflects a non-linear screening contribution with the expected gluon density concentrated in the impact parameter plane within a radius R. This contribution is based on the Balitsky–Kovchegov equation[107, 108].

$$
\begin{aligned}
f(x, k^2) &= f^0(x, k^2) \\
&+ \frac{\alpha_s(k^2) N_c}{\pi} \int_x^1 \frac{dz}{z} \int_{k_0^2}^\infty \frac{dl^2}{l^2} \left[\frac{l^2 f(\frac{x}{z}, l^2) \Theta(\frac{k^2}{z} - l^2) - k^2 f(\frac{x}{z}, k^2)}{|l^2 - k^2|} + \frac{k^2 f(\frac{x}{z}, k^2)}{|4l^4 + k^4|^{\frac{1}{2}}} \right] \\
&+ \frac{\alpha_s(k^2)}{2\pi k^2} \int_x^1 dz \left[\left(P_{gg}(z) - \frac{2N_c}{z} \right) \int_{k_0^2}^{k^2} dl^2 f\left(\frac{x}{z}, l^2 \right) + z P_{gq}(z) \Sigma\left(\frac{x}{z}, k^2 \right) \right] \\
&+ \frac{2\alpha_s^2(k^2)}{R^2} \left[\left(\int_{k^2}^\infty \frac{dl^2}{l^2} f(x, l^2) \right)^2 + f(x, k^2) \int_{k^2}^\infty \frac{dl^2}{l^2} \ln\left(\frac{l^2}{k^2} \right) f(x, l^2) \right] . \quad (4.21)
\end{aligned}
$$

As an input it was used

$$
f^0(x, k^2) = \frac{\alpha_s(k^2)}{k^2} \int_x^1 P_{gg}(z) \frac{x}{z} g\left(\frac{x}{z}, k_0^2 \right) , \quad (4.22)
$$

$$
x g(x, k_0^2 = 1) = 0.994(1 + 82.1x)^{18.6} . \quad (4.23)
$$

which is the parametrization needed to describe structure function $F_2(x, Q_0^2)$, see Fig. 4.2. The proposed method combines the effects of saturation and coherence with a dependence on the hard scale μ of the process. It is also possible to switch off the non-linear gluon fusion term, to obtain a gluon distribution which does not account for stauration effects.

The clue of the construction introducing the hard scale dependence is that the application of the Sudakov form factor does not change the integrated distribution
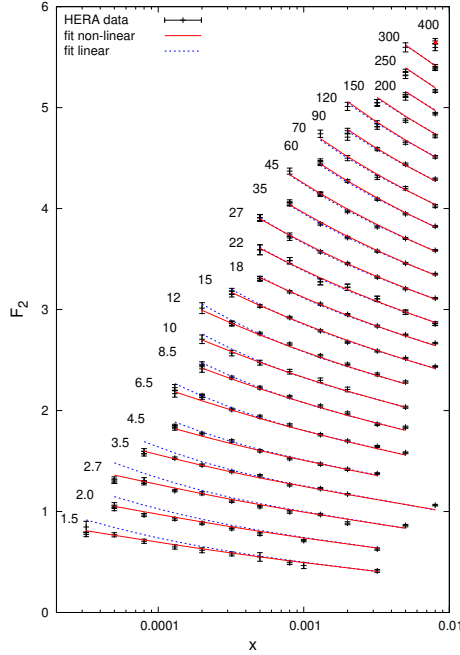
Figure 4.2: The proton structure function $F_2(x, Q^2)$ from Kutak-Sapeta fits to HERA data as a function of x in the range of $1.5\,\text{GeV}^2$ to $400\,\text{GeV}^2$ [109].

Eq. (4.21). Effectively, both integrated gluon densities derived from $\mathcal{F}(x, k^2)$ as well as $\mathcal{F}(x, k^2, \mu^2)$ are the same.

$$f(x, k^2, \mu^2) = \Theta(\mu^2 - k^2)T_g(\mu^2, k^2)\frac{xg(x, \mu^2)}{xg(x, \mu^2)}f(x, k^2) + \Theta(k^2 - \mu^2)f(x, k^2)\,, \quad (4.24)$$

$$xg(x, \mu^2) = \int^{\mu^2} \mathrm{d}k^2 f(x, k^2)\,, \quad (4.25)$$

$$xg_{hs}(x, \mu^2) = \int^{\mu^2} \mathrm{d}k^2 T_g(\mu^2, k^2)f(x, k^2)\,. \quad (4.26)$$

The Sudakov form factor is defined in analogy to the KMR approach

$$T_g(\mu^2, k^2) = \exp\left[-\int_{k^2}^{\mu^2} \frac{\mathrm{d}k'^2}{k'^2}\frac{\alpha_s(k'^2)}{2\pi}\sum_{a'}\int_0^{1-\Delta} \mathrm{d}z' P_{a'a}(z')\right]\,, \quad (4.27)$$

with the splitting function $P_{a'a}(z)$ for specific transition being $zP_{gg}(z)$ or $N_F P_{qg}(z)$ and $\Delta = \mu/(\mu + k)$. The influence of the Sudakov form factor on the gluon distribution appears only in the shape of the UGD.

In our convention the unintegrated gluon distribution reads

$$f(x, k^2, \mu^2) = \frac{\mathcal{F}(x, k^2, \mu^2)}{k^2}\,. \quad (4.28)$$

In further calculations always $\mathcal{F}(x, k^2, \mu^2)$ is used.

4.3 Prompt hadroproduction of $\eta_c(1S)$ and $\eta_c(2S)$ in proton-proton collisions

Recently, new measurements of the prompt η_c production in pp collisions were released by the LHCb Collaboration at $\sqrt{s} = 7\,\text{TeV}$, $\sqrt{s} = 8\,\text{TeV}$ and $\sqrt{s} = 13\,\text{TeV}$ center-of-mass energies, see [110, 111]. These data led to an increased interest in the properties of η_c production in different approaches [112, 90, 113, 114]. The experimental method allows to measure the η_c transverse momentum distribution in the range $p_\perp > 6.5\,\text{GeV}$ and within the rapidity acceptance $2.0 < y_{c.m.s.} < 4.5$. In our analysis, the production of $\eta_c(1S)$ and $\eta_c(2S)$ [7] are discussed also at lower transverse momenta. This low transverse momentum domain is a region where the effects of non-linear evolution of Unintegrated-Gluon-Distribution (UGD) could be manifested. Our adopted Color-Singlet model within the light-cone wave function approach of the $Q\bar{Q}$ state could address some questions, which previously had not been considered.

We recall that at the lowest order, the matrix element for the $\gamma^*\gamma^* \to \eta_c$ is proportional to transition form factor $F_{\gamma\gamma}(Q_1^2, Q_2^2)$. The same situation appears for $g^*g^* \to \eta_c$. Moreover, one can notice that the two form factors are related by

$$F_{g^*g^* \to \eta_c}(Q_1^2, Q_2^2) = \frac{1}{e_c^4 \sqrt{N_c}} F_{\gamma\gamma \to \eta_c}(Q_1^2, Q_2^2), \tag{4.29}$$

where $Q_i^2 = \vec{q}_{\perp i}{}^2$ and $F_{\gamma\gamma \to \eta_c}(Q_1^2, Q_2^2)$ is defined in Chapter 3, see Eq. (3.66). The covariant form of the matrix element with proper coupling and color factors is written as:

$$\mathcal{M}_{\mu\nu}^{ab} = (-i)4\pi\alpha_s\,\varepsilon_{\mu\nu\alpha\beta}q_1^\alpha q_2^\beta \frac{\text{Tr}[\text{t}^\text{a}\text{t}^\text{b}]}{\sqrt{\text{N}_\text{c}}}\, F_{g^*g^* \to \eta_c}(\vec{q}_{1\perp}{}^2, \vec{q}_{2\perp}{}^2)\,. \tag{4.30}$$

Contracting with $n^{+\mu}n^{-\nu}$ and averaging over colors the formula introduced in Eq. (4.9) for the differential cross-section reads

$$\frac{d\sigma}{dy d^2\vec{p}_\perp} = \int \frac{d^2\vec{q}_{1\perp}}{\pi\vec{q}_{1\perp}{}^4}\mathcal{F}(x_1, \vec{q}_{1\perp}{}^2) \int \frac{d^2\vec{q}_{2\perp}}{\pi\vec{q}_{2\perp}{}^4}\mathcal{F}(x_2, \vec{q}_{2\perp}{}^2)\delta^{(2)}(\vec{q}_{1\perp} + \vec{q}_{2\perp} - \vec{p}_\perp)$$
$$\times \frac{\pi^3\alpha_s^2}{N_c(N_c^2 - 1)}|[\vec{q}_{1\perp}, \vec{q}_{2\perp}]\,F_{g^*g^* \to \eta_c}(\vec{q}_{1\perp}{}^2, \vec{q}_{2\perp}{}^2)|^2. \tag{4.31}$$

The vector product can be written as

$$[\vec{q}_{1\perp}, \vec{q}_{2\perp}] = q_1^x q_2^y - q_1^y q_2^x = |\vec{q}_{1\perp}|\,|\vec{q}_{2\perp}|\sin(\phi_1 - \phi_2)\,, \tag{4.32}$$

where the parametrization of the transverse momenta $\vec{q}_{1\perp}$ and $\vec{q}_{2\perp}$ is $\vec{q}_{i\perp} = (q_i^x, q_i^y) = |\vec{q}_{i\perp}|(\cos\phi_i, \sin\phi_i)$. In further numerical calculations, the renormalization scale and strong coupling are taken in the form

$$\alpha_s^2 \Rightarrow \alpha_s(\max\{m_T, \vec{q}_{1\perp}\})\,\alpha_s(\max\{m_T, \vec{q}_{2\perp}\})\,. \tag{4.33}$$

Effectively, the renormalization scale depends on three variables, the transverse mass m_T and the transverse momenta of the fusing partons $\vec{q}_{1\perp}, \vec{q}_{2\perp}$.

4.3.1 Normalization of the form factors and their implications

In Chapter 3, we have explained that the crucial parameter for the inclusive cross-section in the Color-Singlet approach within the NRQCD framework is the radial wave function at the origin. To be precise, there enters the radial wave function $|R_{n0}(0)|$ for pseudoscalar states and the first derivative of the radial wave function at the origin $|R'_{n1}(0)|$ for the P-wave scalar mesons. Within the light-cone form factor approach besides its behavior at the origin, also the shape of the WF has an influence. The key point is now to control the model uncertainty, thus finding the proper normalization of the form factor. The natural choice is to normalize the form factor at the on-shell point, where it is directly related to the decay width. At this point, we meet an ambiguity of the decay width selection. Up to now, the only observed radiative decay is pure photon-photon decay. It would also seem to be acceptable to adopt gluonic width $\Gamma(\eta_c \to gg)$ relating it to the total meson width Γ_{η_c}. Indeed, at the leading order in perturbation theory, the relation between $\Gamma(\eta_c \to gg)$ and $\Gamma(\eta_c \to \gamma\gamma)$ can be found through their vertices being proportional:

$$\Gamma_{\mathrm{LO}}(\eta_c \to gg) = \frac{N_c^2 - 1}{4N_c^2}\frac{1}{e_c^4}\left(\frac{\alpha_s}{\alpha_{\mathrm{em}}}\right)^2 \Gamma_{\mathrm{LO}}(\eta_c \to \gamma\gamma)\,, \tag{4.34}$$

and $\Gamma_{\mathrm{LO}}(\eta_c \to \gamma\gamma)$ was introduced in Eq. (3.71). At next-to-leading order, the respective formulas for the widths read (see e.g. [115, 116])

$$\begin{aligned}
\Gamma_{NLO}(\eta_c \to \gamma\gamma) &= \Gamma_{\mathrm{LO}}(\eta_c \to \gamma\gamma)\left(1 - \frac{20 - \pi^2}{3}\frac{\alpha_s}{\pi}\right), \\
\Gamma_{NLO}(\eta_c \to gg) &= \Gamma_{\mathrm{LO}}(\eta_c \to gg)\left(1 + 4.8\frac{\alpha_s}{\pi}\right),
\end{aligned} \tag{4.35}$$

here the parameter $\alpha_s(m_c) = 0.26$ is used [82]. These two ways of $|F(0,0)|$ interpretation give slightly different results. In Tabs. 4.2, 4.3 the values of $|F(0,0)|$

obtained through the hadronic decay rate and the radiative decay rate respectively, are summarized. In addition in Tab. 4.3 we show the values obtained in the leading order (LO) approximation. The result for $\eta_c(1S)$ at LO can be also found in Tab. 3.1. Although, the $\eta_c(2S)$ situation is not clear due to large error bars, the situation in the case of $\eta_c(1S)$ it is not entirely satisfactory. This is indeed a well-known issue and could hint at an insufficiency of the potential model approach to the pseudoscalar charmonia. A wide range of possible solutions have been considered, including a mixing with light hadron states [117], an admixture with a pseudoscalar glueball [118], or nonperturbative instanton induced potential effects in the hadronic decay [119].

Table 4.2: Hadronic decay widths Γ_{η_c} as well as $|F(0,0)|$ obtained from Γ_{η_c} at the next-to-leading order approximation (see Eq. (4.35)).

	Γ_{η_c} (MeV) [77]	From $\Gamma_{NLO}(\eta_c \to gg)$, Eq.(4.35) $|F(0,0)|_{gg}[\text{GeV}^{-1}]$
$\eta_c(1S)$	31.9±0.7	0.119±0.001
$\eta_c(2S)$	11.3±3.2±2.9	0.053±0.010

Table 4.3: The radiative decay widths $\Gamma(\eta_c \to \gamma\gamma)$ as well as $|F(0,0)|$ obtained from $\Gamma_{\eta_c \to \gamma\gamma}$ using leading order (LO) and next-to-leading order (NLO) approximation (see Eq. (3.71, 4.35)).

	experiment $\Gamma(\eta_c \to \gamma\gamma)(\text{keV})$ [77]	from LO Eq.(3.71) $|F(0,0)|[\text{GeV}^{-1}]$	from NLO Eq.(4.35) $|F(0,0)|_{\gamma\gamma}[\text{GeV}^{-1}]$
$\eta_c(1S)$	5.0 ±0.4	0.067±0.003	0.079±0.003
$\eta_c(2S)$	1.9 ±1.3 $\cdot 10^{-4} \cdot \Gamma_{\eta_c(2S)}$	0.033±0.012	0.038±0.014

4.3.2 The small-x behavior of Unintegrated Gluon Distributions

The $k_\perp$-factorization approach is especially appropriate when small fractions x of the proton momentum carried by gluons are considered. Our analysis below is focused on the kinematic range of the LHCb experiment $2.0 < y_{\eta_c} < 4.5$, which determines $x_1 \sim 10^{-2}$ while the second gluon carries typically $x_2 \sim 10^{-5}$. The typical hard scale
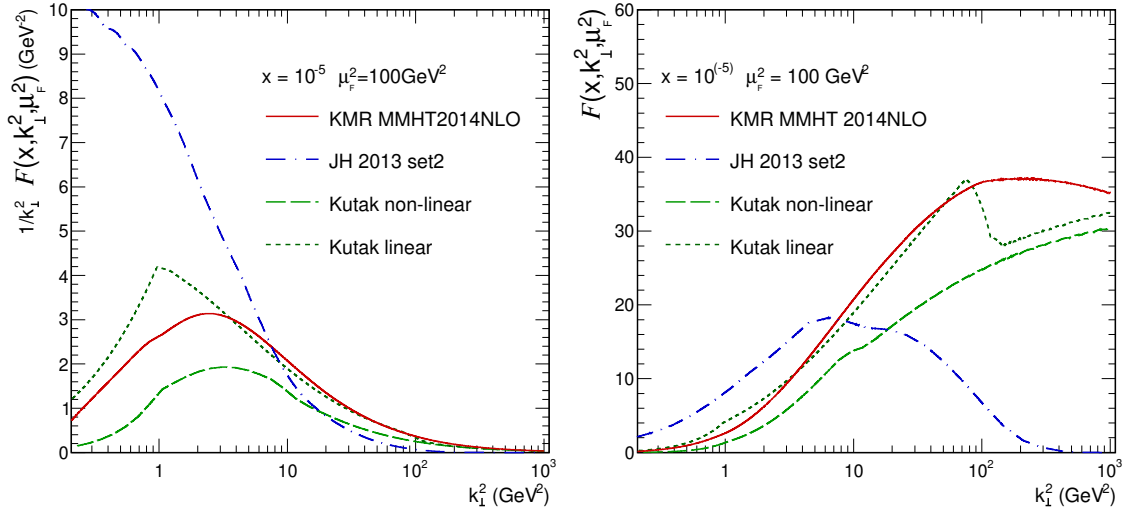
Figure 4.3: Unintegrated Gluon Distributions at the typical scale for $pp \rightarrow \eta_c(1S)$

μ_F of the process $pp \rightarrow \eta_c$ in LHCb kinematics can reach $100\,\mathrm{GeV}^2$. In order to make our results more universal several unintegrated gluon distributions have been examined. The Kutak UGD parameterization is restricted to the region, where $x < 10^{-2}$.

In Fig. 4.3, we depict different UGDs shapes as a function of $\vec{k}_\perp^2$ at a suitably small value of $x = 10^{-5}$. The behavior at small gluon transverse momentum $k_\perp^2$ of each used UGDs is exposed in the left panel. The plot of the dimensionless function $\mathcal{F}(x, k_\perp^2, \mu_F^2)$ (right panel) renders the large $k_\perp$ tails of the UGDs more visible. At the first glance in Fig. 4.3, the KMR glue (blue dashed curve) and Kutak's one (green dotted curve) have similar behavior. Nevertheless, the construction method is different, but both of them are based on integrated gluons distributions, which well describe certain dijet production cross-sections at the LHC. Due to the fact that the Kutak non-linear and linear UGDs have been defined in a specific range of x only, in the practical calculation, the mixture of Kutak's and KMR UGD is used. The KMR glue in our case is built from the collinear gluon from the MMHT20014nlo fit [120], through the next-to leading order Watt procedure.

Another unintegrated gluon was developed by Jung and Hautmann, which is characterized by enhancement at low $k_\perp^2$, while with increasing value of gluon transverse momenta, the distribution becomes flattened.

In the following Fig. 4.4, we present the projections on transverse momenta

of the fusing gluons in the process $pp \to \eta_c(1S)$. In the high energy approximation adopted by us, the gluons' virtualities coincide with their transverse momenta squared. Moreover, the requirement on the transverse momenta of produced mesons provides relatively large values of $q_{1\perp}$ and $q_{2\perp}$ relevant to the perturbative regime.

The two-dimensional plots in Fig. 4.5 clearly depict the kinematical region of interest. Indeed, an interesting kinematic configuration appears, where one of the
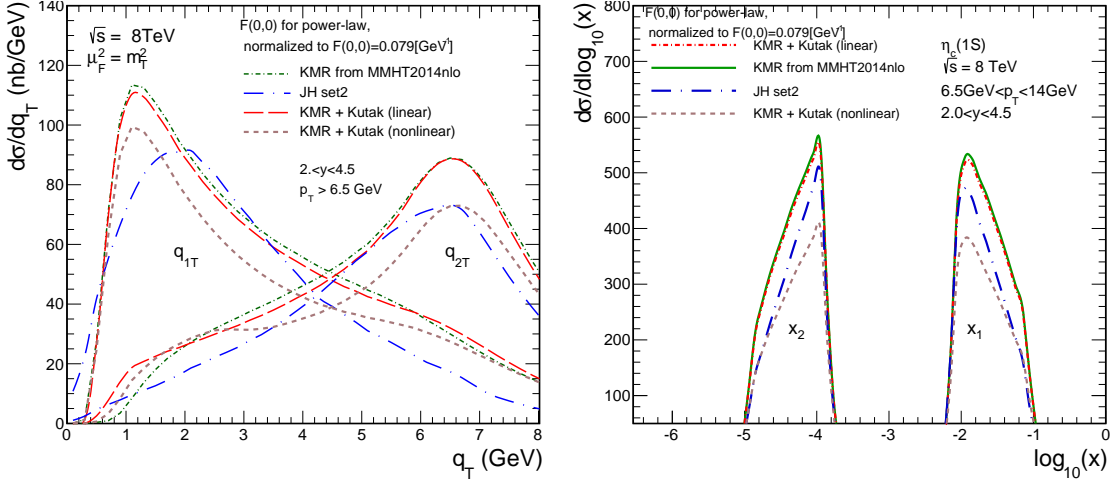
Figure 4.4: The projections on $q_{1T} \equiv q_{1\perp}$ or $q_{2T} \equiv q_{2\perp}$ gluon transverse momenta (left panel). Projections on $\log_{10}(x_1)$ and $\log_{10}(x_2)$ (right panel). The LHCb kinematics is considered at $\sqrt{s} = 8$ TeV within discussed unintegrated gluon distributions.

fusing gluons always carries a large value x_1 and has small $q_{1\perp}$, while at the same time the second gluon carries always small x_2 and has larger transverse momentum $q_{2\perp}$.

Therefore, the gluon characterized by the low value of x transfers the major part of η_c transverse momentum, $p_{\perp\eta_c}$.

4.3.3 Predicted differential distributions

We now present the results of a thorough numerical analysis of promptly produced $\eta_c(1S, 2S)$ performed in the $k_\perp$-factorization framework.

We focus on the hard process of off-shell gluon-gluon fusion into a color-singlet $c\bar{c}$ pair which then turns into a η_c meson. The feed down production via the radiative decay $h_c \to \eta_c\gamma$, as well other possible higher resonances, are not considered.
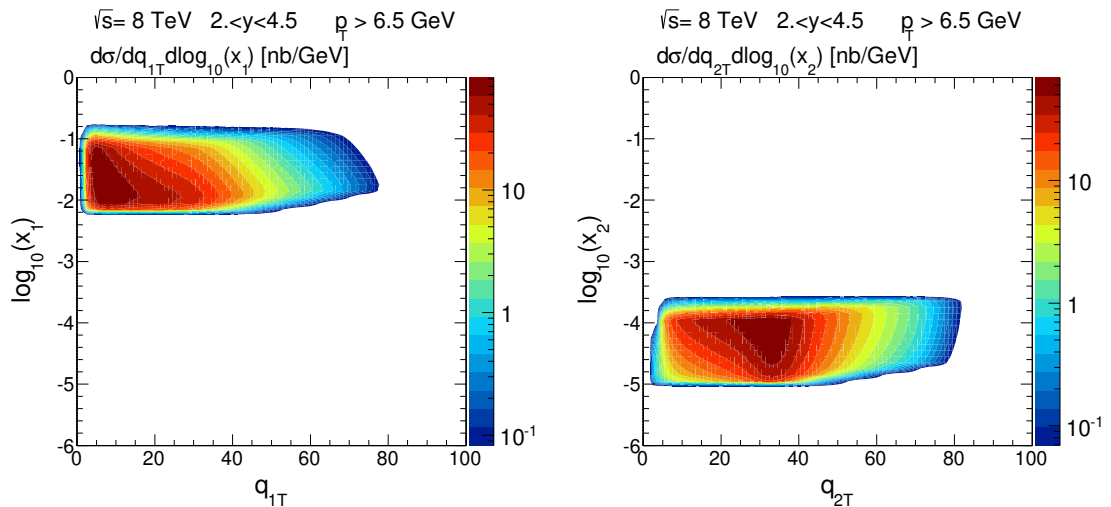
Figure 4.5: Two dimensional projections on $q_{1T} \times \log_{10}(x_1)$ and $q_{2T} \times \log_{10}(x_2)$. As an example the KMR from MMHT2014nlo was used.

The $k_\perp$-factorization approach is based on an off-shell matrix element, which depends directly on the gluon virtualities. These off-shell matrix-elements, or vertices, are constructed from light-cone wave functions for several parametrizations of $c\bar{c}$ interaction potentials. The decay width at NLO (see Tab. 4.3) establishes the normalization of the form factor $F(0,0)$. We make use of the fact that in the lowest order of perturbation theory, the space-like transition form factor for $g^*g^* \to \eta_c$ is equivalent to the $\gamma^*\gamma^* \to \eta_c$ form factor up to color factors.

In the further results presented below, the light-cone wave function for the so-called power-law potential model was applied. This is motivated by the fact that the parametrization of the power-law potential of the $c\bar{c}$ interaction gives the best description of the half off-shell form factor, see Fig. 3.7.

To begin with, Fig. 4.6 summarizes the total cross-section of prompt $\eta_c(1S)$ production as a function of pp c.m.s.-energy collected by the LHCb experimental group indicated by the black dots from 2015 and the black square from 2020. Rhombuses and crosses denote our integrated cross-sections with normalized form factor at the on-shell point and with released normalization, filled and blanked, respectively. The data suggest a faster than linear dependence on c.m.s.-energy, while our calculated cross-sections rather keep a linear tendency.

In Fig. 4.6, we show only results using the KMR UGD. However, other UGDs
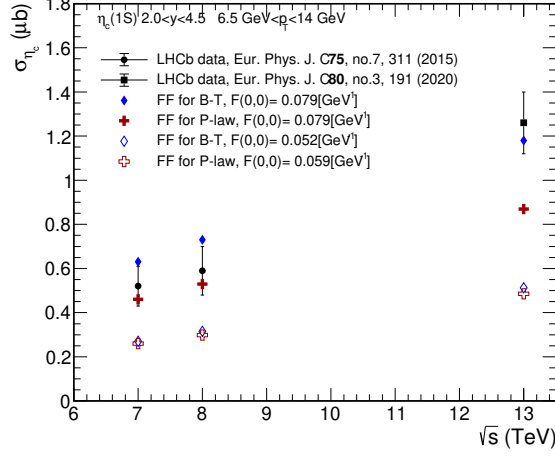
Figure 4.6: The total cross section of the promptly produced $\eta_c(1S)$ within the LHCb kinematic regime.

have been examined by us, and the conclusion is the same.

In Fig. 4.7, our calculations of differential distributions in transverse momentum of the $\eta_c(1S)$ are compared with experimental data points. In the top panels, our predictions are shown with the data published by the LHCb experimental group in 2015 [110] at $\sqrt{s} = 7\,\text{TeV}$(left panel) and $\sqrt{s} = 8\,\text{TeV}$(right panel) for the prompt production of $\eta_c(1S)$ in proton-proton collisions. At the same time, the lower panel displays our predictions with the recent LHCb data [111] at $\sqrt{s} = 13\,\text{TeV}$. Four different sets of unintegrated gluon distributions are adopted, which makes our results quite comprehensive.

At $\sqrt{s} = 7\,\text{TeV}$ and $\sqrt{s} = 8\,\text{TeV}$, all UGDs attain a reasonable description of the data. However, in particular at large η_c transverse momenta our calculations seem to undershoot the data. Substantially below the data are results obtained at $\sqrt{s} = 13\,\text{TeV}$. This feature is independent of the choice of UGD and also observed in Fig. 4.6.

In the range $6.5\,\text{GeV} < p_\perp < 14\,\text{GeV}$, one can observe that KMR+Kutak-linear and KMR overlap as well as do KMR+Kutak-non-linear and JH2013 set2. The significant disparity between different UGDs is noticeable at low $p_T \equiv p_\perp$. One suspicion could be that this effect corresponds to gluon saturation and non-linear evolution. Although, the most valuable range to investigate saturation effect ($p_T < 6\,\text{GeV}$) seems unattainable using the $\eta_c \to p\bar{p}$ decay to measure the η_c meson.

An attractive channel to study this problem could be the $\gamma\gamma$ final state. Therefore, further simulations of the signal and background are desirable.

Since the experimental results are provided in rather broad $p_\perp$ bins, one may prefer a histogram representation of the results. Fig. 4.8 reveals the results for the KMR and Jung-Hautmann distributions in equivalent bins. The agreement between theoretical and experimental results in a few intervals seems to be sufficient. However, the wide histogram bins could generate greater uncertainty. For instance,
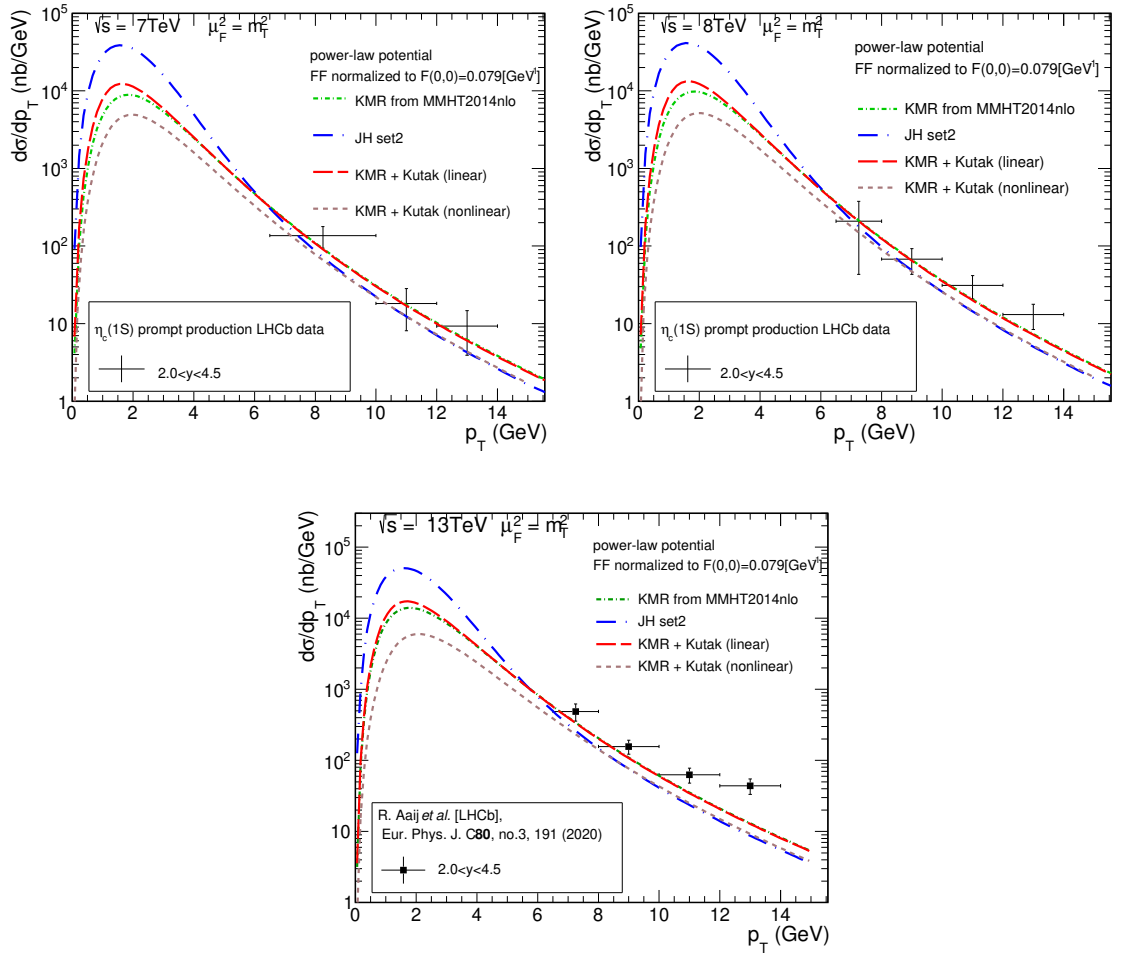
Figure 4.7: Differential cross-section in transverse momentum of $\eta_c(1S)$ at $\sqrt{s} = 7$ TeV (left-top panel), $\sqrt{s} = 8\,\text{TeV}$ (right-top panel) and $\sqrt{s} = 13\,\text{TeV}$ (low panel) within $2.0 < y_{\eta_c} < 4.5$ compared to LHCb data. The power-law potential model normalized to decay width is used with each UGD.
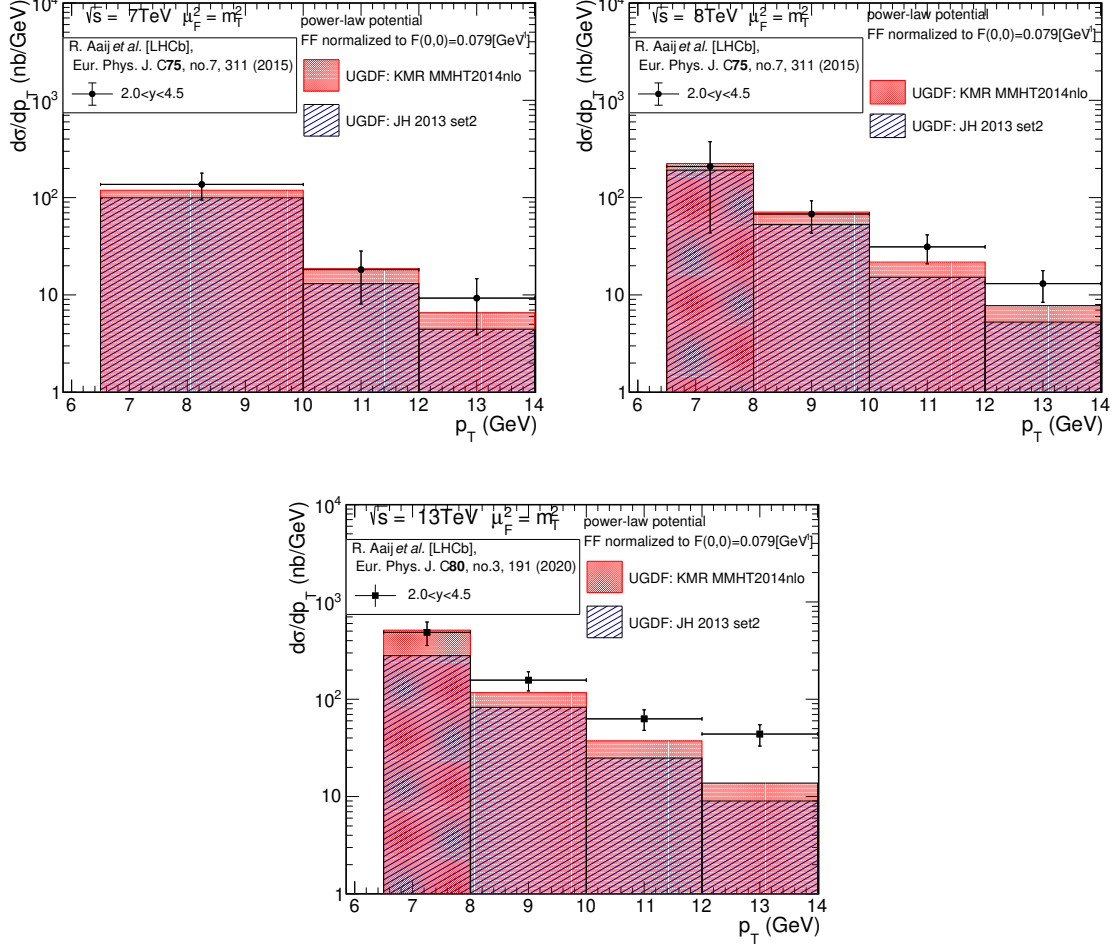
Figure 4.8: Differential cross-section found in bins. For illustration results for two UGD sets are compared to LHCb data at $\sqrt{s} = 7$ TeV (left panel), $\sqrt{s} = 8$ TeV (right panel) and $\sqrt{s} = 13$ TeV (low panel). The calculation was performed within LCWF for the power-law potential model of $c\bar{c}$ interaction. Form factor normalization at the on-shell point is fixed to $F(0,0) = 0.079 \,\mathrm{GeV}^{-1}$.

one can compare top panels in Fig. 4.8.

Another Fig. 4.9 displays predicted distributions in transverse momentum of $\eta_c(2S)$ at three energies in the center of mass system $\sqrt{s} = 7$ TeV, $\sqrt{s} = 8$ TeV and $\sqrt{s} = 13$ TeV. Presented results were performed with restrictions on $\eta_c(2S)$ rapidity $2.0 < y_{\eta_c(2S)} < 4.5$ and as a factorization scale in unintegrated gluon distribution transverse mass $m_\perp = \sqrt{M_{\eta_c}^2 + p_{\perp \, \eta_c}^2}$ was taken.

Similarly as in $\eta_c(1S)$ production process the on-shell point of the form factor, for the power-law potential model, is normalized to radiative decay width (see Tab. 4.3). The difference between examined UGDs appears up to $p_{T\,\eta_c} \sim 8\,\mathrm{GeV}$. With increasing transverse momentum, as in the case of $\eta_c(1S)$, the dispersion among Kutak's and KMR or JH gluon distributions become small.

Now turn to the point of the light-cone wave function and the corresponding potential model of $c\bar{c}$ interaction applied in the computation. In order to understand
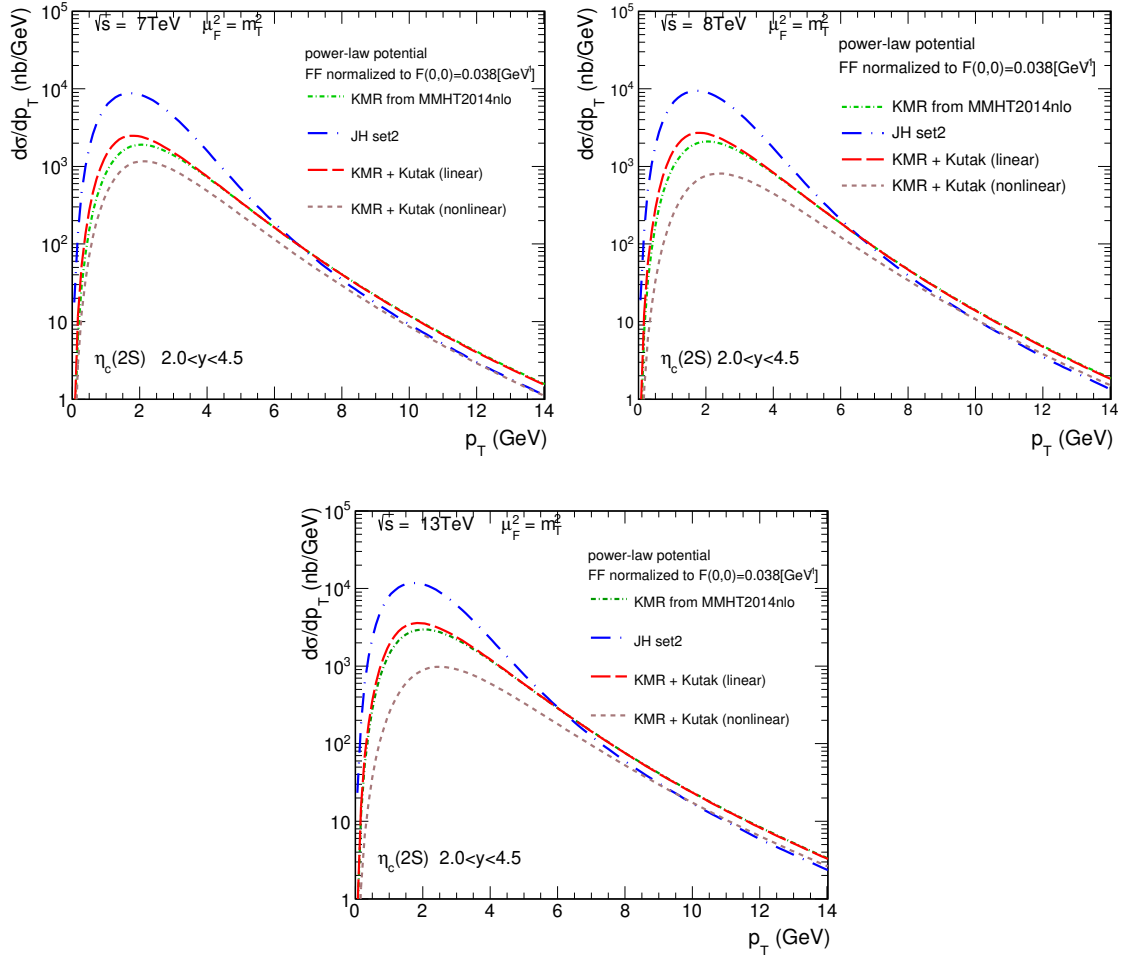
Figure 4.9: Differential cross-section in transverse momentum of $\eta_c(2S)$ at $\sqrt{s} = 7\,\mathrm{TeV}$ (left-top panel), $\sqrt{s} = 8\,\mathrm{TeV}$ (right-top panel) and $\sqrt{s} = 13\,\mathrm{TeV}$ (low panel) within $2.0 < y_{\eta_c} < 4.5$. The power-law potential model normalized to decay width is used with each UGD.

the influence of the particular model on the distribution shape, see Fig. 4.10. There we have fixed the normalization for all models of considered form factors to the radiative decay width.

The right panel of Fig. 4.10 gives a glimpse of the difference between the potential models used in the final results, the power-law potential model, Buchmüller-Tye (B-T) model, and others. The first observation is that the effects of the normalized harmonic oscillator (HO) form factor and the power-law form factor are indistinguishable. The same feature applies to the results for the B-T and the logarithmic model.

In the case of $\eta_c(2S)$ production (the left panel of Fig. 4.10), the spread of the results is a bit changed. Fig. 4.11 brings to light the pure effect of the form factor without any extra normalization.
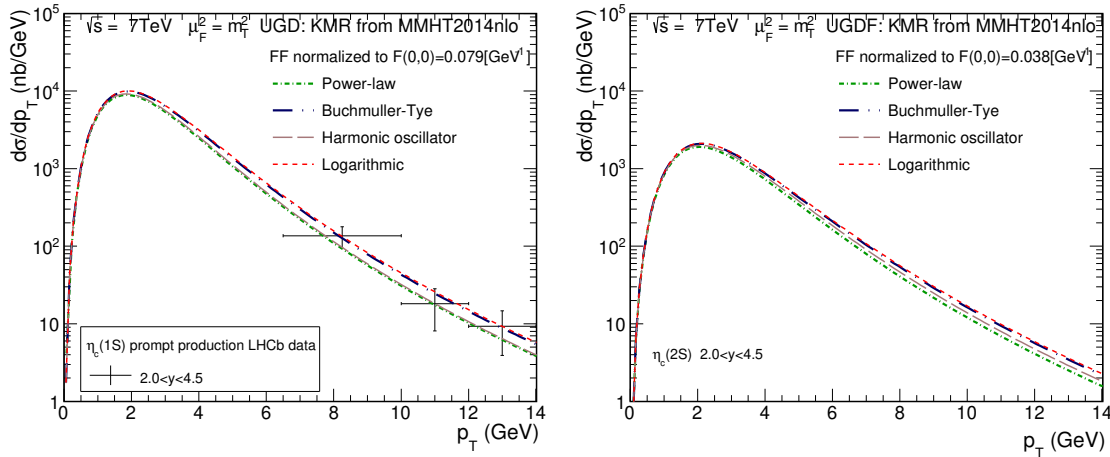
Figure 4.10: Differential distributions in transverse momentum of $\eta_c(1S)$ (left panel) and $\eta_c(2S)$ (right panel) at $\sqrt{s} = 7\,\mathrm{GeV}$. The light-cone wave functions for different potential models were applied in the form factor and the form factor was normalized to the radiative decay width.

A slight difference is drawn between the obtained distributions, can be regarded as the uncertainty of the potential model choice. Notice that the results obtained with not normalized form factor follows the undershoot of the experimental data. On the other hand, from the Tab. 3.1 and Tab. 3.2 it is known that the decay widths from phenomenological potential models of $c\bar{c}$ interaction are below of the experimental value. Moreover, the experimental decay rate is known with some precision and

various values have been obtained [121, 77]. From this analysis the conclusion arises that the off-shell form factor could be more adequate at large q_T of the fusing gluon. We get slightly different results than Baranov et. al in the k_T-factorisation approach within NRQCD formalism including Color-Octet contribution [122].

As a supplement Fig. 4.12 shows the results obtained with the Non-Relativistic form factor. Selected examples of the radial wave functions at the origin $R_{10}(0) = 0.762\,\mathrm{GeV}^{3/2}$ and $R_{10}(0) = 0.699\,\mathrm{GeV}^{3/2}$ correspond, to the power-law potential model (see Tab. 3.4) and radiative decay width at next-to-leading order. The change of the radial wave function at the origin results in a few percent increments of the cross-section independently on the gluon distribution used. The blue curves, which go along with $R_{10}(0)$ extracted from the experiment, are below the red lines. One can also notice in Fig. 4.13 that our findings for the off-shell form factor normalized to $F(0,0)$ value extracted from the experiment gives a better description than the NRQCD form factor with proper radial wave function at origin. An interesting aspect of the distributions appears when the gluon virtualities are neglected in the hard matrix element. Fig. 4.14 reveals the so-called point-like coupling, where only the form factor at the on-shell point is taken into account (red dashed-dotted line). This kind of form factor leads to strongly flattened distributions and dramatically overshoots the experimental data. Finally, the difference between the normalized
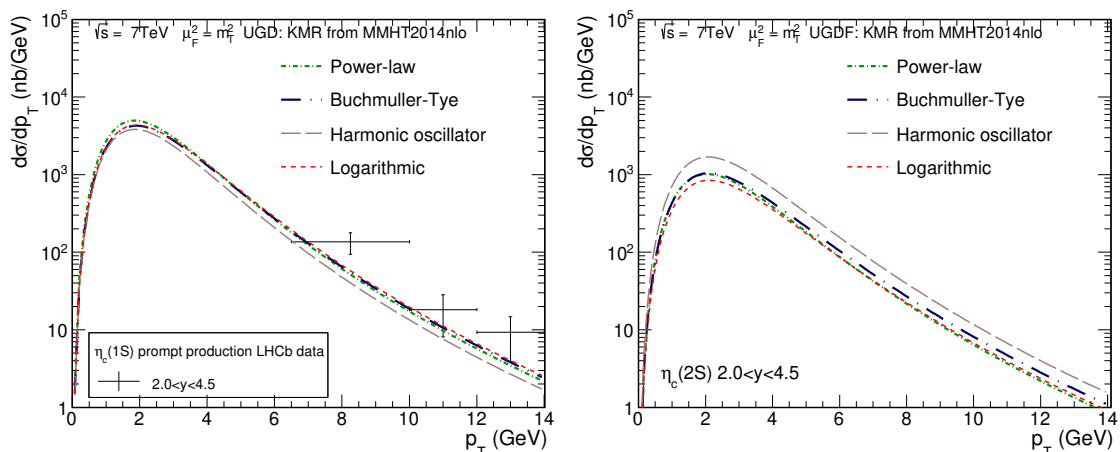
Figure 4.11: Differential cross-section for transverse momenta of $\eta_c(1S)$ (left panel) and $\eta_c(2S)$ (right panel) at $\sqrt{s} = 7\,\mathrm{GeV}$. The light-cone wave functions for different potential models without an extra normalization.
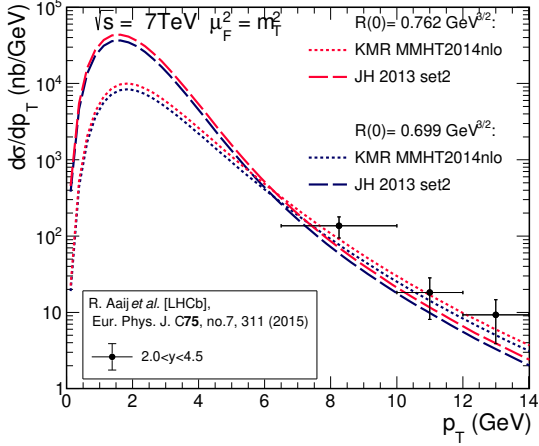
Figure 4.12: Results for NRQCD form factor with $R_{00}(0) = 0.762\,\mathrm{GeV}^{3/2}$, which corresponds to the power-law potential model and $R_{00}(0) = 0.699\,\mathrm{GeV}^{3/2}$, which is related to the radiative decay width $\eta_c(1S) \to \gamma\gamma$.
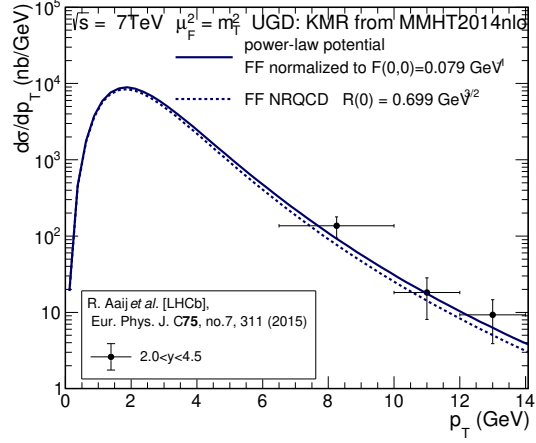
Figure 4.13: Results for NRQCD form factor with $R_{00}(0) = 0.699\,\mathrm{GeV}^{3/2}$ related to radiative decay width $\eta_c(1S) \to \gamma\gamma$ and the form factor for the power-law potential model normalized to the radiative decay width.

form factor from light-cone wave functions and relaxed normalization is exposed by the two blue lines in Fig. 4.14.

Up to now, we have explored the kinematic range of the LHCb experiment at the LHC. The following Fig. 4.15 illustrates momentum fractions x of gluons in the rapidity range $-2.5 < y_{\eta_c} < 2.5$ relevant, say, for the ATLAS detector. Although the presented projections have some numerical fluctuations, the symmetry in x_1 and x_2 is clear as well as $q_{1T} \equiv q_{1\perp}$ and $q_{2T} \equiv q_{2\perp}$. There is no sharp distinction between the KMR and JH gluons. However, Fig. 4.16 shows by the red curves (solid and dashed) that the small difference occurs only in specified p_T intervals within the ATLAS rapidity range.

4.4 Prompt hadroproduction of $\chi_{c0}(1P)$ and $\chi_{b0}(1P)$ proton-proton collisions

Production of P-wave charmonia states has a rich history. The most commonly used approaches, Color-Singlet Model [123] or the later developed Non-Relativistic QCD (NRQCD), faced various problems within Next-to-Leading Order corrections
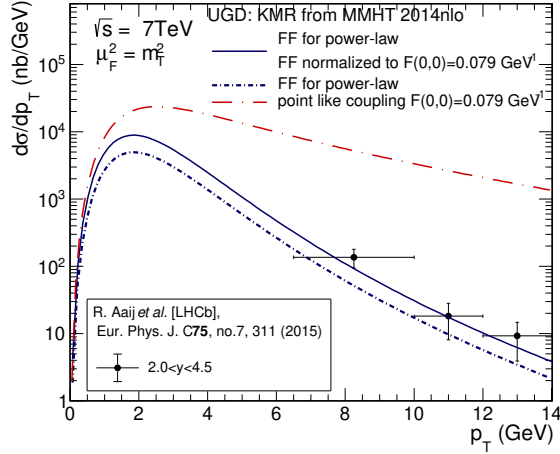
Figure 4.14: Differential distribution for normalized form factor and with relaxed normalization as well as point like coupling.

in collinear approximation [124, 125]. The higher correction in the standard collinear method results in an eventual negative cross-section at high energy at a small factorization scale[124]. Notably, this feature affects differential $p_\perp$ distributions. This effect seems to be related to the constant behavior of the NLO and NNLO cross-sections, which become more singular with the successive corrections.

The major improvement has been attained in the $k_\perp$-factorization framework [126, 86], which encodes the off-shell amplitude of $gg \rightarrow \chi_{cJ}$ process with convoluted off-shell incoming gluons distributions. In the collinear approach, the t-channel gluon exchange is allowed at $\mathcal{O}(\alpha_s^3)$, while k_T-factorization offers to take into account transverse momenta of the incoming partons. Studies on χ_{cJ} production within the NRQCD approach have been performed, including Color-Octet contribution within corresponding Long Distance Matrix Elements (LDME) [127]. This approach is somewhat hampered by the fact that the LDMEs have to be fitted to experimental data. Consequently their values rather strongly depend on the unintegrated gluon distributions and the datasets used for the fit.

In our alternative method to the NRQCD method, with CO contribution effectively incorporates relativistic correction in terms of the light-cone wave function of the $c\bar{c}$ P-wave state.

In general, the matrix element of the gluon fusion to χ_Q can be formulated in
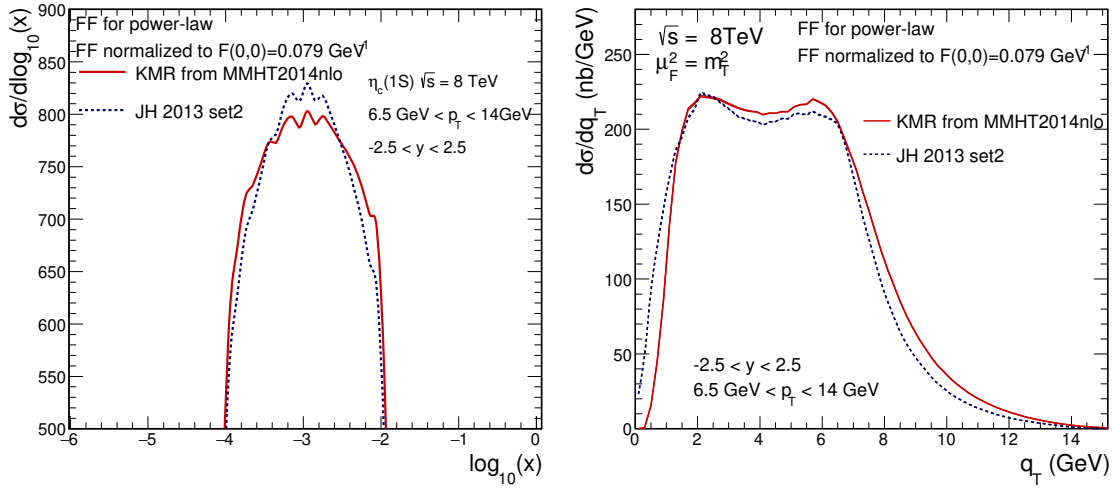
Figure 4.15: The projection on $\log_{10}(x)$ and $q_T \equiv q_\perp$ of the fusing gluon within ATLAS kinematics acceptance at the center of mass energy $\sqrt{s} = 8\,\text{TeV}$.
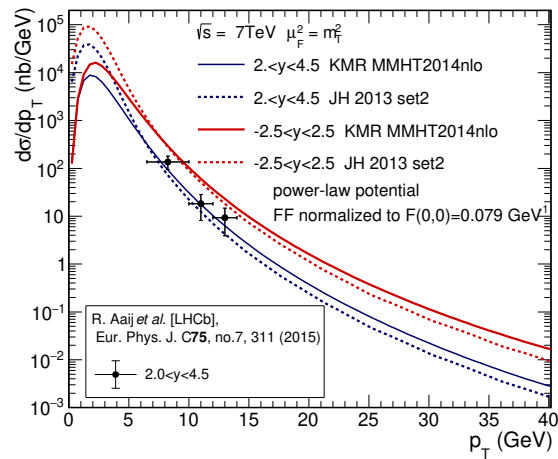
Figure 4.16: Differential distribution in $\eta_c(1S)$ transverse momentum within LHCb rapidity (blue lines) and ATLAS (red lines) rapidity acceptance.

terms of the F_{TT} and F_{LL} form-factors:

$$
\mathcal{M}_{\mu\nu}^{ab} = (-i)4\pi\alpha_s \frac{\mathrm{Tr}[t^a t^b]}{\sqrt{N_c}} \left(-\delta_{\mu\nu}^{\perp}(q_1, q_2) \frac{F_{TT}(q_1^2, q_2^2)}{e_Q^2 \sqrt{N_c}} + e_{\mu}^L(q_1) e_{\nu}^L(q_2) \frac{F_{LL}(q_1^2, q_2^2)}{e_Q^2 \sqrt{N_c}} \right),
$$
(4.36)

with projection on transverse $\delta_{\mu\nu}^{\perp}$ and longitudinal $e_{\mu}^L e_{\nu}^L$ gluon polarization, see Eqs. (3.89, 3.90). The matrix element decomposition into transverse and longitudinal polarizations gives the prominent signal that off-shell gluons fusion receives contributions from transverse and longitudinally polarized gluons as well. Note that incoming longitudinally polarized partons are absent in the approaches based on on-shell partons.

At the same time, at on-shell point only F_{TT} is related to the first derivative of the radial wave function $R'_{01}(0)$:

$$
F_{TT}(0,0) = e_Q^2 \sqrt{N_c} \frac{12}{\sqrt{\pi}} \frac{R'_{01}(0)}{\sqrt{M_{\chi_Q}^3}},
$$
(4.37)

with an electric charge of the quark e_Q and mass M_{χ_Q} of the considered χ_Q. Therefore an extra normalization to the radiative decay width is found to be without merit. The hadroproduction factorization formula for the process $pp \to \chi_{Q0}X$ in gluon-gluon fusion mode is obtained as:

$$
\frac{d\sigma}{dy d^2\vec{p}_\perp} = \int \frac{d^2\vec{q}_{1\perp}}{\pi \vec{q}_{1\perp}^4} \mathcal{F}(x_1, \vec{q}_{1\perp}^2, \mu_F^2) \int \frac{d^2\vec{q}_{2\perp}}{\pi \vec{q}_{2\perp}^4} \mathcal{F}(x_2, \vec{q}_{2\perp}^2, \mu_F^2)
$$
$$
\times \delta^{(2)}(\vec{p}_\perp - \vec{q}_{1\perp} - \vec{q}_{2\perp}) \frac{\pi}{4(N_c^2 - 1)^2} \sum_{a,b} |n_\mu^+ n_\nu^- \mathcal{M}_{\mu\nu}^{ab}|^2, \quad (4.38)
$$

the factorization scale is set up to $\mu_F^2 = m_T^2$. Subsequently, Eq. (4.38) can be altered to a more easy to handle form by restoring indices

$$
\frac{d\sigma}{dy d^2\vec{p}_\perp} = \int \frac{d^2\vec{q}_{1\perp}}{\pi \vec{q}_{1\perp}^4} \mathcal{F}(x_1, \vec{q}_{1\perp}^2, \mu_F^2) \int \frac{d^2\vec{q}_{2\perp}}{\pi \vec{q}_{2\perp}^4} \mathcal{F}(x_2, \vec{q}_{2\perp}^2, \mu_F^2)
$$
$$
\times \delta^{(2)}(\vec{p}_\perp - \vec{q}_{1\perp} - \vec{q}_{2\perp}) \frac{\pi^3 \alpha_s^2}{N_c(N_c^2 - 1)} |\tau_{TT} + \tau_{LL}|^2. \quad (4.39)
$$

In practical calculation the squared strong coupling constant is replaced as

$$
\alpha_s^2 \to \alpha_s(\max\{m_T^2, \vec{q}_{1\perp}^2\}) \alpha_s(\max\{m_T^2, \vec{q}_{2\perp}^2\}).
$$
(4.40)

Transverse τ_{TT} and longitudinal τ_{LL} parts of the reduced amplitude read

$$\tau_{TT} = |\vec{q}_{1\perp}||\vec{q}_{2\perp}|F_{1,TT}(\vec{q}_{1\perp}, \vec{q}_{2\perp}) + (\vec{q}_{1\perp} \cdot \vec{q}_{2\perp})F_{2,TT}(\vec{q}_{1\perp}, \vec{q}_{2\perp}), \qquad (4.41)$$

$$\tau_{LL} = |\vec{q}_{1\perp}||\vec{q}_{2\perp}|F_{1,LL}(\vec{q}_{1\perp}, \vec{q}_{2\perp}) + (\vec{q}_{1\perp} \cdot \vec{q}_{2\perp})F_{2,LL}(\vec{q}_{1\perp}, \vec{q}_{2\perp}), \qquad (4.42)$$

with

$$F_{1,TT} = \frac{|\vec{q}_{1\perp}||\vec{q}_{2\perp}|}{X}\left(\frac{1}{2}\left(M_\chi^2 + {\vec{q}_{1\perp}}^2 + {\vec{q}_{2\perp}}^2\right)F_2 - |\vec{q}_{1\perp}||\vec{q}_{2\perp}|F_1\right), \qquad (4.43)$$

$$F_{2,TT} = \frac{M_\chi^2 + {\vec{q}_{1\perp}}^2 + {\vec{q}_{2\perp}}^2}{2X}\left(\frac{1}{2}\left(M_\chi^2 + {\vec{q}_{1\perp}}^2 + {\vec{q}_{2\perp}}^2\right)F_2 - |\vec{q}_{1\perp}||\vec{q}_{2\perp}|F_1\right), \qquad (4.44)$$

$$F_{1,LL} = \frac{M_\chi^2 + {\vec{q}_{1\perp}}^2 + {\vec{q}_{2\perp}}^2}{2X}\left(\frac{1}{2}\left(M_\chi^2 + {\vec{q}_{1\perp}}^2 + {\vec{q}_{2\perp}}^2\right)F_1 - |\vec{q}_{1\perp}||\vec{q}_{2\perp}|F_2\right), \qquad (4.45)$$

$$F_{2,LL} = \frac{|\vec{q}_{1\perp}||\vec{q}_{2\perp}|}{X}\left(\frac{1}{2}\left(M_\chi^2 + {\vec{q}_{1\perp}}^2 + {\vec{q}_{2\perp}}^2\right)F_1 - |\vec{q}_{1\perp}||\vec{q}_{2\perp}|F_2\right), \qquad (4.46)$$

and auxiliary form factors F_1, F_2 are defined in Eq. (3.99) via light-cone wave functions. Here X is a function of χ_Q mass and gluon transverse momenta, see Eq. (3.94). Besides, the amplitude can be decomposed to transverse and longitudinal part Eq. (4.42), untangling TT and LL components and simplifies to the form factors F_1, F_2. These form factors are translated into numerical grids and then interpolated inside the matrix element.

4.4.1 Numerical analysis

The following subsection is focused on several aspects of the differential cross-sections in the relevant range of χ_c and χ_b rapidities. In particular, we used $\sqrt{s} = 13\,\mathrm{TeV}$, which is the currently achieved center of mass-energy in proton-proton collisions at the LHC. The KMR from MMHT2014nlo unintegrated gluon distribution functions (UGDF) is chosen as a representative example.

We begin with the differential distribution in transverse momentum of χ_c and χ_b shown in Fig. 4.17 with our form factors built from the light-cone wave functions for five $c\bar{c}$ interaction potential models. The disparity between results for each type of potential is almost undistinguished, except the region where $p_T < 5\,\mathrm{GeV}$, see top inlays of the plots in Fig. 4.17. Here the quark mass corresponds to the potential model in the light-cone form factor. For clarity, see Tabs. 3.8, 3.10. An interesting
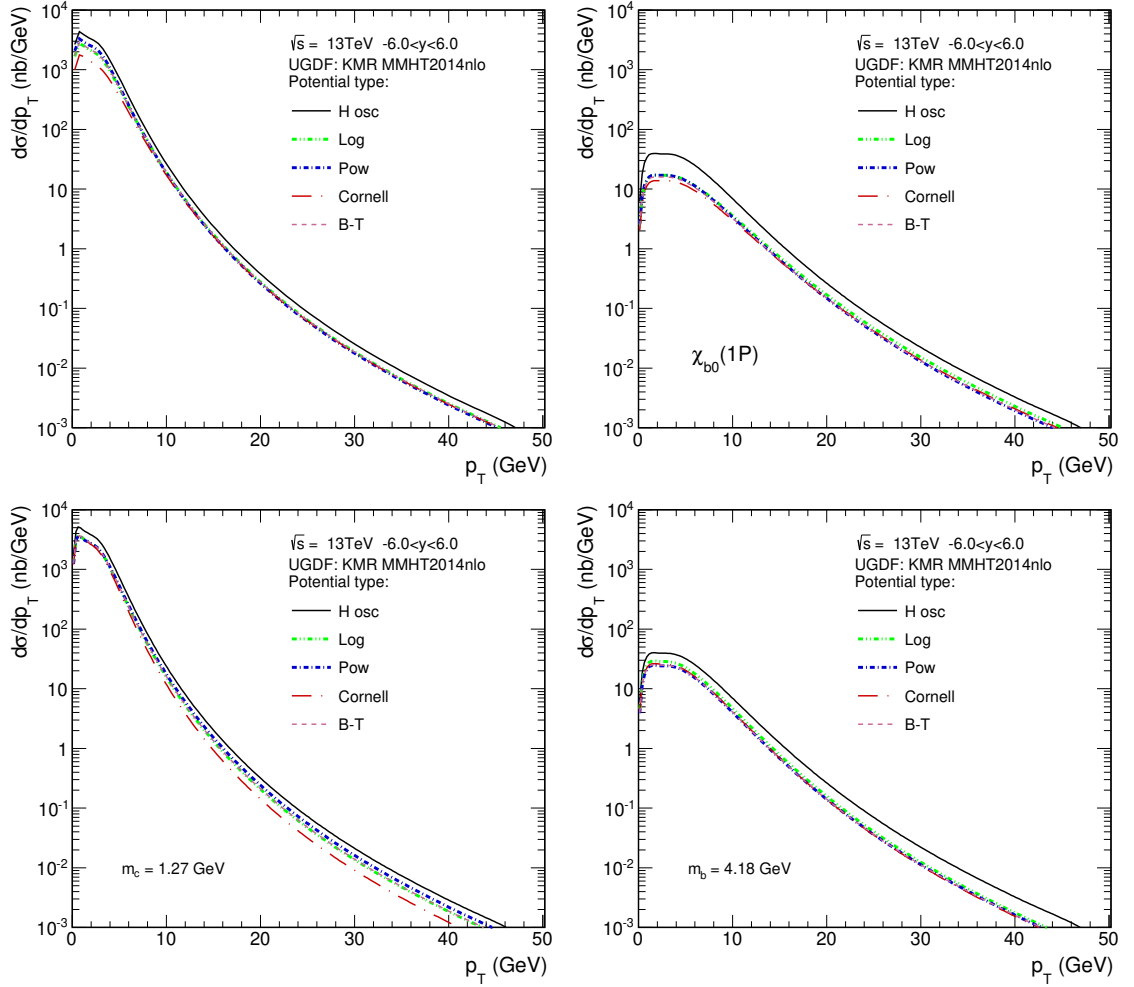
Figure 4.17: Differential distribution in transverse momentum of χ_{c0} (left column) and χ_{b0} (right column) for five distinguished potential models. In the upper row - light-cone form factor with corresponding c-quark/b-quark mass to the specific model, the lower row with neglected dependence of the model quark mass.

behavior occurs when in the light-cone form factors, the quark mass is imposed to be constituent mass established by Particle Data Group [77], $m_c = 1.27\,\text{GeV}$, $m_b = 4.18\,\text{GeV}$. Namely, the discrepancy is evident when $p_\perp$ is greater than $5\,\text{GeV}$, see lower panels of Fig. 4.17. However, the effect is more substantial in the case of χ_{c0} production.

As mentioned above, the difference between results for each type of potential is rather small except for the harmonic oscillator. Therefore in further computations, light-cone form factors obtained from the Buchmüller-Tye potential model were employed. Similarly to η_c hadroproduction, one can note the significant difference between the application of Jung-Hautmann and KMR gluon distributions only at low $p_T < 5\text{GeV}$. Fig. 4.18 also exposes the uncertainty ensued from different quark masses, $m_c = 1.27\,\text{GeV}$ (left panel) or $m_b = 4.18\,\text{GeV}$ (right panel) PDG value - the blue dashed line and $m_c = 1.48\,\text{GeV}$ (left panel) or $m_b = 4.87\,\text{GeV}$ (right panel) the B-T value - the blue dashed-dotted.
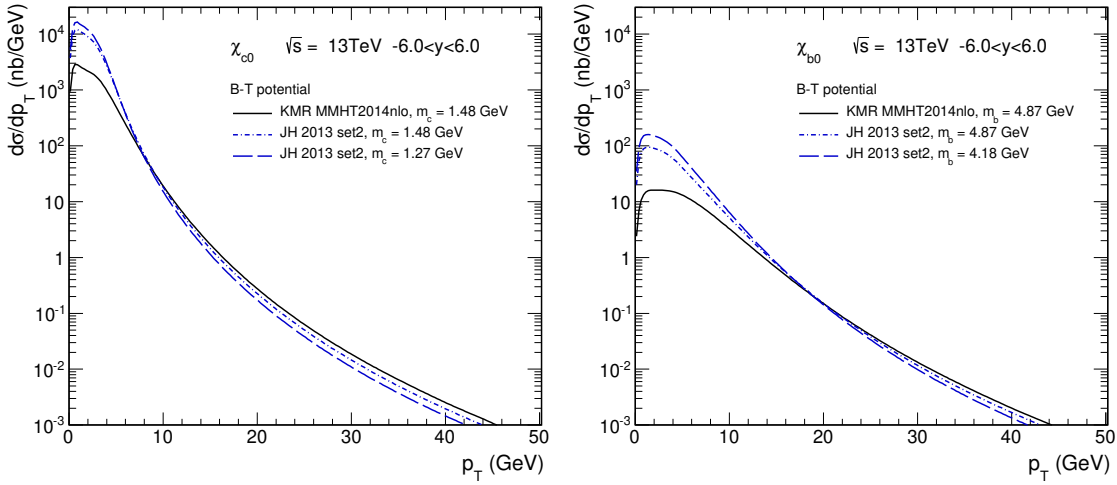
Figure 4.18: Distribution in transverse momentum of the χ_{c0} (left panel) and χ_{b0}(right panel) for Buchmüller-Tye potential model with KMR MMHT2014nlo and JH2013 set2 UGDs.

We now move to the comparison of results with our form factors to the NRQCD method. Here, Fig. 4.19 allows us to clearly see the gap among results with the NRQCD form factors and the B-T form factors. To get a proper outlook of the NRQCD recipe, $R'_{01}(0)$ values are directly related to the B-T potential model, see Tabs. 3.12, 3.13.
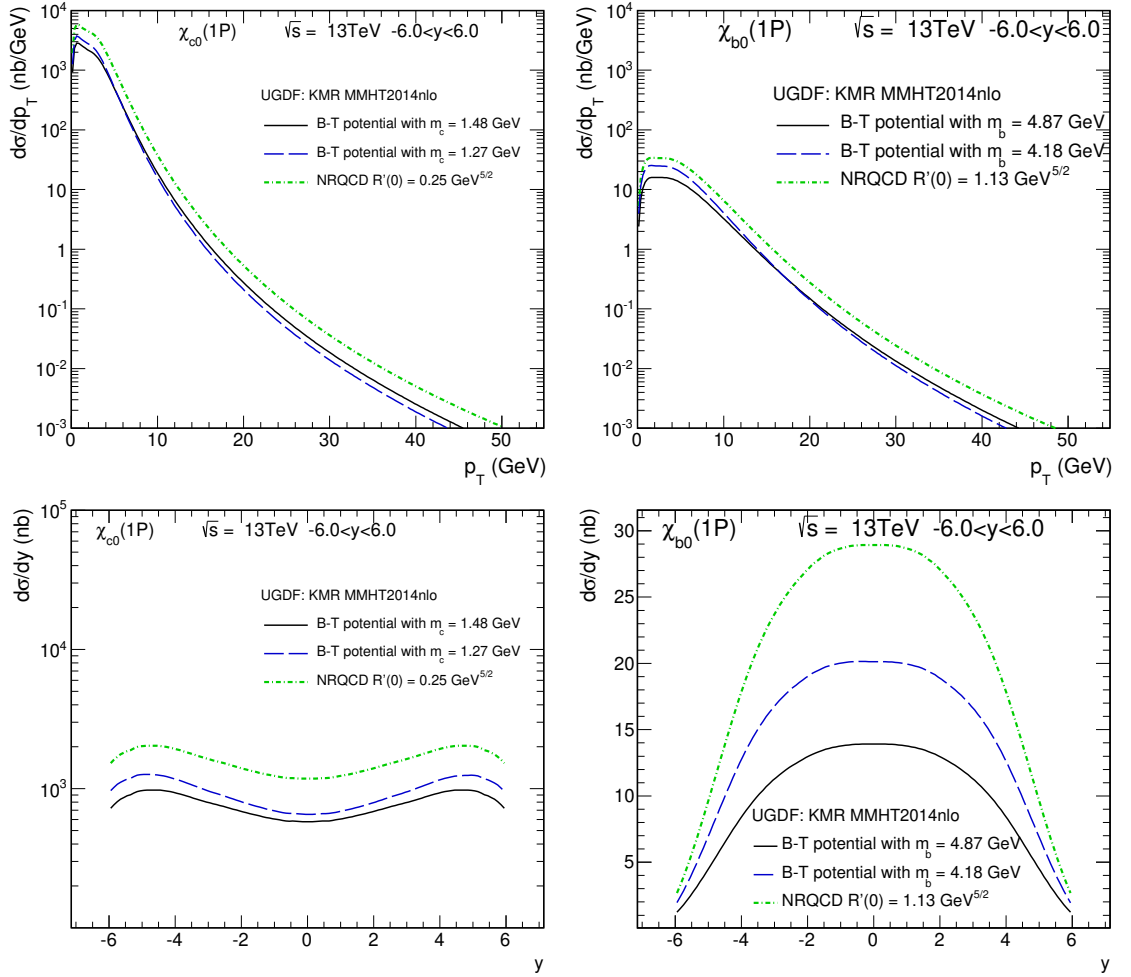
Figure 4.19: Comparison of differential distribution in transverse momentum (top row) and rapidity (low row) of χ_{c0} and χ_{b0} obtained in three ways through form factors based on the B-T potential with corresponding quark mass - black solid curve or with PDG quark mass - blue dashed curve as well as with NRQCD form factors. In the case of χ_{c0} production (left panel), the NRQCD form factors used $R'_{01}(0) = 0.25\,\mathrm{GeV}^{5/2}$ and χ_{b0} (right panel) the form factors with $R'_{01}(0) = 1.13\,\mathrm{GeV}^{5/2}$.

4. PROMPT QUARKONIUM PRODUCTION IN HADRON COLLISIONS

The most striking results from our analysis arise from the involvement of gluon longitudinal polarizations besides the standard transverse ones. In this context, Fig. 4.20 gives an example of the size of the transverse and longitudinal contributions, for χ_{c0} (left column) and χ_{b0} (right column). The major part of the cross-section is provided by the transverse contribution. However, the participation of longitudinally polarized gluons leads to reducing distributions in certain regions. This fact finds explanation in form factors relations. Namely, F_{LL} and F_{TT} have always a negative interference.
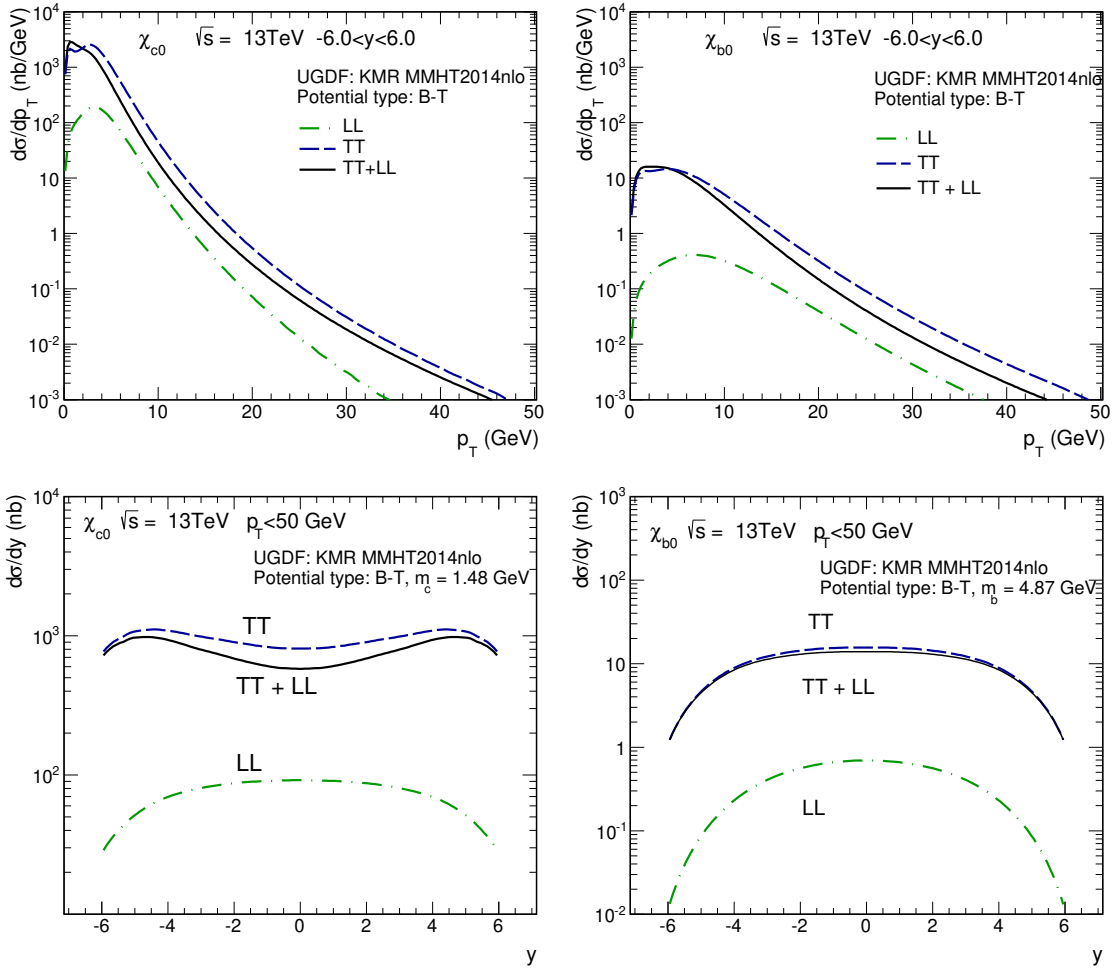
Figure 4.20: Differential cross-sections in transverse momentum and rapidity with decomposition to transverse and longitudinal contribution. In the whole range of the χ_{c0} or χ_{b0} rapidity.

The point of the linearly polarised gluons inside unpolarized hadrons in the context of the $C - even$ quarkonia production was raised in Ref. [128]. They employed a nonrelativistic color-singlet model (NRQCD) in the transverse momentum (TMD) factorization framework. This method provides also linearly polarized gluon through a nonperturbative distribution. This property affects the transverse momentum distribution, when two linearly polarised gluons fuse into the pseudoscalar or scalar meson.
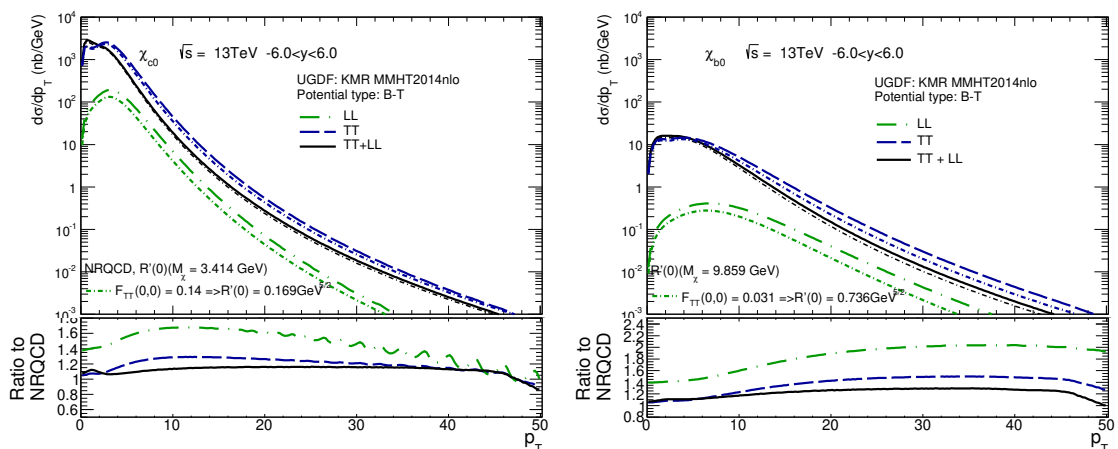
Figure 4.21: Comparison of transverse and longitudinal contribution to corresponding NRQCD components.

In Fig. 4.19 we compare results with light-cone form factors and NRQCD form factors, where $R'_{01}(0)$ is obtained from integration of the $u(k)$ wave-function for the B-T potential model (see Appendix A). This method of calculating $R'_{01}(0)$ gives a reasonably good agreement with the radiative decay width. However, a supplement picture to our analysis could be another way of computing the first derivative of the radial wave function, namely, from the transition form factor at on-shell point $F_{TT}(0,0)$. In Fig. 4.21 we compare each component of distribution from light-cone transitions with the corresponding non-relativistic parts. The transverse form factor is linearly related to $R'_{01}(0)$ by Eq. (4.37), and one of the proportionality factors is the mass of the scalar meson into the appropriate power, here we use $M_{\chi_c} = 3.414 \, \text{GeV}$ or $M_{\chi_b} = 9.859 \, \text{GeV}$. Hence, the relevant values are $R'_{01}(0) = 0.169 \, \text{GeV}^{5/2}$ for χ_{c0} and $R'_{01}(0) = 0.736 \, \text{GeV}^{5/2}$ for χ_{b0}, obtained for the B-T potential model. The ratio of the two compared results exposes the p_T regions, where light-cone form factors could play a key role, see the bottom inlays in Fig. 4.21. The findings for the sum

of $TT + LL$ yield a little variation between these two methods. However, separately the NRQCD longitudinal contribution differs the most from the light-cone one.
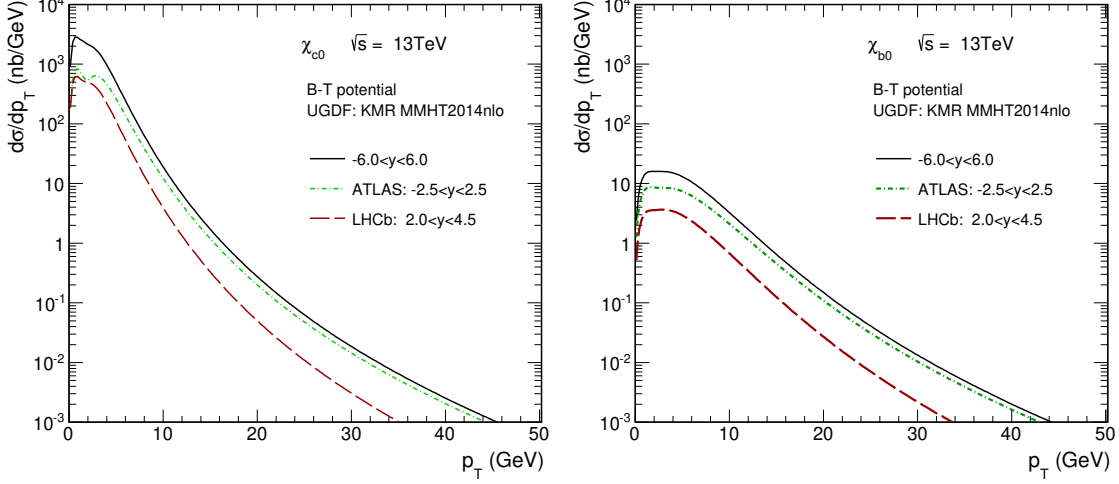
Figure 4.22: Differential cross-section as a function of transverse momentum of the produced meson predicted for the ATLAS and the LHCb rapidity acceptance.
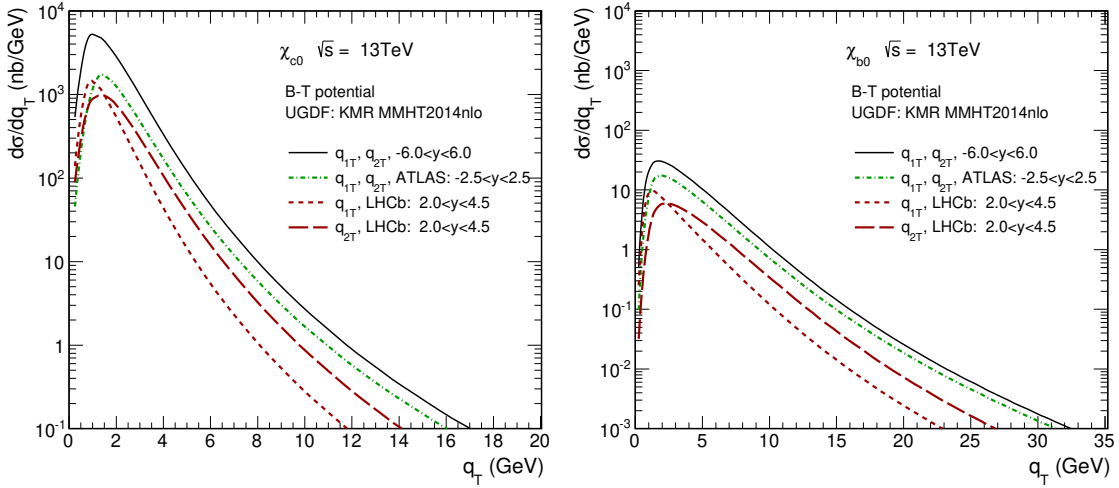
Figure 4.23: The projection on transverse momenta of the incoming gluons $|\vec{q}_{1\perp}| \equiv q_{1T}$ and $|\vec{q}_{2\perp}| \equiv q_{2T}$ within specific cuts on rapidity of the produced meson, χ_{c0} (left panel) and χ_{b0} (right panel).

The particular features of the proposed method based on light-cone form factors have been discussed in details. Therefore, let us now turn to predictions devoted

to specific experiments at the center of mass energy $\sqrt{s} = 13\,\text{TeV}$. Fig. 4.22 shows the differential cross-section in p_T of χ_{c0} (left panel) and χ_{b0} (right panel) mesons in our light-cone model within appropriate kinematics cuts on rapidity relevant for the ATLAS and the LHCb experiments at the LHC. In Fig. 4.23 we put into evidence how the LHCb asymmetric cuts on the meson rapidity influence the transverse momenta of the fusing gluons $q_{1\perp}$ and $q_{2\perp}$.

4.5 Remarks and conclusions

Let us recapitulate the results for three mesons, the pseudoscalar $\eta_c(1S)$, as well as the scalars: $\chi_{c0}(1P)$ and $\chi_{b0}(1P)$. The cross section of $\eta_c(1S)$ production in pp collision is about one order of the magnitude greater than for χ_{c0}. Moreover, the branching ratios to $p\bar{p}$ are: $Br(\chi_{c0} \to p\bar{p}) = (2.21 \pm 0.08) \times 10^{-4}$ and $Br(\eta_c \to p\bar{p}) = (1.44 \pm 0.14) \times 10^{-3}$, which can lead to difficulties in observation of χ_{c0} in this particular channel. The more preferable channel could be $\gamma\gamma$ channel. However, this issue requires further Monte-Carlo studies which are beyond the scope of this thesis. Fig. 4.24 on the r.h.s. illustrates the rapidity distribution of three mesons in the p_T range $p_T < 50\,\text{GeV}$. The pattern of $\chi_{c0}(1P)$ and $\eta_c(1S)$ distribution is similar while $\chi_{b0}(1P)$ differs at mid rapidity. This is the property of the vertex of gluon-gluon fusion into $c\bar{c}$ or $b\bar{b}$ color-singlet bound state.
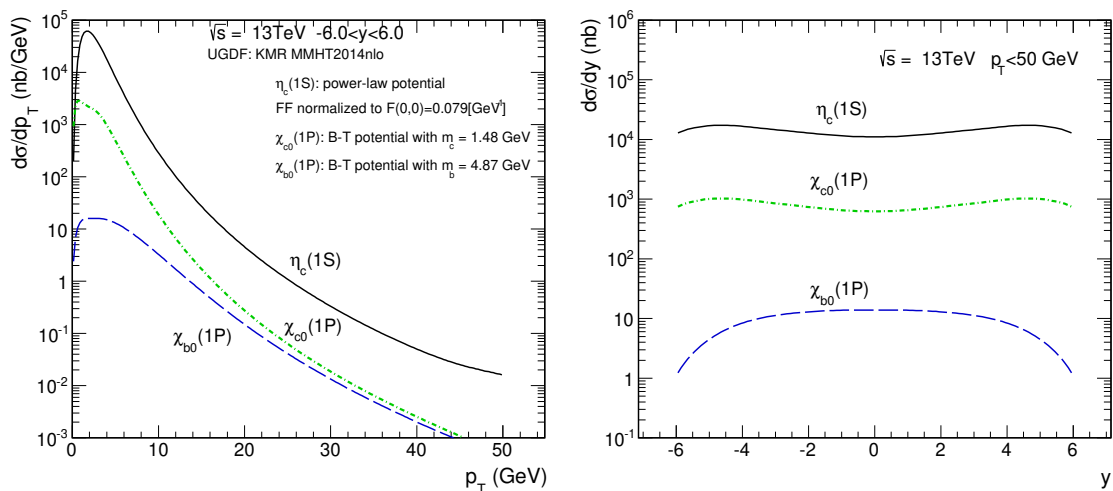
Figure 4.24: Meson distribution in transverse momentum (left panel) and rapidity (right panel) at $\sqrt{s} = 13\,\text{TeV}$ with KMR MMHT2014nlo.

Chapter 5

Central Exclusive Production of C-even Charmonia: the case of $\eta_c(1S)$ and $\chi_{c0}(1P)$

The Large Hadron Collider (LHC) facility at CERN (Conseil Européen pour la Recherche Nucléaire) opened a new era of high-energy physics research. Besides the Higgs boson discovery, this laboratory confirmed a major group of phenomena predicted by the Standard Model and beyond. While the Higgs-boson was eventually discovered in inclusive inelastic processes, as a possibility to observe the searched-for boson, a unique class of events characterized by a *clean* final state was proposed. The idea is based on the assumption that it should be possible to excite the *vacuum* into a real Higgs boson in exclusive proton-proton or proton-antiproton interaction if the Higgs field is responsible for filling the *vacuum* [129]. Indeed, in exclusive processes interacting hadrons or ions avoid a breakup, while the underlying production mechanism involves photons or gluons. The massive boson production has been discussed in detail in *The FP420 R&D Project* research program [130].

So far, exclusive meson production at the LHC has been studied in *pp*, *pPb*, and *PbPb* collisions. Moreover, this type of experiments have also been analyzed at Tevatron in $p\bar{p}$ collisions, at RHIC in *AuAu* and *pAu* collisions. The majority of exclusive reaction measurements have been devoted to light meson such as $\rho^0(770)$ [131, 132] or two pion systems $\pi^0\pi^0$, $\pi^+\pi^-$ [133, 134] at low invariant masses of the produced system [135].

Center of mass energies available at theLHC allowed to study heavy meson production such as J/ψ, $\psi(2S)$, χ_{cJ} family and Υ in proton-proton collisions [136, 137].

5. CENTRAL EXCLUSIVE PRODUCTION OF C-EVEN CHARMONIA: THE CASE OF $\eta_C(1S)$ AND $\chi_{C0}(1P)$

An attractive feature of the heavy particle production is the naturally provided hard scale which allows perturbative quantum chromodynamics methods to be applied. Central exclusive processes (CEP) in hadronic collision due to the specific final state require a proper theory. The sketch of the reaction is the following

$$h_1 h_2 \to h_1 \circ X \circ h_2 \,.$$

Due to to rapidity gap (donated by "$\circ$") between two intact hadron/ions(h_1, h_2), this type of processes could be regarded as double diffractive processes with the exchange of a colorless "particle" called Pomeron ($\mathbb{P}$). Notice that also exchange of a photon can lead to the same phenomenon of a large rapidity gap. An important selection rule in central exclusive processes is the conservation of charge conjugation parity (C-parity). For example, as the Pomeron has even C-parity, the diffractive production of the C-odd vector mesons like $\rho^0, \phi, J/\psi$ involves the photon-Pomeron fusion. As a side remark we mention that recent analyses of elastic pp scattering claim the existence of an Odderon [138, 139] that is a C-odd hadronic exchange that does not vanish with increasing energy.

The hard diffractive procceses are often described through the Ingelman-Schlein model [140] which is based on the evolution of Pomeron structure functions (or parton distributions in the Pomeron), corrected with a gap survival factor. Heavy flavour mesons production with structure functions obtained by the H1 Collaboration at DESY-HERA have been discussed for instance in Ref. [141]. Intensively studied dijet production in single Pomeron exchange has been already computed within the $k_\perp$-factorization framework, see Ref. [17]. However, the modeled structure functions suffer from factorization breaking [142]. These authors emphasize that the main source of factorization breaking is the presence of the possible interaction with spectator partons originating from the proton-proton collision. In Ref. [142], the authors derived a formalism of Single-Diffractive dijet production in dipole representation claiming that spectator interactions included at the amplitude level.

How the multiparton scattering or re-scattering affects the rapidity gap in exclusive reactions is however still under discussion. A good example to study the possible sources of the gap filling are $\mathcal{J}et\,gap\,\mathcal{J}et$ process, also called dijets events with large rapidity separation, due to specific kinematic regime, see Ref. [16, 143].

An alternative formalism has been proposed by the Durham group, which focused on the first development of the perturbative theory of a "Born term" for these

types of reactions, further named the *Durham model*. In our investigations presented below, the salient features of the *Durham model* scheme are kept with some modifications.

5.1 Amplitude and kinematics of CEP reaction

The exclusivity of the process requires that the produced system is in a color-singlet state, while any additional gluon emission present in inclusive reactions is forbidden. The Born-term of the Durham model contains a hard scale dependent amplitude describing two gluon fusion to the heavy meson as well relatively soft gluon exchange called also the screening gluon [144]. The presence of a screening gluon, see Fig. 5.1, serves to fulfill the vacuum number condition in the crossed channel.
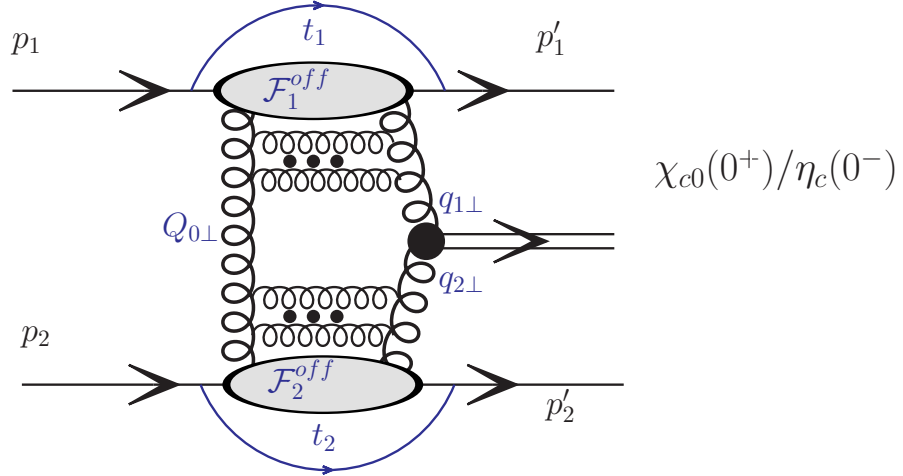
Figure 5.1: Generic diagram for the central exclusive production via gluon fusion.

Following the notation and derivation in Ref. [87] the CEP amplitude reads

$$\mathcal{M}_{CEP} = \frac{s}{2}\pi^2 \frac{1}{2}\frac{\delta_{c_1 c_2}}{N_c^2 - 1}\int d^2\vec{Q}_{0\perp}\; \mathcal{V}^{c_1 c_2}$$
$$\frac{\mathcal{F}_g^{\text{off}}(x_1, x', \vec{Q}_{0\perp}^2, \vec{q}_{1\perp}^2, \mu^2, t_1)\mathcal{F}_g^{\text{off}}(x_2, x', \vec{Q}_{0\perp}^2, \vec{q}_{2\perp}^2, \mu^2, t_2)}{\vec{Q}_{0\perp}^2\, \vec{q}_{1\perp}^2\, \vec{q}_{2\perp}^2}\;, \quad (5.1)$$

including momenta of the *active* gluons q_1, q_2 and the *screening* one Q_0. Above, $\mathcal{V}$ denotes the two gluon fusion vertex into heavy meson, χ_{c0} or η_c. Note that in

5. CENTRAL EXCLUSIVE PRODUCTION OF C-EVEN CHARMONIA: THE CASE OF $\eta_C(1S)$ AND $\chi_{C0}(1P)$

the formula there appears an additional factor $(1/2)$ due to a convention of light-cone base vectors, which differs from the one used in the previous chapters, but corresponds to the one used by Pasechnik, Teryaev and Szczurek [87, 145, 146]. Namely, here we use the light-like basis vectors, which satisfy $n^+n^- = 2$. The total cross section for $2 \to 3$ reaction can be evaluated using the general formula

$$\sigma = \frac{1}{2s} \int |\mathcal{M}_{CEP}|^2 (2\pi)^4 \delta^4(p_1 + p_2 - p_1' - p_2' - p_V)$$
$$\times \left(\frac{1}{2(2\pi)^3}\right)^3 (dy_1' d^2\vec{p}_{1\perp}')(dy_2' d^2\vec{p}_{2\perp}')(dy d^2\vec{p}_{V\perp}), \quad (5.2)$$

which can be simplified to

$$\sigma = \frac{1}{2s} \frac{1}{2^8 \pi^4 s} \int |\mathcal{M}_{CEP}|^2 dt_1 dt_2 dy d\phi, \quad (5.3)$$

as in Ref. [147], where $t_1 = (p_1 - p_1')^2$, $t_2 = (p_2 - p_2')^2$ and relative azimuthal angle between scattered outgoing protons ϕ is within the range $(0, 2\pi)$. The two gluon fusion vertex into χ_{c0} via two gluon involves the light-cone form factors G_{TT} and G_{LL}:

$$\mathcal{V}_{\mu\nu}^{ab}(g^*g^* \to \chi_{c0}) = 4\pi\alpha_s \frac{\text{Tr}[t^a t^b]}{\sqrt{N_c}} 2\mathcal{T}_{\mu\nu} = \frac{4\pi\alpha_s}{\sqrt{N_c}} \delta^{ab}\mathcal{T}_{\mu\nu}, \quad (5.4)$$

$$\mathcal{T}_{\mu\nu} = -\delta_{\mu\nu}^{\perp}(q_1, q_2)G_{TT}(q_1^2, q_2^2) + e_\mu^L(q_1)e_\nu^L(q_2)G_{LL}(q_1^2, q_2^2), \quad (5.5)$$

here the form factors $G_{TT}(q_1^2, q_2^2) = F_{TT}(q_1^2, q_2^2)/(e_c^2\sqrt{N_c})$, $G_{LL}(q_1^2, q_2^2) = F_{LL}(q_1^2, q_2^2)/(e_c^2\sqrt{N_c})$ are counterparts of photon-photon fusion form factors.

For the pseudoscalar meson, we use

$$\mathcal{V}_{\mu\nu}^{ab}(g^*g^* \to \eta_c) = (-i)4\pi\alpha_s \epsilon_{\mu\nu\alpha\beta} q^\alpha q^\beta \frac{\delta^{ab}}{2\sqrt{N_c}} 2F_{g^*g^* \to \eta_c}(\vec{q}_{1\perp}^2, \vec{q}_{2\perp}^2), \quad (5.6)$$

where $F_{g^*g^* \to \eta_c}(\vec{q}_{1\perp}^2, \vec{q}_{2\perp}^2) = F_{\gamma^*\gamma^* \to \eta_c}(\vec{q}_{1\perp}^2, \vec{q}_{2\perp}^2)/(e_c^2\sqrt{N_c})$. In particular for the η_c there exists only a transversal form factor. Hence we can identify $F_{g^*g^* \to \eta_c}(\vec{q}_{1\perp}^2, \vec{q}_{2\perp}^2) = F_{TT}(g^*(q_1)g^*(q_2) \to \eta_c)$.

5.1.1 Off-diagonal gluon concept

The forward limit provides small $t_{1,2} \to 0$ responsible for $\vec{Q}_\perp^2 \simeq \vec{q}_{\perp 1,2}{}^2 \equiv Q_\perp^2$. In this limit, the generalized UGDs (sometimes named unintegrated GPDs) in Eq. (5.1) are simplified and are considered as functions of only one transverse momentum, i.e.

$$\mathcal{F}_g^{\text{off}}(x_1, x', \vec{Q}_{0\perp}^2, \vec{q}_{1\perp}{}^2, \mu^2, t_1) \to \mathcal{F}_g^{\text{off}}(x_1, x', Q_\perp^2, \mu^2, t_1). \tag{5.7}$$

The Khoze-Martin-Ryskin (KMR) prescription for the off-diagonal UGD involves the square root of a Sudakov form factor $T_g(q_\perp^2, \mu^2)$ and its well known form is [148]

$$\mathcal{F}_{g,\text{KMR}}^{\text{off}}(x, x', Q_\perp^2, \mu^2; t) = R_g \frac{d}{d\ln q_\perp^2}\left[xg(x, q_\perp^2)\sqrt{T_g(q_\perp^2, \mu^2)}\,\right]_{q_\perp^2 = Q_\perp^2} F(t), \tag{5.8}$$

with gluon virtualities $q_\perp^2$ used as the momentum scale squared in the collinear gluon density $xg(x, q_\perp^2)$. The nucleon form factor $F(t)$ is often parameterized in one of the following two ways

$$F(t) = \exp\left(\frac{bt}{2}\right), \quad b = 4\,\text{GeV}^{-2} \qquad \text{or} \qquad F(t) = \frac{4m_p^2 - 2.79t}{(4m_p^2 - t)(1 - t/0.71)^2}, \tag{5.9}$$

the first being a Fourier transform of a Gaussian QCD elastic profile factor, while the second corresponds to the isoscalar nucleon form factor [149] with the proton mass m_p, respectively. The Sudakov form factor is taken from the typical formula:

$$T_g(q_\perp^2, \mu^2) = \exp\left[-\int_{q_\perp^2}^{\mu^2} \frac{d\vec{k}_\perp^2}{\vec{k}_\perp^2} \frac{\alpha_s(k_\perp^2)}{2\pi} \int_0^{1-\Delta} \left[zP_{gg}(z) + \sum_q P_{qg}(z)\right] dz\right], \tag{5.10}$$

here the hard scale is taken as $\mu^2 = M_V^2 + q_\perp^2$ and $\Delta = k_\perp/(k_\perp + \mu)$. Considering the involved longitudinal momentum fractions, the central diffractive production is dominated by the region $x' \ll x_{1,2} \ll 1$. Therefore we compute the skewedness correction R_g in Eq. (5.8) taking advantage of a method offered and derived for the collinear off-diagonal gluon distributions [150]:

$$R_g = \frac{2^{2\lambda+3}}{\sqrt{\pi}} \frac{\Gamma(\lambda + 5/2)}{\Gamma(\lambda + 4)}, \qquad \lambda = \frac{d}{d\ln(1/x)}\left[\ln\left(xg(x, q_\perp^2)\right)\right]. \tag{5.11}$$

Regarding the slightly off-forward case, where $t_{1,2} \neq 0$, there is an ambiguity in the choice of $Q_\perp$ in the off-diagonal KMR gluon in Eq. (5.8). Different prescriptions have been proposed in the literature. In our computation, we use the so-called "minimum

5. CENTRAL EXCLUSIVE PRODUCTION OF C-EVEN CHARMONIA: THE CASE OF η_C(1S) AND χ_{C0}(1P)

prescription" proposed by the Durham group. Namely, in Eq. (5.8) we substitute $Q_\perp^2$ with minimum of an active gluon transverse momentum $q_\perp$ and the screening gluon transverse momentum $Q_\perp$:

$$Q_\perp^2 \to \min(Q_{0\perp}^2, q_\perp^2). \tag{5.12}$$

Additionally, we have introduced an option in Eq. (5.8) further called BPSS:

$$Q_\perp^2 \to \sqrt{Q_{0\perp}^2 q_\perp^2}, \tag{5.13}$$

which is a geometrical average of gluon momenta.

In a similar fashion the off-diagonal gluon labeled CDHI [151] was proposed by Cudell et al., which we used in the modified form defined as:

$$\mathcal{F}_{g,\text{CDHI}}^{\text{off}}(x, x', Q_\perp, \mu^2; t) = R_g\left[\frac{\partial}{\partial \log \bar{Q}^2}\sqrt{T_g(\bar{Q}^2, \mu^2)}\, xg(x, \bar{Q}^2)\right] \cdot \frac{2Q_{0\perp}^2 q_\perp^2}{Q_{0\perp}^4 + q_\perp^4} \cdot F(t), \tag{5.14}$$

with arithmetic average $\bar{Q}^2 = (Q_{0\perp}^2 + q_\perp^2)/2$ employed also in the Sudakov form factor.

An alternative group of methods to compute off-diagonal gluon distribution is represented by the models which account for the gluon saturation effects. The saturation-based UGD is inspired by diagonal gluon model derived by Golec-Biernat and Wüsthoff (GBW) [152]. To achieve the off-diagonal domain, we use the extrapolating prescription proposed in Ref. [87] (further referred to as the PST prescription):

$$\mathcal{F}_{\text{GBW}}^{\text{off}} = \sqrt{Q_{0\perp}^2 f^{\text{GBW}}(x', Q_{0\perp}^2) q_\perp^2 f^{\text{GBW}}(x, q_\perp^2)}\sqrt{T_g(q_\perp^2, \mu^2)}\, F(t), \tag{5.15}$$

$$f^{\text{GBW}}(x, q_\perp^2) = \frac{3\,\sigma_0}{4\pi^2\alpha_s} R_0^2\, q_\perp^2\, \exp[R_0^2 q_\perp^2], \tag{5.16}$$

here f^{GBW} is the diagonal GBW UGD, and $x' = |\vec{Q}_\perp^2|/\sqrt{s}$, $R_0 = (x/x_0)^{\lambda/2}$. Precisely, we used the GBW model with the fitted parameters obtained by Golec-Biernat and Sapeta [153]: $\sigma_0 = 29.12$ mb, $\lambda = 0.277$, $x_0/10^{-4} = 0.41$, with $\alpha_s(q_\perp^2) = \min(0.82, \frac{4\pi}{9\log(Q^2/\Lambda_{\text{QCD}}^2)})$ and $Q^2 = \max(q_\perp^2, 0.22\,\text{GeV}^2)$, $\Lambda_{\text{QCD}}^2 = 0.04\,\text{GeV}^2$.

To vary our results, we also applied the model based on the color dipole cross section fitted by Rezaeian and Schmidt [154]. While the GBW model corresponds to the eikonal unitarization, the Rezaeian-Schmidt cross section is motivated by the

BFKL equation and its nonlinear generalizations as proposed by Iancu et al. in Ref. [155]. Therefore, the computed UGD $f_g^{\mathrm{RS}}(x, |\vec{q}_\perp|)$ takes the form

$$\mathcal{F}_{\mathrm{RS}}^{\mathrm{off}} = \sqrt{Q_{0\perp}^2 f^{\mathrm{RS}}(x', |Q_\perp|) q_\perp^2 f^{\mathrm{RS}}(x, |q_\perp|)} \sqrt{T_g(q_\perp^2, \mu^2)} F(t), \qquad (5.17)$$

$$f_g^{RS}(x, |\vec{q}_\perp|) = |\vec{q}_\perp|^2 \frac{\sigma_0}{\alpha_s} \frac{N_c}{8\pi^2} \int_0^\infty r dr\, J_0(|\vec{q}_\perp|r) \Big(1 - \frac{\sigma(x, r)}{\sigma_0}\Big). \qquad (5.18)$$

As an example, we have applied the first set of parameters from Table I in Ref. [154].

5.2 Differential distributions and total cross sections: numerical results

CEP processes at high energies involve parton distributions characterized by relatively low Q^2 and very small fractions of longitudinal momenta. Therefore, in order to achieve relevant off-diagonal constructions and adequate results, it is necessary to discuss the available options of parton distribution functions (PDFs). For this purpose, we have examined three sets of parton distribution functions that is JR14NLO [156]($Q_{min}^2 = 0.8\,\mathrm{GeV}^2$), GJR08NLO ($Q_{min}^2 = 0.5\,\mathrm{GeV}^2$) [157], GRV94NLO [158] ($Q_{min}^2 = 0.4\,\mathrm{GeV}^2$). Fig. 5.2 reveals the shapes of diagonal gluon distribution functions at a typical longitudinal momentum fraction and illustrates the available initial evolution scale Q_{min}^2.

There is a significant difference in the range of scales available in the PDFs published in the literature. In particular, we dropped the popular Durham or CTEQ PDFs due to the fact that they need a relatively large initial evolution scale. These models are somewhat difficult to apply in the context of gluon-induced CEP reactions.

Regarding integrated cross-section computed over full phase-space, we collated results in Tab. 5.1 and Tab. 5.2 for χ_{c0} and η_c, respectively. The calculations have been performed at $\sqrt{s} = 13\,\mathrm{TeV}$. In addition, in the case of the KMR skewed gluon procedure we present results with and without the skewedness correction factor R_g (see Eq. (5.11)). The noticeable increment is obtained in the cross-section including R_g, which is usually assumed to be a constant value ($R_g \sim 1.3$). The dynamic behavior of the effective skewedness correction is illustrated in Fig. 5.3. In the so-called KMR skewed gluon as an input we used the JR14NLO, GJR08NLO or GRV94NLO gluon distribution, while in the PST prescription we avail of the GBW

5. CENTRAL EXCLUSIVE PRODUCTION OF C-EVEN CHARMONIA: THE CASE OF $\eta_C(1S)$ AND $\chi_{C0}(1P)$
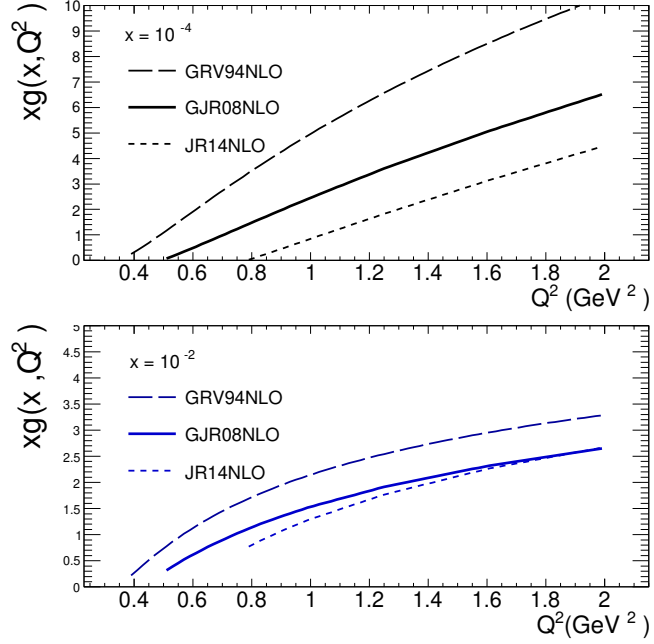
Figure 5.2: Collinear diagonal gluon distributions as a function of hard scale Q^2 with typical momentum fractions: $x = 10^{-4}$ top plot and $x = 10^{-2}$ bottom plot.

or RS model. The total cross-section for χ_{c0} is around $1\,\mu b$, still before applying any absorptive correction, which is estimated to be about $0.13 - 0.2$ below. In the case of η_c production, the cross-section is on average three order of magnitude smaller in comparison to χ_{c0}. Moreover, the spread of the results in the case of η_c was collected in Tab. 5.2 is much broader than for the χ_{c0} in Tab. 5.1.

The distribution in rapidities of χ_{c0} and η_c is revealed in Fig. 5.3. To present the effect of including the $R_g(x, Q^2_\perp)$ correction, as a representative example we chose $\mathcal{F}^{off}_{\text{CDHI}}$(Eq. (5.14)) and $\mathcal{F}^{off}_{\text{KMR}}$(Eq. (5.8) with minimum prescription Eq. (5.12)). After the application of the Shuvaev correction $R_g(x, Q^2_\perp)$ (see Eq. 5.11), we observe an increase of the cross-section by a factor of 3-4 in the case of χ_{c0} as well as η_c, independently on the choice of the off-diagonal gluon.

The transverse momentum distributions are found in Fig. 5.4. The characteristic pattern with a dip in the transverse momentum distribution for the CEP χ_{c0} vertex can be observed in the left panel. One can also notice that these two distributions differ in the position of the maximum: for the η_c it is around $1\,\text{GeV}$, while for the $\chi_{c0} \sim 0.5\,\text{GeV}$.

In Fig. 5.5, we reveal the distribution in relative azimuthal angle between the outgoing scattered protons. The computations have been performed at $\sqrt{s} = 13\,\text{TeV}$ with the help of GJR08NLO using $\mathcal{F}^{off}_{\text{KMR}}$ (see Eq. (5.8)) one time within the Durham

Table 5.1: *Total cross section for χ_{c0} at $\sqrt{s} = 13\,\text{TeV}$ with $R_g = 1.0$ and R_g according to Eq. ([5.11](#)). The light-cone form factor for the $gg \to \chi_{c0}$ coupling was obtained through the Buchmüller-Tye potential. No gap survival factor is included here.*

KMR skewed gluon	σ_{tot} [nb]	σ_{tot} [nb]
$0.8\,\text{GeV}^2 \le Q_{min}^2$, JR14NLO	$R_g = 1.0$	$R_g(x, Q_\perp^2)$
CDHI, $Q_\perp^2 = (Q_{0\perp}^2 + q_\perp^2)/2.$	$0.42 \cdot 10^3$	$1.1 \cdot 10^3$
KMR, $Q_\perp^2 = \sqrt{Q_{0\perp}^2 \cdot q_\perp^2}$	$0.36 \cdot 10^3$	$0.94 \cdot 10^3$
KMR, $Q_\perp^2 = \min(Q_{0\perp}^2, q_\perp^2)$	$0.20 \cdot 10^3$	$0.52 \cdot 10^3$
KMR skewed gluon	σ_{tot} [nb]	σ_{tot} [nb]
$0.5\,\text{GeV}^2 \le Q_{min}^2$, GJR08NLO	$R_g = 1.0$	$R_g(x, Q_\perp^2)$
CDHI, $Q_\perp^2 = (Q_{0\perp}^2 + q_\perp^2)/2.$	$0.46 \cdot 10^3$	$1.57 \cdot 10^3$
KMR, $Q_\perp^2 = \sqrt{Q_{0\perp}^2 \cdot q_\perp^2}$	$0.64 \cdot 10^3$	$2.1 \cdot 10^3$
KMR, $Q_\perp^2 = \min(Q_{0\perp}^2, q_\perp^2)$	$0.34 \cdot 10^3$	$1.1 \cdot 10^3$
KMR skewed gluon	σ_{tot} [nb]	σ_{tot} [nb]
$0.4\,\text{GeV}^2 \le Q_{min}^2$, GRV94NLO	$R_g = 1.0$	$R_g(x, Q_\perp^2)$
CDHI, $Q_\perp^2 = (Q_{0\perp}^2 + q_\perp^2)/2.$	$1.88 \cdot 10^3$	$9.02 \cdot 10^3$
KMR, $Q_\perp^2 = \sqrt{Q_{0\perp}^2 \cdot q_\perp^2}$	$3.03 \cdot 10^3$	$13.4 \cdot 10^3$
KMR, $Q_\perp^2 = \min(Q_{0\perp}^2, q_\perp^2), 0.4\text{GeV}^2 \le Q_{min}^2$	$1.4 \cdot 10^3$	$6.1 \cdot 10^3$
KMR, $Q_\perp^2 = \min(Q_{0\perp}^2, q_\perp^2), 0.8\text{GeV}^2 \le Q_{min}^2$	$0.75 \cdot 10^3$	$3.9 \cdot 10^3$
PST skewed gluon	σ_{tot} [nb]	-
PST prescription, GBW	$0.44 \cdot 10^3$	-
PST prescription, RS	$0.52 \cdot 10^3$	-
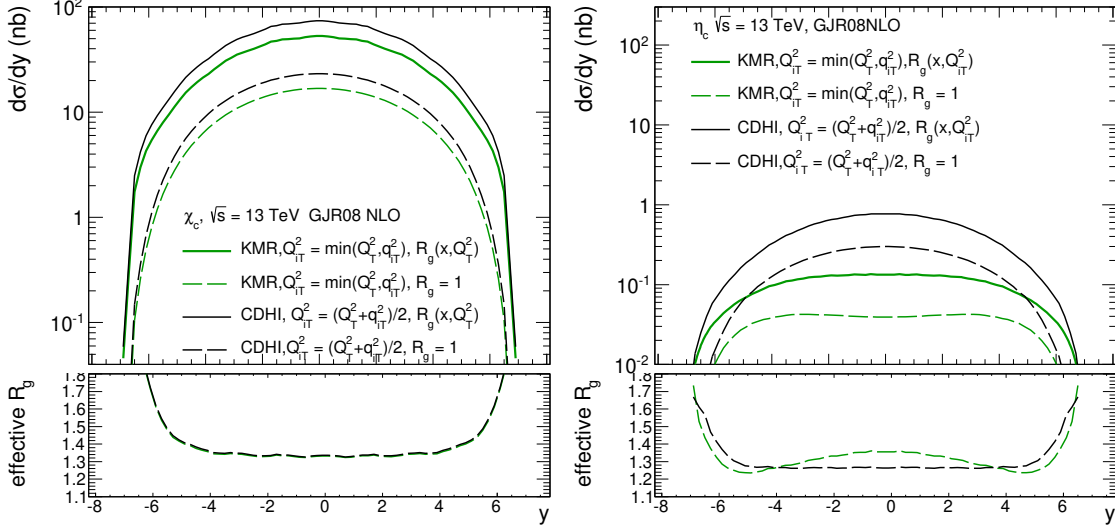
Figure 5.3: Distribution in χ_{c0} (left plot) and η_c (right plot) rapidity with exposition of dynamic behavior of the skewedness correction R_g, see the bottom inlays.
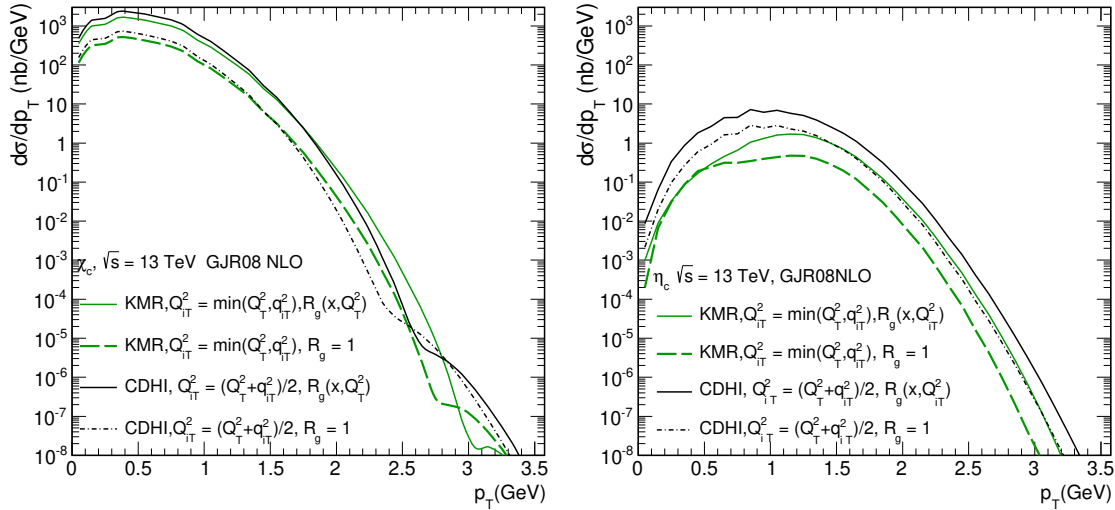
Figure 5.4: Distribution in χ_{c0} (left plot) and η_c (right plot) transverse momentum.

5.2 Differential distributions and total cross sections: numerical results

Table 5.2: Total cross section for η_c at $\sqrt{s} = 13\,\mathrm{TeV}$ with $R_g = 1.0$ and R_g according to Eq. (5.11). The light-cone form factor for the $gg \to \eta_c(1S)$ coupling was obtained through the power-law potential.

KMR skewed gluon	σ_{tot} [nb]	σ_{tot} [nb]
$0.8\mathrm{GeV}^2 \le Q^2_{min}$, JR14NLO	$R_g = 1.0$	$R_g(x, Q^2_\perp)$
CDHI, $Q^2_\perp = (Q^2_{0\perp} + q^2_\perp)/2.$	1.1	2.4
KMR, $Q^2_\perp = \sqrt{Q^2_{0\perp} \cdot q^2_\perp}$	0.39	1.2
KMR, $Q^2_\perp = \min(Q^2_{0\perp}, q^2_\perp)$	0.13	0.25
KMR skewed gluon	σ_{tot} [nb]	σ_{tot} [nb]
$0.5\mathrm{GeV}^2 \le Q^2_{min}$, GJR08NLO	$R_g = 1.0$	$R_g(x, Q^2_\perp)$
CDHI, $Q^2_\perp = (Q^2_{0\perp} + q^2_\perp)/2.$	2.2	5.6
KMR, $Q^2_\perp = \sqrt{Q^2_{0\perp} \cdot q^2_\perp}$	0.52	2.1
KMR, $Q^2_\perp = \min(Q^2_{0\perp}, q^2_\perp), 0.5\mathrm{GeV}^2 \le Q^2_{min}$	0.44	1.3
KMR, $Q^2_\perp = \min(Q^2_{0\perp}, q^2_\perp), 0.8\mathrm{GeV}^2 \le Q^2_{min}$	0.22	0.45
KMR skewed gluon	σ_{tot} [nb]	σ_{tot} [nb]
$0.4\mathrm{GeV}^2 \le Q^2_{min}$, GRV94NLO	$R_g = 1.0$	$R_g(x, Q^2_\perp)$
CDHI, $Q^2_\perp = (Q^2_{0\perp} + q^2_\perp)/2.$	$1.2 \cdot 10^2$	$7.8 \cdot 10^3$
KMR, $Q^2_\perp = \sqrt{Q^2_{0\perp} \cdot q^2_\perp}$	2.2	$1.3 \cdot 10^3$
KMR, $Q^2_\perp = \min(Q^2_{0\perp}, q^2_\perp), 0.4\mathrm{GeV}^2 \le Q^2_{min}$	2.8	$1.0 \cdot 10^1$
KMR, $Q^2_\perp = \min(Q^2_{0\perp}, q^2_\perp), 0.8\mathrm{GeV}^2 \le Q^2_{min}$	1.25	2.9
PST skewed gluon	σ_{tot} [nb]	-
PST, GBW	1.9	-
PST, RS	4.1	

minimum option (Eq. (5.12), KMR-min) and another time employing the BPSS option Eq. (5.13) and using $\mathcal{F}^{off}_{\mathrm{CDHI}}$ (see Eq. (5.14)). The results for χ_{c0} and η_c are completely different. We found one maximum in the middle of the χ_{c0} distribution, which can be related to the back-to-back kinematic situation, whereas in η_c distribution, two maxima can be found. The exact positions of the maxima clearly depend on the choice of the skewed gluon. In this context, experimental verification of the model would be appreciated. Moreover, in the $pp \to p\eta_c p$ process, the distribution at $\phi = \{0°, 180°, 360°\}$ vanishes.

Supplemental figures to our analysis are distributions in four-momenta squared transferred in the proton lines. In Fig. 5.6, we present two dimensional distributions founded for the KMR off-diagonal gluon with the Durham minimum prescription $(Q^2_\perp = \min(q^2_\perp, Q^2_{0\perp}))$ in the left histogram and in the right histogram the KMR
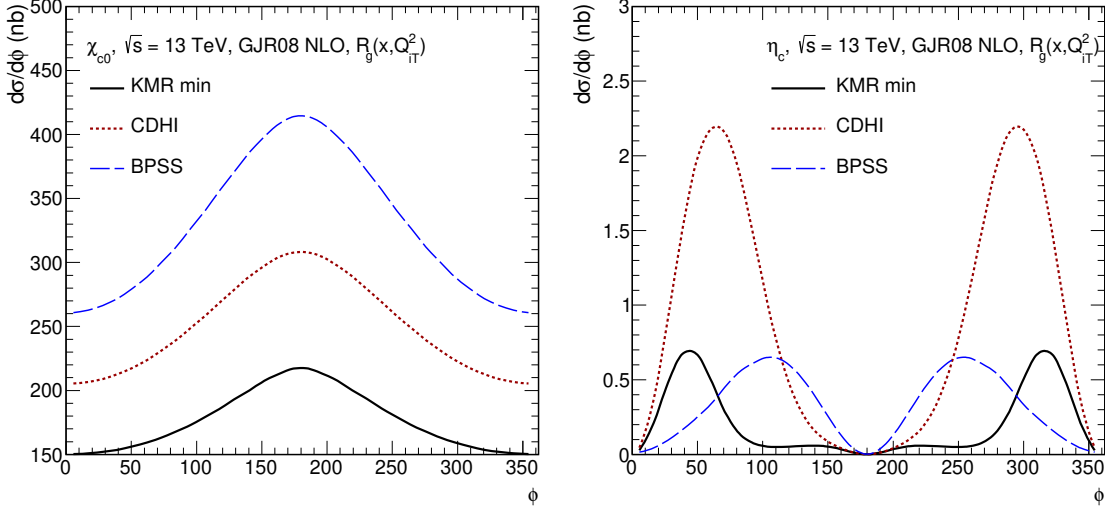
Figure 5.5: Distribution in relative angle ϕ of out-going intact protons at $\sqrt{s} = 13$ TeV including skewedness corrections. In the left panel for the reaction $pp \to p\,\chi_{c0}\,p$, while in the right panel for $pp \to p\eta_c p$. No absorption corrections are included.

off-diagonal gluon with the BPSS prescription $\left(Q_\perp^2 = \sqrt{q_\perp^2, Q_{0\perp}^2}\right)$ for χ_{c0}. The left histogram in Fig. 5.7 represents result for the CDHI off-diagonal gluon and the right the two-dimensional plot presents distribution for the PST off-diagonal prescription with GBW diagonal gluon distribution as an input. The shapes of the obtained results are discernible stable under the change of the off-diagonal model. For clarity, no absorption corrections are considered here.

In Fig. 5.8 and Fig. 5.9, we illustrate similar results for η_c CEP process. The only result obtained from the BPSS prescription has different shape than another variant of skewed gluons. Note that χ_{c0} histograms differ in the pattern in comparison to η_c.
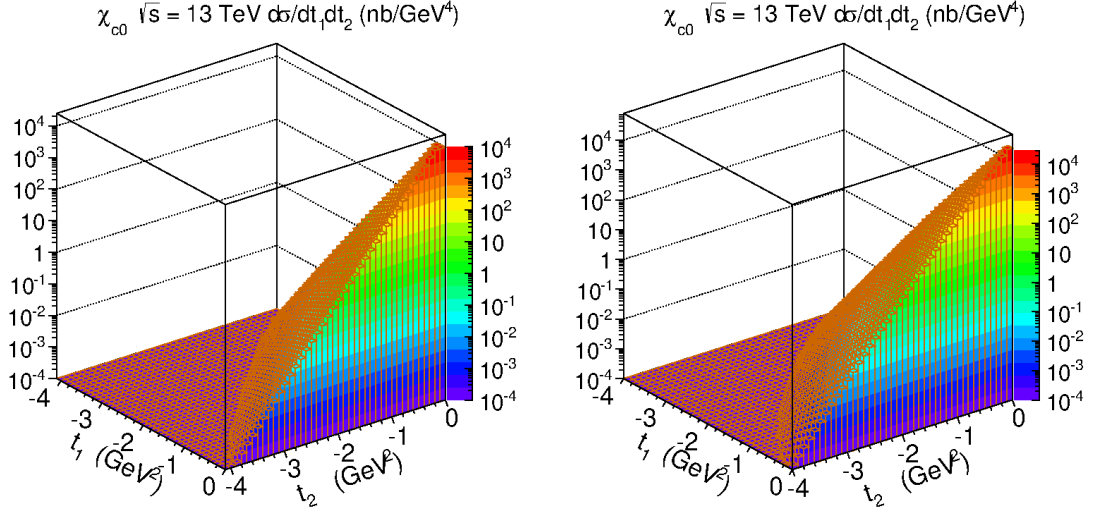
Figure 5.6: Distribution in $t_1 \times t_2$ for the Durham minimum prescription (left plot) and the BPSS geometrical average prescription (right plot) calculated with the GJR08NLO gluon distribution function for χ_{c0} for $\sqrt{s} = 13\,\text{TeV}$. No absorption corrections are included.
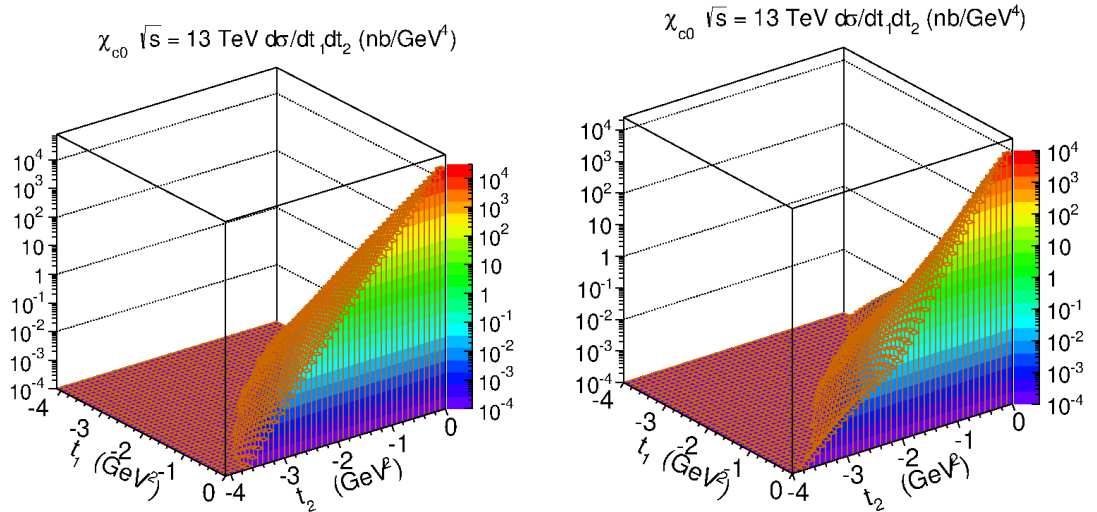
Figure 5.7: Distribution in $t_1 \times t_2$ for the CDHI prescriptions (left plot) calculated with the GJR08NLO gluon distribution function and for the PST off-diagonal UGD computed with the diagonal GBW UGD (right plot) for χ_{c0} for $\sqrt{s} = 13\,\text{TeV}$. No absorption corrections are included.
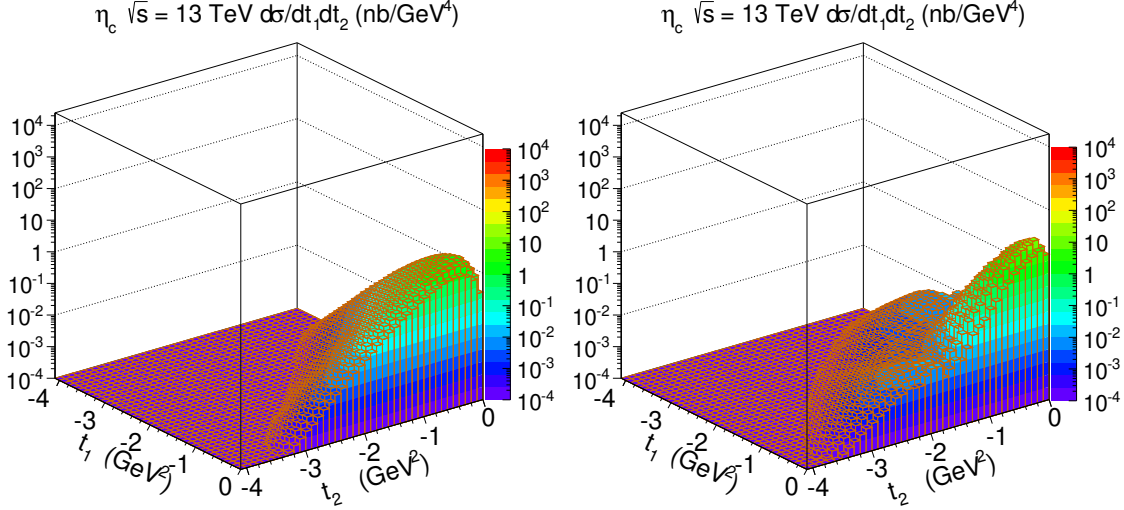
Figure 5.8: Distribution in $t_1 \times t_2$ for the Durham minimum prescription (left plot) and the BPSS geometric average prescription (right plot) with the GJR08NLO gluon distribution function for η_c CEP for $\sqrt{s} = 13$ TeV. No absorption corrections are included.
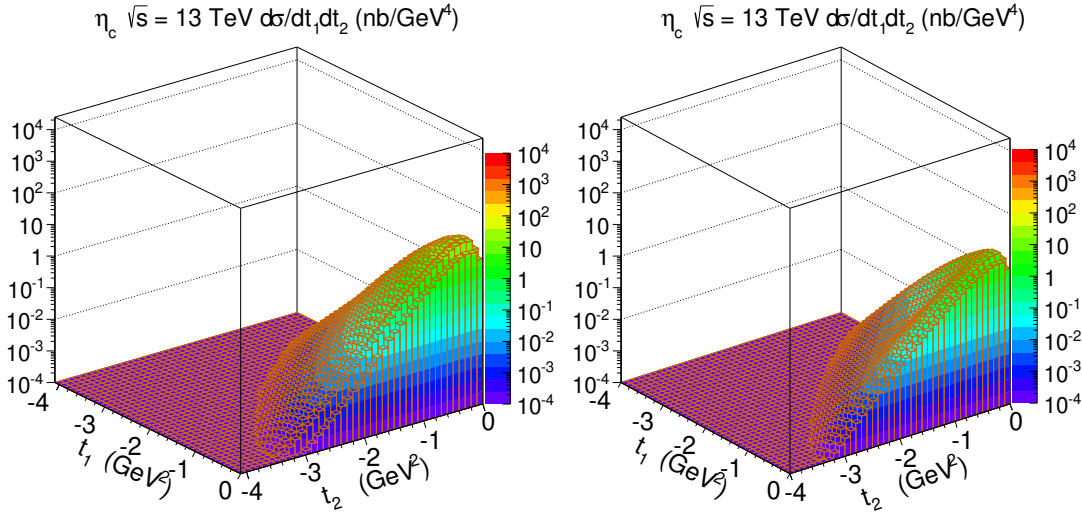
Figure 5.9: Distribution in $t_1 \times t_2$ for the CDHI with the GJR08NLO gluon distribution function (left plot)and for the PST off-diagonal UGD computed with the diagonal GBW UGD (right plot) for η_c CEP for $\sqrt{s} = 13$ TeV. No absorption corrections are included.

5.2.1   Absorptive correction

Central exclusive processes involved hadrons or ions are exposed to absorptive corrections, also known as survival probability or re-scattering effects. The majority of reactions, which populate the gaps or change the shape of the exclusive distribution, originate from the spectator partons of the colliding hadron/ions [159]. This issue is still under consideration and challenges perturbative QCD physics. The wealthy literature exists with a variety of approaches. Some theoretical groups relate the gap survival probability to the influence of the multiparton interactions on the final state [160, 16]. Within this approach it was possible to investigate dependence of the gap survival factors on different kinematic variables. If the rapidity gap survival probability is only a constant factor dependent on the c.m.s. energy. Another concept is based on soft multi-$I\!P$ exchanges [161, 162, 163]. While another way to incorporate absorptive effect is to compute absorptive corrections dynamically at the scattering amplitude level in the dipole picture [145, 146, 142] or the Born term with absorptive correction in the amplitude [164, 165].

To estimate the effect of absorptive corrections, it is convenient to introduce quantum-mechanical picture at the amplitude level, where absorption has simple interpretation.
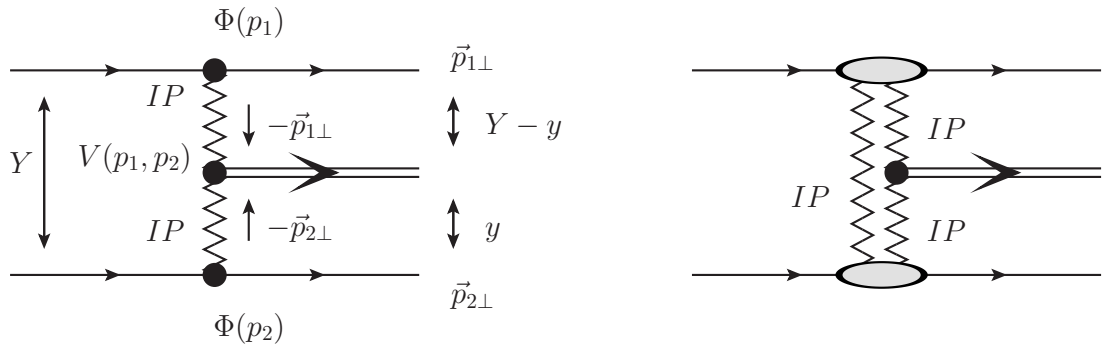
Figure 5.10: The scheme of the absorption to Born level amplitude with specific kinematics.

Regarding the so-called *elastic re-scattering* case the amplitude takes the form

$$\mathcal{A}(Y, y, \vec{p}_{1\perp}, \vec{p}_{2\perp}) = \mathcal{A}^{(0)}(Y, y, \vec{p}_{1\perp}, \vec{p}_{2\perp}) - \delta\mathcal{A}(Y, y, \vec{p}_{1\perp}, \vec{p}_{2\perp}), \qquad (5.19)$$

5. CENTRAL EXCLUSIVE PRODUCTION OF C-EVEN CHARMONIA: THE CASE OF $\eta_C(1S)$ AND $\chi_{C0}(1P)$

where $\vec{p}_{1\perp}$, $\vec{p}_{2\perp}$ are the transverse momenta of outgoing protons, see 5.10 and the rapidity difference between the incoming proton beams is $Y = \log(s/m_p^2)$ at c.m.s.-energy $\sqrt{s}$ and the cm-rapidity of the produced meson χ_{c0}, $J^{PC} = 0^{++}$ or η_c, $J^{PC} = 0^{-+}$ is denoted as y.

The Born term of the amplitude (Eq. 5.19) in a double-Regge scheme can be formulated as follows

$$\mathcal{A}^{(0)}(Y, y, \vec{p}_{1\perp}, \vec{p}_{2\perp}) = is \, \Phi_1(\vec{p}_{1\perp}) \, R_{\mathbb{P}}(Y - y, \vec{p}_{1\perp}{}^2)$$
$$\times V(\vec{p}_{1\perp}, \vec{p}_{2\perp}) \, R_{\mathbb{P}}(y, \vec{p}_{2\perp}{}^2) \, \Phi_2(\vec{p}_{2\perp}), \quad (5.20)$$

where $V(\vec{p}_{1\perp}, \vec{p}_{2\perp})$ is the $\mathbb{P}\mathbb{P} \to \mathcal{Q}$ vertex and $R_{\mathbb{P}}(y, \vec{p}_\perp^2)$ stands for the Pomeron Regge-propagator and for definiteness, we assume that

$$\Phi_{1,2}(\vec{p}_{1,2\perp}) = \Phi_{1,2}(0) \exp\left(-\tfrac{1}{2} B_D \, \vec{p}_{,2\perp}{}^2\right), \quad (5.21)$$

without loss of further generality we can take $\Phi_{1,2}(0) = 1$. The absorptive correction term is found as

$$\delta\mathcal{A}(Y, y, \vec{p}_{1\perp}, \vec{p}_{2\perp}) = \int \frac{d^2\vec{k}_\perp}{2(2\pi)^2} \, T(s, \vec{k}_\perp) \mathcal{A}^{(0)}(Y, y, \vec{p}_{1\perp} + \vec{k}_\perp, \vec{p}_{2\perp} - \vec{k}_\perp), \quad (5.22)$$

with the elastic ansatz $T(s, \vec{k}_\perp) = \sigma_{\text{tot}}^{pp}(s) \exp\left(-\tfrac{1}{2} B_{\text{el}}(s)\vec{k}_\perp^2\right)$. As an elastic $pp \to pp$ integrated cross-section we adopt $\sigma_{\text{tot}}^{pp} = (110.6 \pm 3.4)\,\text{mb}$ and the nuclear slope is taken to be $B_{\text{el}} = (20.36 \pm 0.19)\,\text{GeV}^{-2}$, which are values founded experimentally in Ref. [166] at $\sqrt{s} = 13\,\text{TeV}$. The $\mathbb{P}\mathbb{P}$ fusion vertex to $\mathcal{Q}$, in the case spinless meson $\mathcal{Q}$, can be expanded in Fourier series:

$$V(\vec{p}_{1\perp}, \vec{p}_{2\perp}) = V_0(\vec{p}_{1\perp}{}^2, \vec{p}_{2\perp}{}^2) + \sum_{n \geq 1} \left(V_n^+(\vec{p}_{1\perp}{}^2, \vec{p}_{2\perp}{}^2)\cos(n\phi)\right.$$
$$\left. + V_n^-(\vec{p}_{1\perp}{}^2, \vec{p}_{2\perp}{}^2)\sin(n\phi)\right). \quad (5.23)$$

Note that for the scalar meson 0^{++} all terms containing $\sin(n\phi)$ do vanish, while for the pseudoscalar 0^{+-} terms with $\cos(n\phi)$ and V_0 do not contribute. Let us keep only the first terms up to $n = 1$. Therefore, a useful first ansatz could be:

$$\text{scalar } 0^{++}: \quad V^+(\vec{p}_{1\perp}, \vec{p}_{2\perp}) = V_0 + V_1^+ (\vec{p}_{1\perp} \cdot \vec{p}_{2\perp})$$
$$= V_0\left(1 + \tau B_D(\vec{p}_{1\perp} \cdot \vec{p}_{2\perp})\right) \quad \text{with} \quad \tau \equiv \frac{V_1^+}{B_D V_0} \quad (5.24)$$

$$\text{pseudoscalar } 0^{+-} : \qquad V^-(\vec{p}_{1\perp}, \vec{p}_{2\perp}) = V_1^- \cdot [\vec{p}_{1\perp}, \vec{p}_{2\perp}] . \qquad (5.25)$$

To simplify the problem further, let us focus on the central rapidity region, in particular at the fixed point for meson rapidity $y = 0$ and recapitulate the normalization of our amplitude

$$d\sigma = \frac{1}{256\pi^5 s^2} |\mathcal{A}(Y, y, \vec{p}_{1\perp}, \vec{p}_{2\perp})|^2 dy d^2\vec{p}_{1\perp} d^2\vec{p}_{2\perp} d^2\vec{p}_\perp \, \delta^{(2)}(\vec{p}_\perp + \vec{p}_{1\perp} + \vec{p}_{2\perp}) . \quad (5.26)$$

Subsequently, with the help of the vertices in Eq. (5.25), the differential distribution in transverse momentum of the mesons at the Born level can be parameterized as follows

$$
\frac{d\sigma_{\text{Born}}^{0+}}{dy dp_\perp^2}\bigg|_{y=0} = \frac{\exp[-\frac{1}{2} B_D p_\perp^2] V_0^2}{512\pi^3 B_D} \Big\{ 1 - \tau(1 - \tfrac{1}{2} B_D p_\perp^2) \qquad (5.27)
$$

$$
+ \frac{\tau^2}{2}\Big(1 - \tfrac{1}{2} B_D p_\perp^2 + \frac{1}{8} B_D^2 p_\perp^4 \Big) \Big\}
$$

$$
\frac{d\sigma_{\text{Born}}^{0-}}{dy dp_\perp^2}\bigg|_{y=0} = \frac{(V_1^-)^2}{512\pi^3} \frac{p_\perp^2}{4 B_D^2} \exp[-\tfrac{1}{2} B_D p_\perp^2] . \qquad (5.28)
$$

The calculation of the absorption correction needs some loop integral evaluation

$$
\delta\mathcal{A}(Y, 0, \vec{p}_{1\perp}, \vec{p}_{2\perp}) = \int \frac{d^2\vec{k}_\perp}{2(2\pi)^2} T(s, \vec{k}_\perp) \exp\Big(-\tfrac{1}{2} B_D(\vec{p}_{1\perp} + \vec{k}_\perp)^2 \Big)
$$

$$
\times \exp\Big(-\tfrac{1}{2} B_D(\vec{p}_{2\perp} - \vec{k}_\perp)^2 \Big) V(\vec{p}_{1\perp} + \vec{k}_\perp, \vec{p}_{2\perp} - \vec{k}_\perp)
$$

$$
= \exp\Big(-\tfrac{1}{2} B_D(\vec{p}_{1\perp}^2 + \vec{p}_{2\perp}^2) \Big) \times \int \frac{d^2\vec{k}_\perp}{2(2\pi)^2} \exp\Big(-\tfrac{1}{2}(B_{\text{el}}(s) + 2 B_D)\vec{k}_\perp^2 \Big)
$$

$$
\times \exp\Big(-B_D \vec{k}_\perp \cdot (\vec{p}_{1\perp} - \vec{p}_{2\perp}) \Big) \sigma_{\text{tot}}^{pp}(s) \, V(\vec{p}_{1\perp} + \vec{k}_\perp, \vec{p}_{2\perp} - \vec{k}_\perp) . \quad (5.29)
$$

The following dimensionless quantities control the strength of absorptive corrections and are collected in Tab. 5.3 Tab. 5.4 for χ_{c0} and η_c, respectively:

$$
g_{\text{abs}} = \frac{\sigma_{\text{tot}}^{pp}(s)}{4\pi(B_{\text{el}}(s) + 2 B_D)} \quad \text{and} \quad \beta = \frac{B_D}{B_{\text{el}}(s) + 2 B_D} . \qquad (5.30)
$$

Finally, the absorptive corrections are obtained through formulas below

$$
\delta\mathcal{A}^{0+}(Y, 0, \vec{p}_{1\perp}, \vec{p}_{2\perp}) = g_{\text{abs}} V_0 \exp\Big(-\tfrac{1}{2} B_D(\vec{p}_{1\perp}^2 + \vec{p}_{2\perp}^2) \Big) \exp\Big(\frac{1}{2}\beta B_D(\vec{p}_{1\perp} - \vec{p}_{2\perp})^2 \Big)
$$

$$
\times \Big\{ 1 + \beta(1 + \beta)\tau B_D(\vec{p}_{1\perp}^2 + \vec{p}_{2\perp}^2) + (\vec{p}_{1\perp} \cdot \vec{p}_{2\perp})\tau B_D\Big(1 - 2\beta(1 + \beta) \Big) \Big\}, \quad (5.31)
$$

5. CENTRAL EXCLUSIVE PRODUCTION OF C-EVEN CHARMONIA: THE CASE OF $\eta_C(1S)$ AND $\chi_{C0}(1P)$

Table 5.3: V_0 and τ at midrapidity of χ_{c0}, for several prescriptions for off-diagonal UGDs.

χ_{c0}	V_0^+ $[\sqrt{\text{nb}}/\text{GeV}^2]$	τ	B_D $[\text{GeV}^{-2}]$	g_{abs}	β	$\sigma_{\text{tot}}\|_{y=0}$ [nb]	$\sigma_{\text{tot}}^{\text{abs}}\|_{y=0}$ [nb]	$S^2_{y=0}$
KMR	-2167	-0.11	4.5	0.77	0.15	29	3.7	0.13
BPSS	-3118	-0.135	4.5	0.77	0.15	61	8.0	0.13
CDHI	-2985	-0.135	4.5	0.76	0.15	42	7.5	0.18
GBW	-2062	-0.31	5.7	0.71	0.18	17	3.7	0.21
RS	-2381	-0.28	5.9	0.70	0.18	21	4.5	0.21

Table 5.4: An example of V_1 values at midrapidity of η_c in the CEP process, for several prescriptions for off-diagonal UGDs.

η_c	V_1^- $[\sqrt{\text{nb}}/\text{GeV}^4]$	B_D $[\text{GeV}^{-2}]$	g_{abs}	β	$\sigma_{\text{tot}}\|_{y=0}$ [nb]	$\sigma_{\text{tot}}^{\text{abs}}\|_{y=0}$ [nb]	$S^2_{y=0}$
KMR	1015.	4.7	0.76	0.16	1.3×10^{-1}	3.0×10^{-2}	0.29
BPSS	1490.	7.0	0.66	0.20	5.8×10^{-2}	2.2×10^{-2}	0.38
CDHI	651.	3.5	0.81	0.13	1.8×10^{-1}	4.0×10^{-2}	0.22
GBW	194.	3.4	0.83	0.12	1.8×10^{-2}	3.9×10^{-3}	0.21
RS	400.	3.2	0.84	0.12	9.0×10^{-3}	1.9×10^{-3}	0.21

$$\delta\mathcal{A}^{0-}(Y,0,\vec{p}_{1\perp},\vec{p}_{2\perp}) = (1-\beta)g_{\text{abs}}V_1^- \exp\left(-\tfrac{1}{2}B_D(\vec{p}_{1\perp}^2 + \vec{p}_{2\perp}^2)\right)$$

$$\times \exp\left(\tfrac{1}{2}\beta B_D(\vec{p}_{1\perp} - \vec{p}_{2\perp})^2\right) \times [\vec{p}_{1\perp}, \vec{p}_{2\perp}](1-\beta)\left(1 - \beta B_D(\vec{p}_{1\perp} \cdot \vec{p}_{2\perp})\right). \quad (5.32)$$

In Tab. 5.3 and Tab. 5.4 we show the fitted parameters to our Born level cross-section V_0, V_1, B_D and on this base we construct amplitude with incorporated absorption $\delta\mathcal{A}^{0+}$ or $\delta\mathcal{A}^{0-}$. Further the gap survival probability is defined as

$$S^2 \equiv \frac{d\sigma/dy\Big|_{y=0}}{d\sigma_{\text{Born}}/dy\Big|_{y=0}}. \quad (5.33)$$

We observe that the gap survival probability in the case of $\chi_c(0)$ is placed in the range $13\% - 21\%$, whereas for η_c we found $21\% - 38\%$, depending on the off-diagonal gluon treatment.

In this analysis, we focus only on the elastic re-scattering effect. The commonly used multichannel models encoded eventual diffractively initiated interme-

diate states are designed for purely soft diffraction. In the process, which we put under consideration, we faced semi-hard gluon exchanges, see Fig. 5.1.

5.3   Remarks and outlook

Now, we can assemble our results obtained from inclusive prompt production in proton-proton collision with centrally exclusively produced χ_{c0} (1P) and η_c (1S). Due to the fact that η_c is a pseudoscalar meson, we expect that exclusive production is suppressed according to J_z^{PC} selection rule in the strictly forward limit.

In Fig. 5.11, we reveal the rapidity differential cross sections for the previously discussed off-diagonal gluons inspired by the dipole approach and the ones based on the Durham model. The findings for χ_c (on the l.h.s.) and η_c (on the r.h.s) CEP are contrasted to inclusively produced mesons obtained in the $k_\perp$-factorization approach. In the η_c case, we observe that distribution obtained through the PST prescription, which encodes dipole gluon model (GBW or RS), has a similar pattern as inclusive production.
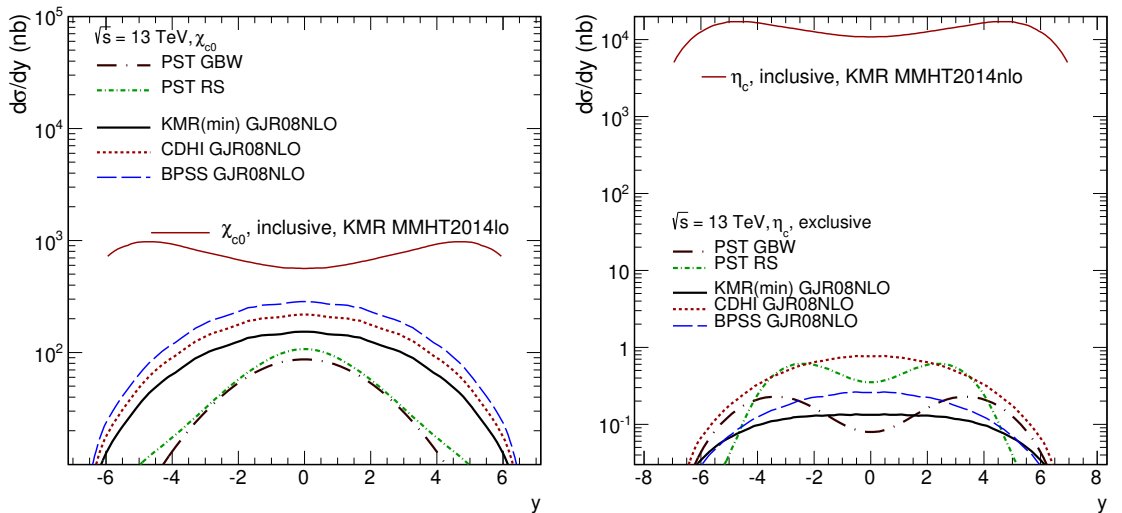
Figure 5.11: Comparison of the distribution from inclusive prompt and exclusive central reaction without absorption correction. The gap survival probability is not incorporated.

A measurement of the cross-section of $pp \rightarrow p\,\eta_c\,p$ would be of great value to check our approach. Here we did not consider other possible "almost exclusive"

channels of production such as $\gamma\mathbb{P} \to J/\psi \to \eta_c\gamma$ with an unregistered soft photon in the final state. Rough order of magnitude estimates suggests that this process is small. A more substantial contribution could come from the $\gamma\gamma \to \eta_c$ process in pp collisions.

It would be interesting to evaluate signal to background ratio in the context of future experiments. Recently, Lebiedowicz et al. [167] have computed the $pp \to ppp\bar{p}$ continuum production. Moreover, the STAR research group at the Relativistic Heavy Ion Collider has found the first evidence [134] of exclusively produced $p\bar{p}$ pairs. The reaction involving photons $pp \to pp\gamma\gamma$ in the final state could be more noteworthy in the context of measuring exclusively produced η_c.

Chapter 6

Summary and Outlook

The physics behind the production of quarkonia is still regarded to have many open problems. Therefore, we put under investigation several charmonium and bottomonium production mechanisms induced by gluons or photons. We have specified the reactions and kinematic regions, where the discussed mechanisms could make a significant contribution.

In the beginning, we have studied the additional gluon emission associated to $\chi_{cJ}\chi_{cJ}$ pair production. For instance, this process is relevant in the context of $J/\psi J/\psi$ pair production as one of feed down mechanisms. However, an extra gluon emission as a leading jet is also one of the proposed processes to be observed at the LHC and is interesting by itself. We have found that in the collinear approach at leading order the $gg \to \chi_{cJ}\chi_{cJ}$ process results in smaller cross-sections than the ones obtained from the $k_\perp$-factorization approach. We expect that the inclusion of two real gluon contributions in collinear approximation will lead to enhancement of the distributions, especially in the case of $\chi_{c1}\chi_{c1}$ production. Another conclusion arising from this analysis, which affects our further research plans, is that in the applied color singlet approximation of the NRQCD model the results crucially depend on the radial part of the wave functions or their derivatives at the origin. These phenomenological parameters can be obtained in two ways: either through their relation to radiative decay rate or through phenomenological potential models of $Q\bar{Q}$ interactions suited to describe the meson mass spectra.

In the $k_\perp$-factorization approach a crucial element are the so-called off-shell matrix elements, What now, if we decompose matrix elements into transition form factors and investigate the situation, where the whole structure of the wave function takes part in the composition of these form factors? In particular, we have

paid attention to space-like transition form factors induced by photons and their relation to gluon-gluon-meson transition form factors at the lowest perturbative order. We have derived a master formula for the transition form factors in terms of light-cone wave function of the pseudoscalar mesons $\eta_c(1S)$, $\eta_c(2S)$ as well scalar χ_{c0}, χ_{b0}. Additionally, in the case of η_c, we have studied the relation to the so-called decay constant f_{η_c} and distributions amplitudes. We have found that all considered potential models' results agree with the experimental value within the error range.

We have performed a thorough analysis of the form factors with our adopted color singlet approach and compared our results with a computation in the strict non-relativistic limit.

For each potential model of $Q\bar{Q}$ interaction, we have computed values of the transverse form factor at the on-shell point $F_{TT}(0,0)$, the radiative decay rate and the corresponding radial part of the wave at the origin or their first derivative. We have compared the normalized light-cone transition $\gamma^*\gamma \to \eta_c(1S)$ form factor $F_{TT}(Q^2,0)/F_{TT}(0,0)$ with current BABAR data with a rather satisfactory agreement for the power-like and oscillator potential model. We have presented the predicted shapes of the $F_{TT}(Q^2,0)/F_{TT}(0,0)$ for χ_{c0} and χ_{b0}. Our results differ in shapes according to the applied potential model. We have noticed that a crucial parameter in the light-cone form factor is the employed quark mass. We have collected three results: for η_c, χ_{c0} and χ_{b0}. The normalized form factor $F_{TT}(Q^2,0)/F_{TT}(0,0)$ in the case of χ_{b0} turned out to have almost linear behaviour as a Q^2 function. This feature can be related to the non-relativistic nature of the $b\bar{b}$ bound state.

In addition, we have analyzed the distribution amplitudes in the case of $\eta_c(1S)$ and $\eta_c(2S)$. We have observed the expected symmetry under exchange $z \leftrightarrow (1-z)$ and have studied the dependence of the DA on the light-cone wave function. We have found that the so-called Brodsky-Lepage limit of $Q^2F(Q^2,0)$ is unattainable in our approach at virtualities $Q^2 \sim 400\,\text{GeV}^2$.

We have then proposed to apply our light-cone form factors to hadron-hadron scattering in $k_\perp$-factorization approach. We have examined four sets of unintegrated gluon distribution functions: KMR/KMRW MMHT2014NLO, JH2013 set2, as well as K.Kutak's solutions of linear and non-linear small-x evolution equations. In particular, we have taken under investigation the asymmetric "forward" kinematical region $2.5 < y_Q < 4$ and $p_T > 6.5\,\text{GeV}$ of the produced meson. We have shown that the fusing gluons are well separated in the carried proton longitudinal momentum fraction x_1 and x_2. In the case of the $\eta_c(1S)$ prompt hadronic production, we have

found relatively good agreement with experimental data at $\sqrt{s} = 7\,\text{TeV}$ and $\sqrt{s} = 8\,\text{TeV}$ center of mass energy. However, at $\sqrt{s} = 13\,\text{TeV}$ our predictions undershoot the data.

In chapter 5, we have investigated the central exclusive production mechanism of charmonium in which our adopted color-singlet vertex could find another justified application. We have found that the exclusively produced $\eta_c(1S)$ is dramatically suppressed in comparison to inclusive production. We have also estimated and discussed the effect of the absorptive corrections, which we found to be about $13\% - 21\%$ for χ_{c0} production and $21\% - 38\%$ in the case of $\eta_c(1S)$ production.

Our master formula 3.60 derived in this thesis is presented in an universal form and can be treated as a tool to investigate heavy $Q\bar{Q}$ bound states. It is in fact valid for C-even states of any spin. In this thesis, we have considered transitions $\gamma^*\gamma^*$ into scalar and pseudoscalar mesons. Our master formula can likewise be used to obtain the three, respectively five independent form factors for spin-1 and spin-2 mesons.

In our approach, we have applied the light-cone wave function constructed on the basis of solutions of the Schrödinger equation. We have used the Terentev prescription to transition to the light-cone wave functions. Nevertheless, the light-cone wave function can also be directly found as a solution of a light-cone Hamiltonian [168] or deriving an effective Hamiltonian problem [169] using renormalization group methods. It would be interesting to study the impact of these recent developments in the future.

It would be an intriguing perspective in the context of the Belle II experiment to search the transition form factors in terms of the photon virtualities Q_1^2, Q_2^2. It would be interesting to study also the transition form factors of the light mesons such as η or ρ.

Appendix A

The radial part of the wave function as a solution of the Schrödinger equation

A.1 Radial WF in configuration and momentum space

Here we briefly summarize some main facts about the potential model description of Quarkonia. Some more details can be found in the appendix of Ref. [170]).

The Schrödinger equation is solved in the bound state rest frame.

We assume that the potential is central, i.e. it only depends on the distance $r = |\vec{r}|$ between quark and antiquark:

$$\left(\frac{\vec{p}^2}{2\mu} + V(r) \right) |E, nlm\rangle \;=\; E |E, nlm\rangle. \tag{A.1}$$

Here $\mu = m_Q/2$ is the reduced mass, m_Q is the mass of the quark, and we denote by n the principal quantum number, and l, m the standard angular momentum quantum numbers. The wave function (WF) in configuration space decomposes into a radial

A. THE RADIAL PART OF THE WAVE FUNCTION AS A SOLUTION OF THE SCHRÖDINGER EQUATION

and angular momentum part:

$$\langle \vec{r} | E, nlm \rangle = \Psi_{nlm}(\vec{r}) = R_{nl}(r) Y_{lm}(\hat{r}) = \frac{u_{nl}(r)}{r} Y_{lm}(\hat{r}), \tag{A.2}$$

with $\hat{r} = \vec{r}/r$ and the well-known spherical harmonics $Y_{lm}(\hat{r})$, see for example a textbook on quantum mechanics, like [171].

After the standard separation of angular and radial variables, the Schrödinger equation for the radial WF reads

$$\frac{\partial^2 u_{nl}(r)}{\partial r^2} = \left(V_{\text{eff}}(r) - \varepsilon \right) u_{nl}(r), \tag{A.3}$$

with

$$V_{\text{eff}}(r) = m_Q V(r) + \frac{l(l+1)}{r^2}, \qquad \varepsilon = m_Q E. \tag{A.4}$$

The WF is normalized as

$$\int d^3 \vec{r} \left| \Psi_{nlm}(\vec{r}) \right|^2 = 1, \tag{A.5}$$

so that

$$\int_0^\infty r^2 dr R_{nl}^2(r) = \int_0^\infty dr u_{nl}^2(r) = 1. \tag{A.6}$$

The momentum space wave function can also be decomposed into "radial" and angular part

$$\langle \vec{p} | E, nlm \rangle = \Psi_{nlm}(\vec{p}) = \phi_{nl}(p) Y_{lm}(\hat{p}) = \frac{u_{nl}(p)}{p} Y_{lm}(\hat{p}). \tag{A.7}$$

It can be obtained by the Fourier-transform

$$\Psi_{nlm}(\vec{p}) = \int d^3 \vec{r} \langle \vec{p} | \vec{r} \rangle \langle \vec{r} | E, nlm \rangle = \int \frac{d^3 \vec{r}}{(2\pi)^{3/2}} \exp(-i \vec{p} \vec{r}) \Psi_{nlm}(\vec{r}). \tag{A.8}$$

and is normalized as

$$\int d^3 \vec{p} \left| \Psi_{nlm}(\vec{p}) \right|^2 = 1, \tag{A.9}$$

Let us calculate the Fourier-transform, to obtain ϕ_{nl} in terms of R_{nl}. To this end, we use the decomposition

$$
\begin{aligned}
\exp(-i\vec{p}\vec{r}) &= \sum_l i^l (2l+1) j_l(pr) P_l(\hat{p}\hat{r}) \\
&= 4\pi \sum_l \sum_{m=-l}^{l} i^l j_l(pr) Y_{lm}(\hat{p}) Y_{lm}^*(\hat{r}).
\end{aligned}
\tag{A.10}
$$

Then we get

$$
\phi_{nl}(p) = \frac{4\pi i^l}{(2\pi)^{3/2}} \int_0^\infty r^2 dr\, j_l(pr) R_{nl}(r) = i^l \sqrt{\frac{2}{\pi}} \int_0^\infty r^2 dr\, j_l(pr) R_{nl}(r)\,, \tag{A.11}
$$

or, equivalently

$$
u_{nl}(p) = i^l \sqrt{\frac{2}{\pi}} \int_0^\infty dr\, pr\, j_l(pr)\, u_{nl}(r)\,. \tag{A.12}
$$

In our calculations we often need the radial wave function at the origin (for s-wave states), or its first derivative at the origin (for p-wave states). Let us express the radial WF at the origin (or its derivative) as an integral over the momentum-space WF. The inverse relation to Eq. (A.11) is

$$
R_{nl}(r) = i^l \sqrt{\frac{2}{\pi}} \int_0^\infty p^2 dp\, j_l(pr) \phi_{nl}(p). \tag{A.13}
$$

For the $S-wave$ state, $l=0$, we obtain then, using

$$
j_0(x) = \frac{\sin x}{x}, j_0(0) = 1\,, \tag{A.14}
$$

the expression for the radial WF at the origin

$$
R_{n0}(0) = \sqrt{\frac{2}{\pi}} \int_0^\infty p^2 dp\, \phi_{n0}(p) = \sqrt{\frac{2}{\pi}} \int_0^\infty p dp\, u_{n0}(p). \tag{A.15}
$$

For the derivative of the radial WF at the origin, we get

$$
\frac{\partial R_{nl}(r)}{\partial r} = i^l \sqrt{\frac{2}{\pi}} \int_0^\infty p^3 dp\, j_l'(pr) \phi_{nl}(p). \tag{A.16}
$$

For the $P-wave$, the derivative of the radial WF at the origin is nonvanishing and can be written as:

$$
\left. \frac{\partial R_{n1}(r)}{\partial r} \right|_{r=0} = i\sqrt{\frac{2}{\pi}}\frac{1}{3} \int_0^\infty dp\, p^3 \phi_{n1}(p) = i\sqrt{\frac{2}{\pi}}\frac{1}{3} \int_0^\infty dp\, p^2 u_{n1}(p)\,. \tag{A.17}
$$

A. THE RADIAL PART OF THE WAVE FUNCTION AS A SOLUTION OF THE SCHRÖDINGER EQUATION

A.2 Models for the $Q\bar{Q}$-potential

Here, several models for the interaction $Q\bar{Q}$ potential, $V(r)$ chosen for our analysis are described.

- Harmonic oscillator[1]:

$$V(r) = \frac{1}{4} m_Q \omega^2 r^2 , \tag{A.18}$$

  where for charmonia it was taken $\omega = 0.42 \, \text{GeV}$, $m_c = 1.4 \, \text{GeV}$, and bottomonia $\omega = 0.396 \, \text{GeV}$, $m_b = 4.2 \, \text{GeV}$. An analytic solution of the the Schrödinger equation (A.3) has straightforward form for the $1S$ state

$$u(r) = \frac{2a^{3/2}}{\pi^{1/4}} r \exp\left[-\frac{1}{2} a^2 r^2\right] , \tag{A.19}$$

  here $a = \sqrt{(m_Q/2)\omega}$ and for the $1P$ state

$$u(r) = r \, a \sqrt{\frac{2}{3}} \frac{2a^{3/2}}{\pi^{1/4}} r \exp\left[-\frac{1}{2} a^2 r^2\right] , \tag{A.20}$$

  which is a Gaussian-like shape of the wave function.

- Cornell potential [172, 173, 174]:

$$V(r) = -\frac{k}{r} + \frac{r}{a^2} , \quad k = 0.52 , \quad a = 2.34 \, \text{GeV}^{-1} , \tag{A.21}$$

  the charm and the beauty quark mass is fixed respectively to $m_c = 1.84$ GeV and $m_b = 5.17$ GeV.

- Logarithmic potential [175]:

$$V(r) = -0.6635 \, \text{GeV} + (0.733 \, \text{GeV}) \log(r \cdot 1 \, \text{GeV}) , \tag{A.22}$$

  with $m_c = 1.5$ GeV and $m_b = 5.0$ GeV.

- Effective power-law potential [176, 177]:

$$V(r) = -6.41 \, \text{GeV} + (6.08 \, \text{GeV}) (r \cdot 1 \, \text{GeV})^{0.106} , \tag{A.23}$$

  adopted $m_c = 1.334$ GeV [178].

---

[1]Here we correct typo in Ref. [7].

- Buchmüller-Tye (BT) potential [179]:

$$
V(r) = \begin{cases} \frac{k}{r} - \frac{8\pi}{27} \frac{v(\lambda r)}{r} \,, & r \geq 0.01 \, \text{fm} \\ -\frac{16\pi}{25} \frac{1}{r \ln w(r)} \left(1 + 2\left(\gamma_E + \frac{53}{75}\right) \frac{1}{\ln w(r)} - \frac{462}{625} \frac{\ln \ln w(r)}{\ln w(r)} \right), & r < 0.01 \, \text{fm} \,, \end{cases}
\tag{A.24}
$$

where the Euler constant is $\gamma_E = 0.5772$, while the function $v(x)$ is known numerically from Ref. [179]. The remaining constants are taken as

$$
w(r) = \frac{1}{\lambda_{\text{MS}}^2 \, r^2} \,, \quad \lambda_{\text{MS}} = 0.509 \, \text{GeV} \,, \quad k = 0.153 \, \text{GeV}^2 \,, \quad \lambda = 0.406 \, \text{GeV} \,.
\tag{A.25}
$$

Here, the charm quark mass is taken as $m_c = 1.48 \, \text{GeV}$ and the beauty quark mass $m_b = 4.87 \, \text{GeV}$. The characteristic feature of BT potential is that at r around 0 has behaviour as Coulomb potential, whereas a string-like shape occurs at large r. Moreover, the main difference between the Cornell and the B-T potentials appears at small r.

Appendix B

Canonical and light-cone spinors, the Melosh transformation

B.1 Particle spinors

The positive energy solutions of the free Dirac equations are the spinors (or four-spinors) $u(p, \sigma)$:

$$(\hat{p} - m)\, u(p, \sigma) = 0 \,, \tag{B.1}$$

where $\hat{p} = p^\mu \gamma_\mu$. The four-momentum p_μ fulfills the mass-shell condition

$$p_\mu p^\mu = E^2 - \vec{p}^2 = m^2 \,, \tag{B.2}$$

and σ is a polarization label. The γ-matrices fulfill

$$\{\gamma_\mu, \gamma_\nu\} = \gamma_\mu \gamma_\nu + \gamma_\nu \gamma_\mu = 2 g_{\mu\nu} \,. \tag{B.3}$$

An explicit representation of the 4×4 matrices γ_μ is

$$\gamma_0 = \begin{pmatrix} \mathbb{1} & 0 \\ 0 & -\mathbb{1} \end{pmatrix} \,,\ \gamma_i = \begin{pmatrix} 0 & \sigma_i \\ -\sigma_i & 0 \end{pmatrix} \,, \tag{B.4}$$

with the 2×2 Pauli matrices

$$\sigma_1 = \begin{pmatrix} 0 & 1 \\ 1 & 0 \end{pmatrix} \,,\ \sigma_2 = \begin{pmatrix} 0 & -i \\ i & 0 \end{pmatrix} \,,\ \sigma_3 = \begin{pmatrix} 1 & 0 \\ 0 & -1 \end{pmatrix} \,. \tag{B.5}$$

B. CANONICAL AND LIGHT-CONE SPINORS, THE MELOSH TRANSFORMATION

One often uses spinors of the form

$$u(p,\sigma) = \sqrt{E+m} \begin{pmatrix} \xi_\sigma \\ \dfrac{\vec{\sigma}\vec{p}}{E+m}\xi_\sigma \end{pmatrix}, \tag{B.6}$$

Here ξ_σ is a two-component Pauli-spinor. The polarization label σ take values ± 1, and its significance is the following: in the rest frame of the particle, i.e. for $\vec{p}=0$, the z-projection of the canonical spin operator is $S_z = \sigma/2$.

Different choices of spinors are in use, and can make calculations more transparent. For example in high energy physics it is common to use spinors which are not eigenstates of the canonical spin operator, but of the so-called helicity operator $\vec{\sigma}\vec{p}/|\vec{p}|$. Here we use still another form, which in somesense interpolates between canonical spin states and helicity states. These are the light-cone spinors, which form was given by Lepage and Brodsky in [67]. They read explicitly:

$$u_{LC}(p,\lambda) = \frac{1}{\sqrt{\sqrt{2}p_+}}\left(\sqrt{2}p_+ + \beta m + \vec{\alpha}\cdot\vec{p}_\perp\right)\tilde{u}_\lambda. \tag{B.7}$$

Here $\lambda/2$ is the light-cone helicity, and

$$\beta = \gamma_0 \,, \quad \vec{\alpha} = \beta\vec{\gamma}. \tag{B.8}$$

The momentum-independent basis spinors $\tilde{u}_\lambda, \lambda = \pm 1$, read

$$\tilde{u}_{+1} = \frac{1}{\sqrt{2}}\begin{pmatrix} 1 \\ 0 \\ 1 \\ 0 \end{pmatrix} \,, \quad \tilde{u}_{-1} = \frac{1}{\sqrt{2}}\begin{pmatrix} 0 \\ 1 \\ 0 \\ -1 \end{pmatrix}, \tag{B.9}$$

which can be summarized as

$$\tilde{u}_\lambda = \begin{pmatrix} \chi_\lambda \\ \vec{\sigma}\vec{n}\,\chi_\lambda \end{pmatrix}. \tag{B.10}$$

Where χ_λ are two–component spinors. From the general theory of the Lorentz-group one can show, that spinors ξ_σ and χ_λ are related by a (momentum-dependent) rotation, the so-called Melosh–Wigner transform. We can give the explicit form of the 2×2 rotation matrix simply by comparing canonical and light-cone spinors.

We start by writing out Eq. B.22 as

$$
\begin{aligned}
u_{LC}(p, \lambda) &= \frac{1}{\sqrt{2\sqrt{2}p_+}} \begin{pmatrix} \sqrt{2}p_+ + m & \vec{\sigma}\vec{p}_\perp \\ \vec{\sigma}\vec{p}_\perp & \sqrt{2}p_+ - m \end{pmatrix} \begin{pmatrix} \chi_\lambda \\ \vec{\sigma}\vec{n}\chi_\lambda \end{pmatrix} \\
&= \frac{1}{\sqrt{2\sqrt{2}p_+}} \begin{pmatrix} \left(\sqrt{2}p_+ + m + (\vec{\sigma}\vec{p}_\perp)(\vec{\sigma}\vec{n})\right)\chi_\lambda \\ \left(\vec{\sigma}\vec{p}_\perp + (\sqrt{2}p_+ - m)\vec{\sigma}\vec{n}\right)\chi_\lambda \end{pmatrix} .
\end{aligned} \tag{B.11}
$$

Let us now introduce the matrix

$$
\hat{R}(p_+, \vec{p}_\perp) \equiv \frac{\sqrt{2}p_+ + m + (\vec{\sigma}\vec{p}_\perp)(\vec{\sigma}\vec{n})}{\sqrt{2\sqrt{2}p_+(E + m)}} = \frac{\sqrt{2}p_+ + m + (\vec{\sigma}\vec{p}_\perp)(\vec{\sigma}\vec{n})}{\sqrt{(\sqrt{2}p_+ + m)^2 + \vec{p}_\perp^2}} , \tag{B.12}
$$

and, using that $(\vec{\sigma}\vec{p}_\perp)(\vec{\sigma}\vec{n}) = -(\vec{\sigma}\vec{n})(\vec{\sigma}\vec{p}_\perp)$ one can immediately see, that $\hat{R}(p_+, \vec{p}_\perp)$ is unitary

$$
\hat{R}(p_+, \vec{p}_\perp)\hat{R}^\dagger(p_+, \vec{p}_\perp) = \mathbb{1} . \tag{B.13}
$$

One also easily convinces oneself, that

$$
\frac{\vec{\sigma}\vec{p}}{E + m}\hat{R}(p_+, \vec{p}_\perp) = \frac{\vec{\sigma}\vec{p}_\perp + (\sqrt{2}p_+ - m)\vec{\sigma}\vec{n}}{\sqrt{2\sqrt{2}p_+(E + m)}} , \tag{B.14}
$$

so that we can write

$$
u_{LC}(p, \lambda) = \sqrt{E + m} \begin{pmatrix} \hat{R}(p_+, \vec{p}_\perp)\chi_\lambda \\ \frac{\vec{\sigma}\vec{p}}{E+m}\hat{R}(p_+, \vec{p}_\perp)\chi_\lambda \end{pmatrix} , \tag{B.15}
$$

Thus, the light-cone spinors χ_λ are related to canonical spinors ξ_σ by

$$
\xi_\sigma = \left[\hat{R}(p_+, \vec{p}_\perp)\right]_{\sigma\lambda}\chi_\lambda . \tag{B.16}
$$

B.2 Antiparticle spinors

The antiparticle spinors (negative energy solutions fulfill

$$
(-\hat{p} - m)v(p, \sigma) = (\hat{p} + m)v(p, \sigma) = 0 . \tag{B.17}
$$

B. CANONICAL AND LIGHT-CONE SPINORS, THE MELOSH TRANSFORMATION

They are related to the particle spinors by the **charge conjugation** operation C:

$$v(p, \sigma) = C\bar{u}^T(p, \sigma).$$ (B.18)

The operator C can be written as

$$C = \eta\, i\gamma_2\gamma_0,$$ (B.19)

where η is an arbitrary phase, so that

$$v(p, \sigma) = \eta\, i\gamma_2 u^*(p, \sigma).$$ (B.20)

We follow Brodsky and Lepage and choose the phase $\eta = -1$. Then, applying the charge conjugation to spinors (B.6), the canonical antiparticle spinors are obtained as:

$$v(p, \sigma) = \sqrt{E + m}\begin{pmatrix}(-i\sigma_2)\frac{\vec{\sigma}^*\vec{p}}{E+m}\xi_\sigma^* \\ i\sigma_2\xi_\sigma^*\end{pmatrix} = \sqrt{E + m}\begin{pmatrix}\frac{\vec{\sigma}\vec{p}}{E+m}i\sigma_2\xi_\sigma^* \\ i\sigma_2\xi_\sigma^*\end{pmatrix}.$$ (B.21)

Here we did use the identity $\sigma_2\vec{\sigma}^*\sigma_2 = -\vec{\sigma}$. The light-cone Brodsky-Lepage antiparticle spinors are

$$v_{LC}(p, \bar{\lambda}) = \frac{1}{\sqrt{\sqrt{2}p_+}}\left(\sqrt{2}p_+ - \beta m + \vec{\alpha}\cdot\vec{p}_\perp\right)\tilde{v}_{\bar{\lambda}},$$ (B.22)

with $\tilde{v}_{\bar{\lambda}} = -i\gamma_2\tilde{u}_{\bar{\lambda}}^*$:

$$\tilde{v}_{\bar{\lambda}} = \begin{pmatrix}(\vec{\sigma}\vec{n})\,i\sigma_2\chi_{\bar{\lambda}}^* \\ i\sigma_2\chi_{\bar{\lambda}}^*\end{pmatrix}.$$ (B.23)

We can write the antiparticle spinor more explicitly:

$$\begin{aligned}
v_{LC}(p, \bar{\lambda}) &= \frac{1}{\sqrt{2\sqrt{2}p_+}}\begin{pmatrix}\sqrt{2}p_+ - m & \vec{\sigma}\vec{p}_\perp \\ \vec{\sigma}\vec{p}_\perp & \sqrt{2}p_+ + m\end{pmatrix}\begin{pmatrix}(\vec{\sigma}\vec{n})\,i\sigma_2\chi_{\bar{\lambda}}^* \\ i\sigma_2\chi_{\bar{\lambda}}^*\end{pmatrix} \\
&= \frac{1}{\sqrt{2\sqrt{2}p_+}}\begin{pmatrix}\left((\sqrt{2}p_+ - m)\vec{\sigma}\vec{n} + \vec{\sigma}\vec{p}\right)i\sigma_2\chi_{\bar{\lambda}}^* \\ \left((\vec{\sigma}\vec{p})(\vec{\sigma}\vec{n}) + \sqrt{2}p_+ + m\right)i\sigma_2\chi_{\bar{\lambda}}^*\end{pmatrix}.
\end{aligned}$$ (B.24)

From here, we can read off the Melosh-transform for the antiparticle spinor as

$$i\sigma_2\xi_\sigma^* = \hat{R}(p_+, \vec{p}_\perp)i\sigma_2\chi_{\bar{\lambda}}^* \iff \xi_\sigma^* = (-i\sigma_2)\hat{R}(p_+, \vec{p}_\perp)i\sigma_2\chi_{\bar{\lambda}}^* = R^*(p_+, \vec{p}_\perp)\chi_{\bar{\lambda}}^*,$$ (B.25)

which shows, that the antiparticle spinor transforms with the complex-conjugate Melosh transform.

B.3   Normalization and polarization sum of spinors

Spinors are normalized in the following way [1] :

$$\bar{u}(p,\lambda')\gamma_\mu u(p,\lambda) = 2p_\mu\,\delta_{\lambda'\lambda}\,, \quad \bar{v}(p,\bar{\lambda}')\gamma_\mu v(p,\bar{\lambda}) = 2p_\mu\,\delta_{\bar{\lambda}'\bar{\lambda}}\,, \tag{B.26}$$

This normalization implies, using the Dirac equation:

$$\bar{u}(p,\lambda')u(p,\lambda) = 2m\,\delta_{\lambda'\lambda}\,, \quad \bar{v}(p,\bar{\lambda}')v(p,\bar{\lambda}) = -2m\,\delta_{\bar{\lambda}'\bar{\lambda}}\,. \tag{B.27}$$

We furthermore have the polarization sums

$$\sum_\lambda u(p,\lambda)\bar{u}(p,\lambda) = \hat{p} + m\,, \quad \sum_{\bar{\lambda}} v(p,\bar{\lambda})\bar{v}(p,\bar{\lambda}) = \hat{p} - m\,. \tag{B.28}$$

B.4   Kinematics for the two-body bound state

Here we briefly derive some relations used in the main text concerning the momenta of Q and $\bar{Q}$ in the bound state. Let the invariant mass of the $Q\bar{Q}$ system be M, then we have in the c.m.-frame of the pair:

$$P_\mu = p_{Q\mu} + p_{\bar{Q}\mu} = (M,\vec{0}) = \left[\frac{M}{\sqrt{2}}, \frac{M}{\sqrt{2}}, \mathbf{0}\right]. \tag{B.29}$$

Because for quarkonia, quark and antiquark are of equal mass m_Q, their four-momenta are

$$p_{Q\mu} = \left(\frac{M}{2}, \vec{p}\right)\,, \quad p_{\bar{Q}\mu} = \left(\frac{M}{2}, -\vec{p}\right). \tag{B.30}$$

From the on-shell condition $p_Q^2 = m_Q^2$ we derive

$$|\vec{p}| = \tfrac{1}{2}\sqrt{M^2 - 4m_Q^2} = \frac{M}{2}\,\beta\,, \quad \text{with} \quad \beta = \sqrt{1 - \frac{4m_Q^2}{M^2}}\,. \tag{B.31}$$

The z-component of $\vec{p}$ is

$$p_z = |\vec{p}|\cos\theta = \frac{M}{2}\beta\cos\theta\,. \tag{B.32}$$

---

[1] we skip the label LC, the normalization condition applies equally for LC and canonical spinors

B. CANONICAL AND LIGHT-CONE SPINORS, THE MELOSH TRANSFORMATION

The light-cone plus momentum of the quark is

$$p_{Q+} = \frac{1}{\sqrt{2}} \frac{M}{2} (1 + \beta \cos \theta) \,, \tag{B.33}$$

and the frame-independent light-cone momentum fraction is

$$z = \frac{p_{Q+}}{P_+} = \tfrac{1}{2}(1 + \beta \cos \theta) \iff \beta \cos \theta = 2z - 1 \,, \tag{B.34}$$

and therefore

$$p_z = \frac{M}{2}(2z - 1) \,. \tag{B.35}$$

This gives the form of the three-momentum used in the Terentev substitution:

$$\vec{p} = (\vec{p}_\perp, (z - \tfrac{1}{2})M) \,. \tag{B.36}$$

We stress again, that M is the invariant mass of the $Q\bar{Q}$-system, which is not equal to the bound-state mass. In terms of LC variables $z, \vec{p}_\perp$ it can be calculated from

$$M^2 = \frac{\vec{p}_\perp^2 + m^2}{z(1 - z)} \,. \tag{B.37}$$

B.5 Parametrization of the Melosh transform

We wish to briefly bring the Melosh transform into the form used in the main text. From Eq. (B.33), we find

$$p_{Q+} = \frac{1}{\sqrt{2}} zM \,, \tag{B.38}$$

and hence

$$R(z, \vec{p}_\perp) \equiv R(p_{Q+}, \vec{p}_\perp) = \frac{m + zM - i\vec{\sigma} \cdot (\vec{n} \times \vec{p})}{\sqrt{(m + zM)^2 + \vec{p}_\perp^2}} \,. \tag{B.39}$$

Here we used the property of Pauli-matrices

$$(\vec{\sigma} \cdot \vec{a})(\vec{\sigma} \cdot \vec{b}) = \vec{a} \cdot \vec{b} + i\vec{\sigma} \cdot (\vec{a} \times \vec{b}) \,. \tag{B.40}$$

Appendix C

Distribution amplitude

The distribution amplitude (DA) of a meson gives us a probability amplitude to find a meson in a state composed out of two collinear partons, a quark and antiquark. They share the light-cone momentum of the meson in fractions $z, 1-z$. From the point of view of the light-front approach, the DA is a sort of projection of the LC-WF, where the transverse momentum of (anti-)quarks is integrated out.

Let us briefly explain, how the DA can be calculated from the lowest Fock-state LC-WF of a meson. We will restrict ourselves to the case of a pseudoscalar meson.

An operator definition of the (leading-twist) DA of the pseudoscalar meson, described by the state vector $|M(P)\rangle$ is:

$$f_M \, \varphi(z) = \int \frac{dx_-}{2\pi} \exp\left[- i(2z-1)\frac{x_- P_+}{2} \right] \langle 0|\bar{\psi}\left(\frac{x}{2}\right)\gamma_+\gamma_5\psi\left(- \frac{x}{2}\right)|M(P)\rangle\Big|_{x_+ = \vec{x}_\perp = 0} \tag{C.1}$$

Here the constraint $x_+ = 0, \vec{x}_\perp = \vec{0}_\perp$ means that the quark and antiquark are separated along the lightcone, i.e. $x = (0, x_-, \vec{0}_\perp)$. The dimensionful constant f_M is the so-called meson decay constant, which is related to the matrix element of the axial vector current as

$$f_M P_\mu = \langle 0|A_\mu(0)|M(P)\rangle \,, \text{ with } A_\mu(0) = \bar{\psi}(0)\gamma_\mu\gamma_5\psi(0) \,. \tag{C.2}$$

Integrating Eq. (C.1) over z, and comparing to the plus-component of Eq. (C.2), we obtain the normalization of the DA:

$$\int_0^1 dz \, \varphi(z) = 1 \,. \tag{C.3}$$

C. DISTRIBUTION AMPLITUDE

In the LF quantization approach, fields at $x_+ = 0$ are free and can be expanded into plane waves. The quark field operator can then be written as

$$\psi(x)\Big|_{x_+=0} = \int \frac{dk_+ d^2\vec{k}_\perp}{k_+ 16\pi^3} \theta(k_+) \sum_\lambda \left(b(k,\lambda)u(k,\lambda)e^{-ik\cdot x} + d^\dagger(k,\lambda)v(k,\lambda)e^{ik\cdot x} \right)\Big|_{x_+=0} \quad \text{(C.4)}$$

Here $u(k,\lambda), v(k,\lambda)$ are the spinors introduced in section App. B and $b, d^\dagger$ are the annihilation/creation operators which allow us to build the Fock-states. For example, the Fock state of a single quark Q is given by

$$|Q_\lambda(k_+, \vec{k}_\perp)\rangle = b^\dagger(k,\lambda)|0\rangle . \quad \text{(C.5)}$$

All states are canonically normalized, i. e.

$$\langle Q_{\lambda'}(k'_+, \vec{k}'_\perp)|Q_\lambda(k_+, \vec{k}_\perp)\rangle = 2k_+(2\pi)^3\delta(k'_+ - k_+)\delta^{(2)}(\vec{k}_\perp - \vec{k}'_\perp) . \quad \text{(C.6)}$$

Now, the operator

$$\hat{A}_+(x)\Big|_{x_+=\vec{x}_\perp=0} \equiv \bar{\psi}\left(\frac{x}{2}\right)\gamma_+\gamma_5\psi\left(-\frac{x}{2}\right)\Big|_{x_+=\vec{x}_\perp=0} , \quad \text{(C.7)}$$

is a bilinear form in creation annihilation operators $b^\dagger, d, \dots$. For our application, we only need the part containing quark and antiquark annihilation operators, which will have nonvanishing matrix elements between vacuum and meson state:

$$\hat{A}_+(x)\Big|_{x_+=\vec{x}_\perp=0} = \int \frac{dk'_+ d^2\vec{k}'_\perp}{k'_+ 16\pi^3} \frac{dk_+ d^2\vec{k}_\perp}{k_+ 16\pi^3} \left(d(k',\lambda')b(k,\lambda) \exp(-i(k_+ - k'_+)\frac{x_-}{2}) \right.$$
$$\left. \times \bar{v}(k',\lambda')\gamma_+\gamma_5 u(k,\lambda) + \dots \right). \quad \text{(C.8)}$$

We now only need the expansion of the meson state – without loss of generality, we can choose $\vec{P}_\perp = 0$:

$$|M; P_+, \vec{0}_\perp\rangle = \sum_{i,j,\sigma\bar{\sigma}} \frac{\delta_j^i}{\sqrt{N_c}} \int \frac{du d^2\vec{l}}{u(1-u)16\pi^3} \Psi_{\sigma,\bar{\sigma}}(u,\vec{l})$$
$$\times |Q_{i\sigma}(uP_+, \vec{l})\bar{Q}_{\bar{\sigma}}^j((1-u)P_+, -\vec{l})\rangle . \quad \text{(C.9)}$$

Then, sandwiching the operator of Eq. (C.8) between vacuum and the meson state and integrating over

$$\int \frac{du d^2\vec{l}}{u(1-u)16\pi^3} \frac{dk'_+ d^2\vec{k}'_\perp}{k'_+ 16\pi^3} \frac{dk_+ d^2\vec{k}_\perp}{k_+ 16\pi^3}$$
$$\sum_{\lambda,\bar{\lambda}\dots} \langle 0|d(k',\lambda')b(k,\lambda)|Q_{i\sigma}(uP_+, \vec{l})\bar{Q}_{\bar{\sigma}}^j((1-u)P_+, -\vec{l})\rangle$$
$$\times \bar{v}(k',\lambda')\gamma_+\gamma_5 u(k,\lambda)\Psi_{\sigma,\bar{\sigma}}(u,\vec{l})\, 2\delta(k_+ - k'_+ + (1-2z)P_+) \quad \text{(C.10)}$$

The spinor matrix element is very simple:

$$\bar{v}(k', \lambda')\gamma_+\gamma_5 u(k, \lambda) = 2\sqrt{k_+ k'_+}\, \lambda\delta_{\lambda',-\lambda}\,, \tag{C.11}$$

and after some algebra using standard rules of second quantization and renaming integration variables, we obtain in the end:

$$f_M \varphi(z) = 2\sqrt{N_c} \int \frac{d^2\vec{k}_\perp}{\sqrt{z(1-z)}16\pi^3} \left(\Psi_{+-}(z, \vec{k}_\perp) - \Psi_{-+}(z, \vec{k}_\perp) \right). \tag{C.12}$$

Inserting the combination of helicity-dependent WFs from Eq. (3.19), we obtain

$$f_M \phi(z) = \frac{m_c \sqrt{N_c}}{4\pi^3} \frac{1}{z(1-z)} \int d^2\vec{k}_\perp\, \psi(z, \vec{k}_\perp)\,. \tag{C.13}$$

The meson decay constant is just the integral over z of the rhs:

$$f_M = \frac{m_c \sqrt{N_c}}{4\pi^3} \int_0^1 \frac{dz}{z(1-z)} \int d^2\vec{k}_\perp\, \psi(z, \vec{k}_\perp)\,. \tag{C.14}$$

Appendix D

Light-cone variables and Lorentz-transformations

In this appendix, we wish to collect some useful facts about Lorentz-transformations acting on four momenta in the light-cone representation. They have been implicitly used in many formulas in the main text, and may help the reader to better understand the frame-invariance of the light-cone approach to bound states.

For the purpose of this appendix, let us write the standard parametrization of four-vectors as

$$a_\mu = (a_0, \vec{a}) = (a_0, a_x, a_y, a_z),$$ (D.1)

while we denote the four-vector in terms of light-cone components as

$$a_\mu = [a_+, a_-, \vec{a}_\perp] = [a_+, a_-, a_x, a_y],$$ (D.2)

with $a_\pm = (a_0 \pm a_z)/\sqrt{2}$. The Lorentz-invariant product of four-vectors is

$$a \cdot b = a_0 b_0 - \vec{a} \cdot \vec{b} = a_+ b_- + a_- b_+ - \vec{a}_\perp \cdot \vec{b}_\perp.$$ (D.3)

We also often use the notation (below $\vec{n} = (0, 0, 1)$):

$$[\vec{a}_\perp, \vec{b}_\perp] \equiv (\vec{a}_\perp \times \vec{b}_\perp) \cdot \vec{n} = a_x b_y - a_y b_x.$$ (D.4)

Notice, that this antisymmetric product can also be written in terms of the totally antisymmetric Levi-Civita symbol $\varepsilon_{\mu\nu\alpha\beta}$ as

$$\varepsilon_{\mu\nu\alpha\beta} n_+^\mu n_-^\nu a^\alpha b^\beta = [\vec{a}_\perp, \vec{b}_\perp].$$ (D.5)

D. LIGHT-CONE VARIABLES AND LORENTZ-TRANSFORMATIONS

D.1 Longitudinal boosts

The longitudinal boosts (boosts along the z-axis) act in a very simple way on light-cone coordinates:

$$\mathcal{L}(\eta) \circ [a_+, a_-, \vec{a}_\perp] = [e^\eta a_+, e^{-\eta} a_-, \vec{a}_\perp].$$ (D.6)

The boost parameter η has a straightforward interpretation. Namely the **rapidity** $y = \frac{1}{2}\log(a_+/a_-)$ transforms as

$$y \mapsto y + \eta.$$ (D.7)

D.2 Transverse boosts

Transverse boosts play a special role in the light-cone formalism, as they belong to the so called kinematical subgroup of the Lorentz-group. They depend on two boost parameters, collected in a transverse vector $\vec{v}_\perp$, and act like

$$\mathcal{B}(\vec{v}_\perp) \circ [a_+, a_-, \vec{a}_\perp] = [a_+, a'_-, \vec{a}_\perp + a_+ \vec{v}_\perp].$$ (D.8)

The explicit form of the a'_- component is not important for us. It is fixed by the Lorentz-invariance of the inner product:

$$2a_+ a_- - \vec{a}_\perp{}^2 = 2a_+ a'_- - (\vec{a}_\perp + a_+ \vec{v}_\perp)^2,$$ (D.9)

thus

$$a_- \mapsto a'_- = a_- + \vec{a}_\perp \cdot \vec{v}_\perp + \tfrac{1}{2} a_+ \vec{v}_\perp{}^2.$$ (D.10)

As an example, let us apply the transverse boost to a two-particle $Q\bar{Q}$ system. Let us discuss a frame in which the bound $Q\bar{Q}$ system has a vanishing total transverse momentum. The four-momenta of quark and antiquark are

$$\begin{aligned}
p_{Q\mu} &= [zP_+, p_{Q-}, \vec{k}_\perp], \\
p_{\bar{Q}\mu} &= [(1-z)P_+, p_{\bar{Q}-}, -\vec{k}_\perp],
\end{aligned}$$ (D.11)

and

$$P_\mu = p_{Q\mu} + p_{\bar{Q}\mu} = [P_+, P_-, \mathbf{0}].$$ (D.12)

If we want to boost P_μ, so that it's transverse momentum becomes $\vec{P}_\perp$, ie.

$$[P_+, P_-, \mathbf{0}] \mapsto [P_+, P'_-, \vec{P}_\perp] \,, \tag{D.13}$$

we should use the boost parameter $\vec{v}_\perp = \vec{P}_\perp/P_+$. Then, the transverse momentum of the quark transforms as

$$\vec{p}_{Q\perp} = \vec{k}_\perp \mapsto \vec{k}_\perp + z P_+ \frac{\vec{P}_\perp}{P_+} = \vec{k}_\perp + z \vec{P}_\perp \,, \tag{D.14}$$

while for the antiquark:

$$\vec{p}_{\bar{Q}\perp} = -\vec{k}_\perp \mapsto -\vec{k}_\perp + (1-z)\vec{P}_\perp \,. \tag{D.15}$$

From these transformation rules, one can see, that the combination

$$(1-z)\vec{p}_{Q\perp} - z\vec{p}_{\bar{Q}\perp} \,, \tag{D.16}$$

is invariant under longitudinal and transverse boost. It is therefore frame-independent, as any frame can be reached by a combination of longitudinal and transverse boosts.

References

[1] J. J. Aubert et al. "Experimental Observation of a Heavy Particle J". In: *Phys. Rev. Lett.* 33 (1974), pp. 1404–1406. DOI: 10.1103/PhysRevLett.33.1404.

[2] T. Appelquist et al. "Charmonium Spectroscopy". In: *Phys. Rev. Lett.* 34 (1975), p. 365. DOI: 10.1103/PhysRevLett.34.365.

[3] E. Chapon et al. *Perspectives for quarkonium studies at the high-luminosity LHC*. 2020. arXiv: 2012.14161 [hep-ph].

[4] J. P. Lansberg. "New Observables in Inclusive Production of Quarkonia". In: *Phys. Rept.* 889 (2020), pp. 1–106. DOI: 10.1016/j.physrep.2020.08.007. arXiv: 1903.09185 [hep-ph].

[5] N. Brambilla, H. S. Chung, and A. Vairo. "Inclusive production of heavy quarkonia in pNRQCD". In: *JHEP* 09 (2021), p. 032. DOI: 10.1007/JHEP09(2021)032. arXiv: 2106.09417 [hep-ph].

[6] I. Babiarz, W. Schäfer, and A. Szczurek. "Associated production of χ_c pairs with a gluon in the collinear-factorization approach". In: *Phys. Rev. D* 99.7 (2019), p. 074014. DOI: 10.1103/PhysRevD.99.074014. arXiv: 1902.08426 [hep-ph].

REFERENCES

[7]   I. Babiarz et al. "$\gamma^*\gamma^* \to \eta_c$(1S,2S) transition form factors for spacelike photons". In: *Phys. Rev. D* 100.5 (2019), p. 054018. DOI: 10.1103/PhysRevD.100.054018. arXiv: 1908.07802 [hep-ph].

[8]   I. Babiarz et al. "Prompt hadroproduction of $\eta_c(1S, 2S)$ in the k_T-factorization approach". In: *JHEP* 02 (2020), p. 037. DOI: 10.1007/JHEP02(2020)037. arXiv: 1911.03403 [hep-ph].

[9]   I. Babiarz et al. "Hadroproduction of scalar P-wave quarkonia in the light-front k_T-factorization approach". In: *JHEP* 06 (2020), p. 101. DOI: 10.1007/JHEP06(2020)101. arXiv: 2002.09352 [hep-ph].

[10]   I. Babiarz et al. "Central exclusive production of scalar and pseudoscalar charmonia in the light-front k_T-factorization approach". In: *Phys. Rev. D* 102 (2020), p. 114028. DOI: 10.1103/PhysRevD.102.114028. arXiv: 2008.05462 [hep-ph].

[11]   I. Babiarz, W. Schäfer, and A. Szczurek. "Production of χ_c meson pairs with additional emission". In: *EPJ Web Conf.* 199 (2019). Ed. by N. Wrońska, A. Magiera, and W. Przygoda, p. 04011. DOI: 10.1051/epjconf/201919904011.

[12]   I. Babiarz et al. "The $\gamma^*\gamma^* \to \eta_c(1S, 2S)$ transition form factor from Quarkonium wave functions". In: *Frascati Phys. Ser.* 69 (2019). Ed. by G. Corcella et al., pp. 96–101.

[13]   I. Babiarz et al. "The $\gamma^*\gamma^* \to \eta_c(1S, 2S)$ transition form factors for two spacelike photons". In: *PoS* EPS-HEP2019 (2020), p. 467. DOI: 10.22323/1.364.0467.

[14] I. Babiarz, W. Schäfer, and A. Szczurek. "Production of $\eta_c(1S, 2S)$ in e^+e^- and pp collisions". In: *PoS* ICHEP2020 (2021), p. 449. DOI: 10.22323/1.390.0449. arXiv: 2012.09721 [hep-ph].

[15] I. Babiarz et al. "Central exclusive production of η_c and χ_{c0} in the light-front $k_\perp$-factorization approach". In: *28th International Workshop on Deep Inelastic Scattering and Related Subjects*. July 2021. arXiv: 2107.14482 [hep-ph].

[16] I. Babiarz, R. Staszewski, and A. Szczurek. "Multi-parton interactions and rapidity gap survival probability in jet–gap–jet processes". In: *Phys. Lett. B* 771 (2017), pp. 532–538. DOI: 10.1016/j.physletb.2017.05.095. arXiv: 1704.00546 [hep-ph].

[17] M. Łuszczak et al. "Single-diffractive production of dijets within the k_t-factorization approach". In: *Phys. Rev. D* 96.5 (2017), p. 054018. DOI: 10.1103/PhysRevD.96.054018. arXiv: 1705.02241 [hep-ph].

[18] Rafał Maciuła et al. "Production asymmetry of ν_τ neutrinos and $\overline{\nu}_\tau$ antineutrinos from a fixed target experiment SHiP". In: *JHEP* 01 (2020), p. 116. DOI: 10.1007/JHEP01(2020)116. arXiv: 1910.01402 [hep-ph].

[19] M.B. Voloshin. "Charmonium". In: *Progress in Particle and Nuclear Physics* 61.2 (2008), pp. 455–511. ISSN: 0146-6410. DOI: https://doi.org/10.1016/j.ppnp.2008.02.001. URL: https://www.sciencedirect.com/science/article/pii/S0146641008000239.

[20] P. A. Zyla et al. "Review of Particle Physics". In: *PTEP* 2020.8 (2020), p. 083C01. DOI: 10.1093/ptep/ptaa104.

REFERENCES

[21] E. Eichten et al. "Quarkonia and their transitions". In: *Rev. Mod. Phys.* 80 (2008), pp. 1161–1193. DOI: `10.1103/RevModPhys.80.1161`. arXiv: `hep-ph/0701208`.

[22] Nora Brambilla et al. "The XYZ states: experimental and theoretical status and perspectives". In: *Phys. Rept.* 873 (2020), pp. 1–154. DOI: `10.1016/j.physrep.2020.05.001`. arXiv: `1907.07583 [hep-ex]`.

[23] B. Fuks et al. "Signatures of toponium formation in LHC run 2 data". In: *Phys. Rev. D* 104.3 (2021), p. 034023. DOI: `10.1103/PhysRevD.104.034023`. arXiv: `2102.11281 [hep-ph]`.

[24] J. -E. Augustin et al. "Discovery of a Narrow Resonance in e^+e^- Annihilation". In: *Phys. Rev. Lett.* 33 (23 Dec. 1974), pp. 1406–1408. DOI: `10.1103/PhysRevLett.33.1406`. URL: `https://link.aps.org/doi/10.1103/PhysRevLett.33.1406`.

[25] H. Fritzsch. "Producing Heavy Quark Flavors in Hadronic Collisions: A Test of Quantum Chromodynamics". In: *Phys. Lett. B* 67 (1977), pp. 217–221. DOI: `10.1016/0370-2693(77)90108-3`.

[26] F. Halzen. "Cvc for Gluons and Hadroproduction of Quark Flavors". In: *Phys. Lett. B* 69 (1977), pp. 105–108. DOI: `10.1016/0370-2693(77)90144-7`.

[27] Y.-Q. Ma and R. Vogt. "Quarkonium Production in an Improved Color Evaporation Model". In: *Phys. Rev. D* 94.11 (2016), p. 114029. DOI: `10.1103/PhysRevD.94.114029`. arXiv: `1609.06042 [hep-ph]`.

[28]   A. Adare et al. "Ground and excited charmonium state production in $p + p$ collisions at $\sqrt{s} = 200$ GeV". In: *Phys. Rev. D* 85 (2012), p. 092004. DOI: 10.1103/PhysRevD.85.092004. arXiv: 1105.1966 [hep-ex].

[29]   R. Aaij et al. "Measurement of $\psi(2S)$ meson production in pp collisions at $\sqrt{s}$=7 TeV". In: *Eur. Phys. J. C* 72 (2012). [Erratum: Eur.Phys.J.C 80, 49 (2020)], p. 2100. DOI: 10.1140/epjc/s10052-012-2100-4. arXiv: 1204.1258 [hep-ex].

[30]   Geoffrey T. Bodwin, Eric Braaten, and G. Peter Lepage. "Rigorous QCD analysis of inclusive annihilation and production of heavy quarkonium". In: *Phys. Rev. D* 51 (1995). [Erratum: Phys.Rev.D 55, 5853 (1997)], pp. 1125–1171. DOI: 10.1103/PhysRevD.55.5853. arXiv: hep-ph/9407339.

[31]   C. H. Kom, A. Kulesza, and W. J. Stirling. "Pair Production of J/psi as a Probe of Double Parton Scattering at LHCb". In: *Phys. Rev. Lett.* 107 (2011), p. 082002. DOI: 10.1103/PhysRevLett.107.082002. arXiv: 1105.4186 [hep-ph].

[32]   Ch. Borschensky and A. Kulesza. "Double parton scattering in pair production of J/ψ mesons at the LHC revisited". In: *Phys. Rev. D* 95.3 (2017), p. 034029. DOI: 10.1103/PhysRevD.95.034029. arXiv: 1610.00666 [hep-ph].

[33]   A. Cisek, W. Schäfer, and A. Szczurek. "Production of χ_c pairs with large rapidity separation in k_T factorization". In: *Phys. Rev. D* 97.11 (2018), p. 114018. DOI: 10.1103/PhysRevD.97.114018. arXiv: 1711.07366 [hep-ph].

[34]   R. Aaij et al. "Observation of J/ψ pair production in pp collisions at $\sqrt{s} = 7TeV$". In: *Phys. Lett. B* 707 (2012), pp. 52–59. DOI: 10.1016/j.physletb.2011.12.015. arXiv: 1109.0963 [hep-ex].

REFERENCES

[35] Roel Aaij et al. "Measurement of the J/ψ pair production cross-section in pp collisions at $\sqrt{s}$ = 13 TeV". In: *JHEP* 06 (2017). [Erratum: JHEP 10, 068 (2017)], p. 047. DOI: 10.1007/JHEP06(2017)047. arXiv: 1612.07451 [hep-ex].

[36] S. P. Baranov. "Pair production of J/ψ mesons in the k_t-factorization approach". In: *Phys. Rev. D* 84 (2011), p. 054012. DOI: 10.1103/PhysRevD.84.054012.

[37] S. P. Baranov et al. "Interparticle correlations in the production of J/ψ pairs in proton-proton collisions". In: *Phys. Rev. D* 87.3 (2013), p. 034035. DOI: 10.1103/PhysRevD.87.034035. arXiv: 1210.1806 [hep-ph].

[38] Vardan Khachatryan et al. "Measurement of Prompt J/ψ Pair Production in pp Collisions at $\sqrt{s}$ = 7 Tev". In: *JHEP* 09 (2014), p. 094. DOI: 10.1007/JHEP09(2014)094. arXiv: 1406.0484 [hep-ex].

[39] Morad Aaboud et al. "Measurement of the prompt J/ ψ pair production cross-section in pp collisions at $\sqrt{s}$ = 8 TeV with the ATLAS detector". In: *Eur. Phys. J. C* 77.2 (2017), p. 76. DOI: 10.1140/epjc/s10052-017-4644-9. arXiv: 1612.02950 [hep-ex].

[40] Rafał Maciuła, Wolfgang Schäfer, and Antoni Szczurek. "On the mechanism of $T_{4c}(6900)$ tetraquark production". In: *Phys. Lett. B* 812 (2021), p. 136010. DOI: 10.1016/j.physletb.2020.136010. arXiv: 2009.02100 [hep-ph].

[41] S. Baranov et al. "The $\gamma\gamma \rightarrow J/\psi J/\psi$ reaction and the $J/\psi J/\psi$ pair production in exclusive ultraperipheral ultrarelativistic heavy ion collisions". In: *Eur. Phys. J. C* 73.2 (2013), p. 2335. DOI: 10.1140/epjc/s10052-013-2335-8. arXiv: 1208.5917 [hep-ph].

[42] J. P. Lansberg et al. "Complete NLO QCD study of single- and double-quarkonium hadroproduction in the colour-evaporation model at the Tevatron and the LHC". In: *Phys. Lett. B* 807 (2020), p. 135559. DOI: 10.1016/j.physletb.2020.135559. arXiv: 2004.14345 [hep-ph].

[43] L. N. Lipatov. "Small x physics in perturbative QCD". In: *Phys. Rept.* 286 (1997), pp. 131–198. DOI: 10.1016/S0370-1573(96)00045-2. arXiv: hep-ph/9610276.

[44] E. N. Antonov et al. "Feynman rules for effective Regge action". In: *Nucl. Phys. B* 721 (2005), pp. 111–135. DOI: 10.1016/j.nuclphysb.2005.013. arXiv: hep-ph/0411185.

[45] L.N. Lipatov. "Gauge invariant effective action for high energy processes in QCD". In: *Nuclear Physics B* 452.1 (1995), pp. 369–397. ISSN: 0550-3213. DOI: https://doi.org/10.1016/0550-3213(95)00390-E. URL: https://www.sciencedirect.com/science/article/pii/055032139500390E.

[46] V. A. Novikov et al. "Charmonium and Gluons: Basic Experimental Facts and Theoretical Introduction". In: *Phys. Rept.* 41 (1978), pp. 1–133. DOI: 10.1016/0370-1573(78)90120-5.

[47] V. S. Fadin, E. A. Kuraev, and L. N. Lipatov. "On the Pomeranchuk Singularity in Asymptotically Free Theories". In: *Phys. Lett. B* 60 (1975), pp. 50–52. DOI: 10.1016/0370-2693(75)90524-9.

[48] F. Caporale et al. "Mueller–Navelet jets in next-to-leading order BFKL: theory versus experiment". In: *Eur. Phys. J. C* 74.10 (2014). [Erratum: Eur.Phys.J.C 75, 535 (2015)], p. 3084. DOI: 10.1140/epjc/s10052-015-3754-5. arXiv: 1407.8431 [hep-ph].

REFERENCES

[49] Ph. Hägler et al. "Towards a Solution of the Charmonium Production Controversy: $k_\perp$ Factorization versus Color-Octet Mechanism". In: *Phys. Rev. Lett.* 86 (8 Feb. 2001), pp. 1446–1449. DOI: 10.1103/PhysRevLett.86.1446. URL: https://link.aps.org/doi/10.1103/PhysRevLett.86.1446.

[50] A. D. Martin et al. "Parton distributions for the LHC". In: *Eur. Phys. J. C* 63 (2009), pp. 189–285. DOI: 10.1140/epjc/s10052-009-1072-5. arXiv: 0901.0002 [hep-ph].

[51] Karol Kovařík, Pavel M. Nadolsky, and Davison E. Soper. "Hadronic structure in high-energy collisions". In: *Rev. Mod. Phys.* 92.4 (2020), p. 045003. DOI: 10.1103/RevModPhys.92.045003. arXiv: 1905.06957 [hep-ph].

[52] V. L. Chernyak and S. I. Eidelman. "Hard exclusive two photon processes in QCD". In: *Progress in Particle and Nuclear Physics* 80 (2015), pp. 1–42. ISSN: 0146-6410. DOI: https://doi.org/10.1016/j.ppnp.2014.09.002. URL: https://www.sciencedirect.com/science/article/pii/S0146641014000581.

[53] A. V. Radyushkin. "Deep Elastic Processes of Composite Particles in Field Theory and Asymptotic Freedom". In: (June 1977). arXiv: hep-ph/0410276.

[54] A. V. Efremov and A. V. Radyushkin. "Asymptotical Behavior of Pion Electromagnetic Form-Factor in QCD". In: *Theor. Math. Phys.* 42 (1980), pp. 97–110. DOI: 10.1007/BF01032111.

[55] A. V. Efremov and A. V. Radyushkin. "Factorization and Asymptotical Behavior of Pion Form-Factor in QCD". In: *Phys. Lett. B* 94 (1980), pp. 245–250. DOI: 10.1016/0370-2693(80)90869-2.

[56] G. P. Lepage and S. J. Brodsky. "Exclusive Processes in Quantum Chromodynamics: Evolution Equations for Hadronic Wave Functions and the Form-Factors of Mesons". In: *Phys. Lett. B* 87 (1979), pp. 359–365. DOI: 10.1016/0370-2693(79)90554-9.

[57] V. L. Chernyak and A. R. Zhitnitsky. "Asymptotic Behavior of Exclusive Processes in QCD". In: *Phys. Rept.* 112 (1984), p. 173. DOI: 10.1016/0370-1573(84)90126-1.

[58] F. Jegerlehner. *The Anomalous Magnetic Moment of the Muon*. Vol. 274. Cham: Springer, 2017. DOI: 10.1007/978-3-319-63577-4.

[59] Stanisław D. Głazek and Jarosław Młynik. "Boost-invariant Hamiltonian approach to heavy quarkonia". In: *Phys. Rev. D* 74 (10 Nov. 2006), p. 105015. DOI: 10.1103/PhysRevD.74.105015. URL: https://link.aps.org/doi/10.1103/PhysRevD.74.105015.

[60] Thomas Gutsche et al. "Light-front potential for heavy quarkonia constrained by the holographic soft-wall model". In: *Phys. Rev. D* 90 (9 Nov. 2014), p. 096007. DOI: 10.1103/PhysRevD.90.096007. URL: https://link.aps.org/doi/10.1103/PhysRevD.90.096007.

[61] Yang Li, Pieter Maris, and James P. Vary. "Quarkonium as a relativistic bound state on the light front". In: *Phys. Rev. D* 96 (1 July 2017), p. 016022. DOI: 10.1103/PhysRevD.96.016022. URL: https://link.aps.org/doi/10.1103/PhysRevD.96.016022.

[62] Thorsten Feldmann and Peter Kroll. "A perturbative approach to the $\eta_c\gamma$ transition form factor". In: *Physics Letters B* 413.3 (1997), pp. 410–415. ISSN: 0370-2693. DOI: https://doi.org/10.1016/S0370-2693(97)01120-

REFERENCES

9. URL: https://www.sciencedirect.com/science/article/pii/S0370269397011209.

[63] Th. Feldmann, P. Kroll, and B. Stech. "Mixing and decay constants of pseudoscalar mesons". In: *Phys. Rev. D* 58 (11 Oct. 1998), p. 114006. DOI: 10.1103/PhysRevD.58.114006. URL: https://link.aps.org/doi/10.1103/PhysRevD.58.114006.

[64] Chao-Qiang Geng and Chong-Chung Lih. "Form factors of η_c in light front quark model". In: *Eur. Phys. J. C* 73.8 (2013), p. 2505. DOI: 10.1140/epjc/s10052-013-2505-8. arXiv: 1307.3852 [hep-ph].

[65] H. J. Melosh. "Quarks: Currents and constituents". In: *Phys. Rev. D* 9 (4 Feb. 1974), pp. 1095–1112. DOI: 10.1103/PhysRevD.9.1095. URL: https://link.aps.org/doi/10.1103/PhysRevD.9.1095.

[66] W. Jaus. "Semileptonic decays of B and D mesons in the light-front formalism". In: *Phys. Rev. D* 41 (11 June 1990), pp. 3394–3404. DOI: 10.1103/PhysRevD.41.3394. URL: https://link.aps.org/doi/10.1103/PhysRevD.41.3394.

[67] G. Peter Lepage and Stanley J. Brodsky. "Exclusive processes in perturbative quantum chromodynamics". In: *Phys. Rev. D* 22 (9 Nov. 1980), pp. 2157–2198. DOI: 10.1103/PhysRevD.22.2157. URL: https://link.aps.org/doi/10.1103/PhysRevD.22.2157.

[68] J. J. Dudek and R. G. Edwards. "Two Photon Decays of Charmonia from Lattice QCD". In: *Phys. Rev. Lett.* 97 (2006), p. 172001. DOI: 10.1103/PhysRevLett.97.172001. arXiv: hep-ph/0607140.

[69] T. Chen et al. "Two-photon decays of η_c from lattice QCD". In: *Eur. Phys. J. C* 76.7 (2016), p. 358. DOI: 10.1140/epjc/s10052-016-4212-8. arXiv: 1602.00076 [hep-lat].

[70] F. Cao and T. Huang. "Large corrections to asymptotic F(eta c gamma) and F(eta b gamma) in the light cone perturbative QCD". In: *Phys. Rev. D* 59 (1999), p. 093004. DOI: 10.1103/PhysRevD.59.093004. arXiv: hep-ph/9711284.

[71] F. Feng, Y. Jia, and W. L. Sang. "Can Nonrelativistic QCD Explain the $\gamma\gamma^* \to \eta_c$ Transition Form Factor Data?" In: *Phys. Rev. Lett.* 115.22 (2015), p. 222001. DOI: 10.1103/PhysRevLett.115.222001. arXiv: 1505.02665 [hep-ph].

[72] S. Q. Wang et al. "Solution to the $\gamma\gamma^* \to \eta_c$ puzzle using the principle of maximum conformality". In: *Phys. Rev. D* 97.9 (2018), p. 094034. DOI: 10.1103/PhysRevD.97.094034. arXiv: 1804.06106 [hep-ph].

[73] W. Lucha and D. Melikhov. "The $\gamma^*\gamma^* \to \eta_c$ transition form factor". In: *Phys. Rev. D* 86 (2012), p. 016001. DOI: 10.1103/PhysRevD.86.016001. arXiv: 1205.4587 [hep-ph].

[74] Jing Chen et al. "Two Photon Transition Form Factor of $\bar{c}c$ Quarkonia". In: *Phys. Rev. D* 95.1 (2017), p. 016010. DOI: 10.1103/PhysRevD.95.016010. arXiv: 1611.05960 [nucl-th].

[75] Hui-Young Ryu, Ho-Meoyng Choi, and Chueng-Ryong Ji. "Systematic twist expansion of $(\eta_c, \eta_b) \to \gamma^*\gamma$ transition form factors in light-front quark model". In: *Phys. Rev. D* 98.3 (2018), p. 034018. DOI: 10.1103/PhysRevD.98.034018. arXiv: 1804.08287 [hep-ph].

REFERENCES

[76] M. Poppe. "Exclusive Hadron Production in Two Photon Reactions". In: *Int. J. Mod. Phys. A* 1 (1986), pp. 545–668. DOI: `10.1142/S0217751X8600023X`.

[77] M. Tanabashi et al. "Review of Particle Physics". In: *Phys. Rev. D* 98.3 (2018), p. 030001. DOI: `10.1103/PhysRevD.98.030001`.

[78] S. R. Hou. "Resonance formation in two photon collisions". In: *AIP Conf. Proc.* 432.1 (1998). Ed. by S. U. Chung and H. J. Willutzki, pp. 745–748. DOI: `10.1063/1.56085`.

[79] J. P. Lees et al. "Measurement of the $\gamma\gamma* --> \eta_c$ transition form factor". In: *Phys. Rev. D* 81 (2010), p. 052010. DOI: `10.1103/PhysRevD.81.052010`. arXiv: `1002.3000 [hep-ex]`.

[80] M. Diehl, P. Kroll, and C. Vogt. "The Annihilation of virtual photons into pseudoscalar mesons". In: *Eur. Phys. J. C* 22 (2001), pp. 439–450. DOI: `10.1007/s100520100830`. arXiv: `hep-ph/0108220`.

[81] Saro Ong. "Improved perturbative QCD analysis of the pion - photon transition form-factor". In: *Phys. Rev. D* 52 (1995), pp. 3111–3114. DOI: `10.1103/PhysRevD.52.3111`.

[82] D. Ebert, R. N. Faustov, and V. O. Galkin. "Two photon decay rates of heavy quarkonia in the relativistic quark model". In: *Mod. Phys. Lett. A* 18 (2003), pp. 601–608. DOI: `10.1142/S021773230300971X`. arXiv: `hep-ph/0302044`.

[83] K. W. Edwards et al. "Study of B decays to charmonium states B —> eta(c) K and B —> chi(c0) K". In: *Phys. Rev. Lett.* 86 (2001), pp. 30–34. DOI: `10.1103/PhysRevLett.86.30`. arXiv: `hep-ex/0007012`.

[84] C. T. H. Davies et al. "Update: Precision D_s decay constant from full lattice QCD using very fine lattices". In: *Phys. Rev. D* 82 (2010), p. 114504. DOI: 10.1103/PhysRevD.82.114504. arXiv: 1008.4018 [hep-lat].

[85] Peter Kroll and Kornelija Passek-Kumerički. "On some implications of the BaBar data on the $\gamma^*\eta'$ transition form factor". In: *Phys. Lett. B* 793 (2019), pp. 195–199. DOI: 10.1016/j.physletb.2019.04.054. arXiv: 1903.06650 [hep-ph].

[86] B. A. Kniehl, D. V. Vasin, and V. A. Saleev. "Charmonium production at high energy in the k_T -factorization approach". In: *Phys. Rev. D* 73 (2006), p. 074022. DOI: 10.1103/PhysRevD.73.074022. arXiv: hep-ph/0602179.

[87] R. S. Pasechnik, A. Szczurek, and O. V. Teryaev. "Central exclusive production of scalar chi(c) meson at the Tevatron, RHIC and CERN LHC energies". In: *Phys. Rev. D* 78 (2008), p. 014007. DOI: 10.1103/PhysRevD.78.014007. arXiv: 0709.0857 [hep-ph].

[88] M. B. Einhorn and S. D. Ellis. "Hadronic Production of the New Resonances - Are Gluons Important?" In: *Phys. Rev. Lett.* 34 (1975), pp. 1190–1193. DOI: 10.1103/PhysRevLett.34.1190.

[89] M. B. Einhorn and S. D. Ellis. "Hadronic Production of the New Resonances: Probing Gluon Distributions". In: *Phys. Rev. D* 12 (1975), p. 2007. DOI: 10.1103/PhysRevD.12.2007.

[90] Yu Feng et al. "Phenomenological NLO analysis of η_c production at the LHC in the collider and fixed-target modes". In: *Nucl. Phys. B* 945 (2019), p. 114662. DOI: 10.1016/j.nuclphysb.2019.114662. arXiv: 1901.09766 [hep-ph].

REFERENCES

[91] Dmitri Diakonov, M. G. Ryskin, and A. G. Shuvaev. "Gluon distribution at
      very small x from C-even charmonia production at the LHC". In: *JHEP*
      02 (2013), p. 069. DOI: 10 . 1007 / JHEP02(2013) 069. arXiv: 1211 . 1578
      [hep-ph].

[92] A. K. Likhoded, A. V. Luchinsky, and S. V. Poslavsky. "Production of η_Q
      meson at LHC". In: *Mod. Phys. Lett. A* 30.07 (2015), p. 1550032. DOI: 10 .
      1142/S0217732315500327. arXiv: 1411.1247 [hep-ph].

[93] J. R. Andersen et al. "Small x Phenomenology: Summary of the 3rd Lund
      Small x Workshop in 2004". In: *Eur. Phys. J. C* 48 (2006), pp. 53–105. DOI:
      10.1140/epjc/s2006-02615-6. arXiv: hep-ph/0604189.

[94] A. Szczurek et al. "Mapping the proton unintegrated gluon distribution in
      dijets correlations in real and virtual photoproduction at HERA". In: *Phys.
      Lett. B* 500 (2001), pp. 254–262. DOI: 10.1016/S0370-2693(01)00084-3.
      arXiv: hep-ph/0011281.

[95] B. Andersson et al. "Small x phenomenology: Summary and status". In: *Eur.
      Phys. J. C* 25 (2002), pp. 77–101. DOI: 10.1007/s10052-002-0998-7. arXiv:
      hep-ph/0204115.

[96] J. R. Andersen et al. "Small x phenomenology: Summary and status". In:
      Eur. Phys. J. C 35 (2004), pp. 67–98. DOI: 10.1140/epjc/s2004-01775-7.
      arXiv: hep-ph/0312333.

[97] H. Jung et al. "The CCFM Monte Carlo generator CASCADE version 2.2.03".
      In: *Eur. Phys. J. C* 70 (2010), pp. 1237–1249. DOI: 10.1140/epjc/s10052-
      010-1507-z. arXiv: 1008.0152 [hep-ph].

[98] F. Hautmann et al. "TMDlib and TMDplotter: library and plotting tools for transverse-momentum-dependent parton distributions". In: *Eur. Phys. J. C* 74 (2014), p. 3220. DOI: `10.1140/epjc/s10052-014-3220-9`. arXiv: `1408.3015 [hep-ph]`.

[99] A. D. Martin, M. G. Ryskin, and G. Watt. "NLO prescription for unintegrated parton distributions". In: *Eur. Phys. J. C* 66 (2010), pp. 163–172. DOI: `10.1140/epjc/s10052-010-1242-5`. arXiv: `0909.5529 [hep-ph]`.

[100] M. A. Kimber, A. D. Martin, and M. G. Ryskin. "Unintegrated parton distributions". In: *Phys. Rev. D* 63 (2001), p. 114027. DOI: `10.1103/PhysRevD.63.114027`. arXiv: `hep-ph/0101348`.

[101] G. Watt, A. D. Martin, and M. G. Ryskin. "Unintegrated parton distributions and electroweak boson production at hadron colliders". In: *Phys. Rev. D* 70 (2004). [Erratum: Phys.Rev.D 70, 079902 (2004)], p. 014012. DOI: `10.1103/PhysRevD.70.014012`. arXiv: `hep-ph/0309096`.

[102] G. Watt, A. D. Martin, and M. G. Ryskin. "Unintegrated parton distributions and inclusive jet production at HERA". In: *Eur. Phys. J. C* 31 (2003), pp. 73–89. DOI: `10.1140/epjc/s2003-01320-4`. arXiv: `hep-ph/0306169`.

[103] M. A. Kimber et al. "The Unintegrated gluon distribution from the CCFM equation". In: *Phys. Rev. D* 62 (2000), p. 094006. DOI: `10.1103/PhysRevD.62.094006`. arXiv: `hep-ph/0006184`.

[104] N. A. Abdulov et al. "TMDlib2 and TMDplotter: a platform for 3D hadron structure studies". In: (Mar. 2021). DOI: `10.1140/epjc/s10052-021-09508-8`. arXiv: `2103.09741 [hep-ph]`.

REFERENCES

[105] K. Kutak. "Hard scale dependent gluon density, saturation and forward-forward dijet production at the LHC". In: *Phys. Rev. D* 91.3 (2015), p. 034021. DOI: 10.1103/PhysRevD.91.034021. arXiv: 1409.3822 [hep-ph].

[106] J. Kwiecinski, A. D. Martin, and A. M. Stasto. "A Unified BFKL and GLAP description of F2 data". In: *Phys. Rev. D* 56 (1997), pp. 3991–4006. DOI: 10.1103/PhysRevD.56.3991. arXiv: hep-ph/9703445.

[107] I. Balitsky. "Operator expansion for high-energy scattering". In: *Nucl. Phys. B* 463 (1996), pp. 99–160. DOI: 10.1016/0550-3213(95)00638-9. arXiv: hep-ph/9509348.

[108] Y. V. Kovchegov. "Unitarization of the BFKL pomeron on a nucleus". In: *Phys. Rev. D* 61 (2000), p. 074018. DOI: 10.1103/PhysRevD.61.074018. arXiv: hep-ph/9905214.

[109] K. Kutak and S. Sapeta. "Gluon saturation in dijet production in p-Pb collisions at Large Hadron Collider". In: *Phys. Rev. D* 86 (2012), p. 094043. DOI: 10.1103/PhysRevD.86.094043. arXiv: 1205.5035 [hep-ph].

[110] Roel Aaij et al. "Measurement of the $\eta_c(1S)$ production cross-section in proton-proton collisions via the decay $\eta_c(1S) \to p\bar{p}$". In: *Eur. Phys. J. C* 75.7 (2015), p. 311. DOI: 10.1140/epjc/s10052-015-3502-x. arXiv: 1409.3612 [hep-ex].

[111] Roel Aaij et al. "Measurement of the $\eta_c(1S)$ production cross-section in pp collisions at $\sqrt{s} = 13$ TeV". In: *Eur. Phys. J. C* 80.3 (2020), p. 191. DOI: 10.1140/epjc/s10052-020-7733-0. arXiv: 1911.03326 [hep-ex].

164

[112]   Hong-Fei Zhang et al. "Impact of η_c hadroproduction data on charmonium production and polarization within NRQCD framework". In: *Phys. Rev. Lett.* 114.9 (2015), p. 092006. DOI: 10.1103/PhysRevLett.114.092006. arXiv: 1412.0508 [hep-ph].

[113]   Miguel G. Echevarria. "Proper TMD factorization for quarkonia production: $pp \rightarrow \eta_{c,b}$ as a study case". In: *JHEP* 10 (2019), p. 144. DOI: 10.1007/JHEP10(2019)144. arXiv: 1907.06494 [hep-ph].

[114]   T. Tichouk, H. Sun, and X. Luo. "Hard diffractive $\eta_{c,b}$ hadroproduction at the LHC". In: *Phys. Rev. D* 101.5 (2020), p. 054035. DOI: 10.1103/PhysRevD.101.054035. arXiv: 2003.09886 [hep-ph].

[115]   J. P. Lansberg and T. N. Pham. "Two-photon width of eta(c) and eta(c)-prime from heavy-quark spin symmetry". In: *Phys. Rev. D* 74 (2006), p. 034001. DOI: 10.1103/PhysRevD.74.034001. arXiv: hep-ph/0603113.

[116]   J. P. Lansberg and T. N. Pham. "Effective Lagrangian for Two-photon and Two-gluon Decays of P-wave Heavy Quarkonium chi(c0,2) and chi(b0,2) states". In: *Phys. Rev. D* 79 (2009), p. 094016. DOI: 10.1103/PhysRevD.79.094016. arXiv: 0903.1562 [hep-ph].

[117]   M. A. Shifman et al. "eta(c) Puzzle in Quantum Chromodynamics". In: *Phys. Lett. B* 77 (1978), pp. 80–83. DOI: 10.1016/0370-2693(78)90206-X.

[118]   N. Kochelev and D. P. Min. "Eta(c): Glueball mixing and resonance X(1835)". In: *Phys. Rev. D* 72 (2005), p. 097502. DOI: 10.1103/PhysRevD.72.097502. arXiv: hep-ph/0510016.

REFERENCES

[119] V. Zetocha and T. Schäfer. "Instanton contribution to scalar charmonium and glueball decays". In: *Phys. Rev. D* 67 (2003), p. 114003. DOI: 10.1103/PhysRevD.67.114003. arXiv: hep-ph/0212125.

[120] L. A. Harland-Lang et al. "Parton distributions in the LHC era: MMHT 2014 PDFs". In: *Eur. Phys. J. C* 75.5 (2015), p. 204. DOI: 10.1140/epjc/s10052-015-3397-6. arXiv: 1412.3989 [hep-ph].

[121] Z. Metreveli. "Charmonium Spectroscopy Below Open Flavor Threshold". In: *eConf* C070805 (2007). Ed. by H. Mahlke and J. Napolitano, p. 16. arXiv: 0710.1884 [hep-ex].

[122] S. P. Baranov and A. V. Lipatov. "Prompt η_c meson production at the LHC in the NRQCD with k_T-factorization". In: *Eur. Phys. J. C* 79.7 (2019), p. 621. DOI: 10.1140/epjc/s10052-019-7134-4. arXiv: 1904.00400 [hep-ph].

[123] R. Baier and R. Ruckl. "Hadronic Collisions: A Quarkonium Factory". In: *Z. Phys. C* 19 (1983), p. 251. DOI: 10.1007/BF01572254.

[124] G. A. Schuler. "Quarkonium production and decays". PhD thesis. Hamburg U., 1994. arXiv: hep-ph/9403387.

[125] J. P. Lansberg and M. A. Ozcelik. "Curing the unphysical behaviour of NLO quarkonium production at the LHC and its relevance to constrain the gluon PDF at low scales". In: *Eur. Phys. J. C* 81.6 (2021), p. 497. DOI: 10.1140/epjc/s10052-021-09258-7. arXiv: 2012.00702 [hep-ph].

[126] P. Hagler et al. "Towards a solution of the charmonium production controversy: k^- perpendicular factorization versus color octet mechanism". In:

Phys. Rev. Lett. 86 (2001), pp. 1446–1449. DOI: `10.1103/PhysRevLett.86.1446`. arXiv: `hep-ph/0004263`.

[127] S. P. Baranov, A. V. Lipatov, and N. P. Zotov. "Prompt charmonia production and polarization at LHC in the NRQCD with kt-factorization. Part II: χ_c mesons". In: *Phys. Rev. D* 93.9 (2016), p. 094012. DOI: `10.1103/PhysRevD.93.094012`. arXiv: `1510.02411 [hep-ph]`.

[128] D. Boer and C. Pisano. "Polarized gluon studies with charmonium and bottomonium at LHCb and AFTER". In: *Phys. Rev. D* 86 (2012), p. 094007. DOI: `10.1103/PhysRevD.86.094007`. arXiv: `1208.3642 [hep-ph]`.

[129] M. Gallinaro. "Diffractive and exclusive measurements at CDF". In: *14th International Workshop on Deep Inelastic Scattering*. June 2006, pp. 231–234. DOI: `10.1142/9789812706706_0048`. arXiv: `hep-ex/0606024`.

[130] M. G. Albrow et al. "The FP420 \& Project: Higgs and New Physics with forward protons at the LHC". In: *JINST* 4 (2009), T10001. DOI: `10.1088/1748-0221/4/10/T10001`. arXiv: `0806.0302 [hep-ex]`.

[131] D. E. Sosnov. "Exclusive Υ and $\rho\,(770)^0$ photoproduction in pPb at $\sqrt{s_{NN}} = 5.02$TeV with CMS". In: *Nucl. Phys. A* 1005 (2021). Ed. by Feng Liu et al., p. 121857. DOI: `10.1016/j.nuclphysa.2020.121857`.

[132] A. M. Sirunyan et al. "Measurement of exclusive $\rho(770)^0$ photoproduction in ultraperipheral pPb collisions at $\sqrt{s_{\mathrm{NN}}} = 5.02$ TeV". In: *Eur. Phys. J. C* 79.8 (2019), p. 702. DOI: `10.1140/epjc/s10052-019-7202-9`. arXiv: `1902.01339 [hep-ex]`.

REFERENCES

[133] T. A. Aaltonen et al. "Measurement of central exclusive $\pi^+\pi^-$ production in $p\bar{p}$ collisions at $\sqrt{s} = 0.9$ and 1.96 TeV at CDF". In: *Phys. Rev. D* 91.9 (2015), p. 091101. DOI: 10.1103/PhysRevD.91.091101. arXiv: 1502.01391 [hep-ex].

[134] J. Adam et al. "Measurement of the central exclusive production of charged particle pairs in proton-proton collisions at $\sqrt{s} = 200$ GeV with the STAR detector at RHIC". In: *JHEP* 07.07 (2020), p. 178. DOI: 10.1007/JHEP07(2020)178. arXiv: 2004.11078 [hep-ex].

[135] P. Lebiedowicz et al. "Central exclusive diffractive production of axial-vector $f_1(1285)$ and $f_1(1420)$ mesons in proton-proton collisions". In: *Phys. Rev. D* 102.11 (2020), p. 114003. DOI: 10.1103/PhysRevD.102.114003. arXiv: 2008.07452 [hep-ph].

[136] R. Aaij et al. "Updated measurements of exclusive J/ψ and $\psi(2S)$ production cross-sections in pp collisions at $\sqrt{s} = 7$ TeV". In: *J. Phys. G* 41 (2014), p. 055002. DOI: 10.1088/0954-3899/41/5/055002. arXiv: 1401.3288 [hep-ex].

[137] R. Aaij et al. "Central exclusive production of J/ψ and $\psi(2S)$ mesons in pp collisions at $\sqrt{s} = 13$ TeV". In: *JHEP* 10 (2018), p. 167. DOI: 10.1007/JHEP10(2018)167. arXiv: 1806.04079 [hep-ex].

[138] T. Csörgő et al. "Evidence of Odderon-exchange from scaling properties of elastic scattering at TeV energies". In: *Eur. Phys. J. C* 81.2 (2021), p. 180. DOI: 10.1140/epjc/s10052-021-08867-6. arXiv: 1912.11968 [hep-ph].

[139] V. M. Abazov et al. "Odderon Exchange from Elastic Scattering Differences between pp and $p\bar{p}$ Data at 1.96 TeV and from pp Forward Scattering Mea-

surements". In: *Phys. Rev. Lett.* 127.6 (2021), p. 062003. DOI: 10.1103/
PhysRevLett.127.062003. arXiv: 2012.03981 [hep-ex].

[140] G. Ingelman and P. E. Schlein. "Jet Structure in High Mass Diffractive Scattering". In: *Phys. Lett. B* 152 (1985), pp. 256–260. DOI: 10.1016/0370-
2693(85)91181-5.

[141] M. V. T. Machado. "An analysis on single and central diffractive heavy flavour production at hadron colliders". In: *Braz. J. Phys.* 38 (2008). Ed. by M. B. Gay Ducati, M. V. Trinidade Machado, and M. A. Betemps, pp. 416–420. DOI: 10.1590/S0103-97332008000400007.

[142] B. Z. Kopeliovich, R. Pasechnik, and I. K. Potashnikova. "Diffractive dijet production: breakdown of factorization". In: *Phys. Rev. D* 98.11 (2018), p. 114021. DOI: 10.1103/PhysRevD.98.114021. arXiv: 1807.05548 [hep-ph].

[143] A. Ekstedt, R. Enberg, and G. Ingelman. "Hard color singlet BFKL exchange and gaps between jets at the LHC". In: Mar. 2017. arXiv: 1703.10919
[hep-ph].

[144] A. D. Martin, M. G. Ryskin, and V. A. Khoze. "Forward Physics at the LHC". In: *Acta Phys. Polon. B* 40 (2009). Ed. by Krzysztof Golec-Biernat and Michal Praszalowicz, pp. 1841–1876. arXiv: 0903.2980 [hep-ph].

[145] R. S. Pasechnik and B. Z. Kopeliovich. "Drell-Yan diffraction: Breakdown of QCD factorisation". In: *Eur. Phys. J. C* 71 (2011), p. 1827. DOI: 10.1140/
epjc/s10052-011-1827-7. arXiv: 1109.6695 [hep-ph].

[146]   R. Pasechnik, B. Kopeliovich, and I. Potashnikova. "Diffractive Gauge Bosons Production beyond QCD Factorisation". In: *Phys. Rev. D* 86 (2012), p. 114039. DOI: 10.1103/PhysRevD.86.114039. arXiv: 1204.6477 [hep-ph].

[147]   A. Szczurek, R. S. Pasechnik, and O. V. Teryaev. "pp —> pp eta' reaction at high energies". In: *Phys. Rev. D* 75 (2007), p. 054021. DOI: 10.1103/PhysRevD.75.054021. arXiv: hep-ph/0608302.

[148]   L. A. Harland-Lang et al. "Central exclusive production within the Durham model: a review". In: *Int. J. Mod. Phys. A* 29 (2014), p. 1430031. DOI: 10.1142/S0217751X14300312. arXiv: 1405.0018 [hep-ph].

[149]   A. Donnachie and P. V. Landshoff. "Exclusive rho Production in Deep Inelastic Scattering". In: *Phys. Lett. B* 185 (1987), p. 403. DOI: 10.1016/0370-2693(87)91024-0.

[150]   A. G. Shuvaev et al. "Off diagonal distributions fixed by diagonal partons at small x and xi". In: *Phys. Rev. D* 60 (1999), p. 014015. DOI: 10.1103/PhysRevD.60.014015. arXiv: hep-ph/9902410.

[151]   J. R. Cudell et al. "Central exclusive production of dijets at hadronic colliders". In: *Eur. Phys. J. C* 61 (2009), pp. 369–390. DOI: 10.1140/epjc/s10052-009-0994-2. arXiv: 0807.0600 [hep-ph].

[152]   K. J. Golec-Biernat and M. Wusthoff. "Saturation in diffractive deep inelastic scattering". In: *Phys. Rev. D* 60 (1999), p. 114023. DOI: 10.1103/PhysRevD.60.114023. arXiv: hep-ph/9903358.

[153] K. Golec-Biernat and S. Sapeta. "Saturation model of DIS : an update". In: *JHEP* 03 (2018), p. 102. DOI: `10.1007/JHEP03(2018)102`. arXiv: `1711.11360 [hep-ph]`.

[154] A. H. Rezaeian and I. Schmidt. "Impact-parameter dependent Color Glass Condensate dipole model and new combined HERA data". In: *Phys. Rev. D* 88 (2013), p. 074016. DOI: `10.1103/PhysRevD.88.074016`. arXiv: `1307.0825 [hep-ph]`.

[155] E. Iancu, K. Itakura, and S. Munier. "Saturation and BFKL dynamics in the HERA data at small x". In: *Phys. Lett. B* 590 (2004), pp. 199–208. DOI: `10.1016/j.physletb.2004.02.040`. arXiv: `hep-ph/0310338`.

[156] P. Jimenez-Delgado and E. Reya. "Delineating parton distributions and the strong coupling". In: *Phys. Rev. D* 89.7 (2014), p. 074049. DOI: `10.1103/PhysRevD.89.074049`. arXiv: `1403.1852 [hep-ph]`.

[157] M. Gluck et al. "On the role of heavy flavor parton distributions at high energy colliders". In: *Phys. Lett. B* 664 (2008), pp. 133–138. DOI: `10.1016/j.physletb.2008.04.063`. arXiv: `0801.3618 [hep-ph]`.

[158] M. Gluck, E. Reya, and A. Vogt. "Dynamical parton distributions of the proton and small x physics". In: *Z. Phys. C* 67 (1995), pp. 433–448. DOI: `10.1007/BF01624586`.

[159] J. D. Bjorken. "Rapidity gaps and jets as a new physics signature in very high-energy hadron hadron collisions". In: *Phys. Rev. D* 47 (1993), pp. 101–113. DOI: `10.1103/PhysRevD.47.101`.

REFERENCES

[160] L. Lönnblad and R. Žlebčík. "Generation of central exclusive final states". In: *Eur. Phys. J. C* 76.12 (2016), p. 668. DOI: 10.1140/epjc/s10052-016-4513-y. arXiv: 1608.03765 [hep-ph].

[161] E. Gotsman, E. Levin, and U. Maor. "The Survival probability of large rapidity gaps in a three channel model". In: *Phys. Rev. D* 60 (1999), p. 094011. DOI: 10.1103/PhysRevD.60.094011. arXiv: hep-ph/9902294.

[162] A. B. Kaidalov et al. "Probabilities of rapidity gaps in high-energy interactions". In: *Eur. Phys. J. C* 21 (2001), pp. 521–529. DOI: 10.1007/s100520100751. arXiv: hep-ph/0105145.

[163] S. Ostapchenko and M. Bleicher. "Rapidity Gap Survival in Enhanced Pomeron Scheme". In: *Eur. Phys. J. C* 78.1 (2018), p. 67. DOI: 10.1140/epjc/s10052-018-5564-z. arXiv: 1712.09695 [hep-ph].

[164] Ch. Flensburg, G. Gustafson, and L. Lönnblad. "Exclusive final states in diffractive excitation". In: *JHEP* 12 (2012), p. 115. DOI: 10.1007/JHEP12(2012)115. arXiv: 1210.2407 [hep-ph].

[165] Ch. O. Rasmussen and T. Sjöstrand. "Hard Diffraction with Dynamic Gap Survival". In: *JHEP* 02 (2016), p. 142. DOI: 10.1007/JHEP02(2016)142. arXiv: 1512.05525 [hep-ph].

[166] G. Antchev et al. "First measurement of elastic, inelastic and total cross-section at $\sqrt{s} = 13$ TeV by TOTEM and overview of cross-section data at LHC energies". In: *Eur. Phys. J. C* 79.2 (2019), p. 103. DOI: 10.1140/epjc/s10052-019-6567-0. arXiv: 1712.06153 [hep-ex].

[167] P. Lebiedowicz, O. Nachtmann, and A. Szczurek. "Central exclusive diffractive production of $p\bar{p}$ pairs in proton-proton collisions at high energies". In: *Phys. Rev. D* 97.9 (2018), p. 094027. DOI: 10.1103/PhysRevD.97.094027. arXiv: 1801.03902 [hep-ph].

[168] Yang Li, Meijian Li, and James P. Vary. "Two-photon transitions of charmonia on the light front". In: (Nov. 2021). arXiv: 2111.14178 [hep-ph].

[169] K. Serafin et al. "Approximate Hamiltonian for baryons in heavy-flavor QCD". In: *Eur. Phys. J. C* 78.11 (2018), p. 964. DOI: 10.1140/epjc/s10052-018-6436-2. arXiv: 1805.03436 [hep-ph].

[170] J. Cepila et al. "Theoretical uncertainties in exclusive electroproduction of S-wave heavy quarkonia". In: *Eur. Phys. J. C* 79.6 (2019), p. 495. DOI: 10.1140/epjc/s10052-019-7016-9. arXiv: 1901.02664 [hep-ph].

[171] L. I. Schiff. *Quantum Mechanics*. McGraw-Hill, 1968, p. 79.

[172] E. Eichten et al. "Charmonium: The model". In: *Phys. Rev. D* 17 (11 June 1978), pp. 3090–3117. DOI: 10.1103/PhysRevD.17.3090. URL: https://link.aps.org/doi/10.1103/PhysRevD.17.3090.

[173] E. Eichten et al. "Erratum: Charmonium: The model". In: *Phys. Rev. D* 21 (1 Jan. 1980), pp. 313–313. DOI: 10.1103/PhysRevD.21.313.2. URL: https://link.aps.org/doi/10.1103/PhysRevD.21.313.2.

[174] E. Eichten et al. "Charmonium: Comparison with experiment". In: *Phys. Rev. D* 21 (1 Jan. 1980), pp. 203–233. DOI: 10.1103/PhysRevD.21.203. URL: https://link.aps.org/doi/10.1103/PhysRevD.21.203.

[175]   C. Quigg and J. L. Rosner. "Quarkonium level spacings". In: *Physics Letters B* 71.1 (1977), pp. 153–157. ISSN: 0370-2693. DOI: https://doi.org/10.1016/0370-2693(77)90765-1. URL: https://www.sciencedirect.com/science/article/pii/0370269377907651.

[176]   A. Martin. "A fit of upsilon and charmonium spectra". In: *Physics Letters B* 93.3 (1980), pp. 338–342. ISSN: 0370-2693. DOI: https://doi.org/10.1016/0370-2693(80)90527-4. URL: https://www.sciencedirect.com/science/article/pii/0370269380905274.

[177]   A. Martin. "Heavy Quark systems". In: *15th Rencontres de Moriond: II: Electroweak and Unified Theory Predictions*. 1980. URL: https://cds.cern.ch/record/133971.

[178]   N. Barik and S. N. Jena. "Fine-hyperfine splittings of quarkonium levels in an effective power-law potential". In: *Physics Letters B* 97.2 (1980), pp. 265–268. ISSN: 0370-2693. DOI: https://doi.org/10.1016/0370-2693(80)90598-5. URL: https://www.sciencedirect.com/science/article/pii/0370269380905985.

[179]   W. Buchmüller and S. H. H. Tye. "Quarkonia and quantum chromodynamics". In: *Phys. Rev. D* 24 (1 July 1981), pp. 132–156. DOI: 10.1103/PhysRevD.24.132. URL: https://link.aps.org/doi/10.1103/PhysRevD.24.132.